# DISSERTATION / DOCTORAL THESIS

Titel der Dissertation / Title of the Doctoral Thesis
## „Mathematical Optimization in Magnetic Simulation"

verfasst von / submitted by
## Dipl.-Ing. Dipl.-Ing. Florian Slanovc, BSc BSc

angestrebter akademischer Grad / in partial fulfilment of the requirements for the degree of
## Doktor der Naturwissenschaften (Dr.rer.nat.)

Wien, 2022 / Vienna, 2022

# Acknowledgements

and beyond with any of my other colleagues.

Life will always offer countless opportunities, but whatever may come in the future, all the experiences and knowledge of the past formative years will always remain a part of me. To all my companions in this exciting time, I wish all the best for their own journey and I look forward to the days when our paths cross again!

A big thank you goes to my family, who raised and educated me and are thus responsible for the essential foundations of this work. In addition to my parents and sister, I would especially like to thank my uncle Christian, who has supported me on my path since childhood and has also inspired me in my choice of studies.

Diana, thank you very much for your great support during the time I finished this thesis! It was far from easy for me, but you managed to help me stay calm and positive all the time. Every moment I needed it, you took the pressure off me and kept my eyes on all the beauty in life. You never let me doubt that I will succeed in my tasks — and that I love you with all my heart.

# Abstract

The optimization of certain processes is not only a topic in industry, economy and politics — also in magnetism and magnetic applications it is possible to optimize certain magnetic systems or the methods to simulate them. In this work, different optimization approaches in computational magnetism are presented.

A new probability-based simulation technique of write and read operations in magnetic recording media leads to an immense reduction of statistical fluctuation at almost constant computational cost. Furthermore, a parameter model enables the systematic investigation of the influence of write and material parameters of magnetic grains on the resulting readout signal. It shows which possible improvements have the most significant effect on the write quality. The analytical derivation of the magnetic field of homogeneously magnetized cylindrical tiles allows precise field calculation without any numerical methods for this geometry. The formulas and their implementation also include all special cases such as cylinder sectors, cylinder rings and full cylinders. In addition, the challenges of analytical magnetic field calculations in general are also discussed. By integrating an additional magnet into a magnetic linear position sensor system, it can become stable against small misalignments in the direction of the air gap. This idea is confirmed by optimizing the spatial dimensions of the additional magnet for the desired air gap stability. To optimize arbitrary magnet shapes, the topology optimization approach can be used. We propose a hybrid optimization algorithm that combines a reasonable global and local optimizer for this approach. It overcomes the problem of local optima occurrence and finds the global optimum, which significantly improves the optimization results. Moreover, the conditions for the existence of local and global optima are discussed at the theoretical level.

In all these examples, we show that the optimization approach always leads to a reduction in computational effort, an increase in accuracy, or an improvement in the magnetic system.

# Kurzfassung

Die Optimierung bestimmter Prozesse ist nicht nur ein Thema in Industrie, Wirtschaft und Politik — auch im Magnetismus und bei magnetischen Anwendungen ist es möglich, bestimmte magnetische Systeme oder die Methoden zu deren Simulation zu optimieren. In dieser Arbeit werden verschiedene Optimierungsansätze im computergestützten Magnetismus vorgestellt.

Eine neue wahrscheinlichkeitsbasierte Simulationstechnik von Schreib- und Auslesevorgängen in magnetischen Speichermedien führt zu einer immensen Reduktion statistischer Fluktuation bei nahezu gleichbleibendem Rechenaufwand. Darüber hinaus ermöglicht ein Parametermodell die gezielte Untersuchung des Einflusses von Schreib- und Materialparametern magnetischer Körner auf das resultierende Auslesesignal. Es zeigt, welche möglichen Verbesserungen sich am signifikantesten auf die Schreibqualität auswirken. Die analytische Herleitung des Magnetfeldes von homogen magnetisierten Zylinderkacheln erlaubt die präzise Feldberechnung ohne jegliche numerische Methoden für diese Geometrie. Die Formeln und ihre Umsetzung umfassen auch alle Sonderfälle wie Zylindersektoren, Zylinderringe und Vollzylinder. Darüber hinaus werden auch die Herausforderungen der analytischen Magnetfeldberechnung im Allgemeinen diskutiert. Durch den Einbau eines zusätzlichen Magneten in ein magnetisches lineares Positionssensorsystem kann dieses stabil gegenüber kleinen Ausrichtungsfehlern in Richtung des Luftspalts werden. Diese Idee wird durch Optimierung der räumlichen Abmessungen des zusätzlichen Magneten für die gewünschte Luftspaltstabilität bestätigt. Um beliebige Magnetformen zu optimieren, kann der Ansatz der Topologieoptimierung verwendet werden. Wir schlagen einen hybriden Optimierungsalgorithmus vor, der einen sinnvollen globalen und lokalen Optimierer für diesen Ansatz kombiniert. Er überwindet das Problem des Auftretens lokaler Optima und findet das globale Optimum, was die Optimierungsergebnisse erheblich verbessert. Außerdem werden die Bedingungen für das Vorhandensein lokaler und globaler Optima auf theoretischer Ebene diskutiert.

In all diesen Beispielen zeigen wir, dass der Optimierungsansatz immer zu einer Verringerung des Rechenaufwands, einer Erhöhung der Genauigkeit oder einer Verbesserung des magnetischen Systems führt.

# Acronyms

**App.** Appendix.

**BEM** boundary elements method.

**BSA** binary search algorithm.

**Chap.** Chapter.

**CSA** cuckoo search algorithm.

**Eq.** Equation.

**FEM** finite elements method.

**Fig.** Figure.

**FWHM** full width at half maximum.

**HA** hybrid algorithm.

**HAMR** heat-assisted magnetic recording.

**LLB** Landau-Lifshitz-Bloch.

**LLG** Landau-Lifshitz-Gilbert.

**NP** noise power.

**PRBS** pseudo random bit series.

**Sec.** Section.

**SNR** signal-to-noise ratio.

**SP** signal power.

**Subsec.** Subsection.

**Tab.** Table.

# Contents

# List of Tables

# List of Figures

# 1. Introduction

Computational modeling and simulation of magnetic systems has become a very important scientific discipline. Due to the increasing performance, capacity and availability of powerful computers, simulations have become an essential part of the magnetic device development process [1–4]. Even before the steps of experimental approval, prototyping and final mass production, they provide a tool to study physical trends and correlations without material costs and manufacturing difficulties. Both deterministic and stochastic approaches range from atomistic [5–9] and density functional theory [10–17], over coarse grained [18–25] and micromagnetic models [26–59] to simulation of the macroscopic Maxwell equation [47, 60–62] and cover several applications. However, as the complexity of the systems increases, the computational capabilities also reach certain limits, which is why reasonable modeling of the problems is of key importance. Focusing on the essentials and neglecting unimportant details is generally easier said than done and must be carefully weighed for each application. In some cases, however, detailed mathematical investigation opens up new possibilities and allows even more advantageous ways of modeling. Such optimizations in computational procedures can reduce the computational cost very drastically in many cases.

The following work will address the challenge of mathematical optimization in magnetic simulation methods in detail and present some key improvement approaches in various aspects and applications of magnetism. They have in common that the underlying investigations allow either a significant reduction in computational effort, an increase in accuracy for the same computational time, or simply an improvement of the whole magnetic system. Use cases include simulation of magnetic write and read-back signals in hard disk devices, magnetic sensing, optimal magnetic shapes, and analytical magnetic field computation. The focus is on both methodology and implementation.

The structure of the thesis is the following:

- Chapter 2 deals with the simulation of a write and read-back process in magnetic recording. While conventional techniques are very costly, requiring multiple simulations of an entire granular medium consisting of many magnetic grains, we show how an efficient combination of a pre-simulated switching probability phase diagram and probability mapping to the grains can greatly increase read-back statistics.

- Chapter 3 follows on from the previous one and shows how a mathematical parameterization of the switching probability phase diagram enables the study of how certain key parameters of the magnetic recording material change the quality of the read-back signal. This enables the observation of certain trends and shows which material properties have the greatest influence on the signal-to-noise ratio.

- Chapter 4 presents the analytical formulas for the magnetic field of the uniformly magnetized cylinder tile. They allow a fast and very accurate point-wise evaluation of the field, the relevance of which is also demonstrated by examples of magnetic simulations.

- Chapter 5 shows how a simple state-of-the-art magnetic linear position system can achieve airgap stability by optimizing an additional magnet and using the resulting stationary points in the magnetic field profile.

- Chapter 6 presents an optimization method for magnetic topology optimization based on a hybrid combination of state-of-the-art global and local optimization algorithms, which allows finding global optima of magnetic structures with respect to a given objective function in the presence of multiple local optima.

- Appendix A explains why the occurrence of singularities in the anti-derivatives of integrals is a serious problem in the analytical solution of magnetic fields for certain geometries and how they can be avoided.

- Appendix B gives an overview of the special functions used in Chap. 4, e.g. elliptic integrals of all three kinds.

- Appendix C provides the tables with the results of the analytical calculation of Chap. 4.

- Appendix D shows the computation of the variational derivatives of the objective function in topology optimization according to Chap. 6 and discusses their role in the solvability of the optimization problem.

- Appendix E gives a simple toy example showing that local optima can easily arise in magnetic topology optimization problems in general.

- Appendix F illustrates the behavior of the binary on/off algorithm used for local optimization in Chap. 6.

- Appendix G discusses the reason why finer mesh refinement does not always lead to better optima in the optimization problem and why this still does not mean that the geometry found is worse.

- Appendix H discusses the symmetry properties of the solution in topology optimization problems.

- Appendix I refers to the supplementary material of this thesis, the implementation of the formulas derived in Chap. 4 for the uniformly magnetized cylinder tile.

Each chapter has its own introductory and concluding sections that embed the optimization approach in its specific physical context and explain all background information and references.

# 2. Statistical analysis of read-back signals in magnetic recording on granular media

The comprehensive simulation of magnetic recording, including the write and read-back process, on granular media becomes computationally expensive if the magnetization dynamics of each grain are explicitly computed. In addition, in heat-assisted magnetic recording (HAMR), the writing of a single track becomes a random process since the temperature must be considered and thermal noise is involved. Further, varying grain structures of various granular media must also be taken into account to obtain correct statistics for the final read-back signal. Hence, it requires many repetitions of the write process to investigate the mean signal as well as the noise.

This chapter presents a method that improves the statistical evaluation of the whole recording process. The idea is to avoid writing the magnetization to one of its binary states. Instead, we assign each grain its probability of occupying one of its stable states, which can be calculated in advance in terms of a switching probability phase diagram. In the read-back process, we combine the probabilities to calculate a mean signal and its variance. Afterwards, repetitions on different media lead to the final read-back signal.

Using a recording example, we show that the statistical behavior of the evaluated signal-to-noise ratio (SNR) can be significantly improved by applying this probability mapping method, while the computational effort remains low.

Parts of this chapter have been previously published in [63] and have been reproduced with permission of the coauthors and in accordance with the publisher's policy. Content that was not generated by the author of this thesis is explicitly denoted, copyright is held by the American Institute of Physics (AIP).

## 2.1. Introduction

In state-of-the-art hard disk drives, which are used as storage media in personal computers as well as in server systems, the information is written as a sequence of bits on a granular medium consisting of magnetic grains. During writing, an applied magnetic field switches the magnetization direction of the magnetic grains in a specific direction [64]. Afterwards this direction can be detected by a reader module via the magnetic stray field. Due to the massive amount of data that is permanently produced, new technologies are required to increase the storage density of hard drives [65–69]. Micromagnetic simulation of write and read-back processes is therefore a valuable tool for analyzing new ideas [70]. Nevertheless, simulations of the entire write and read cycle are computationally expensive. Additionally, concepts such as HAMR [67] must consider temperature, which makes the underlying equation of the magnetization dynamics a stochastic partial differential equation that further increases the required computational effort [25]. Due to the stochastic nature of the solution obtained, repeated simulations are required to reduce the statistical error of the observed results to a sufficient low level [71–74]. In this work we present an efficient calculation method of the SNR based on probability theory. Instead of writing concrete bit series on granular media, we allocate every grain a certain switching probability. In the read-back procedure, those probabilities are further processed to obtain the signal and noise value of the written bit sequence. The goal of this method is a significant improvement of the statistical error within

the SNR evaluation of a given writing and read-back procedure. This reduces the number of necessary computation-intensive writing and read-back simulations required, resulting in an accurate SNR value.

## 2.2. Signal-to-noise ratio

Granular media for magnetic recording consist of single magnetic grains with strong uniaxial anisotropy perpendicular to the film plane, separated by non-magnetic grain boundaries. Due to the high uniaxial anisotropy of the grains, the assumption is valid that the magnetization of every single grain points either in positive or negative $z$-direction (perpendicular direction). Although each grain can only have two magnetic states $-1$ and $+1$, in reality writing a bit series has a stochastic nature. There are two reasons: First, in areas at the transitions between different bits, grains can have different states after consecutive writing processes, despite the fact that the same medium with the same grain pattern is used. Such grains have the probability to occupy the states $-1$ and $+1$ in the range of $[0, 100]\,\%$. Additionally, the randomized positions of grains in different granular media leads to a further stochastic effect, because the probability of the magnetization direction of each grain depends on the position of the grain within the medium during the writing process. A read-back module measures the magnetization of the grains across the bit pattern and produces a corresponding read-back signal $V(x)$ as a function of the down-track position $x$. Since the magnetization of the individual grains is random, $V(x)$ is a random variable with certain expectation value $\mathbb{E}[V(x)]$ and variance $\mathbb{V}[V(x)]$. The signal power (SP) and the noise power (NP) of the whole bit pattern between the down-track positions $x_{\text{start}}$ and $x_{\text{end}}$ can be defined according to e.g. [71] as

$$\text{SP} = \int_{x_{\text{start}}}^{x_{\text{end}}} \mathbb{E}[V(x)^2]\,\mathrm{d}x, \tag{2.1}$$

$$\text{NP} = \int_{x_{\text{start}}}^{x_{\text{end}}} \mathbb{V}[V(x)]\,\mathrm{d}x. \tag{2.2}$$

The quality criterium for a written bit series is the SNR defined by

$$\text{SNR} = \frac{\text{SP}}{\text{NP}}. \tag{2.3}$$

The determination of SP and NP via measurement or simulation is an important goal of magnetic recording as in [71, 72]. In this work we investigate and compare different numerical approaches based on statistic and probability calculation to determine these values in a computational accurate and non-expensive way. We further demonstrate the approaches on the example of simulating a writing process of HAMR, where the switching probability of grains is in particular affected by additional thermal fluctuation.

## 2.3. Switching probability phase diagram for single grains

The investigations in this work are based on the concept of switching probability phase diagrams as presented in [69]. The idea is the calculation of a single grain's switching probability dependent on its possible position on the recording track within the writing process. The advantage of this approach is that the phase diagram has to be computed only once and the switching probability can afterwards be extracted for an arbitrary amount of magnetic grains with no further computational effort. An example for the possible shape of such a diagram is given in Fig. 2.1. In the following, we always assume that

4

such a phase diagram is available. Since a sequence of two or more successive down or up bits can be summed up to one writing operation with multiple bit length, we split the writing process of each bit pattern to $S$ sequential alternating $-1$ or $+1$ mappings of the phase diagram onto the magnetic medium. The detailed realization of this sequential writing process depends on the different modeling approaches and will be discussed in the following sections.
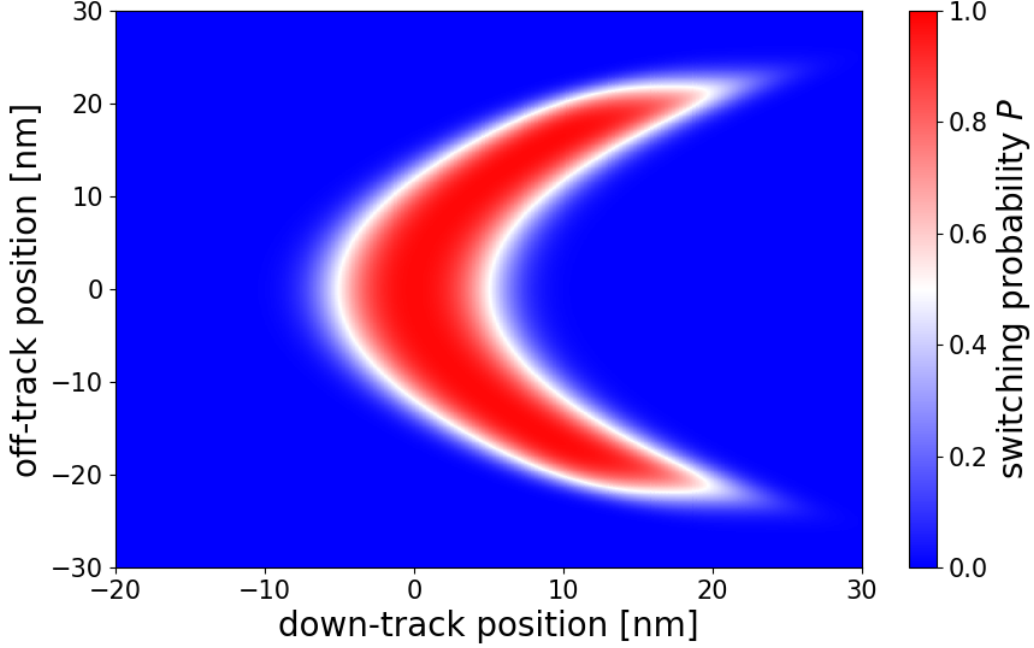


Figure 2.1.: Example for a switching probability phase diagram of one single grain.

## 2.4. Magnetization mapping on grains

### 2.4.1. Writing process

For each bit pattern containing $G$ magnetic grains, we use the phase diagram to extract the switching probability $p_j^i$ for magnetic grain $i, (i = 1, \ldots, G)$ in the $j$-th mapping step $(j = 1, \ldots, S)$ of the bit pattern according to Sec. 2.3. Due to the assumption of only two possible magnetic states $m^i = -1$ and $m^i = +1$ of grain $i$, we assume randomized initialization of the grains, i.e.

$$m_0^i := \text{rand}_0^i(0.5), \tag{2.4}$$

where $\text{rand}(p)$ denotes the outcome of a random experiment with possible outputs $-1$ and $+1$ with probabilities $1 - p$ and $p$. We then update the magnetization in each writing step $j$ recursively as it follows:

For given magnetization $m_{j-1}^i$ from the previous step, we calculate $m_j^i$ by differing two cases:

- If the $j$-th step writes a bit in $-1$ direction, we set:
    - $m_j^i := -1$, if $m_{j-1}^i = -1$

– $m^i_j := \mathrm{rand}^i_j(1 - p^i_j)$, if $m^i_{j-1} = +1$

• If the $j$-th step writes a bit in $+1$ direction, we set:
  – $m^i_j := \mathrm{rand}^i_j(p^i_j)$, if $m^i_{j-1} = -1$
  – $m^i_j := +1$, if $m^i_{j-1} = +1$

Doing $S$ mapping steps, this procedure leads to a sequence of grain magnetization and we receive the final magnetization of every grain $m^i := m^i_S \in \{-1, +1\}$. The result of such a writing procedure is shown in Fig. 2.2.
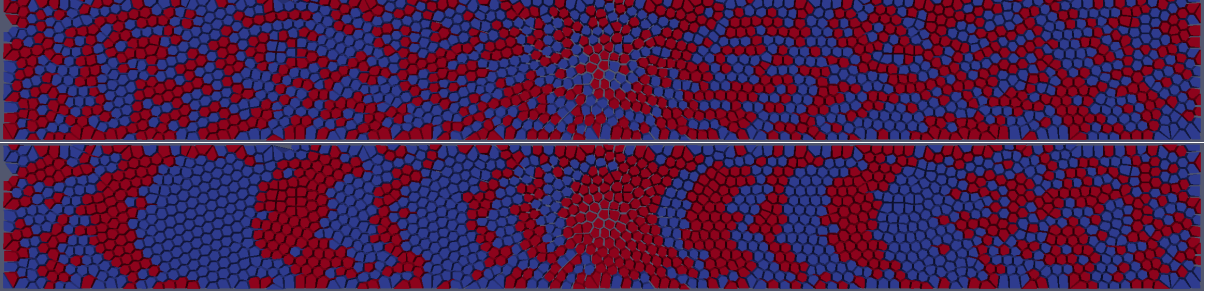


Figure 2.2.: Top: Randomly initialized granular medium ($500\,\mathrm{nm} \times 60\,\mathrm{nm}$ and a thickness of $8\,\mathrm{nm}$) with grain diameter of $4\,\mathrm{nm}$ and $1\,\mathrm{nm}$ gap between neighboring grains. Bottom: Granular medium after the simulated writing process of a pseudo-random bit sequence according to [70].

## 2.4.2. Read-back process

The reader module is defined via its sensitivity function, as defined in [75]. The voltage $V(x)$ of the reader in down-track position $x$ is given by the integral in [75, Eq. (1)]

$$V(x) = c_1 \cdot \int \mathbf{H} \cdot \mathbf{M}\, \mathrm{d}V_m \tag{2.5}$$

with the reader's sensitivity function $\mathbf{H}$, the magnetization of the media $\mathbf{M}$ and a reader dependent constant $c_1$. Since the magnetization is assumed to have negligible dependence on the $z$ direction and grains have strong uniaxial anisotropy, it degenerates to an area integral in the form

$$V(x) = \widetilde{c}_1 \cdot \int H_z \cdot M_z\, \mathrm{d}A_m \tag{2.6}$$

with a constant $\widetilde{c}_1$, which does not affect the SNR value, because both SP and NP are homogeneous of degree 2 in $V$ and therefore the constant $\widetilde{c}_1$ cancels in the ratio SNR = SP/NP. Without loss of generality we set $\widetilde{c}_1 := 1$. We further simplify the notation by skipping the $z$-index and set $H := H_z$ and $M := M_z$. The possible values for $M$ are $-1, +1$ or $0$ depending whether the position is located within a grain with $m^i = \pm 1$ or within the grain boundary. We can therefore rewrite the integral to a sum over the grains

$$V(x) = \sum_{i=1}^{G} \underbrace{\left( \int_{\mathrm{grain}_i} H\, \mathrm{d}A_m \right)}_{=:H^i_G} \cdot m^i = \sum_{i=1}^{G} H^i_G \cdot m^i, \tag{2.7}$$

where $H^i_G$ denotes the sensitivity across the grain $i$ for the reader module in position $x$. Moving the sensitivity function across the medium gives the detected read-back signal of the whole bit pattern.

## 2.4.3. Statistical evaluation

Repeating the previous step on $N$ granular media with different random grain structure and different outcomes of the random experiment rand($p$) (determining the magnetization according to the switching probabilities) leads to $N$ different signal trajectories $V_k$ ($k = 1, \ldots, N$). For large $N$ we can assume to receive a good estimation of SP and NP by substituting the squared expectation value and the variance in Eqs. (2.1) and (2.2) by their unbiased estimators

$$\mathbb{E}[V(x)^2] \approx \frac{1}{N} \overline{V(x)^2},  \tag{2.8}$$

$$\mathbb{V}[V(x)] \approx \frac{1}{N-1} \sum_{k=1}^{N} \left( V_k(x) - \overline{V(x)} \right)^2.  \tag{2.9}$$

Due to the fact that we deal with two uncertainties, the grain magnetization according to the random experiment and the position of the grains in each granular medium, the amount of necessary repetitions $N$ might be relatively large to receive a good statistic for both.

## 2.5. Probability mapping on grains

### 2.5.1. Writing process

In contrast to the previous magnetization mapping method, we now avoid setting the magnetic states to integer numbers $-1$ or $+1$ in every writing step. Instead, we use probability analysis calculation laws to determine the overall probability for the $-1$ or $+1$ state after the entire writing process. This approach allows to calculate the expectation value and variance of the magnetization of each grain and therefore also for the whole read-back signal afterwards.

As before, we consider the writing process of the entire series as a sequence of $S$ independent mapping steps of the bits. In the following, we describe in detail how the magnetization probability in the grains must be updated throughout this process.

In step $j$, the switching probability of the $i$-th grain is denoted by $p_j^i$ and again extracted from the phase diagram. We further denote the probability of grain $i$ for magnetization $+1$ after $j$ mapping steps with $P_j^i$. Since we assume only two possible states, the probability for magnetization $-1$ is therefore $1 - P_j^i$. We initialize with random magnetization, i.e. $P_0^i := 0.5$ for all $i = 1, \ldots, G$ and update the magnetization in each writing step $j$ recursively as it follows:

For given magnetization probability $P_{j-1}^i$, we calculate $P_j^i$ by differing two cases, which are also illustrated in Fig. 2.3. Given our convention that $P_j^i$ is the probability of state $+1$, we aim for this probability in each case:

- If the $j$-th step writes a bit in $-1$ direction, we set $P_j^i := P_{j-1}^i \cdot (1 - p_j^i)$, i.e. the probability that the grain was already in state $+1$ after step $j-1$, times the probability that it is not rewritten to $-1$ in step $j$ (see Fig. 2.3a).

- If the $j$-th step writes a bit in $+1$ direction, we set $P_j^i := P_{j-1}^i + (1 - P_{j-1}^i) \cdot p_j^i$, i.e. the probability that the grain was already in state $+1$ after step $j-1$, plus the probability that it was in state $-1$ after step $j-1$, times the probability that it is successfully rewritten to $+1$ in step $j$ (see Fig. 2.3b).

After writing the whole bit pattern within $S$ steps, we receive the final magnetization probabilities of the whole writing process $P^i := P_S^i$. These probabilities allow to further calculate the expectation value

and variance of the magnetization $m^i$ for each grain $i = 1, \ldots, G$ via the formulas

$$\mathbb{E}[m^i] = -1 \cdot (1 - P^i) + 1 \cdot P^i = 2 \cdot P^i - 1, \tag{2.10}$$

$$\mathbb{V}[m^i] = \mathbb{E}[(m^i)^2] - \mathbb{E}[m^i]^2 = 1 - (2 \cdot P^i - 1)^2$$
$$= 4 \cdot P^i \cdot (1 - P^i). \tag{2.11}$$

Note that in contrast to the previous section, $m^i$ is here regarded as a random variable and not determined by random numbers, so we have no statistical error so far.
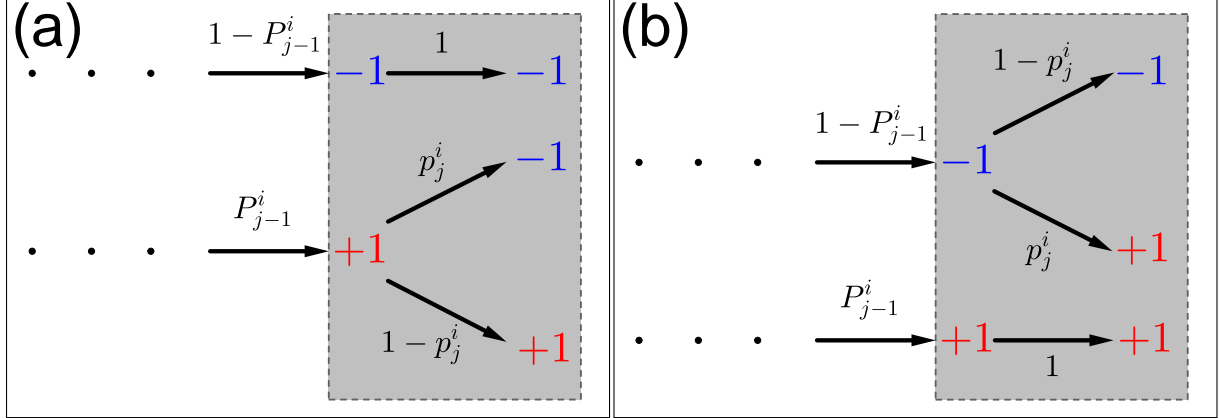


Figure 2.3.: Tree diagram of the different decisions and their corresponding switching probabilities. The gray background marks the $j$-th writing step in the case of a down-bit in (a) and an up-bit in (b). Based on to the previous magnetization of the grain with probabilities $1 - P^i_{j-1}$ and $P^i_{j-1}$ respectively, the magnetization gets either changed from $-1$ to $+1$ or vice versa with switching probability $p^i_j$ or remains in its original direction with probability 1.

### 2.5.2. Read-back process

The derivation of Eq. (2.7) again holds with the only difference that $m^i$ and therefore also $V(x)$ are random variables in this section. By applying $\mathbb{E}(\cdot)$ and $\mathbb{V}(\cdot)$ on both sides of the equation and using that $H^i_G$ is a deterministic value, we receive the expressions

$$\mathbb{E}[V(x)] = \sum_{i=1}^{G} H^i_G \cdot \mathbb{E}[m^i], \tag{2.12}$$

$$\mathbb{V}[V(x)] = \sum_{i=1}^{G} \left(H^i_G\right)^2 \cdot \mathbb{V}[m^i]. \tag{2.13}$$

Additional, we can also calculate the second moment of $V(x)$ by the well known identity

$$\mathbb{E}[V(x)^2] = \mathbb{V}[V(x)] + \mathbb{E}[V(x)]^2. \tag{2.14}$$

### 2.5.3. Statistical evaluation

We again repeat the writing and read-back process on $N$ different granular media. The outcome are $N$ different signal trajectories $V_k$ ($k = 1, \ldots, N$), where $V_k(x)$ denotes a random variable for every $k$ and down-track position $x$. The results of the previous subsection hold for each single medium. To combine them to a final SNR outcome, we state the following lemma for a discrete random variable in a specified random experiment:

**Lemma 1.** *Let $X_k$ be a discrete random variable for all $k = 1,\ldots,N$ with corresponding probability distributions $P(X_k = x_{k\ell}) = p_{k\ell}$ for all $\ell = 1,\ldots,n_k$. We consider the two-step random experiment:*

- *Choose $X_k \in \{X_1,\ldots,X_N\}$ randomly with probability $p_k$.*

- *Do the corresponding random experiment with random variable $X_k$.*

*The final outcome can be described by an overall random variable $X$. Then it holds for $m \in \mathbb{N}$:*

$$\mathbb{E}[X^m] = \sum_{i=1}^{N} p_k \cdot \mathbb{E}[X_k^m] \tag{2.15}$$

*Proof.* Per definition for the expected value of $X^m$ (i.e. the $m$-th moment of $X$), we have to sum over the product of all possible outcomes and their corresponding probabilities. In our case, we can write that as

$$\mathbb{E}[X^m] = \sum_{k=1}^{N} \sum_{\ell=1}^{n_k} x_{k\ell}^m \cdot p_k \cdot p_{k\ell} = \sum_{k=1}^{N} p_k \cdot \underbrace{\sum_{\ell=1}^{n_k} x_{k\ell}^m \cdot p_{k\ell}}_{=\mathbb{E}[X_k^m]}$$

$$= \sum_{k=1}^{N} p_k \cdot \mathbb{E}[X_k^m], \tag{2.16}$$

which concludes the proof. □

We now assume that the grain pattern of each granular medium has the same probability $1/N$. For the moments of the overall trajectory $V(x)$, we can apply Lemma 1 for $m = 1$ and $m = 2$ to get

$$\mathbb{E}[V(x)] = \frac{1}{N} \sum_{k=1}^{N} \mathbb{E}[V_k(x)], \tag{2.17}$$

$$\mathbb{E}[V(x)^2] = \frac{1}{N} \sum_{k=1}^{N} \mathbb{E}[V_k(x)^2]. \tag{2.18}$$

Those values can easily be determined by the results for each trajectory in Eqs. (2.12) and (2.14) and combination also leads to

$$\mathbb{V}[V(x)] = \mathbb{E}[V(x)^2] - \mathbb{E}[V(x)]^2. \tag{2.19}$$

Finally with Eqs. (2.17) and (2.19), we have two formulas for the integrands in Eqs. (2.1) and (2.2) and are able calculate the SP and NP.

In contrast to the magnetization mapping method of the previous section, we avoid the statistical error coming from the "projections" of the probabilities to the $-1$ and $+1$ magnetization states. The only statistical uncertainty probability mapping method comes from the random pattern of the grains in the different media.

## 2.6. Results and discussion

We now compare the SNR calculation methods of Secs. 2.4 (magnetization mapping) and 2.5 (probability mapping) based on a concrete example. Therefore we use the switching probability phase diagram in Fig. 2.1 and for demonstration purpose we step-wise reduce the curvature of its shape (see [73, 74]).

For each curvature we calculate the SNR by writing on $N = 50$ different granular media and determine the read-back signal $V(x)$ via a Gaussian shaped reader sensitivity function with a full width at half maximum of 13.26 nm in down-track and 30.13 nm in off-track direction. The SNR values are plotted in Fig. 2.4. We clearly observe that for the magnetization mapping method, the statistical variations on 50 different granular media have large impact on the calculated SNR values, so no clear trend of the SNR can be observed. When we use the probability mapping method, we can massively reduce those variations and receive a much smoother curve with a clear trend, even though the same number of granular media was used. The reason for the improvement is the avoided reduction of the magnetization probability to one of the magnetic end states $-1$ and $+1$ for each grain, which leads to a statistical error in the magnetization mapping method. Since each bit pattern contains a large number of grains, many repeated writings are necessary to obtain a sufficiently accurate mean read-back signal and its variance. The more sophisticated probability mapping writing method prevents this statistical issue and leads to very accurate results with comparatively few repetitions. Furthermore it is important to note that an implementation of both methods has asymptotically the same computational effort. In the writing process, the allocations of the magnetization or probabilities bases on similar approaches and have to be done $S$ times for $G$ grains in both methods. The additional calculation of $G$ times Eqs. (2.10) and (2.11) can be neglected. The read-back process requires summations over $R$ data points for every down-track position $x$ in both cases. The only noteworthy difference is that for the probability mapping method, it is unavoidable to calculate the grain sensitivity $H_G^i$ explicitly, since the square is used for the variance formula. This can be achieved by clever rearrangement of the sum and does not cause additional effort. In the final step the statistical evaluation in both cases is done via summation over $N$ granular media.
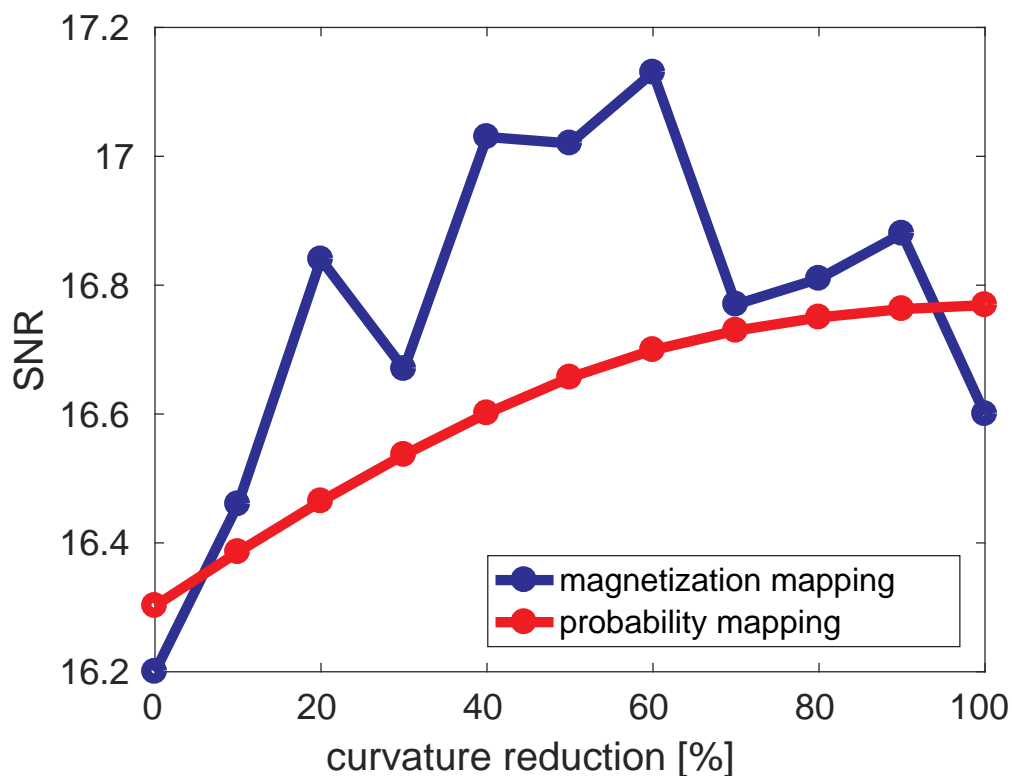


Figure 2.4.: Comparison of the SNR of a pseudo random bit sequence for varied bit curvature calculated by the methods of Secs. 2.4 and 2.5.

## 2.7. Conclusion and outlook

In this chapter we presented a SNR calculation method based on probability theory. We could show that for a given switching probability phase diagram and given granular media it is statistically unfavorable to emulate the procedure of a real write processes in which each grain obtains a certain magnetic state according to its switching probability. Although it is the more obvious way to receive an estimate for the SNR, it reduces the switching probability $p \in [0, 100]\,\%$ to a binary value $m \in \{-1, +1\}$ representing the direction of the magnetization, which clearly means a loss of information. We were able to show that a prevention of this loss leads to a more sophisticated evaluation, which significantly improves the statistic and can furthermore be applied without additional computational effort. Although we demonstrated our approach as an application for SNR calculation in HAMR, similar ideas could also be used for conventional recording and other statistical evaluations on granular media. Since we successfully eliminated the statistical error of the reduction from $p$ to $m$, the only statistical error in our SNR value remains from the pattern of different granular media. The question arises whether this error could also be corrected by a suitable grain size distribution model instead of randomly sampling $N$ different media.

# 3. Systematic parameterization of HAMR switching probabilities and the consequences for the resulting SNR

The SNR of a bit series written with HAMR on granular media depends on a large number of different parameters. The choice of material properties is essential for the obtained switching probabilities of single grains and therefore for the written bits' quality in terms of SNR. Studies where the effects of different material compositions on transition jitter and the switching probability are evaluated were done, but it is not obvious, how significant those improvements will finally change the received SNR. To investigate that influence, we developed an analytical model of the switching probability phase diagram, which contains independent parameters for, inter alia, transition width, switching probability and curvature. Different values lead to corresponding bit patterns on granular media, where a reader model detects the resulting signal, which is finally converted to a parameter dependent SNR value. For grain diameters between 4 and 8 nm, we show an increase of $\sim 10$ dB for bit lengths between 4 and 12 nm, an increase of $\sim 9$ dB for maximum switching probabilities between 0.64 and 1.00, a decrease of $\sim 5$ dB for down-track-jitter parameters between 0 and 4 nm, a decrease of 1 to 3 dB for off-track-jitter parameters between 0 and 50 K and an increase of $\sim 0.5$ dB for reduced bit curvature. Those results are furthermore compared to the theoretical formulas for the SNR. We obtain a good agreement, even though we show slight deviations.

Parts of this chapter have been previously published in [76] and have been reproduced with permission of the coauthors and in accordance with the publisher's policy. Content that was not generated by the author of this thesis is explicitly denoted, copyright is held by the American Institute of Physics (AIP).

## 3.1. Introduction

The quality of a written bit pattern on granular media is mostly determined by the SNR. A high SNR means low noise and a sharp edge between neighboring bits. The SNR depends either on suitable magnetic material properties of the grains to provide a good switching probability in the writing process but also on the size and position distribution of the grains in the granular medium. There are different methods to calculate the switching probability of a grain model during HAMR, which is subject to a heat pulse and an external magnetic field [67]. One method is solving the stochastic Landau-Lifshitz-Gilbert (LLG) equation for each atom of the grain [8], another is solving the stochastic coarse-grained Landau-Lifshitz-Bloch (LLB) equation [25]. Depending on the down-track position $d$ and off-track position $y$, the repetition of switching trajectories for a given parameter set results in the approximate switching probability of a grain. Calculating the probability for various $d$ and $y$ yields a phase diagram of the writing process. Instead of the off-track direction $y$, the peak temperature $T_{peak}$ can be used, because then there is no need to specify the maximum temperature at the track center beforehand. For each peak temperature $T_{peak}$ the off-track direction $y$ can be easily determined under the assumption of a Gaussian heat pulse via the relation

$$T_{peak}(y) = (T_{max} - T_{min}) \cdot \exp\left(-\frac{y^2}{2\sigma^2}\right) + T_{min}, \tag{3.1}$$

where $T_{\text{min}}$ and $T_{\text{max}}$ are the overall minimum and maximum temperatures of the whole heat pulse and $\sigma = \text{FWHM}/\sqrt{8\ln 2}$ its standard deviation related to its full width at half maximum (FWHM) [69]. The final phase diagrams for the switching probability $P(d, T_{\text{peak}})$ as in [69] allow the simulation of writing processes of bit patterns on granular media as we will describe in Sec. 3.3. The advantage of this approach is that the phase diagram has to be created only once and the switching probability can afterwards be extracted for an arbitrary amount of magnetic grains with no further computational effort. The disadvantage is that every grain is regarded individually and therefore it is not obvious how to take stray-field interactions into account. This can be done by adjusting the intrinsic distribution of the Curie temperature as shown in [77]. The phase plots contain much information about the size and characteristics of the magnetic grains as well as the parameters of the writing process (velocity, external applied field etc.). In [78] for instance, the shape of the phase diagram depending on the composition of a bi-layer material is investigated. This information only refers to a single grain but a priori tells very little about the resulting SNR of the read-back signal of a bit series. Hence, there is need to systematically investigate the influence of changes of the phase diagram on the final SNR. In this work we will develop a mathematical model of a phase diagram, which allows to vary certain parameters and perform writing processes with the resulting diagrams. The read-back signal then gives some indication of the potential SNR-improvement. The mathematical formulation of the phase plot is presented in Sec. 3.2. In Sec. 3.3, we will describe the simulation of the writing and read-back processes with the method of Chap. 2 and Sec. 3.4 will summarize and discuss the results of the received SNR and compare those to theoretical formulas.

## 3.2. Mathematical model of a phase plot

In HAMR the switching probability of a magnetic grain can be represented as a phase diagram. In contrast to the previous chapter and Fig. 2.1, we make use of the symmetric heat pulse and replace the off-track position coordinate by the corresponding peak temperature at that position according to Eq. (3.1). As in [69], the area of the highest switching probability has a C-like shape in the coordinate plane spanned by the down-track position $d$ and the peak temperature of the heat pulse $T_{\text{peak}}$ (see e.g. Fig. 3.1). In the following we define an analytical function $P(d, T)$, which allows to fit such a phase plot.

### 3.2.1. Model parameters

We use eight parameters that fully determine the shape of the phase plot:

- down-track-jitter parameter: $\sigma_d$ [nm]

- off-track-jitter parameter: $\sigma_o$ [K]

- maximum switching probability: $P_{\text{max}}$

- half maximum temperature: $F$ [K]

- bit length: $b$ [nm]

- curvature parameter: $p_1$ [nm/K$^2$]

- position in $T_{\text{peak}}$-direction: $p_2$ [K]

- position in $d$-direction: $p_3$ [nm]

The detailed significance of those values for the model is introduced in Subsec. 3.2.2.
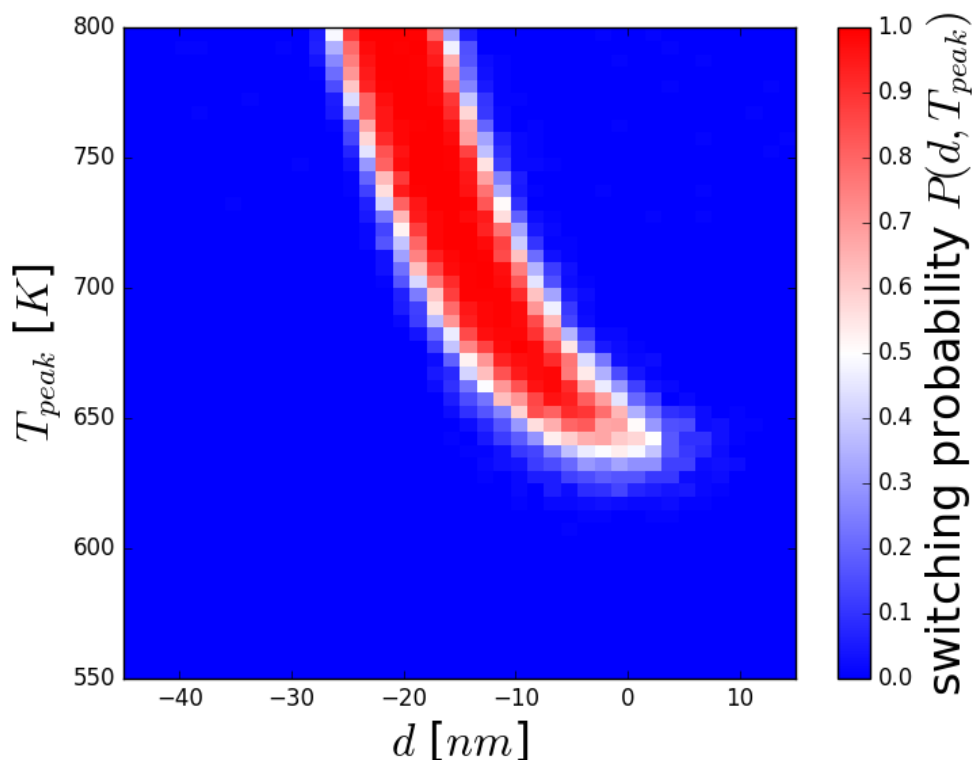
Figure 3.1.: Simulated switching probability phase diagram for a grain diameter of $D = 7\,\mathrm{nm}$ via LLB model and material parameters as shown in Tab. 3.1.

### 3.2.2. Mathematical model

We now define the model function $P$ in three steps with two help functions $h_1$ and $h_2$, which depend on the upper parameters. First the down-track- and off-track-jitter is modeled as the slope of the probability function graph along a cut through the phase diagram for fixed $d$ and $T_{\text{peak}}$, respectively. As in [78] we use the Gaussian cumulative distribution function

$$\Phi(x, \mu, \sigma) = \frac{1}{2}\left(1 + \text{erf}\left(\frac{x - \mu}{\sqrt{2}\sigma}\right)\right) \tag{3.2}$$

with the properties

$$\lim_{x \to -\infty} \Phi(x) = 0, \lim_{x \to +\infty} \Phi(x) = 1, \Phi(\mu) = \frac{1}{2} \tag{3.3}$$

and $\sigma$ determining the slope of $\Phi$. We write

$$h_1(d, T) := \Phi(d, 0, \sigma_d) \cdot \Phi(T, F, \sigma_o) \tag{3.4}$$

and receive a function as in Fig. 3.2a that models the down-track-jitter parameter $\sigma_d$ via the vertical and the off-track-jitter parameter $\sigma_o$ via the horizontal contour sharpness. Furthermore, the half maximum temperature $F$ denotes the temperature at which the function value is reduced to half of its maximum in a fixed down-track position. When a bit is written, the switching probability should again decrease after a certain writing distance in down-track direction, therefore we additionally multiply a mirrored and shifted function $h_1$ in the form

$$h_2(d, T) := h_1(d, T) \cdot h_1(b - d, T) \tag{3.5}$$

and receive a function graph as in Fig. 3.2b. The maximum function value is one, but note that according to the asymptotic convergence of $\Phi$, this only holds in the limit of large bit lengths $b$ and temperatures $T$. Finally we receive the complete model via transformation into a parabolic shape via

$$P(d, T) := P_{\text{max}} \cdot h_2\left(d - \left(p_1(T - p_2)^2 - p_3\right), T\right) \tag{3.6}$$

to get the C-like curvature as in Fig. 3.2c, which is usually observed [69]. The factor $P_{\text{max}}$ furthermore represents the (asymptotic) maximum of the function. If $P_{\text{max}} \approx 1$, the function value at the half maximum temperature $F$ reaches approximately 0.5. i.e. the probability for each magnetization direction becomes $\approx 50\,\%$. Therefore, $F$ can be interpreted as approximately the temperature at which the coercivity of the material is just compensated by the external field. In literature, this temperature is often referred to as the write temperature [79, 80]. The impact of the model parameters defined in Subsec. 3.2.1 on the shape of the model function can also be visually observed in Fig. 3.2c.

### 3.2.3. Reference system and variation of the parameters

We aim to investigate the influence of the described switching probability phase plots on the resulting SNR. Of course, it is desirable to start all variations from a realistic basic parameter set. We therefore compute reference phase plots via LLB model as in [25]. Thereby we use parameters of FePt-like material according to the Advanced Storage Technology Consortium [81] with bulk Curie temperature $T_C^{\text{bulk}} = 708.9\,\text{K}$ and anisotropy field $H_k = 8.2\,\text{T}$ at room temperature $T = 300\,\text{K}$ that can be seen in
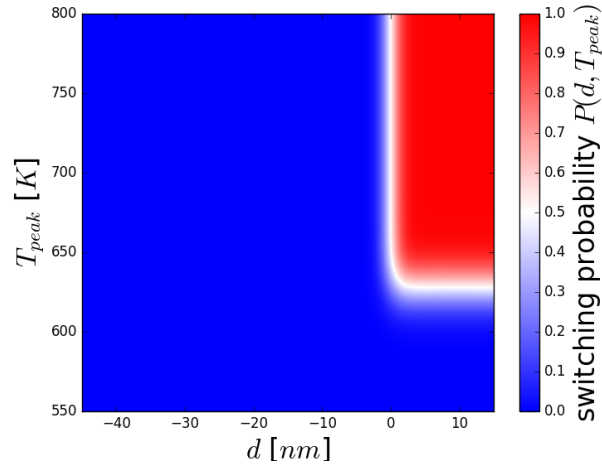
(a)
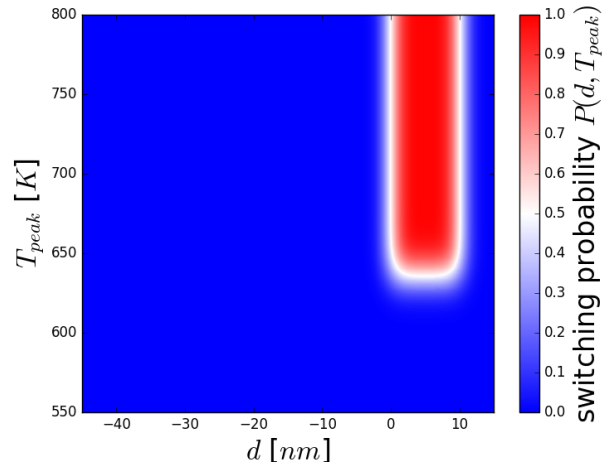


(b)
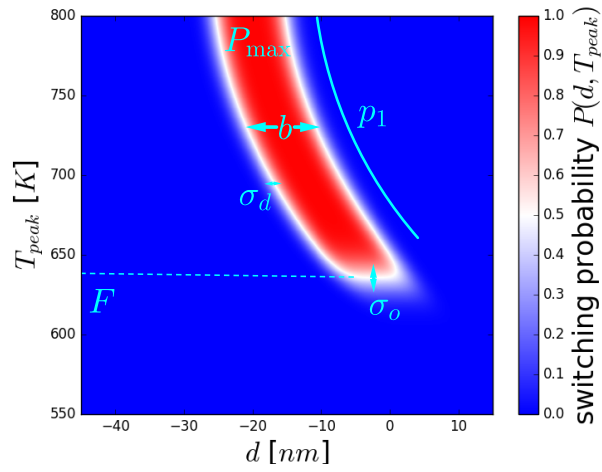


(c)

Figure 3.2.: (a) and (b) show the graphs of the help functions $h_1$ and $h_2$. In (c), the final model phase plot can be observed with detailed impact of the different model parameters of Subsec. 3.2.1.

Tab. 3.1. The grain height is 8 nm and the external magnetic field is trapezoidal with 0.8 T, tilted with an angle of 22° with respect to the $z$-direction and a duration of 0.67 ns including rise and fall times of 0.05 ns each. Further a moving Gaussian heat pulse with a velocity of $v = 15$ m/s and a FWHM of 60 nm is assumed. Note that in this simulation step each grain is considered identical, so the uncertainty of the switching process imposed on the switching probability is an exclusive consequence of thermal effects. Possible $T_C$ and $H_k$ variations could also be considered in this step [77] but are neglected in the context of this work.

The resulting phase diagram for a grain diameter of $D = 7$ nm is illustrated in Fig. 3.1. The reference parameters of the plots in Fig. 3.2 are determined via a least square fit of the simulated diagram in Fig. 3.1. For different grain sizes the eight resulting fitted parameters according to Subsec. 3.2.1 are given in Tab. 3.2 and the estimated fitting parameter errors in Tab. 3.3.

In Sec. 3.4 we investigate the influence of $\sigma_d, \sigma_o, P_{\max}, b$ and $p_1$ on the read-back SNR. The parameter variations are taken in the ranges of Tab. 3.4 and in Fig. 3.3a-e their influence on the phase diagram is visualized.

## 3.3. Bit patterns on granular media

We aim to use a phase plot, which determines the switching probability of a single cylindrical grain, to write bit patterns on granular media. In the following, we describe the framework in which this is possible. Each medium contains approximately equally sized magnetic grains with a diameter of $D = 4, 5, 6, 7$ or 8 nm. The diameter's standard deviation of about 0.31 nm is neglected in the following writing process, so we assume that each grain within the granular medium has the same size. Nonmagnetic material separates neighboring grains by $B = 1$ nm (see Fig. 3.4, illustrated for a diameter of 4 nm). We assume a Gaussian heat pulse moving across the medium with a velocity of $v = 15$ m/s, a FWHM of 60 nm and a maximum temperature of $T_C + 60$ K, which is slightly dependent on the Curie temperature $T_C$ for different grain sizes of about 700 K (see Fig. 3.5). This results in a maximum thermal gradient of about 11 K/nm. The writing process is justified due to the assumption that every grain is approximated by a cylinder with a certain diameter that is subject to the Gaussian heat pulse and trapezoidal magnetic field. The peak temperature of the heat pulse $T_{\text{peak}}$ depends on the off-track position $y$ of the grain (see Fig. 3.5) via Eq. (3.1). We neglect a spatially varying temperature within a single grain and therefore assume, that the whole grain volume receives the same temperature within the entire grain. The magnetic field is aligned according to the written pseudo random bit series (PRBS) of [70]:

$$(-1\ +1\ +1)\ -1\ -1\ -1\ -1\ -1\ +1\ +1\ +1\ -1\ -1\ +1\ -1\ -1\ -1\ +1\ -1$$
$$+1\ -1\ +1\ +1\ +1\ +1\ -1\ +1\ +1\ -1\ +1\ -1\ -1\ +1\ +1\ (-1\ -1\ -1),$$

| | |
|---|---|
| $K_1$ [J/m$^3$] | $6.6 \cdot 10^6$ |
| $J_{k,l}$ [J/link] | $6.72 \cdot 10^{-21}$ |
| $\mu_s$ [$\mu_B$] | 1.6 |
| $J_s$ [T] | 1.35 |
| $a$ [nm] | 0.24 |
| $\lambda$ | 0.02 |

Table 3.1.: Used material parameters in the LLB model.
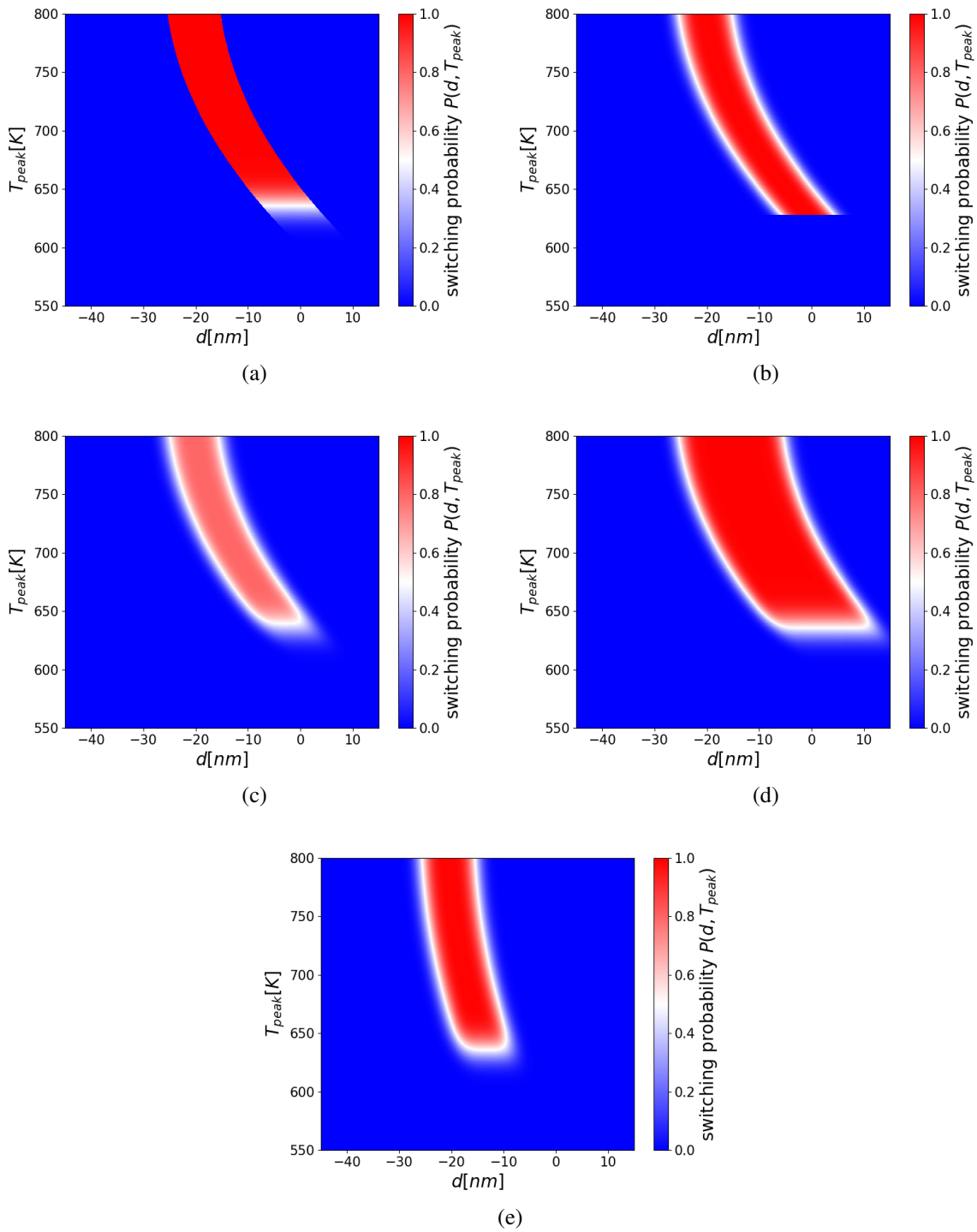
Figure 3.3.: In contrast to Fig. 3.2c, each picture shows only one changed parameter value. The phase plot in (a) has a reduced down-track-jitter parameter $\sigma_d = 0\,\text{nm}$, in (b) a reduced off-track-jitter parameter $\sigma_o = 0\,\text{K}$, in (c) a reduced $P_{\max} = 0.8$, in (d) an extended bit-length of $b = 20\,\text{nm}$ and in (e) a reduced curvature parameter $p_1$ by $60\,\%$.

where -1 represents a down and +1 an up bit (i.e. field in negative, respectively positive direction). A sequence of two or more successive down respectively up bits is summed up to one writing process with multiple bit length. The $2 \times 3$ bits in the brackets of the are used for padding and the remaining 31 bits in-between represent the desired bit series, the signal is always truncated by three bit lengths on both sides. The stray-field is not taken into account directly and thus different grains do not influence the switching probability of each other. Its impact is only considered via an added variation to $T_C$ as discussed in [77]. Under these assumptions, writing is done by mapping the switching probabilities of the corresponding phase plot to the grains of the granular medium according to their positions. For the evaluation of the entire writing and read-back process over 50 random granular media we use the method of Chap. 2 to finally obtain the SNR. The reader module is defined via its sensitivity function as discussed in [75] and illustrated in Fig. 3.6a. A possible mean reader signal is illustrated in Fig. 3.6b.



Figure 3.4.: Visualization of a granular medium with approximately equally sized magnetic grains (here: 4 nm diameter) surrounded by nonmagnetic material separating neighboring grains by 1 nm.

| | grain diameter | | | | |
| --- | --- | --- | --- | --- | --- |
| | 4 nm | 5 nm | 6 nm | 7 nm | 8 nm |
| $\sigma_d$ [nm] | 2.51 | 2.03 | 1.74 | 1.50 | 1.37 |
| $\sigma_o$ [K] | 27.7 | 22.5 | 18.0 | 14.4 | 13.6 |
| $P_{\max}$ | 0.993 | 0.995 | 0.993 | 0.997 | 1.000 |
| $F$ [K] | 571 | 602 | 617 | 628 | 639 |
| $b$ [nm] | 10.2 | 10.2 | 10.3 | 10.2 | 10.1 |
| $p_1$ [$10^{-4}$ nm/K$^2$] | 3.28 | 3.88 | 4.33 | 4.89 | 5.16 |
| $p_2$ [K] | 839 | 839 | 836 | 830 | 832 |
| $p_3$ [nm] | 29.5 | 27.5 | 26.5 | 25.8 | 25.8 |

Table 3.2.: Reference parameters that are evaluated via least square fit of the simulated phase diagrams for grain diameters from 4 to 8 nm.
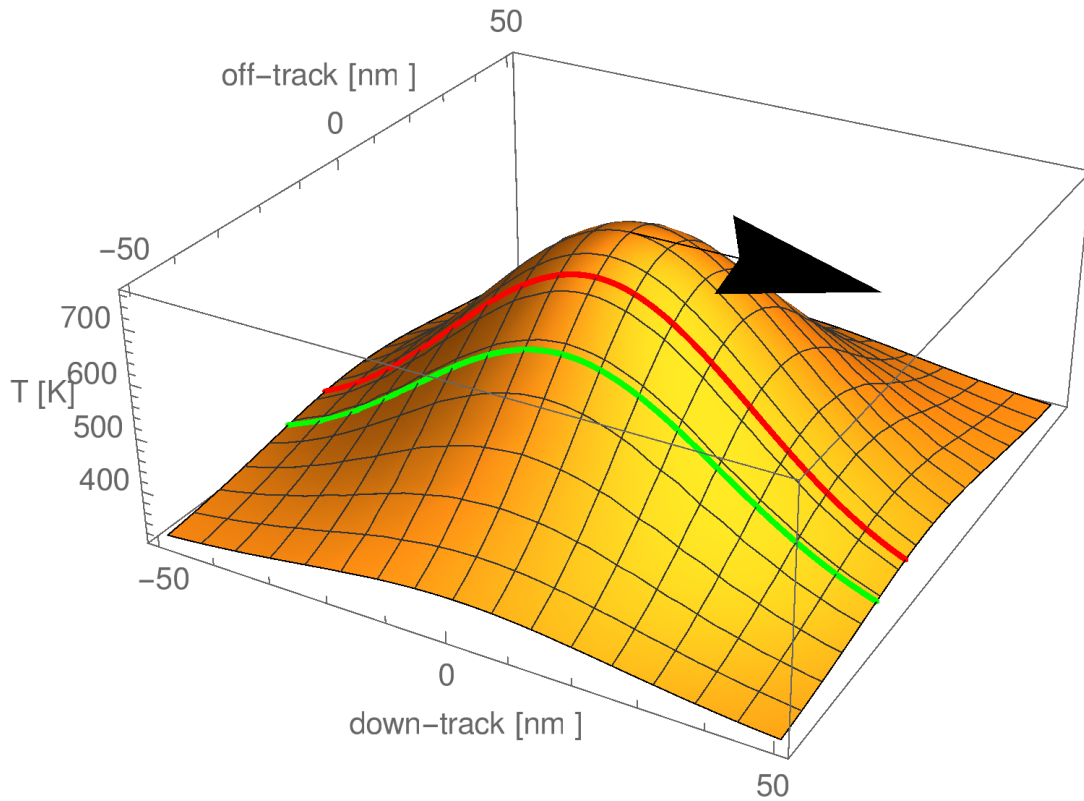
Figure 3.5.: Visualization of the applied Gaussian heat pulse that moves across the granular medium in the direction of the arrow. Together with an applied magnetic field it performs the writing process. The red and green curve demonstrate that grains are exposed to different peak temperatures depending on their off-track position.



(a)



(b)
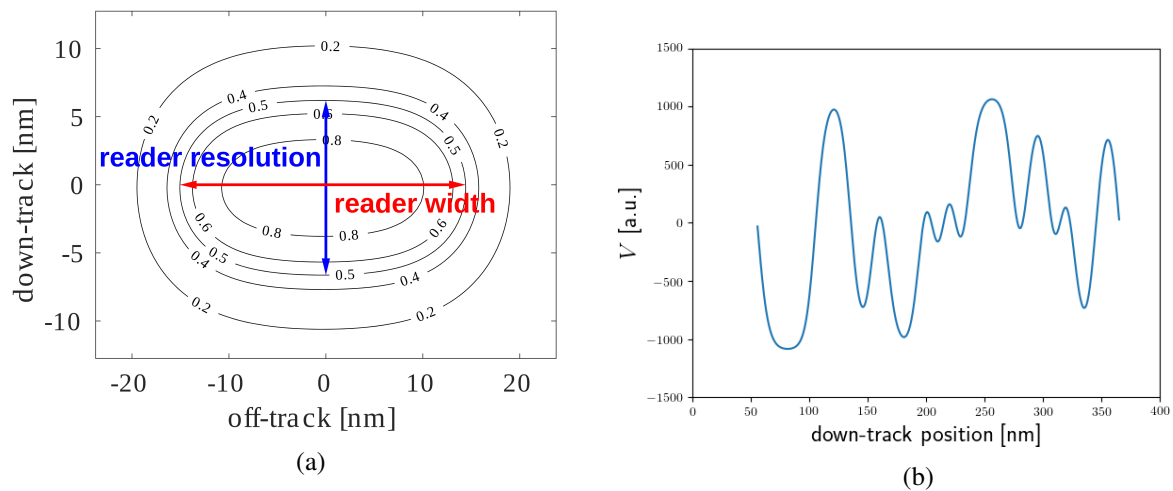
Figure 3.6.: (a): Contour plot of the *z*-component of the sensitivity function. The reader width (width of the 0.5 contour line in off-track direction) is 30.13 nm and the reader resolution (width of the 0.5 contour line in down-track direction) is 13.26 nm. (b) Example of a mean read-back curve of the 31 bit PRBS determined by the reader with sensitivity function in (a) across granular media as in Fig. 2.2, bottom.

## 3.4. Results and discussion

### 3.4.1. SNR curves

For various parameter variations, the resulting SNR curves are plotted in Fig. 3.7. For selected values of the parameters, Figs. 3.8 - 3.12 visualize the corresponding bit pattern. Note that in this subsection, apart from the varied parameter, the other parameters are fixed and have the values of Tab. 3.2. The impact on the SNR can clearly be observed. The curves describing the dependence on the bit length, curvature, $P_{\max}$, down-track-jitter $\sigma_d$ and off-track-jitter $\sigma_o$ demonstrate an increase of $\sim 10\,\text{dB}$ for bit lengths between 4 and 12 nm, an increase of $\sim 0.5\,\text{dB}$ for reduced curvature, an increase of $\sim 9\,\text{dB}$ for maximum switching probabilities between 0.64 and 1.00, a decrease of $\sim 5\,\text{dB}$ for down-track-jitter parameters between 0 and 4 nm and a decrease of 1 to 3 dB for off-track-jitter parameters between 0 and 50 K. Note that for small bit lengths the reader needs a better resolution (see Fig. 3.6a) to achieve a suitable read-back signal, therefore we scale the reader resolution in down-track direction $R$ according to the bit length $b$ in the form

$$R = R_0 \cdot \frac{b}{b_0}, \tag{3.7}$$

where $R_0 = 13.26\,\text{nm}$ denotes the initial reader resolution (see Fig. 3.6a) and $b_0 = 10.2\,\text{nm}$ is the mean initial bit length of Tab. 3.2 according to the phase diagram. The results in Fig. 3.7, top show a sharp decrease of the SNR for low bit lengths, so the possible reachable linear density is limited. $P_{\max}$ and $\sigma_d$ are clearly two parameters with significant impact on the SNR, so it is recommendable to consider those values in terms of material optimization as in [78]. Furthermore the variation of two parameters simultaneously lead to SNR contours as in Fig. 3.13.

### 3.4.2. Comparison with theory

In [66], the SNR-dependence on the media magnetic transition parameter $a$, grain size $S$ ($S = D + B$, i.e. sum of grain diameter $D$ and nonmagnetic boundary $B$, see Fig. 3.4), bit length $b$, read-back pulse width $T_{50}$ and reader width $W$ is given by

$$\text{SNR} \propto \left(\frac{b}{a}\right)^2 \cdot \frac{T_{50}}{b} \cdot \frac{W}{S}. \tag{3.8}$$

In the following, we avoid other SNR dependencies on the off-track-jitter $\sigma_o$, maximum switching probability $P_{\max}$ and the curvature parameter $p_1$ by keeping those parameters constant and associate them

|  | grain diameter | | | | |
|---|---|---|---|---|---|
|  | 4 nm | 5 nm | 6 nm | 7 nm | 8 nm |
| $\Delta\sigma_d$ [nm] | 0.04 | 0.02 | 0.02 | 0.02 | 0.02 |
| $\Delta\sigma_o$ [K] | 0.6 | 0.5 | 0.4 | 0.3 | 0.3 |
| $\Delta P_{\max}$ | 0.007 | 0.005 | 0.003 | 0.003 | 0.003 |
| $\Delta F$ [K] | 0.5 | 0.3 | 0.3 | 0.2 | 0.2 |
| $\Delta b$ [nm] | 0.07 | 0.04 | 0.03 | 0.03 | 0.02 |
| $\Delta p_1$ [$10^{-4}\,\text{nm}/\text{K}^2$] | 0.04 | 0.05 | 0.05 | 0.05 | 0.05 |
| $\Delta p_2$ [K] | 2 | 2 | 1 | 1 | 1 |
| $\Delta p_3$ [nm] | 0.1 | 0.1 | 0.1 | 0.1 | 0.1 |

Table 3.3.: Estimated fitting parameter errors of the fit values of Tab. 3.2.
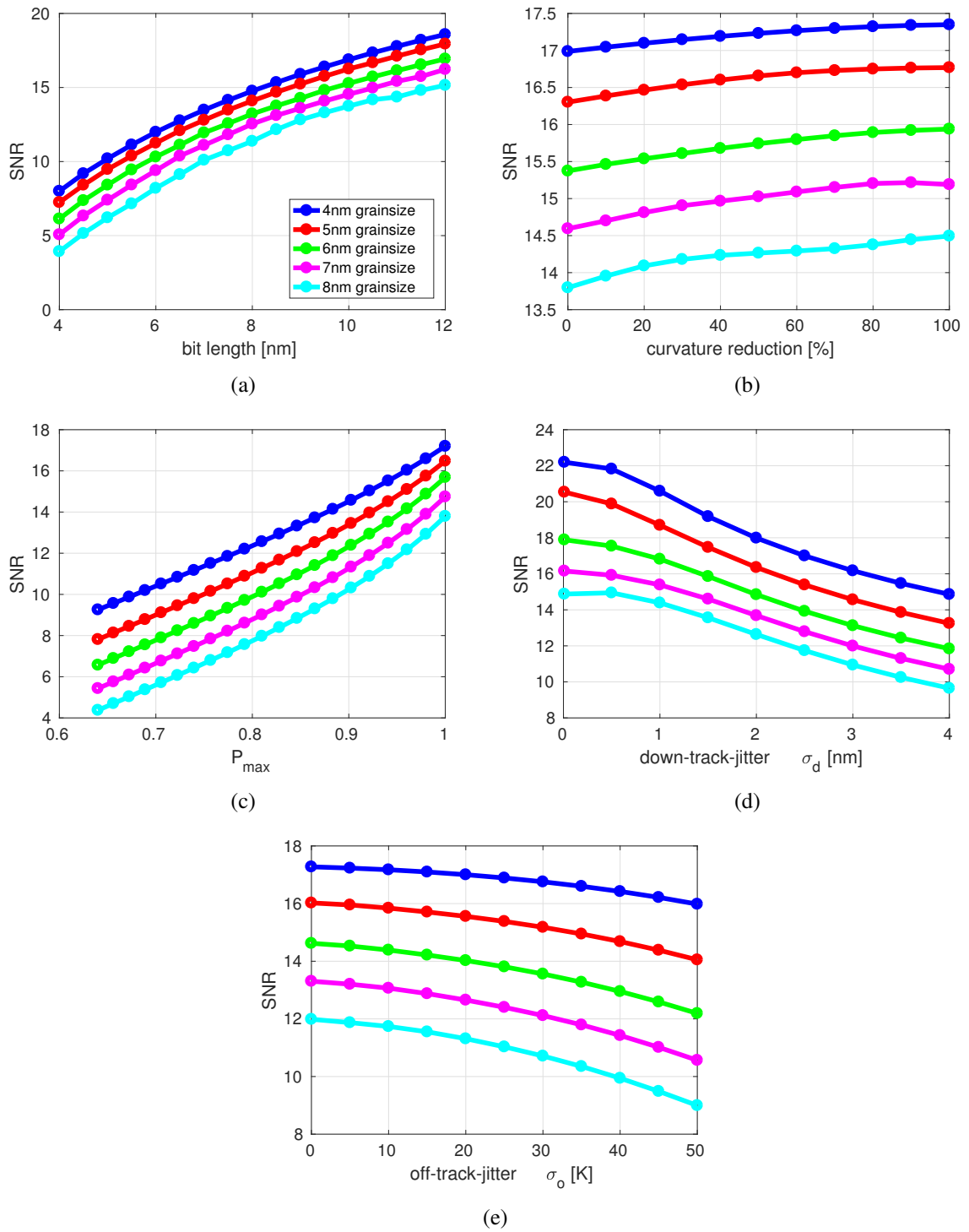
Figure 3.7.: SNR as a function of: (a) the bit length (with scaled reader), (b) curvature reduction, (c) $P_{\max}$, (d) $\sigma_d$ and (e) $\sigma_o$.

| parameter | min value | max value |
|---|---|---|
| $\sigma_d$ [nm] | 0.01 | 4.00 |
| $\sigma_o$ [K] | 0 | 50 |
| $P_{\max}$ | 0.64 | 1.00 |
| $b$ [nm] | 4.0 | 12.0 |
| curvature reduction [%] | 0 | 100 |

Table 3.4.: Range of variation for the model parameters.
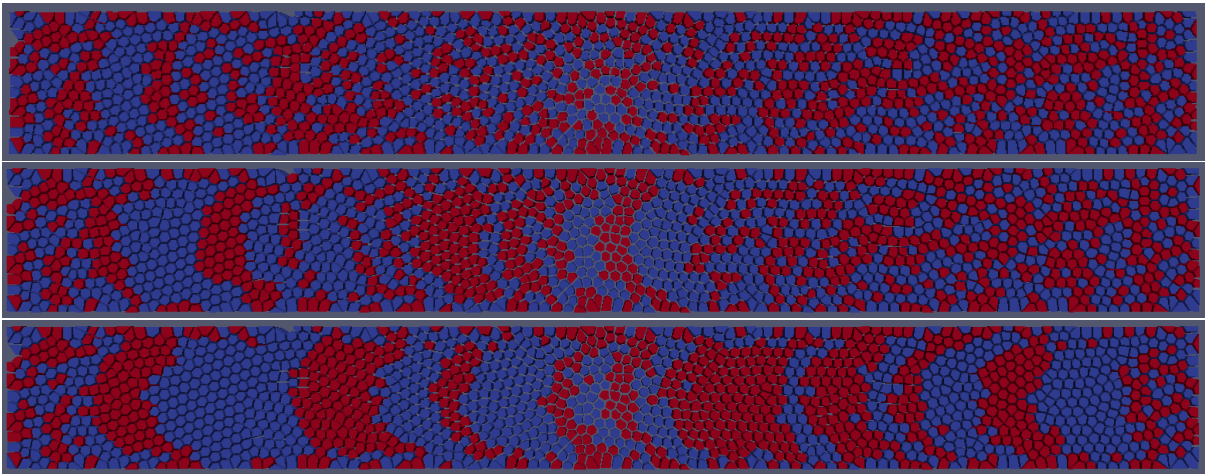


Figure 3.8.: Bit pattern for bit lengths of $4, 7$ and $12\,$nm (top to bottom).
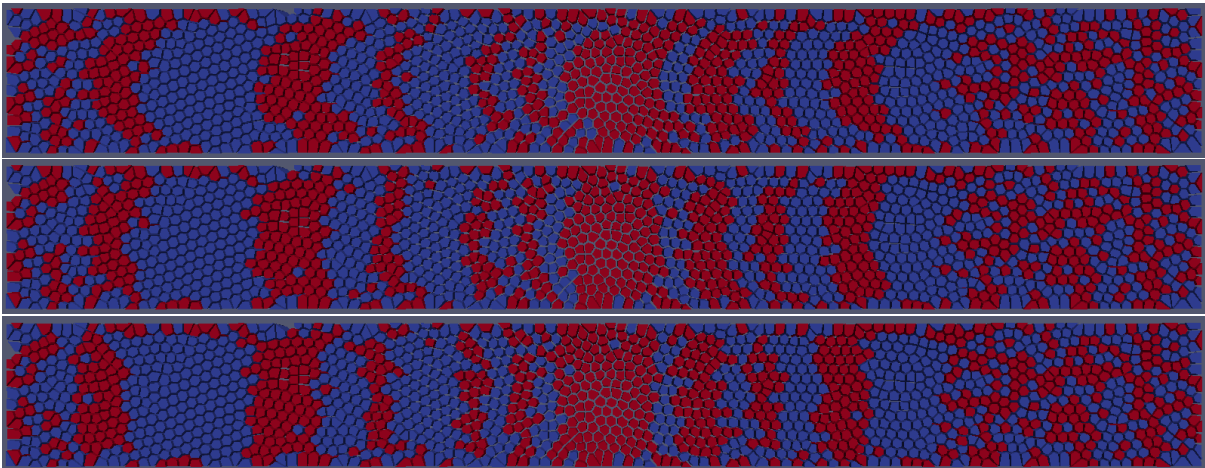


Figure 3.9.: Bit pattern for curvature reductions of $0, 50$ and $100\,\%$ (top to bottom).
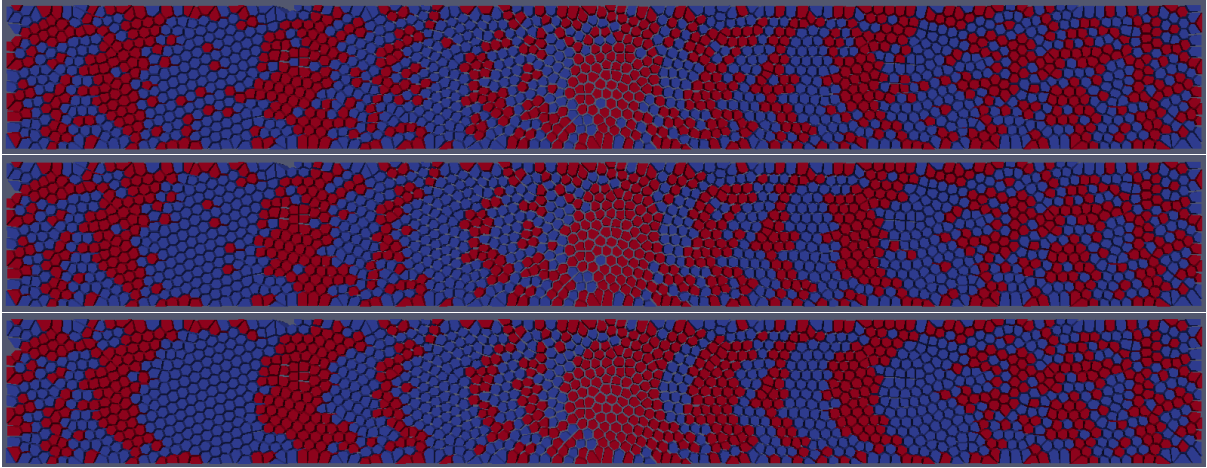
Figure 3.10.: Bit pattern for $P_{\max} = 0.64, 0.81$ and $1.00$ (top to bottom).
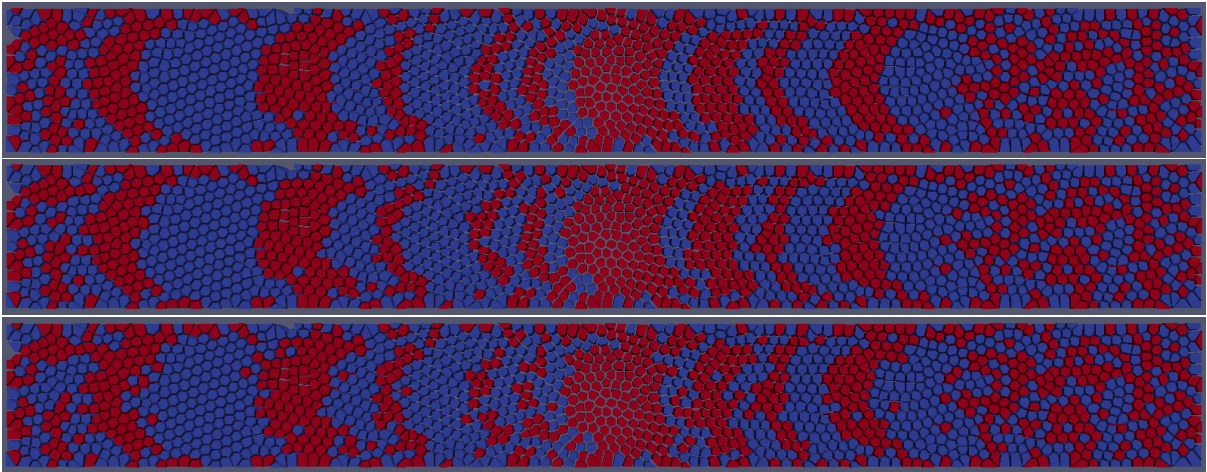


Figure 3.11.: Bit pattern for $\sigma_d = 0.01, 2.00$ and $4.00\,\mathrm{nm}$ (top to bottom).
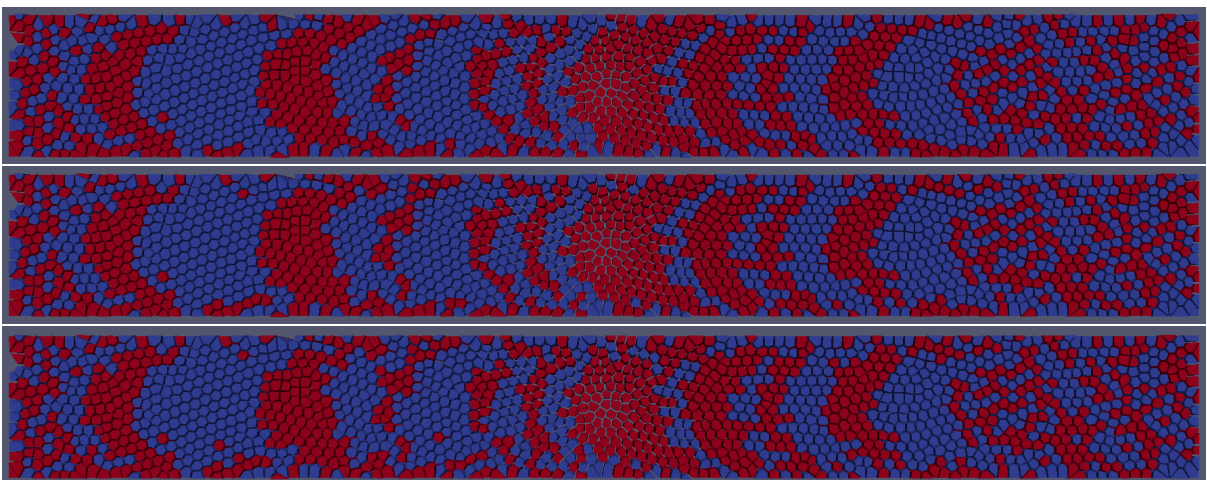


Figure 3.12.: Bit pattern for $\sigma_o = 0, 25$ and $50\,\mathrm{K}$ (top to bottom).
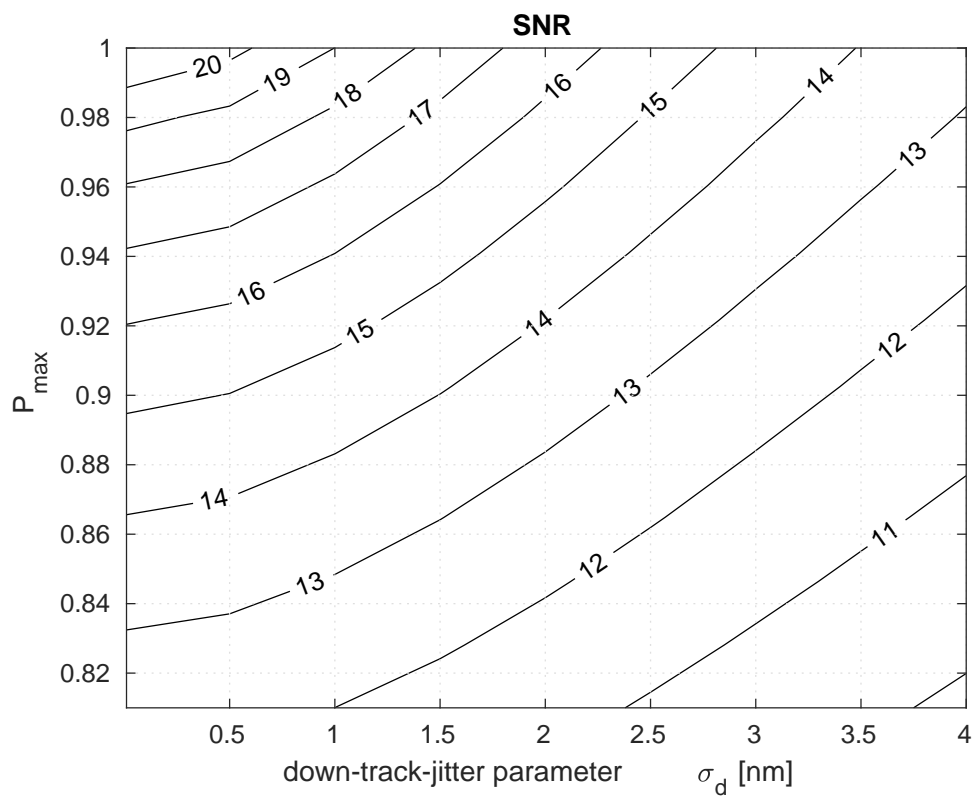
Figure 3.13.: SNR values for simultaneous variation of $\sigma_d$ and $P_{\max}$ for 5 nm grain diameter.

to the proportionality constant. As in [65, 82, 83], the media magnetic transition parameter $a$ can be separated into two independent parts:

- the down-track-jitter parameter $\sigma_d$, that originates from the probability distribution in the phase diagram

- the grain-jitter parameter $\sigma_g$, that comes from the grain distribution in the granular medium

Whereas $\sigma_d$ decreases as the grain diameter increases due to the higher thermal stability of larger grains (see Tab. 3.2), $\sigma_g$ shows the opposite effect. The stochastic independence ensures that the total jitter of these two parts can be written as

$$a = \sqrt{\sigma_d^2 + \sigma_g^2}. \tag{3.9}$$

The grain-jitter parameter $\sigma_g$ usually depends on the mean and the variation of the grain sizes. In our simulations, we assume the distribution to be very sharp, i.e. we neglect the dependence on the variations and assume all grains to have approximately the same size $S$. In this case $\sigma_g$ only depends on $S$ and a very simplified model with square grains in [82] shows

$$\sigma_g = \frac{S}{\sqrt{12}}. \tag{3.10}$$

Since the size of the nonmagnetic grain boundary is constant $B = 1\,\mathrm{nm}$ in our media (see Fig. 3.4), the grain size $S = D + B$ only depends on the grain diameter $D$. Furthermore, the proportionality in Eq. (3.8) may only hold, if the read-back pulse width $T_{50}$ is chosen in a realistic ratio to the bit length $b$. Otherwise, one might be able to increase the total SNR value just by increasing $T_{50}$, which in general is obviously not true. Therefore, we again scale the reader resolution $R$ (which is proportional to $T_{50}$) with the bit length $b$ according to Eq. (3.7) to keep the factor $T_{50}/b$ in Eq. (3.8) constant. Finally, we note that the reader width $W$ is also kept constant. Under these assumptions, we can write the SNR value as a function of the remaining variables and a proportionality constant $f$ in the form

$$\mathrm{SNR}(f, \sigma_d, D, b) = f \cdot \left( \sigma_d^2 + \frac{(D+B)^2}{12} \right)^{-1} \cdot (D+B)^{-1} \cdot b^2. \tag{3.11}$$

For the given values for $\sigma_d \in [0.01, 4.00]$ nm, $b \in [4.0, 12.0]$ nm, $d \in [4, 8]$ nm and the corresponding calculated SNR values, this function can be fitted with the fitting parameter $f$. Note that in contrast to the plots in Fig. 3.7, we now choose a uniform basic parameter set for all grain diameters, namely the values for 5 nm grain diameter in Tab. 3.2. Otherwise, we would additionally have to consider the grain size dependent variation of parameters, which are not included in the model function in Eq. (3.11). We obtain the value of the fitting parameter $f = 17.9011$ nm and the results are illustrated in Figs. 3.14 and 3.15.

The plots show that the trend of the fit agrees quite well with the actual SNR curves, however for $\sigma_d \longrightarrow 4$ nm and $b \longrightarrow 4$ nm we obtain deviations. The square root of the mean squared error over all data points of the fit is 0.63 dB. Taking into account the approximations in both the writing process (neglection of grain size distribution) and the derivation of the formula in Eq. (3.11) (simple model of square grains for Eq. (3.10), no dependency on $P_{\max}$ etc.), those deviations seem acceptable and the model agreement reasonable.
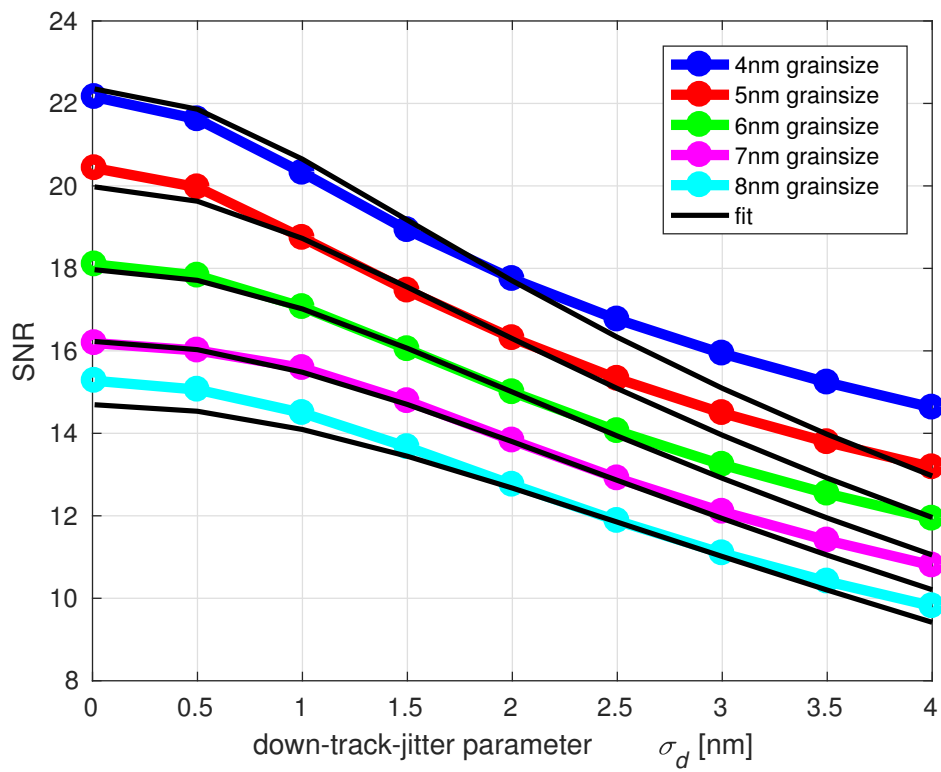
Figure 3.14.: Fitting curves of the SNR calculation for various down-track-jitter parameters and constant bit length $b = 10\,\text{nm}$.
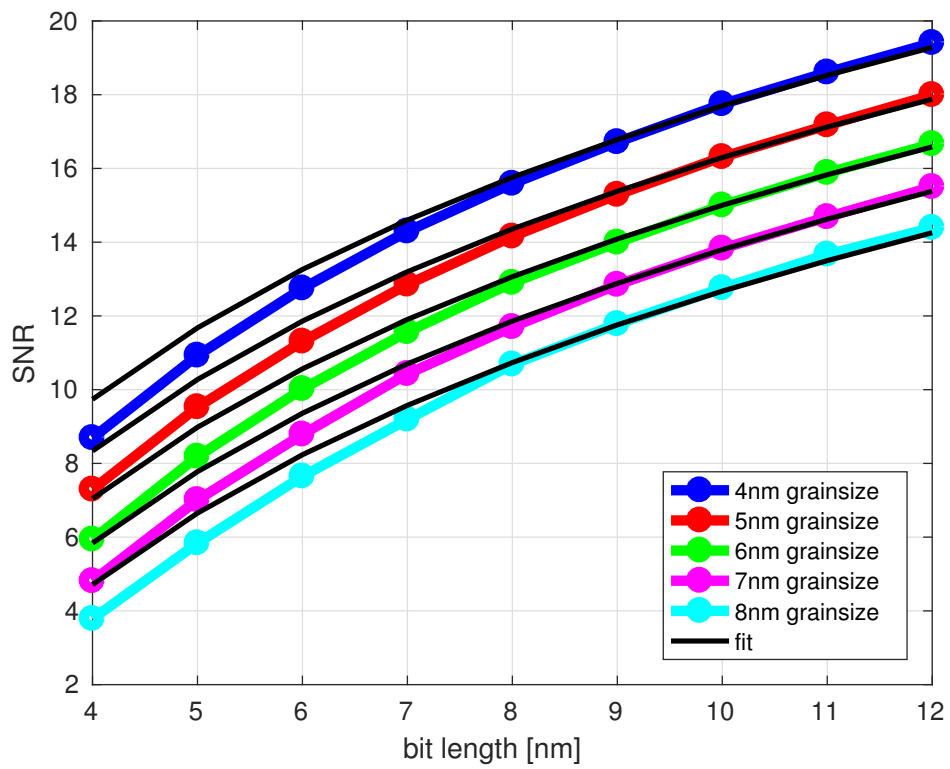
Figure 3.15.: Fitting curves of the SNR calculation for various bit lengths and constant down-track-jitter parameter $\sigma_d = 2\,\text{nm}$.

## 3.5. Conclusion and remarks

We developed an analytical model for the switching probability phase diagram of a magnetic grain in a recording medium during HAMR. Such a phase diagram describes the switching probability of the grain depending on its down-track and off-track position and is thus very valuable to evaluate the performance of a given recording setup. The proposed model has eight input parameters, determining the bit's position, its dimensions, its jitter in down-track and off-track direction, its curvature and the maximum switching probability in the center of the bit. By mapping the switching probabilities onto a recording medium and calculating the read-back signal with a given sensitivity function it is possible to model the whole HAMR write and read cycle with little computational effort. Additionally, due to the possibility of independent parameter variation in the model, we could investigate the influence of each parameter on the resulting SNR separately. Our results showed the impact of the bit length, curvature, maximum switching probability and down-track-jitter on the final SNR of written bit patterns. Whereas the variation of the bit length, maximum switching probability and down-track-jitter led to differences of $10, 9$ and $5\,\mathrm{dB}$, respectively, we could only show a gain of about $0.5\,\mathrm{dB}$ for the reduction of bit curvature and $1$ to $3\,\mathrm{dB}$ for off-track-jitter variations. Furthermore, the comparison with theoretical equations led to good agreement.

Since there are considerable efforts to optimize the bit quality in HAMR containing material design and writing techniques, our approach of using an analytical model for the whole recording cycle could provide a qualitative a priori indication about the cost-benefit ratio of a recording setup in terms of the SNR with low computational effort. In addition, with the proposed model the effects of individual changes, such as the down-track-jitter or the transition curvature, on the SNR can be studied separately. This is not possible with direct simulations of the write process, where only material parameters of the recording grains or write parameters of the recording head can be changed, which then has an impact on many aspects of the resulting footprint.

# 4. Full analytical solution for the magnetic field of uniformly magnetized cylinder tiles

We present an analytical solution for the magnetic field of a homogeneously magnetized cylinder tile and by extension solutions for full cylinders, rings, cylinder sectors and ring segments. The derivation is done by direct integration in the magnetic surface charge picture. Results are closed-form expressions and elliptic integrals. All special cases are treated individually, which enables the field computation for all possible position arguments $\mathbf{r} \in \mathbb{R}^3$. An implementation is provided in Python together with a performance analysis. The implementation is tested against numerical solutions and applied to compute the magnetic field in a discrete Halbach cylinder.

Parts of this chapter have been previously published in [84] and have been reproduced with permission of the coauthors and in accordance with the publisher's policy. Content that was not generated by the author of this thesis is explicitly denoted, copyright is held by Elsevier.

## 4.1. Introduction

Permanent magnets are widely used in numerous technical applications [85–92]. Among all conceivable geometries, simple magnet shapes such as cuboids or cylinders are especially popular and widespread as they are mass-produced and available at short notice in various dimensions, magnetization and materials [93, 94]. When the magnet geometry is simple and the magnetization is homogeneous, it is often possible to derive analytical expressions for the field generated by such magnets [95–105]. These expressions provide excellent approximations to the real fields when modern, high-grade magnetic materials, like SmCo, NdFeB or ferrites with susceptibilities $\chi < 0.1$ are involved [92, 106].

The main advantage over common numerical methods such as finite elements method (FEM) approaches or direct numerical integration is the fast computation times of the order of microseconds [106, 107], which enables highly efficient multivariate parameter space analysis and solving global optimization problems for permanent magnet arrangements [108–110].

The analytical formulas for cuboid magnets [92, 98, 111, 112] are particularly useful since cuboids can be trivially subdivided into smaller cuboid cells to which the formulas are again applicable. This allows modeling of the material response with the magnetostatic method of moments [113], a common approach of computing dipole interactions in micromagnetic software [27, 42, 48, 59, 114–116]. In contrast, the analytical expression of a cylinder [99–104] is not sufficient for such calculations, as the cylindrical volume element is a cylinder tile, i.e., a cylindrical ring segment. In addition, many geometric shapes used in magnetic position systems, such as the cylindrical quadrupole [117, 118] or rotary encoder wheels [119, 120], can be constructed with such tiles, motivating us to find analytical expressions for this geometry.

Finding an analytical expression for the homogeneously magnetized cylinder tile was attempted in many previous works [121–126], but to date all solutions contain integral expressions which can only be solved numerically. In this work we present for the first time a complete analytical solution for the magnetic field of a homogeneously magnetized cylinder tile. All expressions contain only basic arithmetic operations, trigonometric functions and special functions like elliptic integrals, which can be computed

very efficiently [127–135]. In previous works, only the most general case is treated, while indeterminate forms, that typically appear at surface extensions, are neglected. We provide expressions for all such cases, which allows us to compute the field at any point in space. In addition, we include the limiting cases with inner radius $r_1 = 0$ (cylinder sector), constricting sector angles $\varphi_1 = 0$, $\varphi_2 = 2\pi$ (cylinder ring) and the full cylinder as the combination of the two cases.

The structure of the chapter is as follows: In Sec. 4.2 we establish the notation and describe the surface charge method, which enables us to express the total magnetic field as the sum of various surface integrals, and discuss its limitations. The first and second integration steps are shown in Sec. 4.3 and Sec. 4.4, respectively. In Sec. 4.5 we validate our results by comparison with solutions from numerical integration and finite element method. A discrete Halbach cylinder application example is demonstrated in Sec. 4.6. Another application is demonstrated in Sec. 4.7, where a rotation sensor system based on a quadrupole magnet is simulated and the angle errors calculated analytically. We close with a brief discussion of the results and outlook in Sec. 4.8.

## 4.2. Method

It is convenient to describe the problem in cylindrical coordinates $(r, \varphi, z) \in [0, \infty) \times [0, 2\pi) \times (-\infty, \infty)$. The cylinder tile is defined through six boundaries at $r_1 < r_2$, $\varphi_1 < \varphi_2$, and $z_1 < z_2$, see Fig. 4.1a. We define the homogeneous magnetization vector $\mathbf{M}$, through its magnitude $M$, azimuth angle $\varphi_M$ and polar angle $\theta_M$, see Fig. 4.1b.

In Cartesian coordinates the magnetization is then given by

$$\mathbf{M} = M \left( \cos \varphi_M \sin \theta_M \mathbf{e}_x + \sin \varphi_M \sin \theta_M \mathbf{e}_y + \cos \theta_M \mathbf{e}_z \right). \tag{4.1}$$

### 4.2.1. Field calculation with magnetostatic potential

In [136, Sec. 5.9 C], the scalar magnetic potential $\Phi_M$ is derived for volumes $V$ with homogeneous magnetization $\mathbf{M}$ in the absence of electric currents,

$$\Phi_M(\mathbf{r}) = \frac{1}{4\pi} \oint_{\partial V} \frac{\sigma(\mathbf{r}')}{|\mathbf{r} - \mathbf{r}'|} \, dA', \tag{4.2}$$

with the magnetic surface charge $\sigma$ given by the inner product of the magnetization vector with the surface normal vector $\mathbf{n}$,

$$\sigma(\mathbf{r}') = \mathbf{M}(\mathbf{r}') \cdot \mathbf{n}(\mathbf{r}'). \tag{4.3}$$

The magnetic field $\mathbf{H}$ is then given by

$$\mathbf{H}(\mathbf{r}) = -\nabla \Phi_M(\mathbf{r}) = \frac{1}{4\pi} \oint_{\partial V} \frac{\sigma(\mathbf{r}')(\mathbf{r} - \mathbf{r}')}{|\mathbf{r} - \mathbf{r}'|^3} \, dA'. \tag{4.4}$$

### 4.2.2. Magnetic surface-charge density

The tile boundary $\partial V$ includes three types of surfaces. Each type is denoted by its normal vector, see Fig. 4.1a. We calculate the magnetic surface charge density $\sigma$ according to Eq. (4.3) in cylindrical coordinates for each surface type.

$$\begin{aligned} \sigma_{r_i}(\varphi') &= (-1)^i \mathbf{M} \cdot \left( \cos \varphi' \mathbf{e}_x + \sin \varphi' \mathbf{e}_y \right) \\ &= (-1)^i M \sin \theta_M \left( \cos \varphi_M \cos \varphi' + \sin \varphi_M \sin \varphi' \right) \\ &= (-1)^i M \sin \theta_M \cos(\varphi_M - \varphi') \end{aligned} \tag{4.5}$$
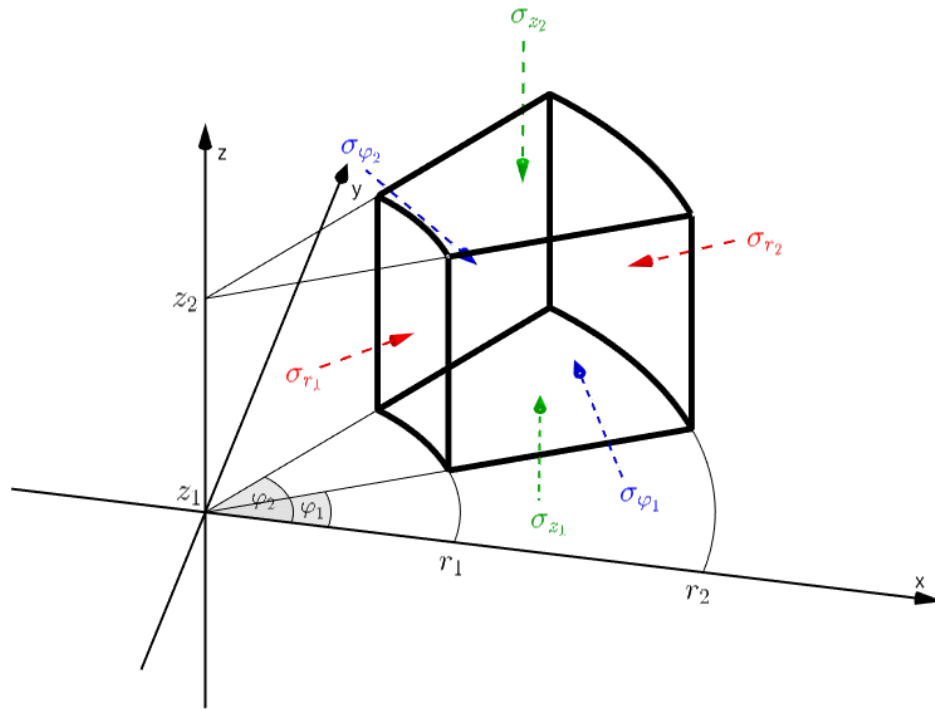
(a)
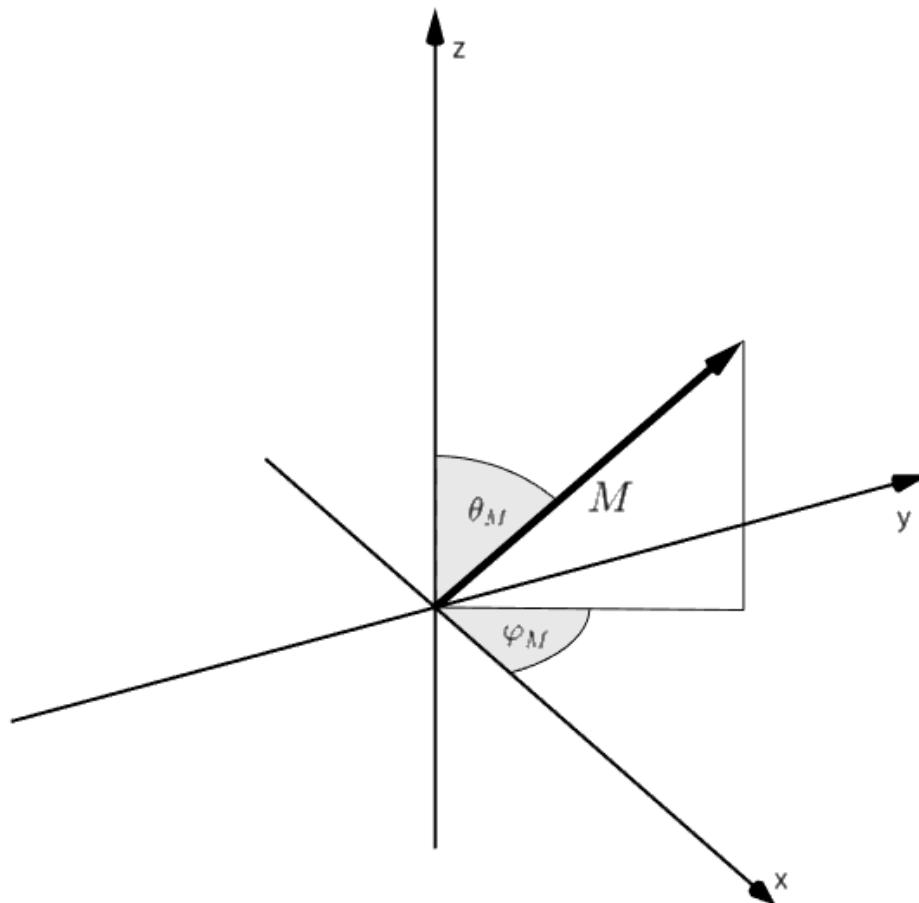


(b)

Figure 4.1.: (a) Dimensions of the cylinder tile in cylinder coordinates and the resulting magnetic surface charges $\sigma$. We assume $0 \leq r_1 < r_2$, $\varphi_1 < \varphi_2$ and $z_1 < z_2$. (b) Magnetization vector $\mathbf{M}$ described by the three coordinates $M, \varphi_M$ and $\theta_M$.

$$\sigma_{\varphi_j} = (-1)^j \mathbf{M} \cdot (-\sin\varphi_j \mathbf{e}_x + \cos\varphi_j \mathbf{e}_y)$$
$$= (-1)^j M \sin\theta_M \left(-\cos\varphi_M \sin\varphi_j + \sin\varphi_M \cos\varphi_j\right) \tag{4.6}$$
$$= (-1)^j M \sin\theta_M \sin(\varphi_M - \varphi_j)$$
$$\sigma_{z_k} = (-1)^k \mathbf{M} \cdot \mathbf{e}_z$$
$$= (-1)^k M \cos\theta_M \tag{4.7}$$

It will be useful for our derivation to omit magnetization and powers of $(-1)$ and define the dashed (sign reduced) surface charge densities by

$$\sigma'_{r_i}(\varphi') = \sin\theta_M \cos(\varphi_M - \varphi'), \tag{4.8}$$
$$\sigma'_{\varphi_j} = \sin\theta_M \sin(\varphi_M - \varphi_j), \tag{4.9}$$
$$\sigma'_{z_k} = \cos\theta_M. \tag{4.10}$$

### 4.2.3. Surface integrals

To express the the surface integrals Eq. (4.4) in cylindrical coordinates, we use the usual transformations,

$$x = r\cos\varphi, \tag{4.11}$$
$$y = r\sin\varphi, \tag{4.12}$$
$$\mathbf{e}_r = \cos\varphi\,\mathbf{e}_x + \sin\varphi\,\mathbf{e}_y, \tag{4.13}$$
$$\mathbf{e}_\varphi = -\sin\varphi\,\mathbf{e}_x + \cos\varphi\,\mathbf{e}_y. \tag{4.14}$$

To simplify the notation, we do not explicitly write the dependency of the coordinates $r$, $\varphi$ and $z$, although almost every term depends on them. With the abbreviation

$$\xi(r', \varphi', z') := \left|\mathbf{r} - \mathbf{r}'\right| = \sqrt{r^2 + r'^2 - 2rr'\cos(\varphi - \varphi') + (z - z')^2}, \tag{4.15}$$

every field component can be expressed as a sum of six terms, each originating from one tile surface, as

$$H_r = \frac{M}{4\pi} \Bigg( \sum_{i=1}^{2}(-1)^i \int_{\varphi_1}^{\varphi_2}\int_{z_1}^{z_2} \underbrace{\frac{\sigma'_{r_i}(\varphi')(r - r_i\cos(\varphi - \varphi'))}{\xi(r_i, \varphi', z')^3}r_i \; \mathrm{d}z'\mathrm{d}\varphi'}_{=:H_{r,r_i}(\varphi',z')} +$$

$$\sum_{j=1}^{2}(-1)^j \int_{r_1}^{r_2}\int_{z_1}^{z_2} \underbrace{\frac{\sigma'_{\varphi_j}(r - r'\cos(\varphi - \varphi_j))}{\xi(r', \varphi_j, z')^3} \; \mathrm{d}z'\mathrm{d}r'}_{=:H_{r,\varphi_j}(r',z')} +$$

$$\sum_{k=1}^{2}(-1)^k \int_{\varphi_1}^{\varphi_2}\int_{r_1}^{r_2} \underbrace{\frac{\sigma'_{z_k}(r - r'\cos(\varphi - \varphi'))}{\xi(r', \varphi', z_k)^3}r' \; \mathrm{d}r'\mathrm{d}\varphi'}_{=:H_{r,z_k}(r',\varphi')} \Bigg) \tag{4.16}$$

$$H_\varphi = \frac{M}{4\pi} \left( \sum_{i=1}^{2} (-1)^i \int_{\varphi_1}^{\varphi_2} \int_{z_1}^{z_2} \underbrace{\frac{\sigma_{r_i}(\varphi')r_i^2 \sin(\varphi-\varphi')}{\xi(r_i,\varphi',z')^3}}_{=:H_{\varphi,r_i}(\varphi',z')} \, \mathrm{d}z'\mathrm{d}\varphi' + \right.$$

$$\sum_{j=1}^{2} (-1)^j \int_{r_1}^{r_2} \int_{z_1}^{z_2} \underbrace{\frac{\sigma_{\varphi_j}r' \sin(\varphi-\varphi_j)}{\xi(r',\varphi_j,z')^3}}_{=:H_{\varphi,\varphi_j}(r',z')} \, \mathrm{d}z'\mathrm{d}r' + \tag{4.17}$$

$$\left. \sum_{k=1}^{2} (-1)^k \int_{\varphi_1}^{\varphi_2} \int_{r_1}^{r_2} \underbrace{\frac{\sigma_{z_k}r'^2 \sin(\varphi-\varphi')}{\xi(r',\varphi',z_k)^3}}_{=:H_{\varphi,z_k}(r',\varphi')} \, \mathrm{d}r'\mathrm{d}\varphi' \right)$$

$$H_z = \frac{M}{4\pi} \left( \sum_{i=1}^{2} (-1)^i \int_{\varphi_1}^{\varphi_2} \int_{z_1}^{z_2} \underbrace{\frac{\sigma_{r_i}(\varphi')(z-z')}{\xi(r_i,\varphi',z')^3}r_i}_{=:H_{z,r_i}(\varphi',z')} \, \mathrm{d}z'\mathrm{d}\varphi' + \right.$$

$$\sum_{j=1}^{2} (-1)^j \int_{r_1}^{r_2} \int_{z_1}^{z_2} \underbrace{\frac{\sigma_{\varphi_j}(z-z')}{\xi(r',\varphi_j,z')^3}}_{=:H_{z,\varphi_j}(r',z')} \, \mathrm{d}z'\mathrm{d}r' + \tag{4.18}$$

$$\left. \sum_{k=1}^{2} (-1)^k \int_{\varphi_1}^{\varphi_2} \int_{r_1}^{r_2} \underbrace{\frac{\sigma_{z_k}(z-z_k)}{\xi(r',\varphi',z_k)^3}r'}_{=:H_{z,z_k}(r',\varphi')} \, \mathrm{d}r'\mathrm{d}\varphi' \right)$$

In the following sections, we present the analytical solution of the above nine surface integrals. In our derivations below, we denote the solution to the above integrals using upper indices, e.g.

$$\int_{z_1}^{z_2} H_{r,r_i}(\varphi',z') \, \mathrm{d}z' = H_{r,r_i}^{z_2}(\varphi') - H_{r,r_i}^{z_1}(\varphi') \tag{4.19}$$

which allows us to express the final solution in a very compact manner,

$$H_\alpha = \frac{M}{4\pi} \sum_{i,j,k=1}^{2} (-1)^{i+j+k} \left( H_{\alpha,r_i}^{\varphi_j,z_k} + H_{\alpha,\varphi_j}^{r_i,z_k} + H_{\alpha,z_k}^{r_i,\varphi_j} \right) \tag{4.20}$$

for $\alpha \in \{r,\varphi,z\}$.

### 4.2.4. Limitation

The whole derivation in the previous subsection and the final formula in Eq. (4.20) is strongly based on the assumption of homogeneous magnetization within the cylindrical tile. Due to thermal and demagnetization effects, this is an idealization that is unattainable in real magnets. However, recent developments in magnet fabrication show that very high coercive fields of several teslas and thus very low magnetic susceptibilities $\chi_m$ can be achieved with certain magnetic materials consisting of rare earth elements even at room temperature [90, 137–139]. When these materials are magnetized in a very strong homogeneous external field in a particular direction, the resulting magnetization direction remains nearly homogeneous in that direction even after the external field is removed. For these materials, our formulas provide an excellent approximation.
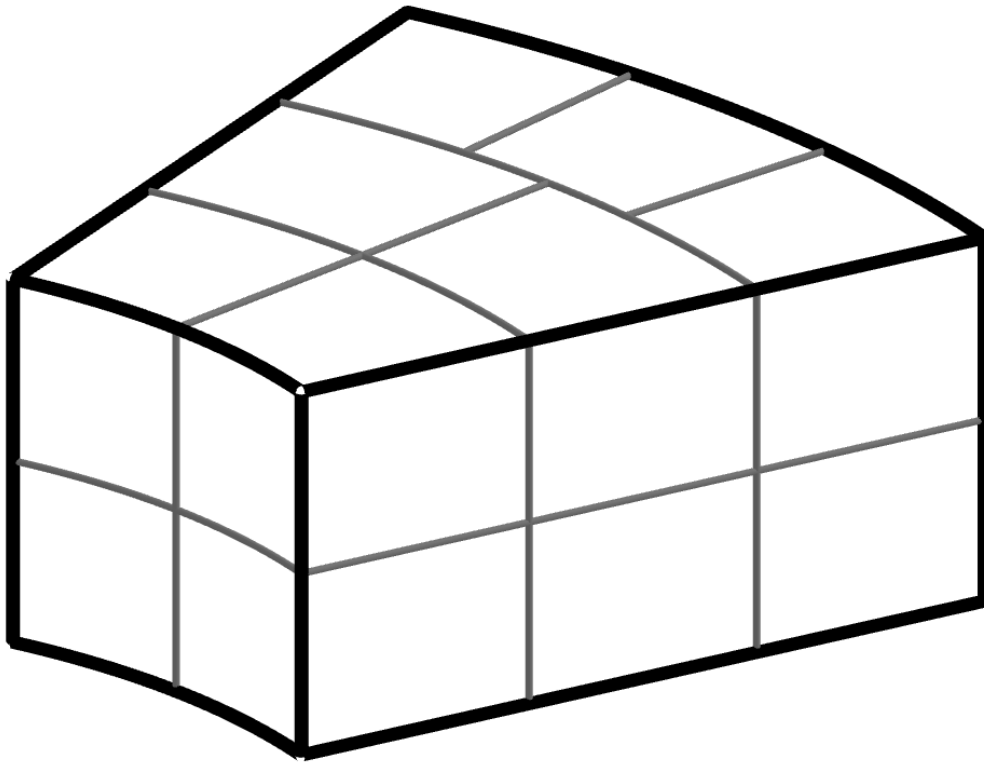
Figure 4.2.: Illustration how each cylinder tile (including also all limiting cases as cylinder sectors, cylinder rings and full cylinders) can be perfectly subdivided into smaller cylinder tile cells. Each cell can have a different magnetization direction, which leads to an inhomogeneous magnetization of the whole cylinder tile. This allows to simulate demagnetization effects for instance, where the magnetization directions are aligned according to the demagnetization field. Unlike common lattice subdivisions, such as cubes in finite difference and tetrahedra in finite element approaches, there is no geometry approximation error because the subdivision perfectly preserves the cylindrical shape.

However, for higher temperatures, poorer material properties, large demagnetization due to very large ratios between the spatial dimensions of the cylindrical tiles, and high external fields, we naturally expect deviations from perfect homogeneous magnetization. If this is the case, our formulas can still be used to simulate the deviations with a subdivision of the whole cylinder tile into smaller pieces, as shown in Fig. 4.2. Then a method of moment approach [113] can be used to align the magnetization in each subcell individually, resulting in an inhomogeneous magnetization over the entire geometry. In principle, the exact magnetization can be approximated with arbitrary accuracy in the limit for very small subcells. The MagTense software presented in [59] uses the general approach to calculate demagnetization based on analytical formulas for various homogeneously magnetized geometries [126].

## 4.3. First integration

The first integration can be easily achieved with modern computer algebra systems and was demonstrated in previous works [122]. To simplify the notation, we introduce the following short forms:

$$\bar{r}_i := r - r_i \tag{4.21}$$

$$\bar{r}' := r - r' \tag{4.22}$$

$$\overline{\varphi}_j := \varphi - \varphi_j \tag{4.23}$$

$$\overline{\varphi}' := \varphi - \varphi' \tag{4.24}$$

$$\overline{\varphi}_M := \varphi_M - \varphi \tag{4.25}$$

$$\overline{\varphi}'_M := \varphi_M - \varphi' \tag{4.26}$$

$$\overline{\varphi}_{Mj} := \varphi_M - \varphi_j \tag{4.27}$$

$$\bar{z}_k := z - z_k \tag{4.28}$$

$$\bar{z}' := z - z' \tag{4.29}$$

The first integration then yields:

$$H_{r,r_i}^{z_k}(\varphi') = \left[\int H_{r,r_i}(\varphi',z')\,\mathrm{d}z'\right]_{z'=z_k} = \begin{cases} -\sin\theta_M r_i \bar{z}_k \dfrac{\cos\overline{\varphi}_M'\left(r-r_i\cos\overline{\varphi}'\right)}{\left(r^2+r_i^2-2rr_i\cos\overline{\varphi}'\right)\xi(r_i,\varphi',z_k)} & \text{for } r \neq r_i \text{ and } r > 0 \\[4mm] -\dfrac{\sin\theta_M \bar{z}_k}{2}\dfrac{\cos\overline{\varphi}_M'}{\sqrt{2r^2\left(1-\cos\overline{\varphi}'\right)+\bar{z}_k^2}} & \text{for } r = r_i \text{ and } r > 0 \\[4mm] \dfrac{\sin\theta_M \bar{z}_k}{\sqrt{r_i^2+\bar{z}_k^2}}\cos\overline{\varphi}_M'\cos\overline{\varphi}' & \text{for } r = 0 \text{ and } r_i > 0 \\[4mm] 0 & \text{for } r_i = 0 \end{cases} \tag{4.30}$$

$$H_{r,\varphi_j}^{r_i}(z') = \left[\int H_{r,\varphi_j}(r',z')\,\mathrm{d}r'\right]_{r'=r_i} = \begin{cases} 2\sin\theta_M\sin\overline{\varphi}_{Mj}\dfrac{\bar{z}'^2\cos\overline{\varphi}_j+rr_i\sin^2\overline{\varphi}_j}{\left(r^2+2\bar{z}'^2-r^2\cos\left(2\overline{\varphi}_j\right)\right)\xi(r_i,\varphi_j,z')} & \text{for } \overline{\varphi}_j \notin \pi\mathbb{Z} \text{ and } r > 0 \\[4mm] \sin\theta_M\sin\overline{\varphi}_{Mj}\dfrac{1}{\sqrt{r_i^2+\bar{z}'^2}} & \text{for } \overline{\varphi}_j \in 2\pi\mathbb{Z} \text{ and } r > 0 \\[4mm] -\sin\theta_M\sin\overline{\varphi}_{Mj}\dfrac{1}{\sqrt{(r+r_i)^2+\bar{z}'^2}} & \text{for } \overline{\varphi}_j \in 2\pi\mathbb{Z}+\pi \text{ and } r > 0 \\[4mm] \sin\theta_M\sin\overline{\varphi}_{Mj}\dfrac{\cos\overline{\varphi}_j}{\sqrt{r_i^2+\bar{z}'^2}} & \text{for } r = 0 \end{cases} \tag{4.31}$$

$$H_{r,z_k}^{r_i}(\varphi') = \left[\int H_{r,z_k}(r',\varphi')\,\mathrm{d}r'\right]_{r'=r_i} = \begin{cases} \cos\theta_M\left(\dfrac{r_i\left(r^2+2\bar{z}_k^2\right)\cos\overline{\varphi}'-r\left(r^2+\bar{z}_k^2-\left(r^2+\bar{z}_k^2\right)\cos\left(2\overline{\varphi}'\right)-rr_i\cos\left(3\overline{\varphi}'\right)\right)}{\left(r^2+2\bar{z}_k^2-r^2\cos\left(2\overline{\varphi}'\right)\right)\xi(r_i,\varphi',z_k)}\right. \\[4mm] \qquad\qquad \left.-\cos\overline{\varphi}'\log\left(r_i-r\cos\overline{\varphi}'+\xi\left(r_i,\varphi',z_k\right)\right)\right) & \text{for } z \neq z_k \text{ and } r > 0 \\[4mm] \cos\theta_M\left(\dfrac{2r_i\cos\overline{\varphi}'-r}{\sqrt{r^2+r_i^2-2rr_i\cos\overline{\varphi}'}}\right. \\[4mm] \qquad\qquad \left.-\cos\overline{\varphi}'\log\left(r_i-r\cos\overline{\varphi}'+\sqrt{r^2+r_i^2-2rr_i\cos\overline{\varphi}'}\right)\right) & \text{for } z = z_k \text{ and } r > 0 \\[4mm] \cos\theta_M\left(\dfrac{r_i}{\sqrt{r_i^2+\bar{z}_k^2}}-\operatorname{artanh}\left(\dfrac{r_i}{\sqrt{r_i^2+\bar{z}_k^2}}\right)\right)\cos\overline{\varphi}' & \text{for } z \neq z_k \text{ and } r = 0 \\[4mm] -\cos\theta_M\log r_i\cos\overline{\varphi}' & \text{for } z = z_k \text{ and } r = 0 \end{cases} \tag{4.32}$$

$$H_{\varphi,r_i}^{z_k}(\varphi') = \left[\int H_{\varphi,r_i}(\varphi',z')\,\mathrm{d}z'\right]_{z'=z_k} = \begin{cases} -\sin\theta_M r_i^2 \bar{z}_k \dfrac{\cos\overline{\varphi}_M'\sin\overline{\varphi}'}{\left(r^2+r_i^2-2rr_i\cos\overline{\varphi}'\right)\xi(r_i,\varphi',z_k)} & \text{for } r\neq r_i \text{ and } r>0 \\[4mm] -\dfrac{\sin\theta_M}{2}\dfrac{\cos\overline{\varphi}_M'\sin\overline{\varphi}'}{\left(1-\cos\overline{\varphi}'\right)}\dfrac{\bar{z}_k}{\sqrt{2r^2\left(1-\cos\overline{\varphi}'\right)+\bar{z}_k^2}} & \text{for } r=r_i \text{ and } r>0 \text{ and } \overline{\varphi}_j\notin 2\pi\mathbb{Z} \text{ for } j=1 \text{ and } j=2 \\[4mm] -\dfrac{\sin\theta_M}{2}\dfrac{\cos\overline{\varphi}_M'\sin\overline{\varphi}'}{\left(1-\cos\overline{\varphi}'\right)}\left(\dfrac{\bar{z}_k}{\sqrt{2r^2\left(1-\cos\overline{\varphi}'\right)+\bar{z}_k^2}}-\mathrm{sign}\,\bar{z}_k\right) & \text{for } r=r_i \text{ and } r>0 \text{ and } \overline{\varphi}_j\in 2\pi\mathbb{Z} \text{ for } j=1 \text{ or } j=2 \\[4mm] -\dfrac{\sin\theta_M \bar{z}_k}{\sqrt{r_i^2+\bar{z}_k^2}}\cos\overline{\varphi}_M'\sin\overline{\varphi}' & \text{for } r=0 \text{ and } r_i>0 \\[4mm] 0 & \text{for } r_i=0 \end{cases}$$

$$\tag{4.33}$$

$$H_{\varphi,\varphi_j}^{z_k}(r') = \left[\int H_{\varphi,\varphi_j}(r',z')\,\mathrm{d}z'\right]_{z'=z_k} = \begin{cases} -\sin\theta_M\sin\overline{\varphi}_{Mj}\sin\overline{\varphi}_j\bar{z}_k\dfrac{r'}{\left(r^2+r'^2-2rr'\cos\overline{\varphi}_j\right)\xi(r',\varphi_j,z_k)} & \text{for } \overline{\varphi}_j\notin\pi\mathbb{Z} \\[4mm] 0 & \text{for } \overline{\varphi}_j\in\pi\mathbb{Z} \end{cases}$$

$$\tag{4.34}$$

$$H_{\varphi,z_k}^{\varphi_j}(r') = \left[\int H_{\varphi,z_k}(r',\varphi')\,\mathrm{d}\varphi'\right]_{\varphi'=\varphi_j} = \begin{cases} \dfrac{\cos\theta_M}{r}\dfrac{r'}{\xi(r',\varphi_j,z_k)} & \text{for } r>0 \\[4mm] \cos\theta_M\cos\overline{\varphi}_j\dfrac{r'^2}{\sqrt{r'^2+\bar{z}_k^2}^3} & \text{for } r=0 \end{cases}$$

$$\tag{4.35}$$

$$H_{z,r_i}^{z_k}(\varphi') = \left[\int H_{z,r_i}(\varphi',z')\,\mathrm{d}z'\right]_{z'=z_k} = \sin\theta_M r_i\dfrac{\cos\overline{\varphi}_M'}{\xi(r_i,\varphi',z_k)}$$

$$\tag{4.36}$$

$$H_{z,\varphi_j}^{z_k}(r') = \left[\int H_{z,\varphi_j}(r',z')\,\mathrm{d}z'\right]_{z'=z_k} = \sin\theta_M\sin\overline{\varphi}_{Mj}\dfrac{1}{\xi(r',\varphi_j,z_k)}$$

$$\tag{4.37}$$

$$H_{z,z_k}^{r_i}(\varphi') = \left[\int H_{\varphi,z_k}(r',\varphi')\,\mathrm{d}r'\right]_{r'=r_i} = \begin{cases} -2\cos\theta_M\bar{z}_k\dfrac{r^2+\bar{z}_k^2-rr_i\cos\overline{\varphi}'}{\left(r^2+2\bar{z}_k^2-r^2\cos(2\overline{\varphi}')\right)\xi(r_i,\varphi',z_k)} & \text{for } z\neq z_k \\[4mm] 0 & \text{for } z=z_k \end{cases}$$

$$\tag{4.38}$$

$$\tag{4.39}$$

|   | $\ell$ | $m$ | $n$ |
|---|---|---|---|
| 1 | $z = z_k$ | $\overline{\varphi}_j \in 2\pi\mathbb{Z}$ | $r = r_i = 0$ |
| 2 | $z \neq z_k$ | $\overline{\varphi}_j \in 2\pi\mathbb{Z} + \pi$ | $r = 0, r_i > 0$ |
| 3 |  | $\overline{\varphi}_j \notin \pi\mathbb{Z}$ | $r > 0, r_i = 0$ |
| 4 |  |  | $r = r_i > 0$ |
| 5 |  |  | $r, r_i > 0, r \neq r_i$ |

Table 4.1.: All possible values of the three-digits index $\mathscr{I} = \ell mn$ and associated special cases. The general case is $\mathscr{I} = 235$, i.e. $z \neq z_k$, $\overline{\varphi}_j \notin \pi\mathbb{Z}$ and $r, r_i > 0, r \neq r_i$.

|  | $\varphi_j$ | $\operatorname{sign} \overline{z}_k \log |\overline{z}_k|$ |
|---|---|---|
| $H_{r,\varphi_j}^{r_i,z_k}$ | 0 | $-\sin\theta_M \sin\overline{\varphi}_M$ |
| $H_{z,z_k}^{r_i,\varphi_j}$ | $-\cos\theta_M \operatorname{sign}\overline{z}_k$ | 0 |

Table 4.2.: Example table for $\mathscr{I} = 211$. The field components are computed by summation over all functions multiplied by coefficients.

The first integration leads to several singularities which must be treated with care within the second integration step. In App. A we discuss these problems in detail.

## 4.4. Second integration

With the second integration step, the number of special cases to be distinguished increases massively. To identify the special cases outlined in Tab. 4.1, a three-digit index $\mathscr{I} := \ell mn$ is introduced. For example, the index $\mathscr{I} = 213$ denotes the case $z \neq z_k$, $\overline{\varphi}_j \in 2\pi\mathbb{Z}$, $r > 0$, $r_i = 0$. The special cases $\mathscr{I} = 111, 114, 121, 131$ are unphysical as they refer to a field evaluation on corners and edges of the tile.

For each case we provide a table with all expressions and coefficients that make up the components of Eq. (4.20). The special functions used for this are defined in App. B. An individual field component is computed by summing over all functions multiplied by coefficients given in the tables. An example is demonstrated for the case $\mathscr{I} = 211$ with Tab. 4.2 from which the field components calculate as

$$H_{r,\varphi_j}^{r_i,z_k} = 0 \cdot \varphi_j - \sin\theta_M \sin\overline{\varphi}_M \cdot \operatorname{sign}\overline{z}_k \log|\overline{z}_k|, \tag{4.40}$$

$$H_{z,z_k}^{r_i,\varphi_j} = -\cos\theta_M \operatorname{sign}\overline{z}_k \cdot \varphi_j + 0 \cdot \operatorname{sign}\overline{z}_k \log|\overline{z}_k|, \tag{4.41}$$

while all other field components not indicated are equal to zero in this case, i.e.

$$H_{r,r_i}^{\varphi_j,z_k} = H_{r,z_k}^{r_i,\varphi_j} = H_{\varphi,r_i}^{\varphi_j,z_k} = H_{\varphi,\varphi_j}^{r_i,z_k} = H_{\varphi,z_k}^{r_i,\varphi_j} = H_{z,r_i}^{\varphi_j,z_k} = H_{z,\varphi_j}^{r_i,z_k} = 0. \tag{4.42}$$

The tables for all cases can be found in App. C, the implementation in App. I.

## 4.5. Numerical verification

### 4.5.1. Implementation and performance

The analytical formulas are lengthy and tedious to implement numerically. For public use, we have integrated our fully tested and vectorized code into the upcoming version 4 of the open-source package

| | $r_1$ [mm] | $r_2$ [mm] | $\varphi_1$ [rad] | $\varphi_2$ [rad] | $z_1$ [mm] | $z_2$ [mm] | $\mu_0 M$ [T] | $\varphi_M$ [rad] | $\theta_M$ [rad] |
|---|---|---|---|---|---|---|---|---|---|
| test geometry 1 | 10 | 15 | 0 | $\pi/4$ | 0 | 3 | 1 | $9\pi/8$ | $\pi/2$ |
| test geometry 2 | 25 | 30 | 0 | $\pi/4$ | 0 | 3 | 1 | $9\pi/8$ | $\pi/2$ |

Table 4.3.: Test geometries for comparison to numerical integration.



(a)  (b)  (c)
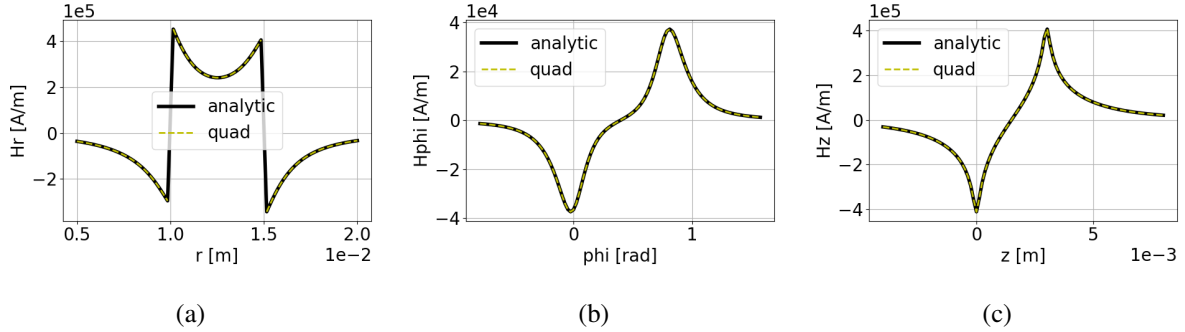
Figure 4.3.: Comparison between the derived analytical solution in Sec. 4.4 (analytic) and the direct numerical integration of the integrals in Eqs. (4.16)-(4.18) with quadrature (quad). (a) $H_r$ component as function of radial coordinate $r$ at $\varphi = \pi/8$ rad and $z = 0.0015$ m for test geometry 1. (b) $H_\varphi$ component as function of angular coordinate $\varphi$ at $r = 0.022$ m and $z = 0.001$ m for test geometry 2 (c) $H_z$ component as function of angular coordinate $z$ at $r = 0.0249$ m and $\varphi = \pi/8$ rad for test geometry 2.

Magpylib [106] under the source name `CylinderSegment`. Although the program flow of the implementation is, at this time, not optimal, we still achieve computation times of the order of few milliseconds (single points) and few tens of microseconds (vectorized evaluation of 2000 points) on mobile CPUs such as Intel i5-8365U, 1.60 GHZ. In comparison, a computation by numerical integration with the precision of Subsec. 4.5.2 takes a few tens of seconds (single points, no vectorization possible), while the performance trimmed finite element code from Subsec. 4.5.3 takes several hours (complete solution) on the same machine.

## 4.5.2. Comparison to numerical integration

We demonstrate the correctness of the solution and our implementation by comparing with direct numerical integration via `scipy.integrate.dblquad` [140, 141] of the integrals Eqs. (4.16)-(4.18). The dimensions of the cylinder tiles and field evaluation points are chosen similarly to [122, Figs. 6-8] and are listed in Tab. 4.3 and the results in Fig. 4.3. All graphs are in perfect agreement.

## 4.5.3. Comparison to FEM

Finally, we compare our Magpylib implementation with the state-of-the-art FEM computations from ANSYS Maxwell [142]. To this end, we place three different uniformly magnetized cylinder tiles with the dimensions given in Tab. 4.4 in a circle, as illustrated in Fig. 4.4a. The field is then computed on four rings, see Tab. 4.5, above, outside, inside and on the inside of the tiles (blue in the figure) to cover many different special cases. The agreement between analytical implementation and the numerical evaluation via FEM can be observed in Fig. 4.4b-e, and is only limited by the numerical stability due to cancellation effects etc. of the analytical formulas, the numerical precision of the finite element computation and possible boundary effects in the case of an insufficiently large airbox in the finite element simulation.

41
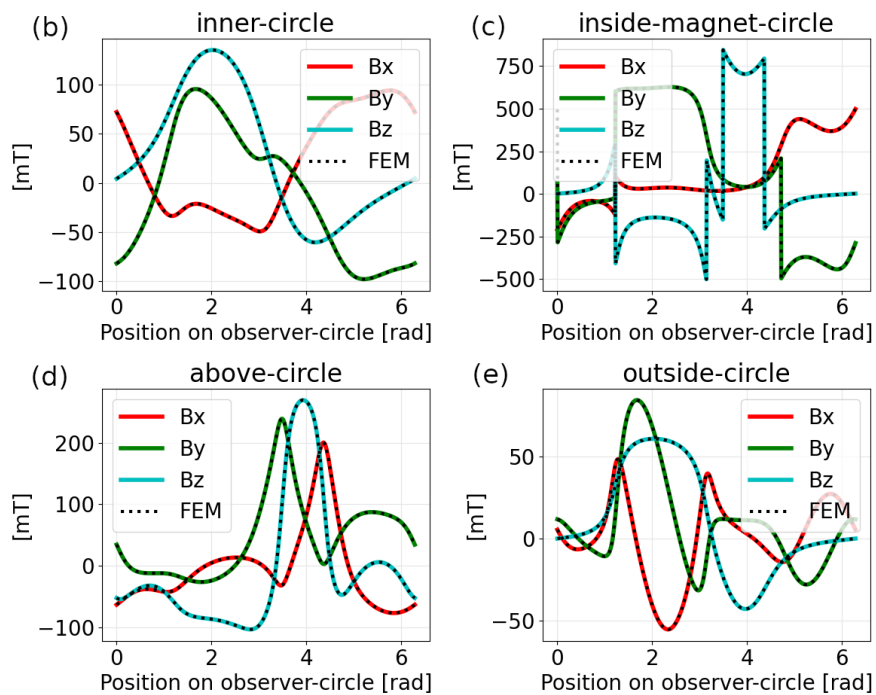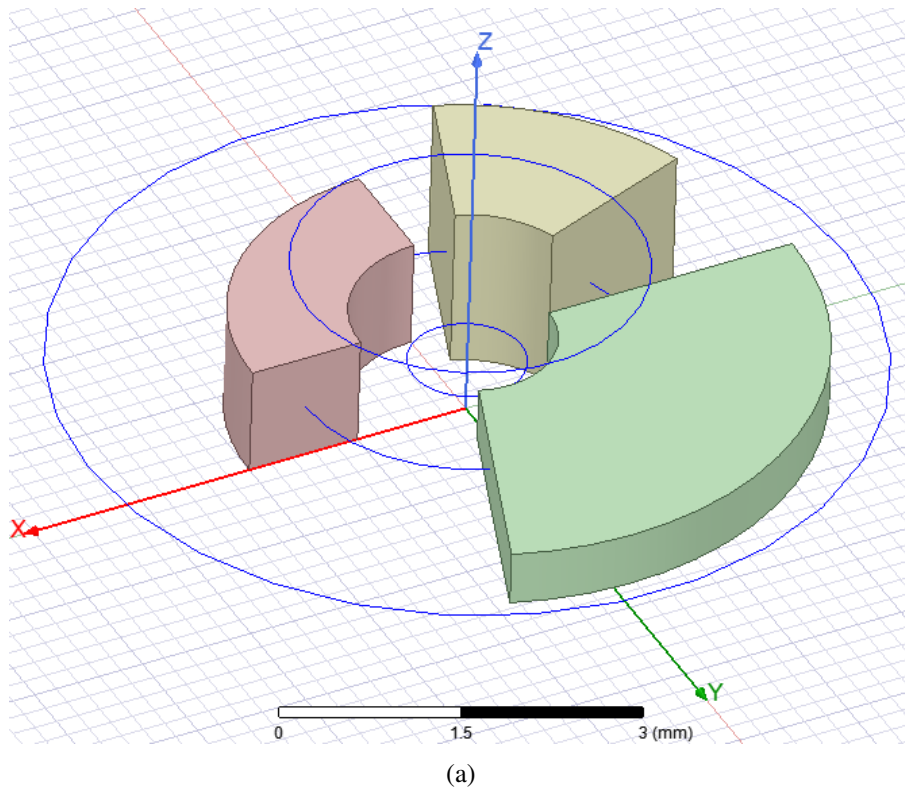
Figure 4.4.: (a) Position of the three cylinder tiles in red, amber and green. The blue circles illustrate the paths, along which the magnetic field is evaluated (see also Tab. 4.5). (b) Cartesian field components along the inner-circle. (c) Cartesian field components along the inside-magnet-circle. (d) Cartesian field components along the above-circle. (e) Cartesian field components along the outside-circle.

| | $r_1$ [mm] | $r_2$ [mm] | $\varphi_1$ [rad] | $\varphi_2$ [rad] | $z_1$ [mm] | $z_2$ [mm] | $\mu_0 M$ [T] | $\varphi_M$ [rad] | $\theta_M$ [rad] |
|---|---|---|---|---|---|---|---|---|---|
| tile 1 | 1 | 2 | $3\pi/2$ | $2\pi$ | $-0.5$ | 0.5 | 1 | $7\pi/4$ | $\pi/2$ |
| tile 2 | 1 | 2.5 | $10\pi/9$ | $25\pi/18$ | $-0.75$ | 0.75 | 1 | 0 | 0 |
| tile 3 | 0.75 | 3 | $7\pi/18$ | $\pi$ | $-0.25$ | 0.25 | 1 | $\pi/2$ | $3\pi/4$ |

Table 4.4.: Position and magnetization of the three cylinder tiles, as illustrated in Fig. 4.4a.

| | center [mm] | radius [mm] | rotation axis [mm] |
|---|---|---|---|
| inner-circle | $(0,0,0)$ | 0.5 | $(0,0,1)$ |
| inside-magnet-circle | $(0,0,0)$ | 1.5 | $(0,0,1)$ |
| above-circle | $(0,0,1)$ | 1.5 | $(0,0,1)$ |
| outside-circle | $(0,0,0)$ | 3.5 | $(0,0,1)$ |

Table 4.5.: Center, radius and rotation axis of the four circles along which the magnetic field is evaluated as illustrated in Fig. 4.4.

## 4.6. Halbach cylinder application

The computation of the field of discrete Halbach cylinders is a perfect use-case for our analytical computation method. Classical Halbach cylinders are magnetized hollow cylinders with a very specific azimuth angle dependent magnetization pattern,

$$\mathbf{M}_n(\varphi) = M_r\big(\cos(2m\varphi), \sin(2m\varphi), 0\big), \quad m \in \mathbb{N} \tag{4.43}$$

that results for the case $m = 1$ in a perfectly homogeneous field on the inside of the cylinder and no field on the outside, see Fig. 4.5a. Halbach cylinders and their derivatives are magnetically the most efficient structures to generate homogeneous fields with large field amplitudes [143]. They are commonly used for magnetic resonance imaging [144], magnetic refrigeration [145], energy harvesting [146] and many other modern applications.

For practical purposes, it is very difficult to achieve the magnetization pattern Eq. (4.43). However, a common approach replaces the continuous magnetization pattern with a discrete one, [144]. In Fig. 4.5b we show such a discretization, where a discrete Halbach cylinder is constructed from homogeneously magnetized cylinder tiles.

The analytical formulas presented in this work enable users to quickly compute and test the field of such discrete Halbach structures for different cylinder radii, cylinder heights, discretizations, magnetization patterns, target regions and all other variables that come into play when designing or optimizing an experiment [147–149]. A specific example for a discretization into $n = 12$ segments is shown in Fig. 4.5c.

## 4.7. Stray-field immunity of rotation sensors

We apply our analytical method to study the angular error due to the stray field influence of a current wire. It is inspired by [118, 150], where this error is measured in experimental setups. Thereby we demonstrate, how the analytical formulas allow to simulate the whole system for different input parameters without much effort and with very high accuracy, which allows a detailed analysis of its behavior. Therefore, we choose the arrangement of the sensor system as shown in Fig. 4.6.

The inner and outer diameters of the magnets are 5 mm and 14 mm, the height is 3.5 mm. The sensor array is aligned below the magnets with an airgap distance of 1.5 mm. The sensors are aligned
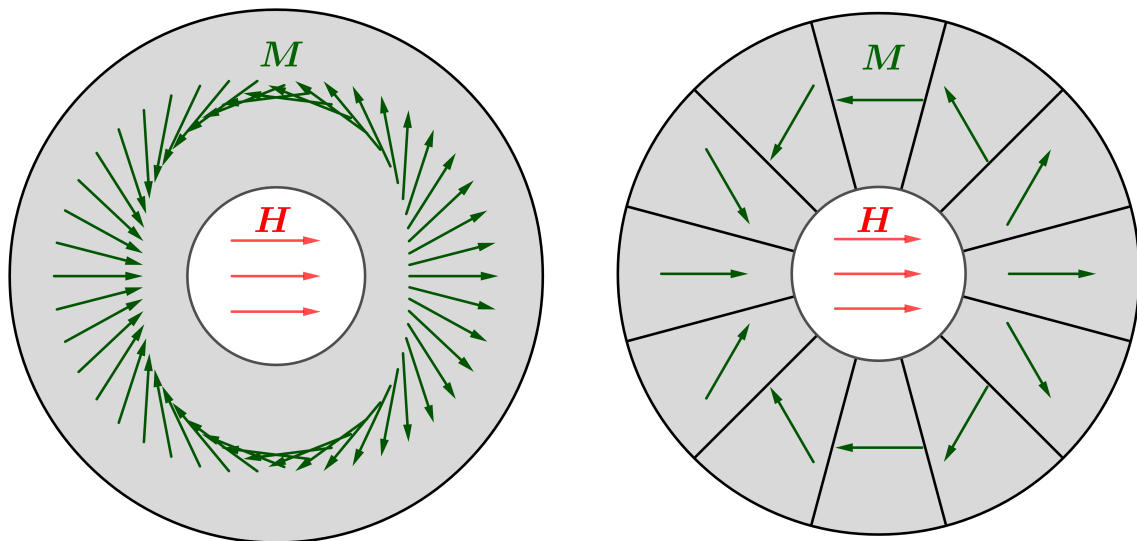
(a)                                          (b)
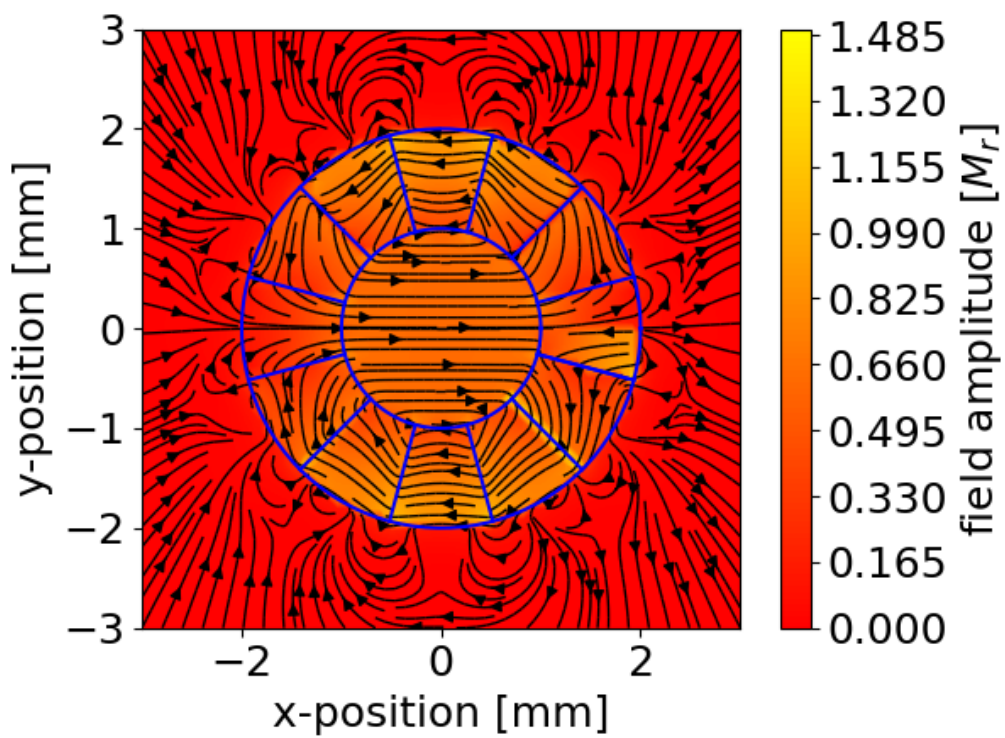


(c)

Figure 4.5.: (a) Sketch of magnetization **M** in a Halbach cylinder with perfectly homogeneous field **H** inside. (b) Sketch of a discrete Halbach cylinder with $n = 12$ cylinder tiles. (c) Magnetic flux density in the discrete Halbach cylinder with a height of $4\,\text{mm}$, computed with the analytical solution.
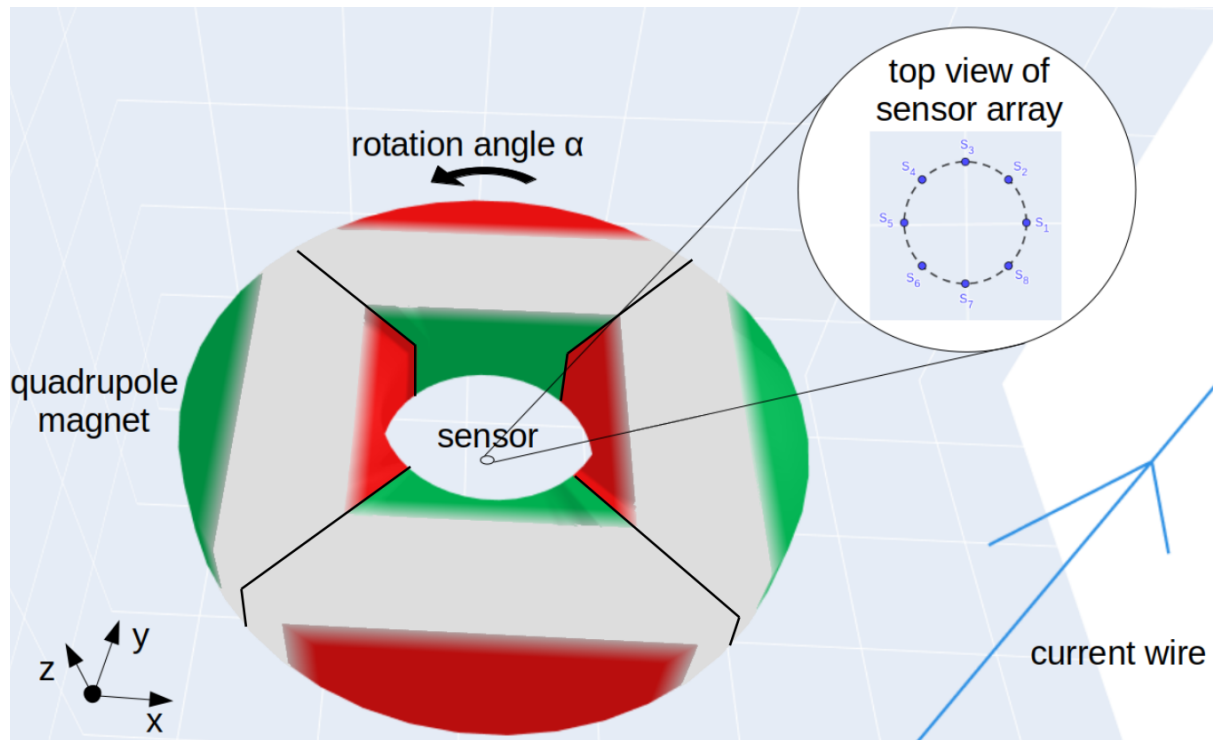
Figure 4.6.: Sketch of quadrupole magnet consisting of four cylinder tile magnets alternately magnetized in the positive and negative radial directions. Its magnetic north poles are colored red, the south poles in green. The sensor arrays consists of eight 1D Hall sensor elements, each measuring the field in radial direction that oscillates due to the rotation of the magnet by the angle $\alpha$. The current flows in positive $z$-direction.

equidistant on a circle with radius 0.25 mm and detect the magnetic field in radial direction. We choose the magnetization so that the maximum measured field is $B_0 := 8.25$ mT for one full rotation of the quadrupole magnet. It is assumed that the straight wire has a distance 30 mm from the center of the magnet. Then the current creates a circular field at the sensor position.

### 4.7.1. No current in wire

In the current-less ideal case, all sensor signals $s_1, \ldots, s_8$ result approximately in the course of a harmonic oscillation shown in Fig. 4.7a.

The field measured by each of the four sensors with odd and even indices can therefore be combined into a cosine and sine signal as

$$C := s_1 - s_3 + s_5 - s_7, \tag{4.44}$$
$$S := s_2 - s_4 + s_6 - s_8, \tag{4.45}$$
$$\tag{4.46}$$

and we receive the signal illustrated in Fig. 4.7b.

Due to the identity

$$\alpha = \arctan2\big(\cos(\alpha), \sin(\alpha)\big) \tag{4.47}$$

for all $\alpha \in [0°, 360°)$, the sensor measured rotation angle $\hat{\alpha} \in [0°, 180°)$ can be defined as

$$\hat{\alpha} := \frac{\arctan2(C, S)}{2}. \tag{4.48}$$

The deviation from the real rotation angle $\hat{\alpha} - \alpha$ can be seen in Fig. 4.8a. Since the analytical solution allows to calculate the error exactly, one can observe in detail in which angular positions the largest errors are to be expected. However, in our case, without the external stray field of the wire, the angle measurement is very accurate and we observe errors down to only $\sim 10^{-4°}$.

### 4.7.2. With stray field from wire

In case of an additional magnetic field caused by the current in the electric wire (see Fig. 4.6), the symmetry is broken and this leads to a larger but still manageable error of the measured angle $\hat{\alpha}$. If the current line in Fig. 4.6 is additionally tilted by e.g. 45° in the $x$-$z$-plane, the maximum error is even larger and reaches even about 0.4°, which is in very good agreement with the results in [150]. Figure 4.8b shows the error in the angle measurement for different currents and the respective resulting fields at the sensor position for a straight and tilted wire. Even with the assumption of very high currents $750 - 3750$ A that result in circular fields of $5 - 25$ mT at the central sensor position in the setup of the straight wire in Fig. 4.6, we observe that the error is kept within limits.

The analytical solution enables fast and accurate analysis of even more details of the sensor system (error analysis, error phase diagrams for various system parameters). The details are the subject of more detailed investigations, which are not presented here for reasons of non-disclosure and may also be published separately with a detailed discussion of the consequences.

## 4.8. Conclusion & outlook

In this work, we have presented fully analytical expressions for the magnetic field of a homogeneously magnetized cylinder tile. The solution was implemented in Python and validated against numerical
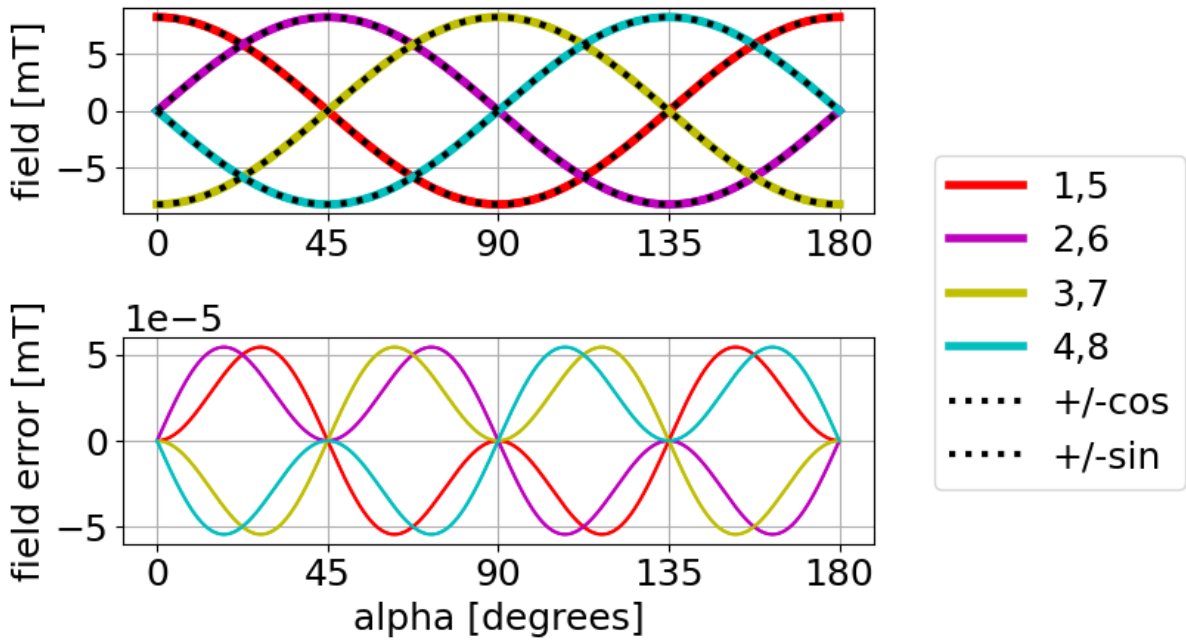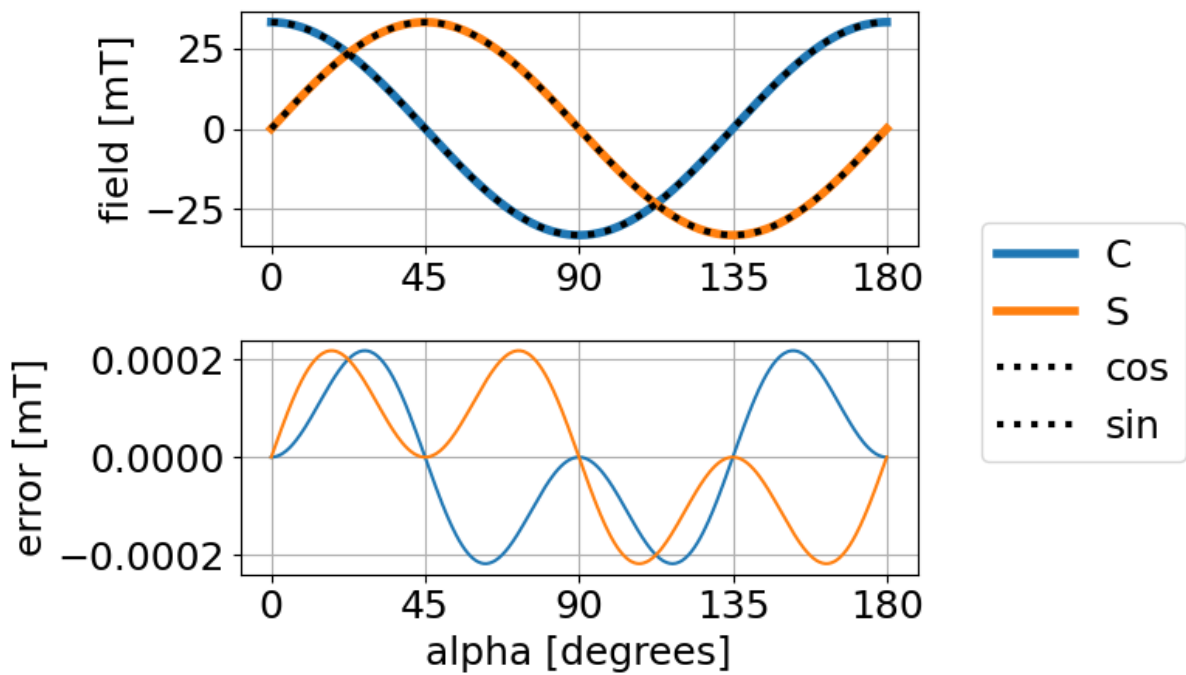
Figure 4.7.: (a) Signals from the eight sensors $s_1, \ldots, s_8$ during a rotation of the magnetic quadrupole by $180°$ in the absence of additional fields originating from the current wire. In comparison, the graphs of $\pm B_0 \cos(2\alpha)$ and $\pm B_0 \sin(2\alpha)$ show almost perfect agreement. The errors are calculated as deviation from the perfect harmonic oscillation, i.e. differences $s_i \mp B_0 \cos(2\alpha)$ for odd $i$ and $s_i \mp B_0 \sin(2\alpha)$ for even $i$. (b) The combination of four sensors each leads to the two main branches of the signal, which approximately follow the function graphs of $4B_0 \cos(2\alpha)$ and $4B_0 \sin(2\alpha)$. The errors are calculated as deviation from the perfect harmonic oscillation, i.e. differences $C - 4B_0 \cos(2\alpha)$ and $S - 4B_0 \sin(2\alpha)$.
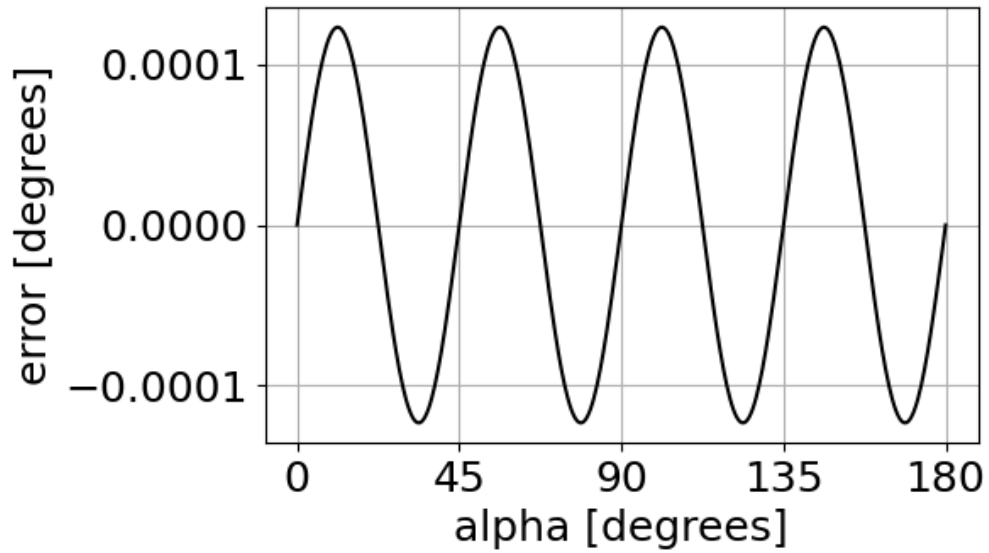
(a)
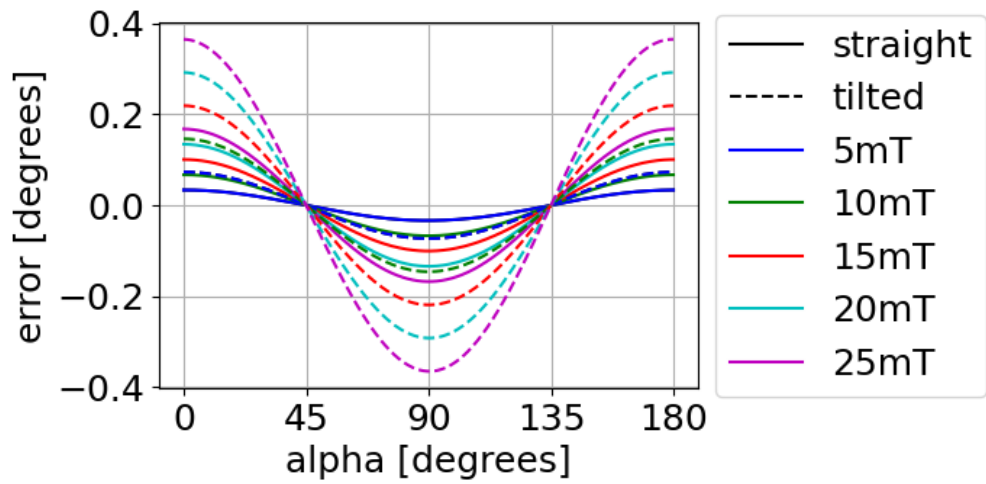


(b)

Figure 4.8.: Deviation of the sensor output $\hat{\alpha}$ compared to the real rotation angle $\alpha$. (a) without external fields and (b) for different external fields and straight and tilted wire (by $45°$ in the $x$-$z$-plane).

computations. The usefulness of this work was demonstrated by computing the field in a discrete Halbach cylinder and analyzing the angle error of a rotation sensor system. The examples have shown that with the use of the analytical solution, various application can easily be modeled and analyzed very accurately. In addition, the limitation of homogeneous magnetization is discussed and a method of moments for demagnetization effects is proposed.

While the provided formula set is complete from a mathematical point of view, floating point based implementations still suffer from numerical instabilities in the vicinity of special cases, indeterminate forms and at large distances. To address this problem, methods of reformulation and series expansion are planned to provide a higher level of stability.

By including the code in the open-source Python package Magpylib, the benefits of this work are also immediately accessible to the general public. Future work is dedicated to improve the Magpylib implementation work flow, stability and computation speed.

# 5. Designing airgap-stable magnetic linear position systems

This work addresses the topic of magnetic linear position detection, a common method used in modern industries to determine linear displacement by magnetic means. One major shortcoming of this method is the inherent airgap instability, which puts strong constraints on mechanical construction tolerances and limits resolution and sensitivity. We propose a method to improve the airgap stability by adding a second magnet, which makes the field and by extension the system output (locally) independent of the distance from the source. It is shown that the measurement error for 1D systems can be reduced by a factor of $\sim 14$ and for 2D systems by a factor of $\sim 5$ by application of this method for a realistic example.

Parts of this chapter have been previously published in [151] and have been reproduced with permission of the coauthors and in accordance with the publisher's policy. Content that was not generated by the author of this thesis is explicitly denoted, copyright is held by IEEE.

## 5.1. Introduction

Magnetic position and orientation detection systems determine the relative motion of mechanical parts. A permanent magnet is mounted on one part and a magnetic field sensor on the other, so that the relative motion can be calculated from the modulation of the magnetic field [94, 125]. Such sensor systems that are widely used in modern industrial applications due to their excellent properties (cost, robustness, non-contact) [152–158], are constantly opening new sensing possibilities [92, 159, 160] and have started to replace existing mechanical, electronic and optical technologies [161–163]. Today there are more than 100 applications for magnetic position sensor systems in the automotive sector alone [93, 164, 165].

Magnetic linear position sensing is one common representative, with prominent applications like automotive shift forks, gas and brake pedals, detection of shifting shafts, flexible arms, lifting systems, in the gearbox and many others. In this case, a permanent magnet moves along a straight line with a sensor mounted centrally above in a distance $g$ termed the airgap. The range of the system is given by the stroke $s$ with the magnet position $x \in [-s, s]$ (see Fig. 5.1a).

The magnetic field at the position of the sensor is given by $\mathbf{B}(x)$ and the sensor output $\beta(\mathbf{B})$ is assumed to be proportional to it, $\beta \propto \mathbf{B}$, which is characteristic for the commonly used linear Hall sensors. The system output signal $\zeta(\beta)$ is determined from the sensor output, and the position is calculated from it,

$$x \rightarrow \mathbf{B} \rightarrow \beta \rightarrow \zeta \Rightarrow x. \tag{5.1}$$

For a typical linear position system, based on the magnet configuration from Fig. 5.1c, the field $\mathbf{B}(x)$ is shown in Fig. 5.1b as a function of the position for a $12 \times 5 \times 5\,\text{mm}^3$ magnet with magnetization $\mu_0 M = 1000\,\text{mT}$ and an airgap of $g = 5\,\text{mm}$. Due to the symmetry, there are only two non-zero field components, $B_x(x)$ with even and $B_z(x)$ with odd behavior. While there are several other ways to choose magnet configurations (see Fig. 5.1c-e), in each case there is an even and an odd field component, $B_{\text{eve}}$ and $B_{\text{odd}}$, on which the linear position sensing schemes rely.
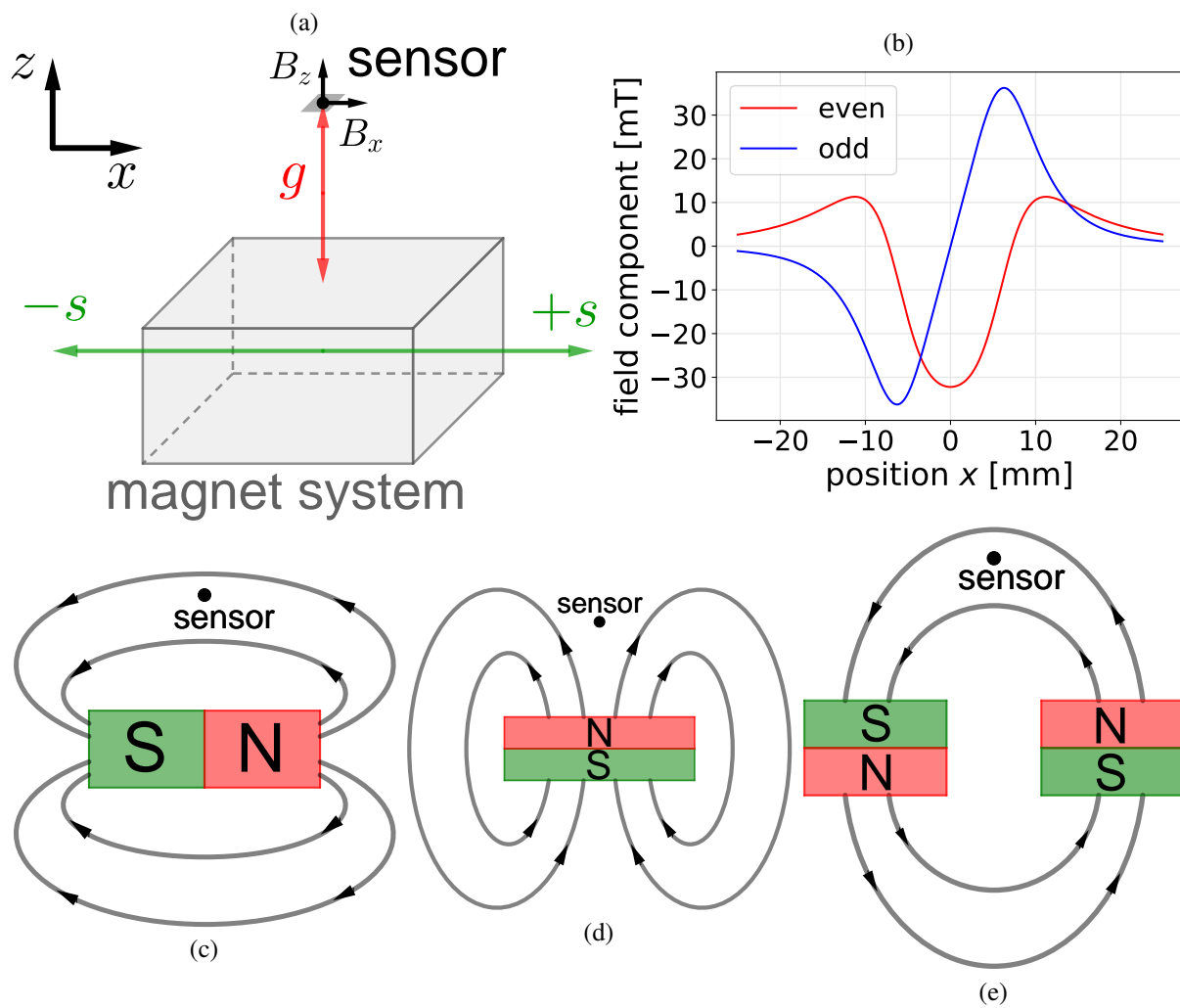
Figure 5.1.: In (a) the moveable magnet system beneath a sensor is illustrated. It may consist of different magnet assemblies (c)-(e), which all generate an even and an odd component of the magnetic field as shown in (b).

If only a 1D sensor is available, it must detect $B_{\text{odd}}$ for a linear and unique relation between position and output,

$$\zeta_{1D} = \beta_{\text{odd}}. \tag{5.2}$$

The potential range of such a system is then given by the central, monotonous linear part of the curve. A more sophisticated scheme can be used with a 2D sensor,

$$\zeta_{2D} = \text{atan}_2(\beta_{\text{odd}}, \beta_{\text{eve}}), \tag{5.3}$$

where $\text{atan}_2$ denotes the common two-argument arctangent function, see [108]. While the 2D method features a higher level of signal stability, precision and measurement range when compared to the 1D counterpart, the latter is still used for its cost efficiency.

Finally, a sensor system is characterized by its sensitivity $S$. It is given by the change of the system output with variation of the observable (here magnet position $x$),

$$S(x_0, z_0) := \frac{d\zeta}{dx}(x_0, z_0). \tag{5.4}$$

A more detailed analysis of 1D and 2D sensing schemes, sensors and systems can be found in [108, 109]. In Tab. 5.1 below, we show a list of system parameters and their typical sizes for state-of-the-art Hall-based industrial linear position systems.

| parameter | symbol | unit | typical size |
|---|---|---|---|
| stroke | $s$ | mm | 5-20 |
| position | $x$ | mm | [-s,s] |
| airgap | $g$ | mm | 2-8 |
| Magnetization | $\mu_0 M$ | mT | 200-1400 |
| B-field | $\mathbf{B}$ | mT | 10-100 |
| sensor output | $\beta$ | V | 0-5 |
| sensitivity 1D | $S$ | mT/mm | 10-100 / s |
| sensitivity 2D | $S$ | rad/mm | $\pi$ / s |
| system output | $\zeta$ | - | - |

Table 5.1.: System parameter names and typical values.

## 5.2. Problem

One of the biggest problems when dealing with linear magnetic position sensing is the inherent instability with respect to airgap variations $\Delta g$. Industrial and automotive systems are only competitive if they are cost-efficient, and fabrication tolerances are expensive to control. In automotive shift-fork systems airgap variations of up to $\pm 20\%$ are common. Such variations are usually calibrated out in an end-of-the-line process which ultimately results in large variations of the sensitivity. In addition, dynamic airgap variations of few percent over lifetime and during system operation must also be accounted for.

The sketch in Fig. 5.2 shows how an airgap variation leads to a inaccurate output signal $\zeta(x_0, z)$ instead of $\zeta(x_0, g)$, which further results in a wrong position estimation $\widetilde{x}_0$ for the real position $x_0$. In first order, the position error $\Delta x := x_0 - \widetilde{x}_0$, which results from airgap variation, is directly connected to the system output error $\Delta \zeta := \zeta(x_0, g) - \zeta(x_0, z)$ through the nominal sensitivity $S(x_0, g)$. We can therefore write

$$\Delta x(x_0, z) = \frac{\Delta \zeta(x_0, z)}{S(x_0, g)} \tag{5.5}$$

at position $x_0$. For convenience we have expressed everything through $z$, which is connected to the airgap variation through $z = g + \Delta g$. Clearly $\Delta x(x_0, g) = 0$ for all positions $x_0 \in [-s, s]$.
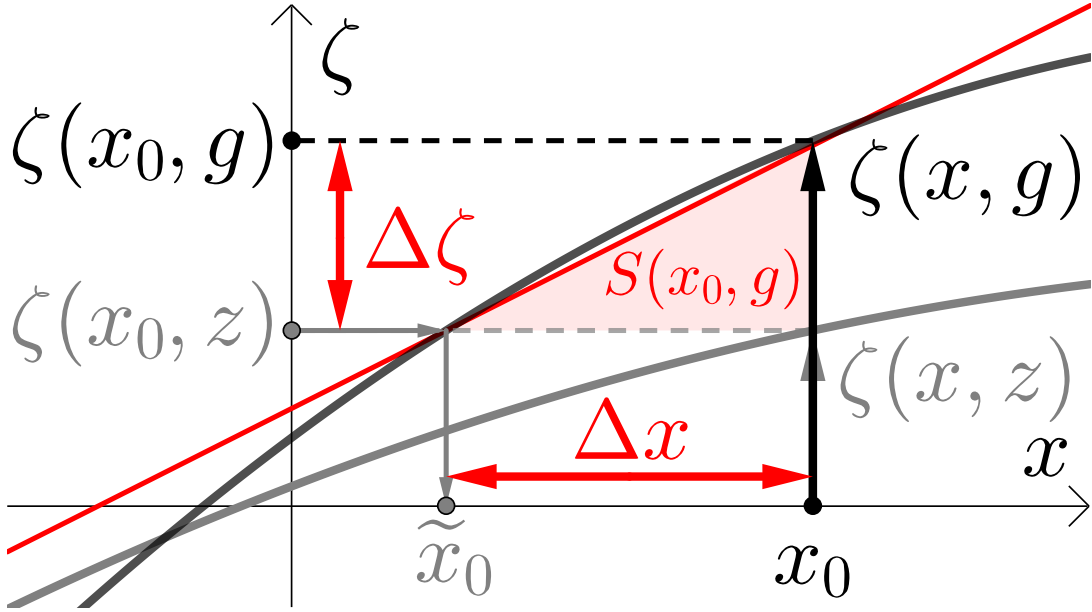


Figure 5.2.: Sketch of the system response. The airgap variation leads to a measurement error $\Delta x$, which is determined by $\Delta \zeta$ and the local slope $S(x_0, g)$ of the function $\zeta(x, g)$.

To demonstrate the effects of airgap variations, we show the magnetic field of the example system from Sec. 5.1 for different airgaps in Fig. 5.3a. The maximal position error $\Delta x_{\max} := \max_{x_0 \in [-s,s]} \Delta x(x_0, z)$ as a function of the airgap variation $\Delta g$ is given in Fig. 5.3b for $s = 5\,\mathrm{mm}$. The inherent higher stability of the 2D scheme is clearly visible.

## 5.3. Proposal

To improve airgap stability in linear position systems, we propose to make the magnetic field $\mathbf{B}(x, z)$ or rather the system output $\zeta(x, z)$ locally independent of the airgap by combining the fields of several simple magnets in the spirit of [108, 166]. A sketch of the main idea is outlined in Fig. 5.4. There, the quick decay of the magnetic field of a small, close magnet is superposed with the slow decay of a large, distant magnet with reversed magnetization. By suitable arrangement of the two magnets (or magnet systems) we can achieve stationary points $z_s$ of the field components in airgap direction, $\mathrm{d}\mathbf{B}/\mathrm{d}z(x, z_s) = 0$. Ideally, this is achieved for both components simultaneously and all positions $x$ so that the system output becomes locally airgap independent,

$$\frac{\mathrm{d}\zeta}{\mathrm{d}z}(x, z_s) = \frac{\mathrm{d}\zeta}{\mathrm{d}\mathbf{B}} \cdot \underbrace{\frac{\mathrm{d}\mathbf{B}}{\mathrm{d}z}(x, z_s)}_{=0} = 0. \tag{5.6}$$

The system output error is closely connected to the derivative of $\zeta$ in z-direction,

$$\Delta \zeta(x, z) = \zeta(x, g) - \zeta(x, z) \simeq \frac{\mathrm{d}\zeta}{\mathrm{d}z}(x, z) \cdot \Delta g, \tag{5.7}$$
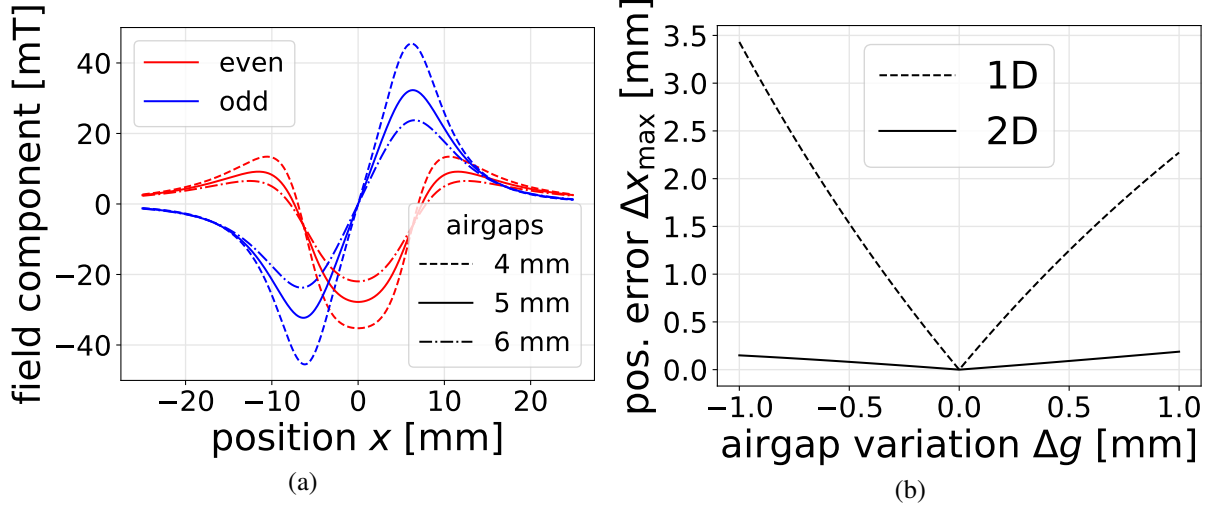
Figure 5.3.: Airgap dependence of the field (a) and resulting position error $\Delta x_{\mathrm{max}}$ for 1D and 2D sensor schemes (b).

so that the property in Eq. (5.6) translates directly to the position error in Eq. (5.5).

Note that stationary points of field $\mathbf{B}$ are sufficient, but in the 2D case not necessary for the desired stationary points of the system output $\zeta$. While it is difficult to achieve stationarity for all positions $x$ at the same time, it is enough to sample the "low slope area" near $z_{\mathrm{s}}$ to improve stability (see Fig. 5.4b).

## 5.4. Method

We compare 1-magnet (state-of-the-art) and 2-magnet (proposal) systems with 1D and 2D sensors respectively. For good magnetic stability the 2-magnet system is constructed as indicated in Fig. 5.5 with magnet dimensions $a_1, b_1, c_1, a_2, b_2, c_2$ and distance $d$. This work is based on a multivariate optimization of these magnet system parameters to reduce the position error as much as possible. For comparison with optimal 1-magnet systems a similar optimization with $a_1 = b_1 = c_1 = 0$ is performed.

One must take care in the optimization process that the sensitivity does not tend to small or even negative values. This would violate the fundamental requirement that the system output $\zeta$ is a bijective map of the observable of interest.

### 5.4.1. Cost function

The optimal system is found by global minimization of a cost function $F$ which expresses the desired system qualities. We choose a weighted position error,

$$\overline{\Delta x}(x_0) := \left( \int_{g-\Delta g}^{g+\Delta g} w(z) \cdot |\Delta x(x_0, z)|^2 \, \mathrm{d}z \right)^{1/2} \tag{5.8}$$

introducing the Gaussian weight function $w(z)$ with $\mu = g$ and $\sigma = \Delta g/3$ to account for realistic stochastic deviations of industrial systems. A corresponding cost function can then be defined as the maximal weighted position error over the whole range,

$$F_p := \max_{x_0 \in [-s,s]} \overline{\Delta x}(x_0). \tag{5.9}$$
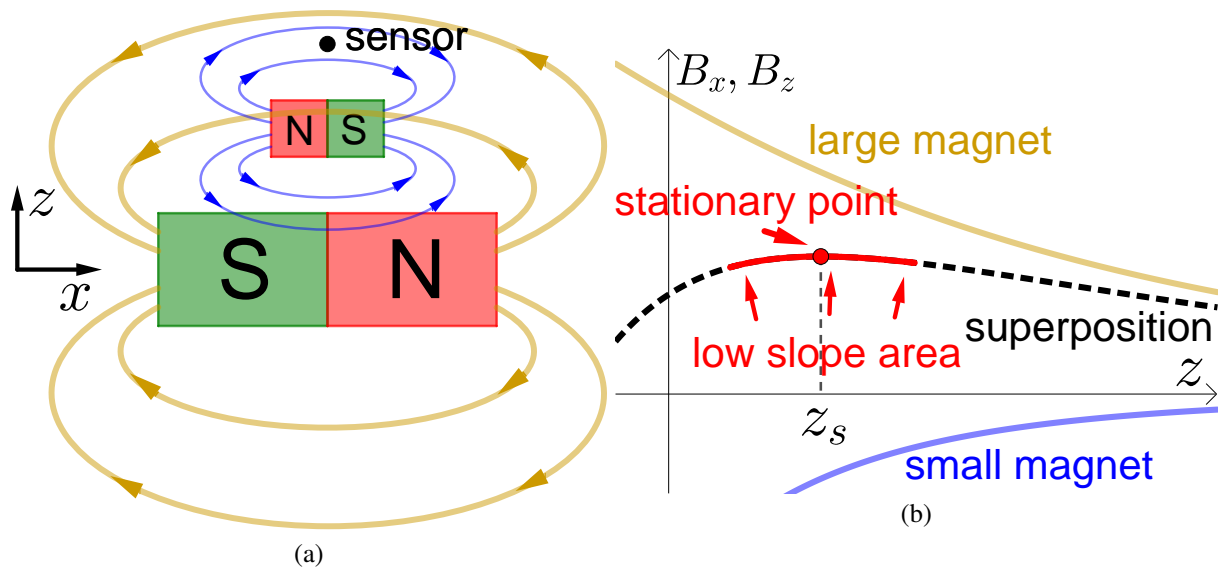
Figure 5.4.: The antiparallel permanent magnet arrangement (a) leads to a beneficial field superposition (b). For well-chosen dimensions, the sketch in (b) is approximately valid for both $B_x$ and $B_z$ and all $x$ simultaneously (possibly with reversed sign).
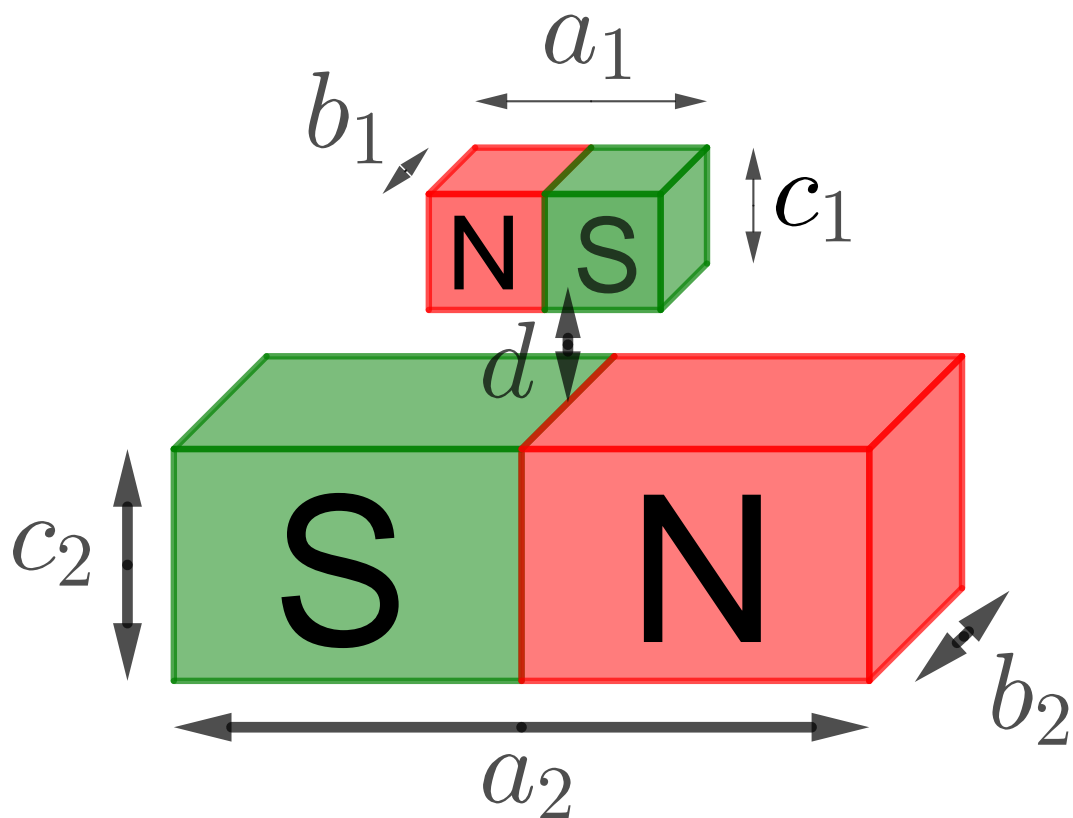


Figure 5.5.: Sketch of the magnet system variation parameters.

At the same time, the quality of a sensor system is strongly related to its sensitivity Eq. (5.4) which can be represented through another cost function $F_s$ that could, for example, be given by the minimal sensitivity over the whole range.

A total cost function $F$ can then be written as a convex combination of these two terms, i.e.

$$F := (1 - \lambda)F_p - \lambda F_s \tag{5.10}$$

with $\lambda \in [0, 1]$. Minimization of $F$ leads to minimized position error and maximized sensitivity at the same time, where $\lambda$ specifies the balance between $F_p$ and $F_s$.

In this work we set $\lambda = 0$ and neglect the sensitivity term $F_s$ because the sensitivity must always be related to sensor resolution and noise behavior and we do not want to focus on one specific sensor type.

## 5.4.2. Scaling invariance

A system where the sources are only ideal hard magnets is invariant with respect to the scaling of the spatial dimensions. This means that transformations of the form

$$(x, y, z) \longmapsto k_1 \cdot (x, y, z) \tag{5.11}$$

with $k_1 > 0$ on the whole system (i.e. stroke, airgap, magnet dimensions) result in the same magnetic field at the scaled sensor position. Furthermore, the scaling of the magnetization amplitude

$$M \longmapsto k_2 \cdot M \tag{5.12}$$

has no influence on the optimization problem, as the fields are directly proportional to it, $|\mathbf{B}| \propto M$.

The optimization is independent of the scaling, i.e. for different system sizes and materials the same optimum solution is found up to the scaling factor $k_1$ for geometric parameters and $k_2$ for field and magnetization. With Eqs. (5.11) and (5.12) we can define a characteristic length $l_0$ and magnetic field $M_0$ and express all spatial variables, magnetizations and fields as dimensionless multiples of these parameters. Eventually, $l_0$ and $M_0$ can be used after solving the optimization problem, to set a system size and a material for practical applications.

## 5.4.3. Reasonable system constraints

When dealing with realistic problems the end-user has specific requirements which must be included in the optimization process. These "reasonable system constraints" include

- the detection range or length of the stroke $s$,

- the airgap $g$ and airgap tolerance $\Delta g$,

- a required resolution given by choice of sensor and sensitivity $S$,

- the construction space with maximal magnet system dimensions $x_{\max}, y_{\max}, z_{\max}$ typically limited to $\sim s$,

- the construction costs reflected in magnet volume $V$ and magnetic material (magnetization $M$).

For our demonstration in the next section we choose $l_0 = 1\,\mathrm{mm}$, $\mu_0 M_0 = 1\,\mathrm{mT}$ and a set of reasonable constraints in Tab. 5.2 that reflect standard system parameters for a linear position system.

| $s$ $[l_0]$ | $g$ $[l_0]$ | $\Delta g$ $[l_0]$ | $x_{\max}$ $[l_0]$ | $y_{\max}$ $[l_0]$ | $z_{\max}$ $[l_0]$ | $V$ $[l_0^3]$ | $M_1$ $[M_0]$ | $M_2$ $[M_0]$ |
|---|---|---|---|---|---|---|---|---|
| 5 | 5 | 1 | 12 | 10 | 14 | 300 | 1000 | 1000 |

Table 5.2.: Realistic system parameters and constraints.

### 5.4.4. Simulation method

The fields are calculated by an analytical method using the magpylib package [106] which is based on the expressions from [98, 111, 112]. The speed of the analytical solution (effective sub-microsecond computation times) enables highly efficient multivariate parameter variation which is not feasible with common numerical methods like FEM or BEM. The error of the analytical solution is below 1% field amplitude and 1° angle for magnet L/D ratios of the order of 1 (cubical magnet dimensions) when compared to FEM results of hard magnets with linear demagnetization slopes of $\mu_r < 1.05$ [92].

## 5.5. Results

The optimization procedure described in the previous section is carried out to find optimal configurations for 1D and 2D systems with one or two magnets. Optimization bounds and results are given in Tab. 5.3.

| parameter | magnet 1 | | | magnet 2 | | |
|---|---|---|---|---|---|---|
| | bound | 1D | 2D | bound | 1D | 2D |
| $a_1$ | - | - | - | 12 | 9.9 | 8.4 |
| $b_1$ | - | - | - | 10 | 0.7 | 9.9 |
| $c_1$ | - | - | - | 3 | 3.0 | 0.2 |
| $a_2$ | 12 | 12.0 | 12.0 | 12 | 12.0 | 12.0 |
| $b_2$ | 10 | 4.2 | 10.0 | 10 | 7.8 | 9.8 |
| $c_2$ | 6 | 6.0 | 2.5 | 3 | 3.0 | 2.4 |
| $d$ | 3 | 3.0 | 0.0 | 3 | 3.0 | 3.0 |

Table 5.3.: Bounds and optimization results of the magnet system parameters shown in Fig. 5.5.

For each of the four cases the resulting sensor output is shown in Fig. 5.6. Two effects can be observed there: On the positive side the 2-magnet systems show increasing airgap stability confirming the original proposal. However, one has to pay for this stability with reduced field amplitudes and sensitivities. This is directly visible in the figures and is given quantitatively in Tab. 5.4.

| | 1-magnet | | 2-magnet | |
|---|---|---|---|---|
| | 1D | 2D | 1D | 2D |
| $F_p$ | 0.766 mm | 0.042 mm | 0.053 mm | 0.009 mm |
| $S(0, g)$ | 3.39 | 0.26 rad/mm | 0.65 | 0.19 rad/mm |

Table 5.4.: Sensitivity $S(0, g)$ for all configurations.

In Fig. 5.7 we shown the actual position error of the sensor output $\Delta x$ as a function of the position $x$ and the airgap variation $\Delta g$. The lower level of position error within the working area (10 mm $\times$ 2 mm rectangle in the figure) is clearly visible.
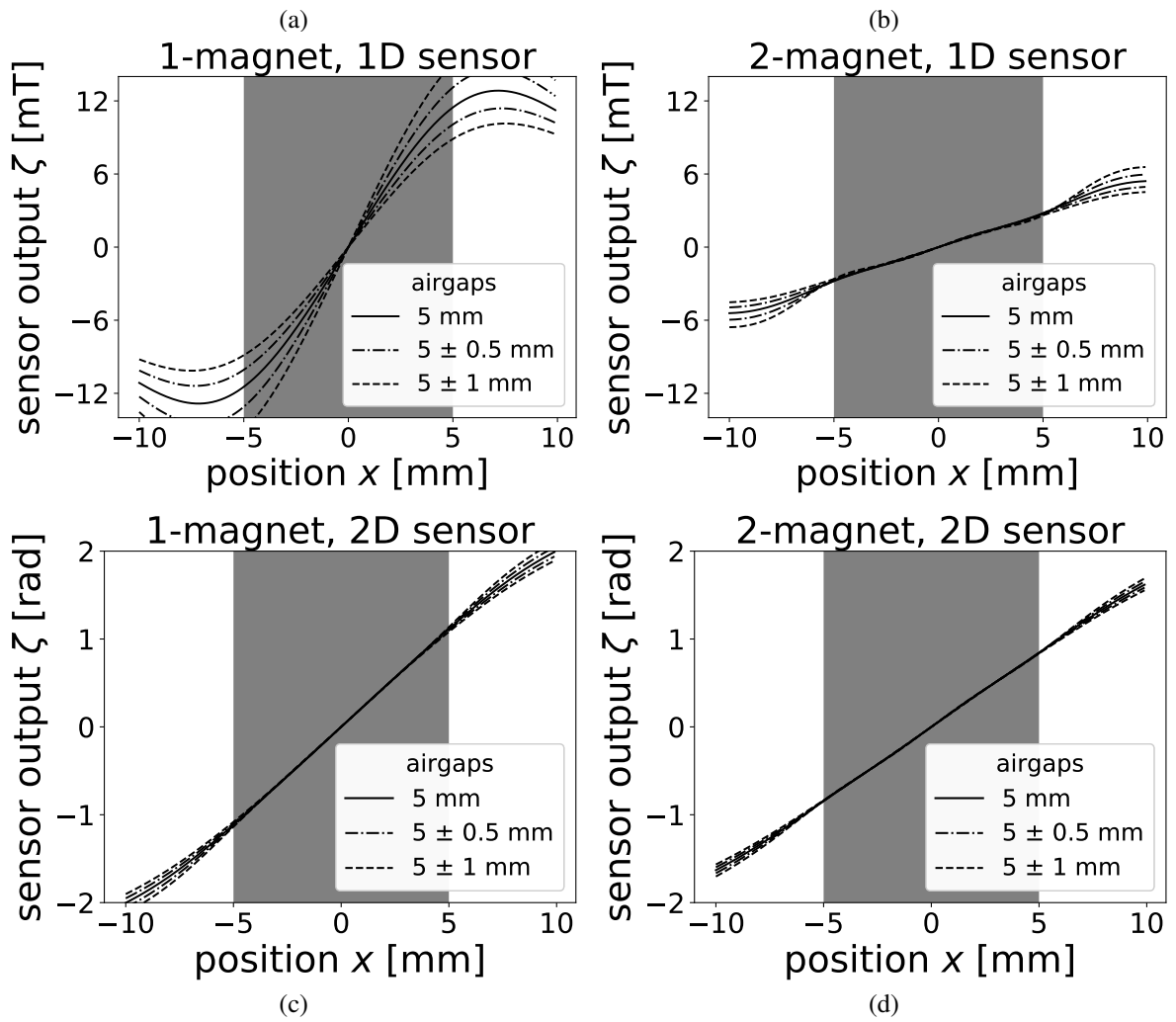
Figure 5.6.: Sensor output of optimum configuration in four different cases.
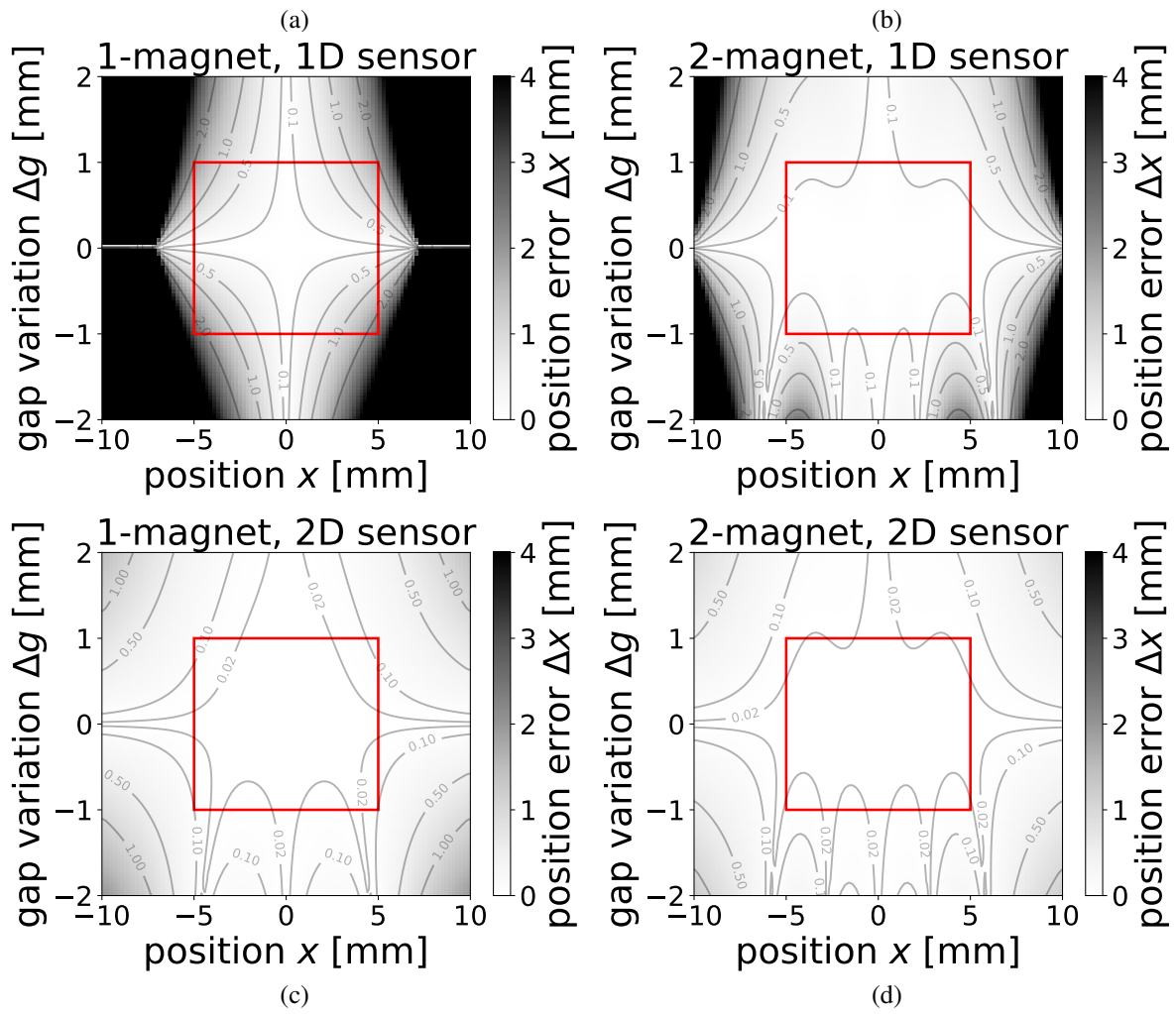
Figure 5.7.: Position error $\Delta x$ for all four configurations. The red rectangle marks the working area ($\pm \Delta g$ airgap variation) of the sensor system.

Finally, we compare the weighted position error $\overline{\Delta x}(x_0)$ from Eq. (5.8) as well as the maximal position error $\Delta x(x_0, z)$ for $z \in [g - \Delta g, g + \Delta g]$ for all four configurations in Fig. 5.8a and b. The 2-magnet systems are visibly improved over their 1-magnet counterparts.
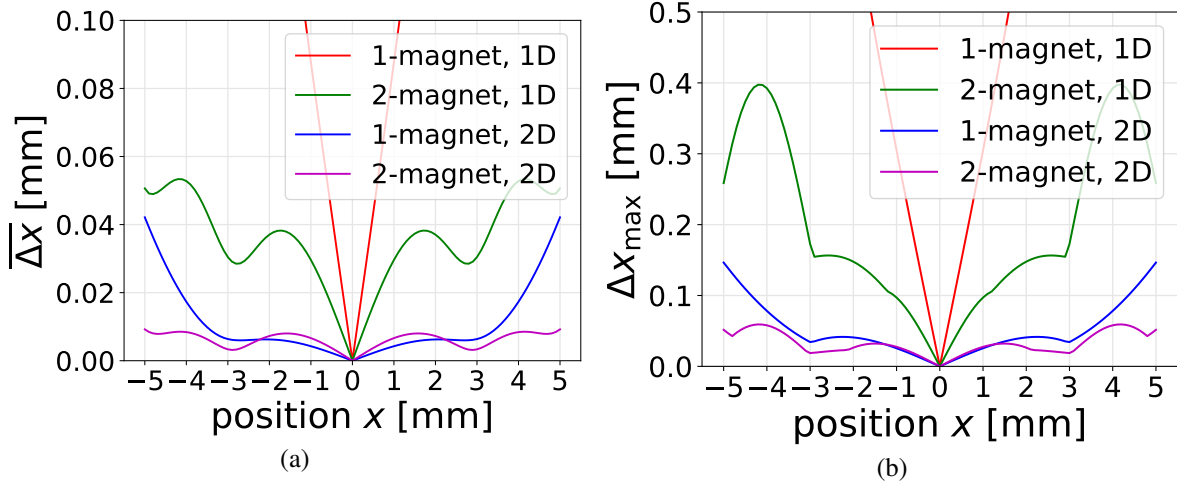


Figure 5.8.: Quantitative comparison of weighted position error $\overline{\Delta x}$ and maximal position error $\Delta x_{max}$ of the four optimized systems with ranges of $\pm 5$ mm and airgap variations $\Delta g$ of $\pm 1$ mm.

## 5.6. Discussion and outlook

In this work we show how to design an airgap stable linear position sensor system by adding a second magnet which stabilizes the field. Here stabilization means a reduction of the position error resulting from airgap variation. It was shown that the proposed method works for both, 1D and 2D sensor systems. For our model problem with airgap variation of $\pm 1$ mm, 5 mm nominal airgap and a range of 10 mm, this can lead to a reduction of the maximal weighted position error by a factor of $\sim 14$ for 1D systems and by a factor of $\sim 5$ for 2D systems within our chosen system requirements. It must be noted that these factors depend on the chosen system. Further improvements are possible which is also visible in Tab. 5.3 by the fact that the optimization returns boundary values. In general, we find that position error reduction by one order of magnitude in 1D and a factor of 3-5 in 2D is easily achieved for the typical linear position systems outlined in Tab. 5.1.

The major downside of the proposed method is the reduction of field amplitude, which translates directly to the sensitivity and potential resolution. However, our results are just a proof of principle where we have demonstrated a novel airgap stabilization mechanism for magnetic systems. With additional constraints and the choice $\lambda > 0$ in Eq. (5.10), the balance between stability and field amplitudes can be adjusted at will.

While the proposed method is based on only two cuboid magnets, it is easily extended to more complex magnet structures as proposed in [108].

Finally, we note that the odd component of a single magnet's field already has natural stationary points with a high level of airgap stability. However, these extrema lie very close to the magnet surface (assuming cuboids) so that if the system is scaled up to achieve desired airgaps, the magnet size exceeds our reasonable system constraints. Further investigation and exploitation of this effect is planned.

# 6. Global magnetic topology optimization

In this chapter, a global approach to magnetic topology optimization is presented and discussed, which makes use of a hybrid optimization algorithm that combines the advantages of local and global optimization methods. The ideas, advantages and disadvantages of such approaches are discussed in detail and tested and illustrated on suitable selected model problems. The results show that global approaches are generally necessary to achieve significantly lower minima of the objective function.

Parts of this chapter have been previously published in [167] and have been reproduced with permission of the coauthors and in accordance with the publisher's policy. Content that was not generated by the author of this thesis is explicitly denoted, copyright is held by SSRN.

## 6.1. Introduction

In various applications of magnetic materials like sensor systems and motors, the profile of the magnetic field (in addition to the sensor properties) has a significant influence on the quality of the system. Therefore, it makes sense to use magnets with optimized shapes that generate fields suitable for the specific application [168–170].

One possible way to improve the magnetic field in some desired way is magnetic topology optimization, where the shape of the magnets is adjusted by optimization [171]. In general, there exist many different approaches to solving the optimization problem [172–180]. Especially recent publications include interesting modern approaches based on genetic algorithms [181], a level set method [182], clustering [183], segmentation [184–186], Gaussian networks [187] and deep learning [188]. In the past, several works have presented possible optimization algorithms that allow the magnets to be optimized with respect to a predefined objective function that measures the quality of the obtained field [189–193]. The basic idea is to describe the geometry by a scalar density field that discretizes the presence or absence of magnetic material in a predefined design region. This may lead to an enormous number of degrees of freedom, however. Most algorithms in the literature use the adjoint method [194–196], which provides a computationally cheap and direct way to compute the derivative of the objective function. This allows the use of common gradient-based optimization algorithms that provide fast convergence in the very high-dimensional discrete magnetic topology space. It has to be mentioned that besides the adjoint method focused in this work, other ways of determining the derivatives [197–199] also exist.

Since gradient-based optimization algorithms [200–202] tend to converge to nearby local minima, there is no guarantee that the minimum reached is global. Even simple toy examples show that, in general, multiple local minima can occur. This problem has been addressed for instance in [203] and the proposed solution is a combination of an on/off sensitivity method and a genetic algorithm [204–208]. In contrast to these approaches, which take into account practically nice looking solutions, we focus more on global optima and present another hybrid topology optimization algorithm that combines the global cuckoo search optimization algorithm [209, 210] with a very fast and efficient local binary on/off optimization algorithm [203, 211]. We discuss why our approach is predestined for optimization problems in the case of a very high-dimensional domain (number of magnetic cells), only two desirable states (magnetic material or not), available gradient (adjoint method), and the possible presence of multiple local minima.

Our algorithm can find significantly better solutions than pure local or global optimization methods and has fast convergence properties due to the possible parallel computation.

The chapter is organized as follows: The fundamental equation of the hard magnetic stray field calculation is given in Sec. 6.2 and the formulation of the optimization problem in Sec. 6.3. In Sec. 6.4, our proposed hybrid optimization algorithm is described and in Sec. 6.5 applied to the example of optimizing a magnetic sensor system. The main part of the chapter finishes with a conclusion and outlook on the topic in Sec. 6.6. Moreover, we give a derivation of the variational derivatives of the objective function in App. D, where we also discuss the existence of local optima. Appendix E presents a toy example with multiple local minima and App. F discusses the behavior of the used local optimizer. In App. G we discuss the influence of the mesh-fineness on the optimization and in App. H the symmetry properties of the solution.

## 6.2. Theoretical background

The basis of our magnetic optimization are the static and current-free Maxwell equations in vacuum [136]

$$\nabla \times \mathbf{H} = 0, \tag{6.1}$$

$$\nabla \cdot \mathbf{B} = 0, \tag{6.2}$$

with the magnetic field $\mathbf{H}$ and the magnetic flux density $\mathbf{B}$. Equation (6.1) allows introducing the scalar magnetic potential $u$ with

$$-\nabla u = \mathbf{H}. \tag{6.3}$$

Application of the divergence on both sides of the relation $\mathbf{B} = \mu_0(\mathbf{H} + \mathbf{M})$ with magnetization $\mathbf{M}$ and inserting Eq. (6.2) leads to the equation

$$\Delta u = \nabla \cdot \mathbf{M}. \tag{6.4}$$

This formula allows calculating the scalar magnetic potential $u$ for a given magnetization $\mathbf{M}$ (i.e. solution of the magnetic forward problem), which is the basis of the optimization algorithm, which is presented in the following section.

## 6.3. Optimization problem

The formulation of the optimization problem follows the already established approach of magnetic topology optimization [190–193, 212]. Therefore, we divide the whole space into two regions of interest, the magnetic region $\Omega_m$ and the target region $\Omega_t$. The scalar function $\rho : \Omega_m \longrightarrow [0,1]$ denotes the magnetic material density within the magnetic region, where $\rho(\mathbf{x}) = 0$ means no magnetic material and $\rho(\mathbf{x}) = 1$ means full magnetic material at position $\mathbf{x}$. Values in between are in principle allowed and scale the saturation magnetization $M_s$ in the form

$$M_s(\rho) = \rho M_{s0}, \tag{6.5}$$

where $M_{s0}$ denotes the highest possible saturation magnetization meaning full magnetic material and is assumed to be constant in $\Omega_m$. In the following, a perfectly hard magnetic material is assumed so that the normalized magnetization direction $\mathbf{m}$ is constant throughout the optimization process. This is only a

simplification in the simulation and the presented theory could be easily generalized to the soft magnetic case as described in Sec. 6.6. Thus, overall, we obtain the relation

$$\mathbf{M}(\rho) = M_s(\rho)\mathbf{m} = \rho M_{s0}\mathbf{m} = \rho \mathbf{M}_0. \tag{6.6}$$

The objective function $J$ to be minimized in general depends on the scalar magnetic potential $u$ and its derivatives (i.e. the magnetic field $\mathbf{H}$ and its derivatives) in the target region $\Omega_t$, which in turn depends on the magnetization $\mathbf{M}$ and thus on the magnetic material density $\rho$ in the form ($\mathscr{H}$ denoting the Hessian matrix)

$$J(\rho) = \int_{\Omega_t} \mathscr{F}\big(u(\rho), \nabla u(\rho), \mathscr{H}u(\rho)\big) \, \mathrm{d}\mathbf{x}. \tag{6.7}$$

The function $\mathscr{F}$ can in principle be any scalar-valued transformation. However, if the derivative $\mathrm{d}J/\mathrm{d}\rho$ is used and computed efficiently by the adjoint method (see [190–193, 195]), the partial derivatives of $\mathscr{F}$ according to its arguments must be computed analytically (see Eqs. (D.2) and (D.8)).

This chapter will now present an efficient optimization algorithm predestined for solving such problems, i.e., optimizing objective functions under the following conditions:

There are over countable degrees of freedom since arbitrary functions $\rho : \Omega_m \longrightarrow [0, 1]$ are possible as solutions and they modelize the geometric shape of magnets. Any function evaluation of $J$ is very effortful since it requires the numerical solution of Poisson's equation in Eq. (6.4), and the computation of the derivative $\mathrm{d}J/\mathrm{d}\rho$ by the adjoint method is approximately as effortful. Moreover, depending on the application, several local minima are possible.

## 6.4. Optimization algorithm

We propose an algorithm with the following properties that takes into account all the special characteristics of the topology optimization problem:

To numerically treat the framework of the previous section, it is useful to discretize the (bounded) regions of interest $\Omega_m$ and $\Omega_t$ to make the function spaces discrete. Since the purpose of magnetic topology optimization is to determine an unknown geometry without specific knowledge of its shape, we choose the simplest possible partitioning of the space into small cubic cells of identical dimension and assume that all functions are constant over the individual cells [190]. In particular, $\rho$ in each cell has a value $\rho_i \in [0, 1]$, which must be determined as part of the optimization process. Nevertheless, this procedure leads to a large (but finite) number of degrees of freedom to achieve a reasonable resolution of the resulting geometric shapes of the magnets. Based on this finite difference mesh scheme, fast algorithms for computing the stray magnetic field are available for the necessary solution of the Poisson equation [44, 116, 190] and GPU acceleration is used [115, 213]. In a fine discretization, the derivative $\mathrm{d}J/\mathrm{d}\rho_i$ still has many components. However, using the adjoint method (see [190–193, 195]), the components as a whole can be computed with about the same computational effort as the scalar function value of $J$. This is a very good reason for using the gradient within the optimization algorithm as in gradient descent [214], Newton-like methods [215, 216] or similar approaches [217]. In simple applications of topological optimization with convex objective functions, the objective function $J$ may have only a single local minimum to which a local optimization algorithm converges regardless of the starting point (see App. D.3). In the general case, however, it is completely unknown whether the function landscape has multiple local minima that are not global (see App. E). Therefore, it is useful to use ideas of global optimization algorithms to find the best solution without getting stuck in local minima.

In the following subsection, we describe the structure of a possible algorithm with the above properties.
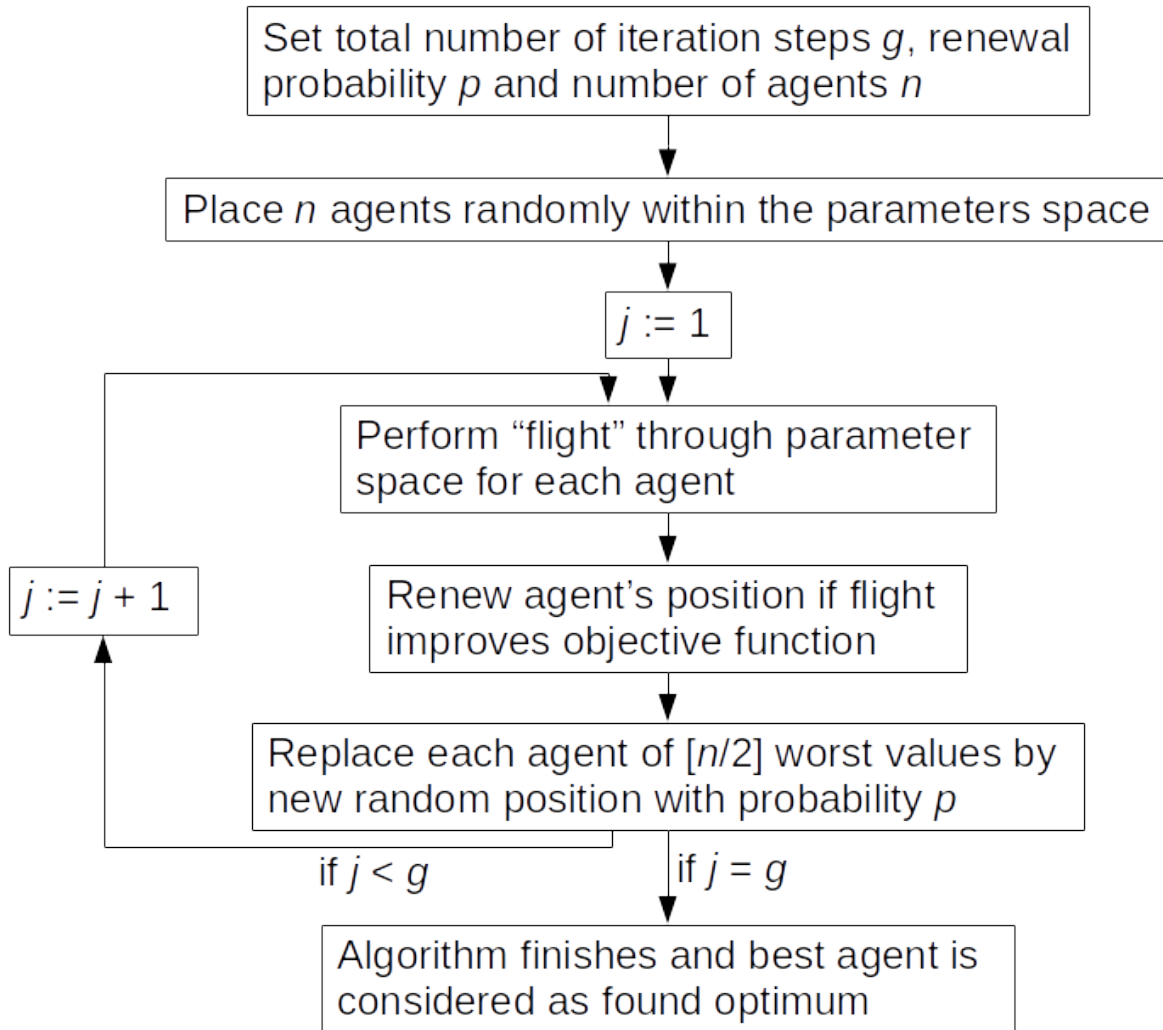
Figure 6.1.: Procedure of our simplified version of the CS algorithm.

### 6.4.1. Cuckoo search algorithm (CSA)

The CSA is a modern global optimization algorithm that mimics the brooding behavior of cuckoo birds [209]. Their property of laying their eggs in nests of foreign bird species is emulated in the form of a group of cuckoos flying around to find the best nest for their eggs to hatch. Once they find a good nest, there is a quality-dependent probability that the cuckoo egg will be recognized by the host bird and a new nest will be required. Cuckoos also fly around and compare the quality of surrounding nests to the best ones they have already found.

Our adapted version of the CSA goes through the steps shown in Fig. 6.1. The original global CSA [209] on its own behaves very badly for the application of topology optimization, since the parameter space is high dimensional and the algorithm lacks a fast and efficient way to seek through it. However, having access to gradient calculation, it is reasonable to use it to determine the flight direction in order to reduce the function value of the objective function more efficiently. This approach was performed and studied in [218].

To perform the "flight" in a reasonable way for the approach of magnetic topology optimization, a very fast convergent algorithm for local optimization is stated in the next section.

## 6.4.2. Binary search algorithm (BSA)

In [211], a binary on/off method for topology optimization is presented. It takes advantage of the fact that the magnetic density $\rho$ should only take the values 0 or 1 for ease of fabrication in the application since intermediate values $\rho \in (0,1)$ are very difficult to realize anyway. So we want to find the optimum within the finitely many possible states where $\rho_i \in \{0,1\}$ for all $i$. Since the total number of configurations increases exponentially with the number of cells, it is not possible to simply explore all possibilities and compare the corresponding values. Instead, one could use the algorithm in Fig. 6.2.

Note that because of the discrete binary states, one can no longer speak of a local minimum in the mathematical sense of a function on a continuous domain. It is clear that even if the gradient indicates a possible improvement in a cell, this does not mean that the binary change from 0 to 1 or vice versa will eventually improve the function value of the objective function. In App. F, we therefore analyze the behavior of the algorithm in more detail. However, to obtain the optimum on the discrete domain with certainty, we would need to check all states. This is not possible in practice due to the large number of different combinations, so the second-best requirement for the algorithm is to provide at least a procedure to obtain a result in a reasonable time frame. Note also that the final *local optimum* (the configuration in which the algorithm terminates) depends very much on the value chosen for the renewal probability $p$ and the "flight" method.

The quick switch between the states $\rho_i = 0$ and $\rho_i = 1$ makes this algorithm very useful for the purpose of magnetic topology optimization. However, on its own, it is still a local optimization algorithm and is therefore limited in seeking global optima.

## 6.4.3. Hybrid algorithm (HA)

We now combine the two previous algorithms into an HA that basically replaces the "flight" in the CSA of Subsec. 6.4.1 with a BSA of Subsec. 6.4.2. The detailed procedure is shown in Fig. 6.3.

There, updating $j \cdot \ell$ steps guarantees that the new agents also have the opportunity to take as many local iteration steps in total as the current best solution. However, it also has the effect that the number of iteration steps of the worst agent can reach $\sum_{j=1}^{g} j \cdot \ell = \ell \cdot g(g+1)/2$ and thus be quadratic in the number of global iteration steps $g$, even though the number of local iteration steps of the best solution is at most $\ell \cdot g$. This additional computational effort is invested in searching the entire parameter space and can contribute to a successful global minimization.

The formulation makes it clear that any other local optimizer besides the BSA could be used. Furthermore, it is also conceivable to "hybridize" other global optimization approaches [219, 220].

## 6.5. Applications

In the following, we present an application to demonstrate the utility of our presented method HA.

## 6.5.1. Optimization problem

We apply our algorithm to a model problem with objective function

$$J(\rho) = \int_{\Omega_t} \left| -\frac{\partial^2 u}{\partial z^2}(\rho) + \frac{\partial H_{\text{ext},z}}{\partial z} \right|^2 \, d\mathbf{x} \stackrel{\text{Eq.(6.3)}}{=} \int_{\Omega_t} \left| \frac{\partial (H_z(\rho) + H_{\text{ext},z})}{\partial z} \right|^2 \, d\mathbf{x} \longrightarrow \min \qquad (6.8)$$

with optimization and target area shown in Fig. 6.4. The additional magnet in the region of $\Omega_{\text{ext}}$ is included in the optimization process only as a constant magnetic field source renerating $\mathbf{H}_{\text{ext}}$. We choose magnetization $\mathbf{m} = (1,0,0)$ and $\mu_0 M_{s0} = 1\,\text{T}$ in $\Omega_{\text{ext}}$ and $\mathbf{m} = (-1,0,0)$ and $\mu_0 M_{s0} = 1\,\text{T}$ in $\Omega_m$. Thus,
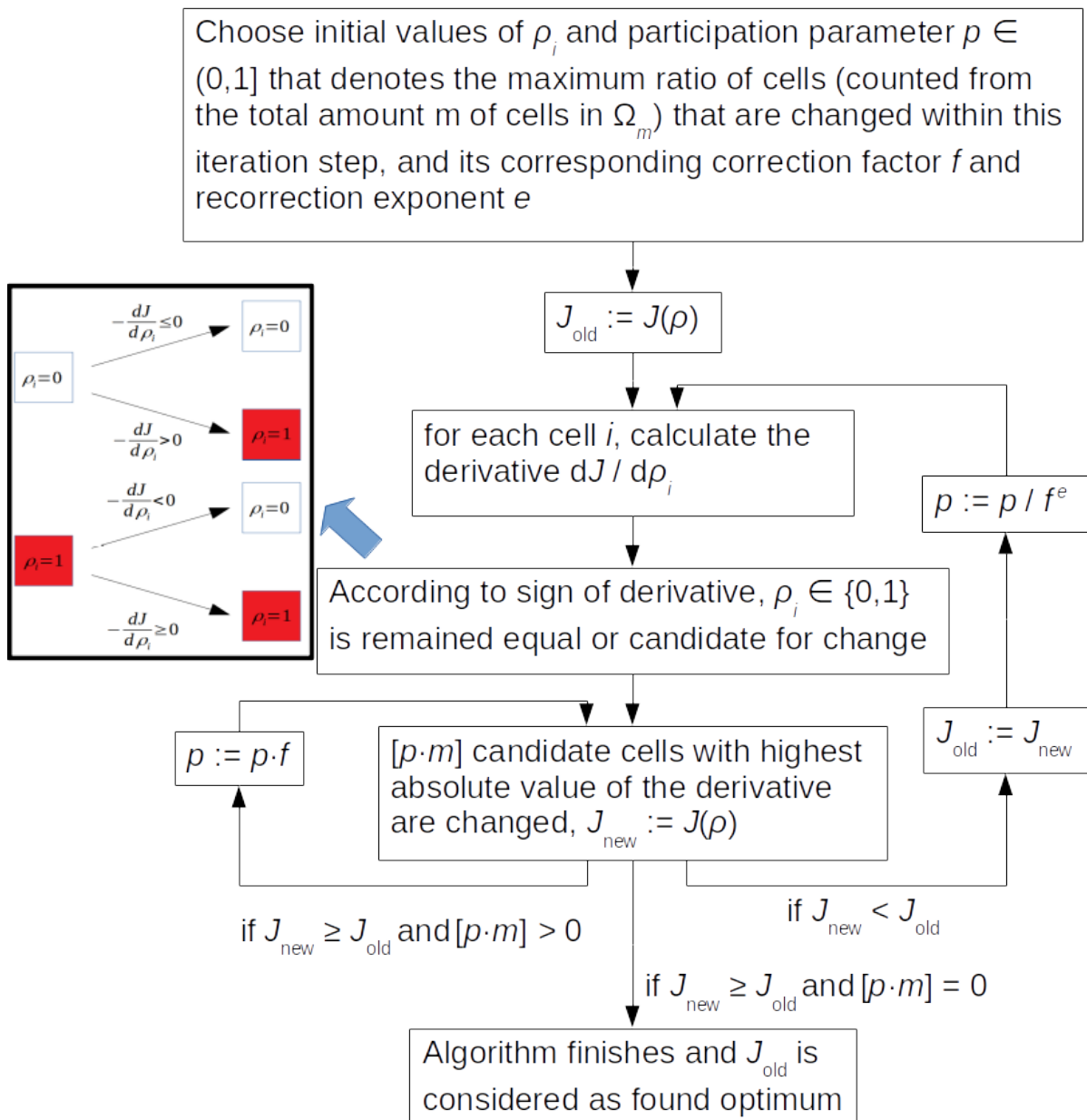
Figure 6.2.: Sequence of BSA. It starts with an arbitrary initial binary state ($\rho_i \in \{0, 1\}$) for all $i$ and ends in finitely many steps. How the sign of the derivative determines the candidates for modified cells is visualized in the sub-image. Depending on the present value of $\rho_i$ and the sign of the derivative $\mathrm{d}J/\mathrm{d}\rho_i$, the cell is either a candidate for a change or not.

Set total number of iteration steps $g$, renewal probability $p$, number of agents $n$ and number of local iteration steps $\ell$

Place $n$ agents randomly within the parameters space

$j := 1$

Perform $\ell$ iteration steps with local optimizer for each agent

Renew agent's position if flight improves objective function

$j := j + 1$

Replace each of $[n/2]$ worst agents by new random position with probability $p$

Perform $j \cdot \ell$ iteration steps with local optimizer for each new agent

if $j < g$      if $j = g$

Algorithm finishes and best agent is considered as found optimum

Figure 6.3.: Procedure of the HA.

| parameter | value |
|:---:|:---:|
| $p$ | 1 |
| $f$ | 0.9 |
| $e$ | 10 |
| $\rho_i$ | 1    $\forall i$ |
| $g$ | — |
| $p$ | 0.25 |
| $n$ | 8 |
| $\ell$ | 1 |

Table 6.1.: Parameter used for the BSA (upper part) and additional parameters for the HA (lower part). The value of $g$ is taken as the number of iteration steps the BSA needs to converge.

the total magnetic field consists of two parts: This constant field generated in $\Omega_{\text{ext}}$ and an overlapping opposing fields depending on the magnetic material density in $\Omega_m$. The idea of this alignment and optimization is to obtain a minimal $z$ derivative in the total magnetic field to make the system robust to misalignment in the $z$ direction, which could be interesting in certain sensing applications, as described in [151].

### 6.5.2. Symmetry

This optimization problem is symmetric in $x$ and $y$ directions according to the discussion in App. H. Although it is shown there, that the optimal solution does not necessarily have the same symmetry, we still allow only symmetric solutions in the optimization by updating just a quarter of the region and copy it to the remaining parts, because this reduces the degrees of freedom by a factor of four. This allows for faster optimization and also a solution with high symmetry might have benefits in production processes. Thus, it is worth mentioning that in the function space of all (even asymmetric) configurations of $\rho$, the minimum could in principle also be lower than our result.

### 6.5.3. Results

The optimization result of the BSA from Subsec. 6.4.2 is compared to the HA in Subsec. 6.4.3 for different mesh sizes. We use the parameters from the upper part of Tab. 6.1 for the BSA. Under these circumstances, the local optimization in terms of the algorithm in Fig. 6.2 converges after a certain number of iterations. This number can vary for different mesh sizes and is used for the maximum iteration steps of the HA together with the parameters of the full Tab. 6.1 (except for $\rho_i$ initialization, which is random for each agent). The number of iterations, the results of each optimum and the numerical effort measured as the number of required evaluations of $J$ and $\mathrm{d}J/\mathrm{d}\rho$ (due to the adjoint method, both evaluations have approximately the same effort) is given in Tab. 6.2 and visualized in Fig. 6.5.

For the mesh size of $1/10\,\text{mm}$, we additionally calculate the results of the BSA for different random start configurations in Tab. 6.3 and visualize the results in Fig. 6.6. It can be observed that although there are different local solutions, they have certain similarities in certain parts of the magnetic region.

### 6.5.4. Discussion

Looking at the results in Tab. 6.2, it can be observed that for the model problem, the BSA with initial value $\rho_i = 1$ for all $i$ converges to a solution already in 19–37 iteration steps. When comparing the values for different mesh resolutions, we have to take into account that for simplicity and to make the stray field
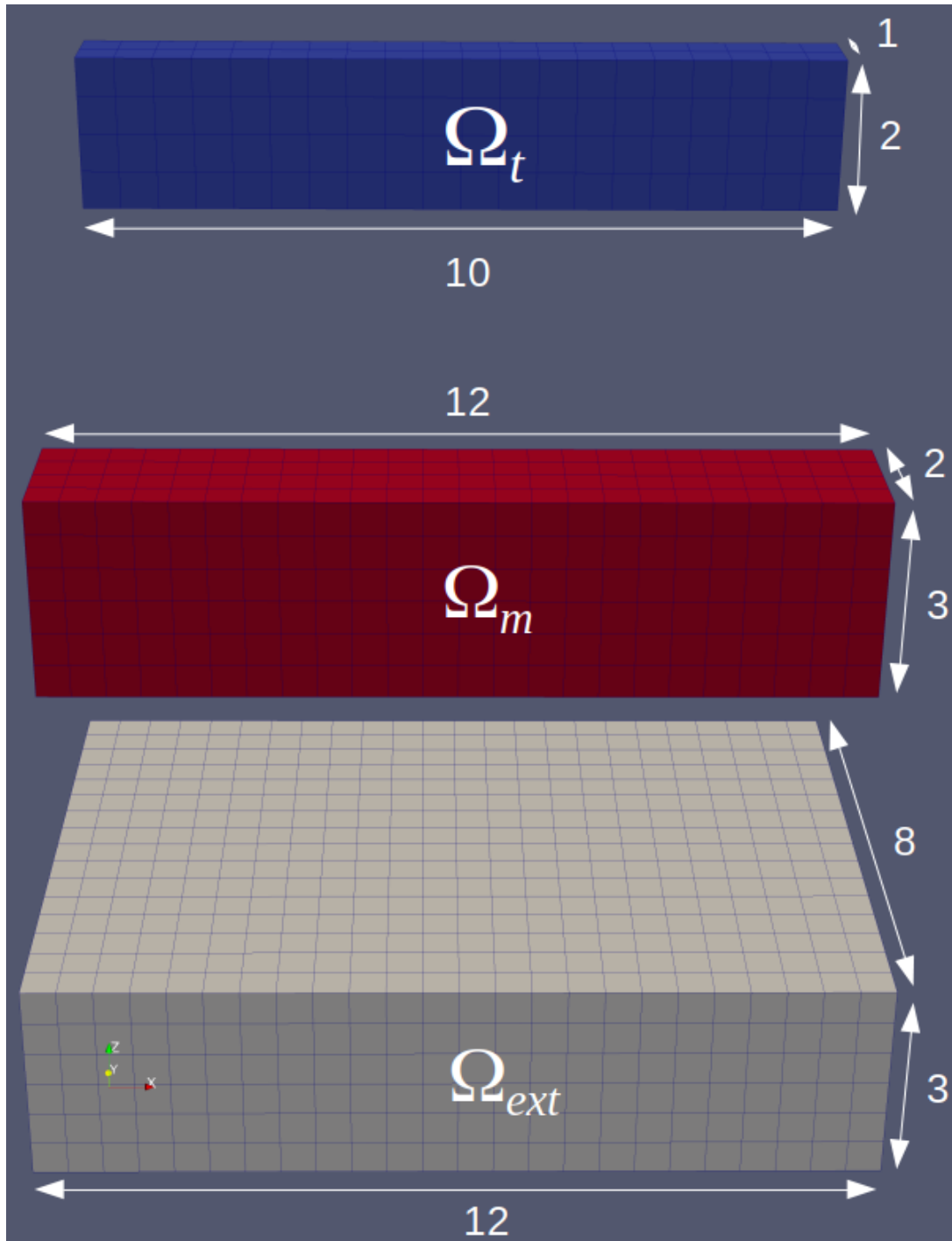
Figure 6.4.: Alignment and dimensions of the optimization regions. $\Omega_t$ denotes the blue target region, $\Omega_m$ the red magnetic region and $\Omega_{\text{ext}}$ the gray region representing the additional magnet whose geometry is left constant and which is not changed during the optimization process. The numerical values are given in mm. The mesh illustrates a possible subdivision into cubic cells with a edge length of $0.5\,\text{mm}$.

| cell edge length [mm] | iteration steps | $J_{min}$ BSA [A$^2$/m] | $J_{min}$ HA [A$^2$/m] | gain [%] | $J$ and d$J$/d$\rho$ evaluations BSA | $J$ and d$J$/d$\rho$ evaluations HA |
|---|---|---|---|---|---|---|
| 1/2 | 20 | 62.569 | 31.144 | 50.2 | 544 | 13424 |
| 1/4 | 25 | 36.852 | 35.580 | 3.5 | 694 | 20593 |
| 1/6 | 20 | 55.986 | 27.958 | 50.1 | 606 | 9470 |
| 1/8 | 24 | 61.394 | 32.464 | 47.1 | 690 | 10529 |
| 1/10 | 28 | 40.206 | 28.229 | 29.8 | 812 | 28256 |
| 1/12 | 32 | 42.429 | 29.918 | 29.5 | 890 | 29932 |
| 1/14 | 31 | 46.685 | 34.240 | 26.7 | 896 | 17166 |
| 1/16 | 31 | 31.487 | 36.844 | $-17.0$ | 904 | 19812 |
| 1/18 | 25 | 37.878 | 32.476 | 14.3 | 778 | 21624 |
| 1/20 | 37 | 53.844 | 29.178 | 45.8 | 1008 | 63306 |
| 1/22 | 22 | 41.404 | 48.550 | $-17.3$ | 724 | 16152 |
| 1/24 | 26 | 44.555 | 29.099 | 34.7 | 798 | 21685 |
| 1/26 | 19 | 131.202 | 30.838 | 76.5 | 668 | 11585 |

Table 6.2.: Number of iteration steps, found optimum values and numerical effort for the BSA (see Subsec. 6.4.2) and HA (see Subsec. 6.4.3).

| seed | $J_{min}$ BSA [A$^2$/m] |
|---|---|
| 0 | 52.725 |
| 1 | 46.164 |
| 2 | 63.728 |
| 3 | 64.291 |
| 4 | 57.503 |

Table 6.3.: Optimum values of the objective function $J$ according to the BSA for different random initial configurations with given seed and cell size $1/10$ mm.

(a)

(b)

(c)

(d)

(e)

(f)

(g)

(h)

(i)

(j)

(k)

(l)

(m)

(n)
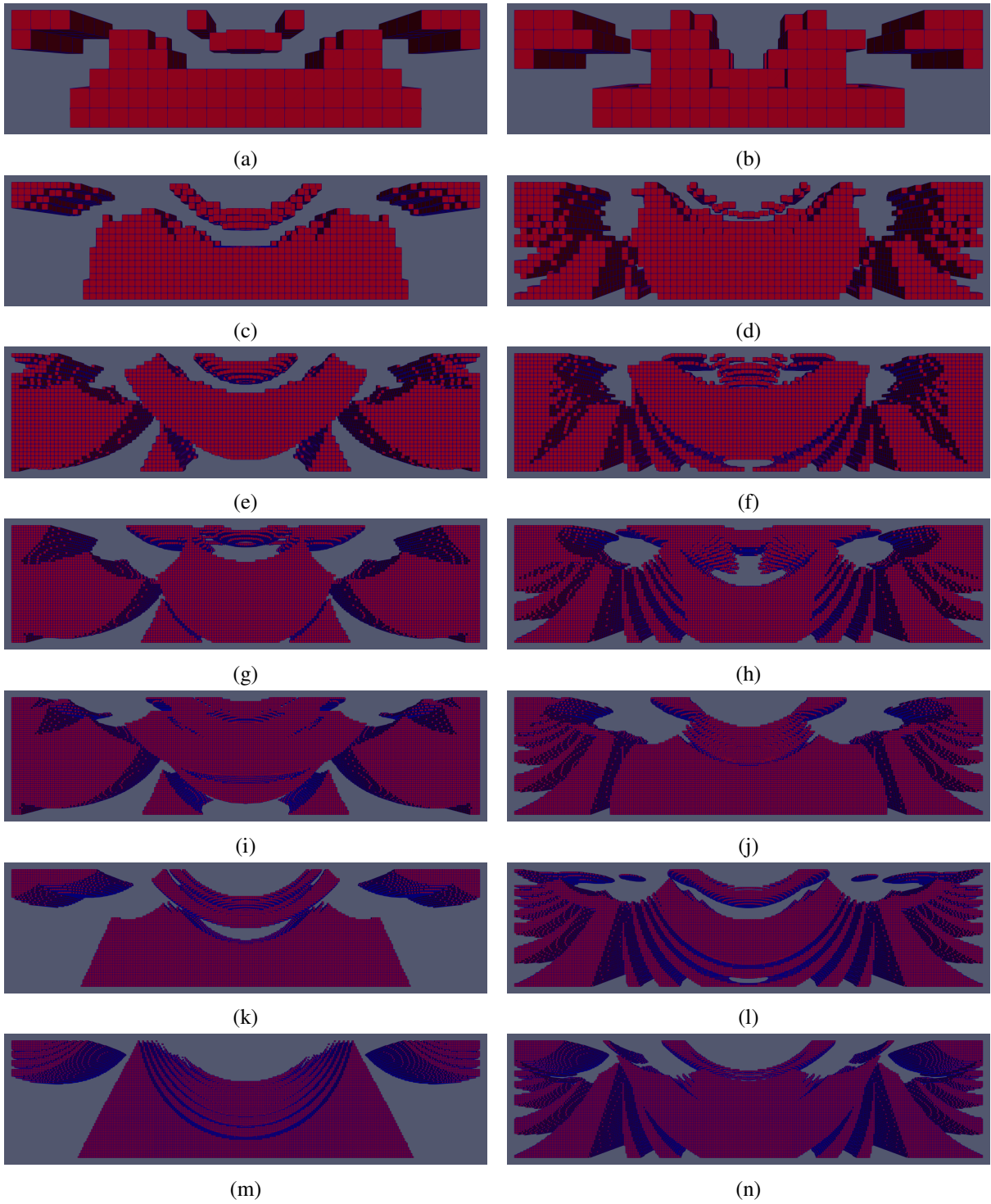
Figure 6.5.: Optimum configuration of $\Omega_m$ in Fig. 6.4 according to the algorithms for the different cubic cell sizes: (a), (b) for $1/2$ mm, (c), (d) for $1/6$ mm, (e), (f) for $1/10$ mm, (g), (h) for $1/16$ mm, (i), (j) for $1/20$ mm, (k), (l) for $1/22$ mm, (m), (n) for $1/26$ mm. The left pictures depicts the result of the local BSA, the right pictures of the HA.
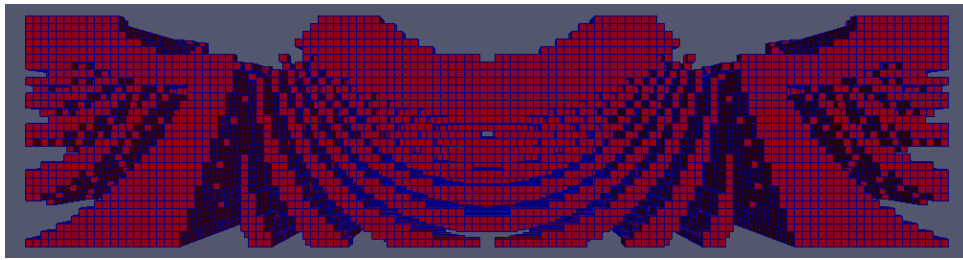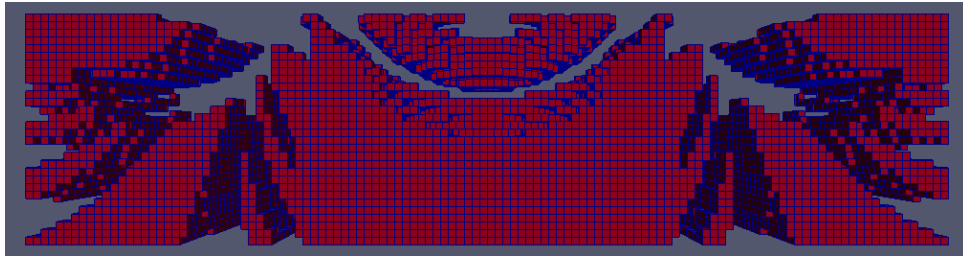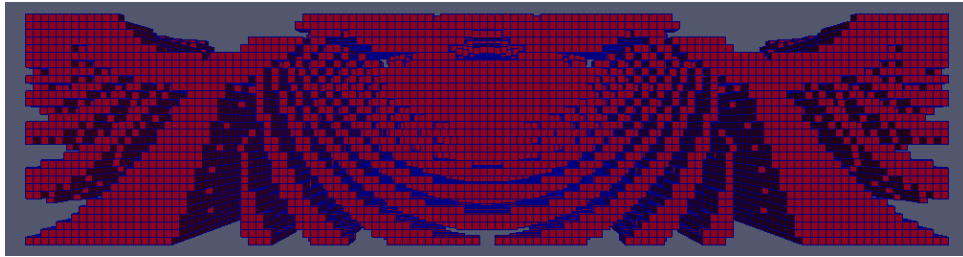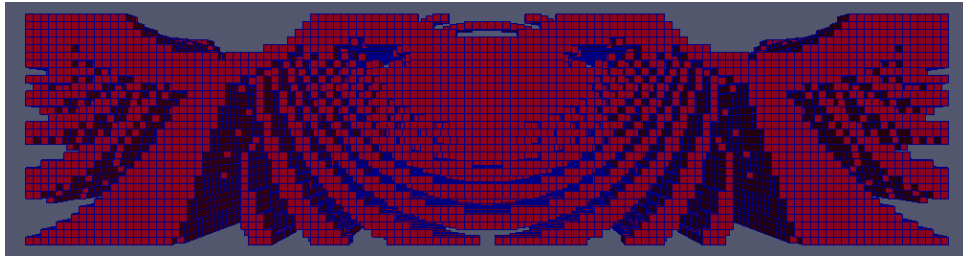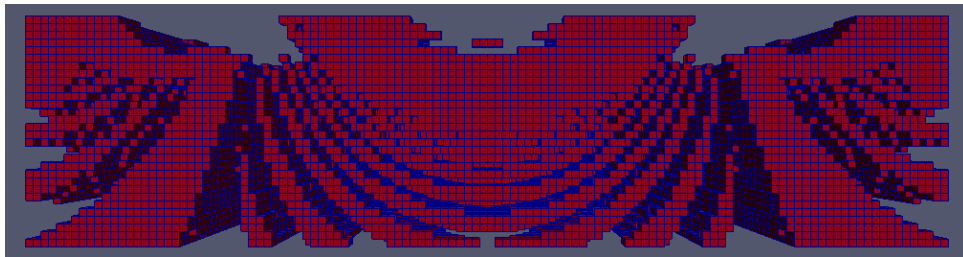
Figure 6.6.: Optimum configuration of $\Omega_m$ in Fig. 6.4 according to the BSA for different random initial configurations and cell size $1/10$ mm. The corresponding optimum values are given in Tab. 6.3.

calculation with the Fourier transform [221, 222] easily accessible, we always use the same mesh fineness for $\Omega_t$ and $\Omega_m$. This leads to a finer resolution of the geometry and the integral in the objective function Eq. (6.7) sequentially. In particular, fluctuations of the field on a short length scale can then provide an additional contribution to the integral that can only be detected at a sufficiently fine resolution. This explains that the found minima vary for different resolutions and do not exhibit monotonic decreasing behavior for finer resolutions and is explored in detail in App. G.

We can observe that in most cases the HA leads to a much better result with improvements up to 76.5%, even if the computational effort increases by at least a factor of 15. However, there are also two cases where the BSA already converges to a very good local minimum that cannot be outperformed by the HA. The comparison of the geometries can be seen in Fig. 6.5g,h,k,l, where the "simple" shapes in Fig. 6.5g,k surprisingly lead to lower minima than the challenging shapes in Fig. 6.5h,l. In these cases, the parameters of the HA from Tab. 6.1 can be adjusted to find an even better optimum with more computational effort.

For different cell sizes Fig. 6.5 illustrated that the HA optimization results tend to converge to a certain stripe geometry, whereas the BSA with initialization $\rho_i = 1$ for all $i$ gets stuck in local optima with a different shape.

The listed optima of Tab. 6.3 further show that running the BSA with various random initial configurations is not as effective as the HA, since the found minima are larger. This confirms the existence of several local minima and the importance of global optimization techniques in the search for minima.

## 6.6. Conclusion and outlook

In this work, we presented a hybrid algorithm for the purpose of magnetic topology optimization. The combination of two optimization algorithms (cuckoo search algorithm and binary search algorithm) allowed us to develop a method that is specifically adapted to the requirements and circumstances in the context of magnetic topology optimization but can also be used for any other application. In doing so, we addressed various discussion points such as objective function evaluation, gradient-based optimization, discretization, local minima, accuracy, etc., and demonstrated the behavior of our algorithm. Using an example, we were able to show that hybrid optimization leads to significantly lower minima compared to pure local optimization and that the objective function could be lowered by up to an additional 76.5%. The existence of grids with better performance of the local optimizer only further emphasizes the relevance of many local minima in the optimization process. Further it indicates that the completely random choice of the starting values $\rho_i$ for each agent in the cuckoo search algorithm is not very beneficial. It will be advantageous to use global optimization algorithms that choose new starting points in a clever way using the information of the success of already chosen starting values in the past. This also underlines the necessity of good global optimization approaches with suitably chosen parameters to find the best possible magnet geometries. The advantage of hybrid optimization lies in the possible parallel computation of multiple optimization paths ("agents") that can be immediately compared. Even though the overall numerical effort of hybrid optimization is higher by a factor between 15 and 63 and also quadratic in the number of total iteration steps, the additional effort is favorably invested when optimizing along multiple paths on different positions of the parameter space. Parallel calculations, can, however, reduce the effective calculation time.

The description of our method was deliberately done using a building block approach – the hybrid idea could also work with other local and global optimization approaches. Further investigation is possible and desirable.

Even though our simulations were limited to the pure hard magnetic case, exactly the same approach can be applied to any soft magnetic case. The only difference in the calculation is a more complex

calculation of the stray field due to demagnetization effects. The iteration procedure is then exactly the same, only the individual steps are numerically more complex (see e.g. [193]).

Even though magnetic shapes as in Fig. 6.5 might be difficult to produce with standard magnetic fabrication methods, recent 3D printing approaches [117, 192, 223–231] combining magnetic and non-magnetic filament to successfully realize such geometries.

We hope that our work will provide an impulse for work on global and hybrid magnetic topology optimization in general since many engineering applications are affected by the need to find good magnetic geometries where global minimization of the cost function is desirable.

# 7. Conclusion

Although there is no general recipe for how to optimize and improve models for computational simulation, we have shown in the examples of magnetic recording, analytical field calculation, and magnetic shape optimization that there are several anchor points for improvement. They are not obvious to find and also the mathematical implementation can be challenging, but in many applications the effort can be worthwhile because the results allow faster and more accurate numerical simulation. This is a particularly relevant issue in magnet simulation due to the wide application of magnets and magnetic devices in industry.

We were able to show that a simple simulation of a magnetic writing process is very time consuming, especially because it has to be repeated many times to obtain meaningful information about the noise of the signal. Instead, we proposed a systematic simulation technique based on the switching behavior of a single grain. In contrast to setting the magnetization to one of the two binary states along their uniaxial anisotropy directions, it was set to its probability value. This switching probability can be used to calculate the signal-to-noise ratio very quickly and very accurately by using the given data in a sophisticated way.

Even though magnetic fields of arbitrary geometries can nowadays be calculated very efficiently by numerical methods, analytical solutions are still of interest since they allow a fast and accurate point-by-point evaluation of the field, which has already been analyzed for different geometries in previous works. In particular, since cylindrical tile geometry is found in important sensor applications, we have derived the formulas and made them available in an open-source Python package for easy and fast use. We have also discussed the challenges in such analytical approaches and hope to inspire the analytical solution of other geometries as well.

In the final chapters, we discussed the common approach to the optimization of magnetic geometries. We were first able to show how an additional magnet can increase the properties of a sensor system. However, it must have the correct dimensions and position, which we found out by solving a suitable explained optimization problem. Furthermore, we proposed a hybrid solution algorithm for global topology optimization that overcomes the problem of multiple local minima in the parameter space. Using the example, we have shown that global optimization is necessary and can significantly improve the properties compared to local optimization, because with the wrong optimization algorithm there is a risk of getting stuck in a local minima, which is not the very best solution.

Although the search for the "optimal" solution is always a matter of perspective, we have shown in this work that significant improvements are possible in many areas of magnetic simulation with the right mathematical treatment. Every case is different and we could only present a limited selection, but the scope of the work hopefully stimulates further development of mathematical methods for magnetic and physical applications in general.

# A. How to avoid integration singularities

Parts of this chapter have been previously published in [84] and have been reproduced with permission of the coauthors and in accordance with the publisher's policy. Content that was not generated by the author of this thesis is explicitly denoted, copyright is held by Elsevier.

## A.1. Motivation

It is not surprising if singularities appear in the magnetic field $\mathbf{H}$ when crossing magnetically charged surfaces. However, it is also possible that single anti-derivatives contributing to the total field Eq. (4.20) have singularities off-surface. As the field itself must be continuous, these singularities cancel by summation with the singularities of other anti-derivatives.

For example, if we consider Eq. (4.32) for the special case $z = z_k, r > 0$, the term has a logarithmic singularity at $\varphi = \varphi'$ if $r > r_i$, which disappears after the following integration step. In contrast, for the case $r = r_i$ in Eq. (4.33), the denominator vanishes for $\overline{\varphi}' \in 2\pi\mathbb{Z}$ and reveals a significant singularity that persists even after integration in the case $\overline{\varphi}_j \in 2\pi\mathbb{Z}$, making straight-forward evaluation of this term impossible.

It is crucial to understand how to eliminate the occurrence of these singularities, especially in the second integration step. Our study reveals that they are the result of poorly chosen integration constants by the computer algebra systems. How this happens and how to avoid it will be shown in the following sections.

## A.2. Notation

Let $A \subseteq \mathbb{R}^{n+2}$ be a domain for the function

$$
\begin{aligned}
f : A &\longrightarrow \mathbb{R} \\
(x, y, p_1, \ldots, p_n) &\longmapsto f(x, y, p_1, \ldots, p_n)
\end{aligned}
$$

in two variables $x, y$ and $n$ additional parameters $p_1, \ldots, p_n$. We are looking for an anti-derivative $F : A \longrightarrow \mathbb{R}$ satisfying $\partial_x \partial_y F = f = \partial_y \partial_x F$. It exists if $f$ is continuous and bounded, then $F$ does exist in the whole domain $A$ but is not unique. Suppose we compute $F$ in two steps (e.g. using a computer algebra system):

- calculating an $x$-anti-derivative $F_x$ of $f$

- calculating an $y$-anti-derivative $F_{x,y}$ of $F_x$

The order of integration is mathematically irrelevant, but it should be noted that it can lead to different expressions when using computer algebra systems. This is demonstrated and explained in the following sections.

## A.3. Singularities in the integration constants

Since in the calculation of $F_x = \int f \, \mathrm{d}x$ all variables except $x$ are fixed, the integration constant can be an arbitrary function of $(y, p_1, \ldots, p_n)$. This constant may have any number of singularities in $A$, so $F_x$ with integration constant may have a restricted domain $A' \subset A$. The same problem may arise in the second integration step, the integration of $F_x$ with integration constant by $y$. Again, another integration constant may occur depending on $(x, p_1, \ldots, p_n)$ with possible singularities in the result.

When integrating, computer algebra systems attempt to choose good integration constants. This possibility, together with the ambition to write results in "simple" and "closed" form, can result in adding singular integration constants. These unwanted singularities are hidden in the resulting deceptively simple looking expressions. We illustrate this with examples in the following subsections.

## A.4. Example 1

The function

$$f(x, p) := \frac{1}{\sqrt{x^2 + p}}$$

on the domain $\{(x, p) \in \mathbb{R}^2 \,|\, p \geq 0, (x, p) \neq (0, 0)\}$ is continuous and bounded if one removes a small region around $(0, 0)$, so the anti-derivative $F$ must exist for all $p$ in the domain. The integration of $f$ by $x$ can lead to one of the following three anti-derivatives in computer algebra systems:

$$F_{x,1}(x, p) = \log\left(\sqrt{x^2 + p} + x\right)$$

$$F_{x,2}(x, p) = -\log\left(\sqrt{x^2 + p} - x\right)$$

$$F_{x,3}(x, p) = \operatorname{artanh}\left(\frac{x}{\sqrt{x^2 + p}}\right)$$

Mathematica version 10.1 [232] for instance produces $F_{x,1}$ with its standard integrator. The additionally loaded Rubi integrator [233] results in $F_{x,3}$.

It is easy to see that all three functions are well-defined in the case $p > 0$ for all $x$. However, for $p = 0$ we see that $F_{x,1}$ is defined only for $x > 0$, $F_{x,2}$ is defined only for $x < 0$ and $F_{x,3}$ is not defined for any $x \in \mathbb{R}$ since the domain of artanh is $(-1, 1)$. Further computations show that the three possible outputs of a computer algebra system, although looking different at first glance, differ only by a $p$-dependent integration constant, which has a singularity at $p = 0$, i.e. $F_{x,1}(x, p) - F_{x,2}(x, p) = \log(p)$ and $F_{x,3}(x, p) - F_{x,2}(x, p) = \log(p)/2$. As described above, we observe an implicit integration constant that reduces the domain for which our anti-derivative can be used. The automatic simplification of the term to known mathematical function as $\log$, artanh covers this problem.

## A.5. Example 2

We now study an example function similar to $H_{\varphi, r_i}$ in Eq. (4.17) and its anti-derivative in Eq. (4.33):

$$f(\varphi, z) := \frac{\sin\varphi}{\sqrt{1 - \cos\varphi + z^2}^3}$$

on the domain

$$\{(\varphi, z) \in [0, 2\pi) \times \mathbb{R} \,|\, (\varphi, z) \neq (0, 0)\}. \tag{A.1}$$

For $z \neq 0$, the function term is obviously well-defined for all $\varphi$, since $(1 - \cos\varphi) \geq 0$. For $z = 0$, however, L'Hospital's rule reveals significant singularities,

$$\lim_{\varphi \to 0} \frac{\sin\varphi}{\sqrt{1 - \cos\varphi}^3} = \lim_{\varphi \to 0} \frac{\cos\varphi}{3/2\sqrt{1 - \cos\varphi}\sin\varphi} = \frac{1}{0}.$$

An anti-derivative of $f$ by $z$ is given by

$$F_{z,1}(\varphi, z) = \frac{z\sin\varphi}{(1 - \cos\varphi)\sqrt{1 - \cos\varphi + z^2}},$$

however, the additional factor $(1 - \cos\varphi)$ in the denominator also generates a pole for $z \neq 0$ at $\varphi = 0$, which again can be seen with L'Hospital's rule,

$$\lim_{\varphi \to 0} \frac{\sin\varphi}{1 - \cos\varphi} = \lim_{\varphi \to 0} \frac{\cos\varphi}{\sin\varphi} = \frac{1}{0}.$$

Thus $F_{z,1}$ can be used only for the case $\varphi \neq 0$. The same applies to the following anti-derivation by $\varphi$

$$F_{z,\varphi,1}(\varphi, z) = -2\operatorname{artanh}\left(\frac{z}{\sqrt{1 - \cos\varphi + z^2}}\right),$$

which is again undefined in the case $\varphi = 0$ for all $z \in \mathbb{R}$. In order to obtain a proper anti-derivative also for the case $\varphi = 0$, we first note that our goal is to calculate definite integrals of the form

$$\int_{\varphi_1}^{\varphi_2} \int_{z_1}^{z_2} f(\varphi, z) \, \mathrm{d}z \, \mathrm{d}\varphi.$$

It is justified to restrict our domain of interest to a rectangular subset of Eq. (A.1). That is, if $\varphi = 0$ lies in the interval $[\varphi_1, \varphi_2]$, then we can assume that $z = 0$ is not in $[z_1, z_2]$ since $(0, 0)$ is excluded from the domain, and moreover that $z_1, z_2$ are either both positive or both negative, see Fig. A.1.

This argument allows us to add to $F_{z,1}$ a sign-dependent integration constant that also depends on $\varphi$ and compensates the pole for $\varphi = 0$. We define

$$F_{z,2}(\varphi, z) := \frac{\sin\varphi}{1 - \cos\varphi}\left(\frac{z}{\sqrt{1 - \cos\varphi + z^2}} - \operatorname{sign} z\right),$$

where the term in parentheses vanishes for $\varphi = 0$ and thus compensates the pole of the prefactor. Integration of this function by $\varphi$ gives

$$F_{z,\varphi,2}(\varphi, z) = -2\operatorname{sign} z \log\left(\sqrt{1 - \cos\varphi + z^2} + |z|\right).$$

which has no singularity in the case $\varphi = 0, z \neq 0$ any more, and can be used to compute the definite integral when $\varphi_1 = 0$ or $\varphi_2 = 0$.
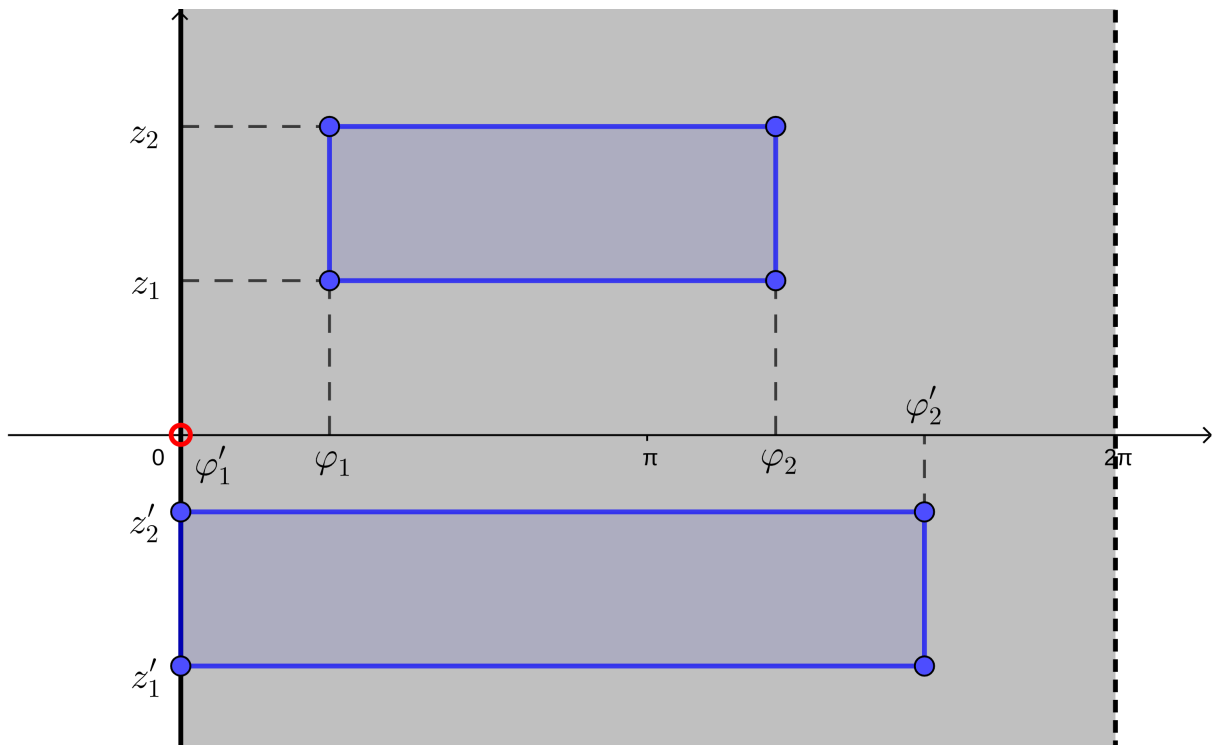
Figure A.1.: The upper rectangle represents the integration area $[\varphi_1, \varphi_2] \times [z_1, z_2]$. In this case, $z_1$ could be moved below the horizontal axis without leaving the grayed region, i.e. the sign of $z_1$ could also be changed. However, the lower rectangle would intersect the point $(0,0)$ if the upper boundary $z_2$ is moved to the positive part of the vertical axis, since $\varphi'_1 = 0$.

# B. Special functions

Parts of this chapter have been previously published in [84] and have been reproduced with permission of the coauthors and in accordance with the publisher's policy. Content that was not generated by the author of this thesis is explicitly denoted, copyright is held by Elsevier.

## B.1. Elliptic integrals

In accordance with [234, Chap. 8] we define the elliptic integrals in the angular form:

- First kind:

$$F(\varphi, m) = \int_0^\varphi \frac{\mathrm{d}\varphi'}{\sqrt{1 - m\sin^2\varphi'}} \tag{B.1}$$

- Second kind:

$$E(\varphi, m) = \int_0^\varphi \sqrt{1 - m\sin^2\varphi'}\,\mathrm{d}\varphi' \tag{B.2}$$

- Third kind:

$$\Pi(\varphi, n, m) = \int_0^\varphi \frac{\mathrm{d}\varphi'}{\left(1 - n\sin^2\varphi'\right)\sqrt{1 - m\sin^2\varphi'}} \tag{B.3}$$

These integrals exist and yield real numbers for $\varphi \in \mathbb{R}$ and $m, n \in (-\infty, 1)$. For $\varphi = \pi/2$ they are called *complete*, otherwise *incomplete* elliptic integrals. There are several very efficient numerical algorithms to compute these integrals with effective computation times between 10 ns and 1 $\mu$s for single-core evaluation on state-of-the-art i5 or i7 mobile CPUs [100, 127, 130, 235, 236].

## B.2. Angle scaling function

For some results in App. C, we make use of the following angle scaling function

$$\mathrm{Sc}(\varphi, k) := \pi n + \arctan\left(k\tan\left(\varphi/2 - \pi n\right)\right),$$

where $n := [\varphi/2\pi]$, i.e. the integer value closest to $\varphi/2\pi$, which is a periodic continuation of the anti-derivative $\arctan(k\tan(\varphi/2))$ with $k > 0$ (see Fig. B.1).
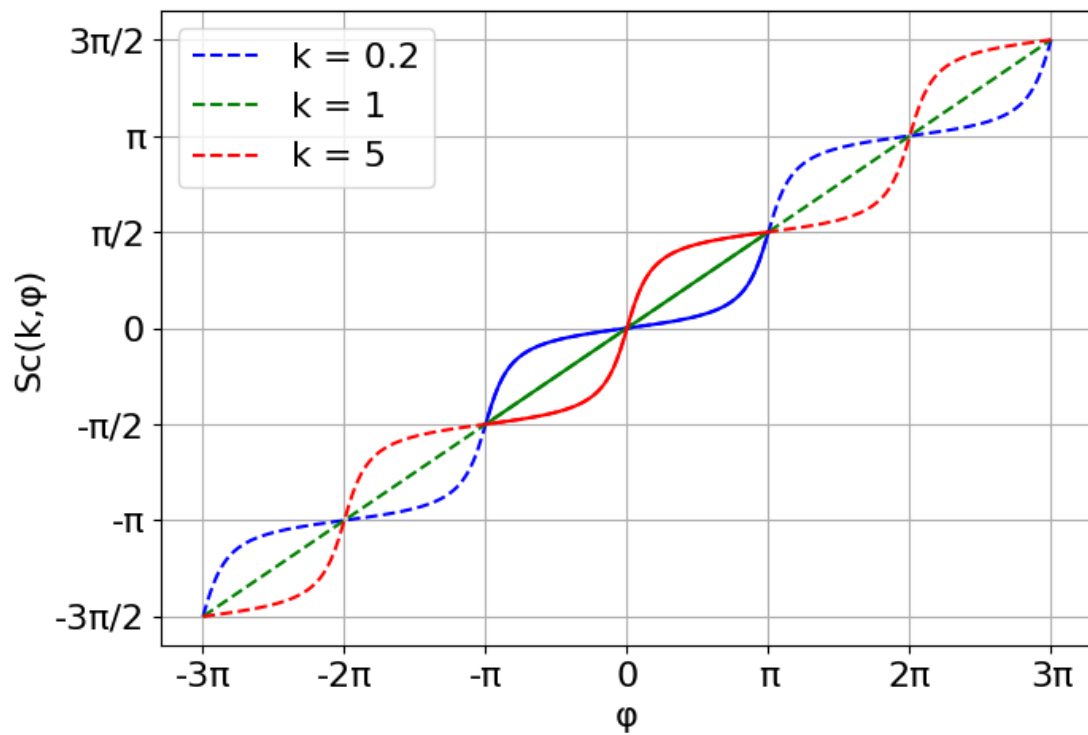
Figure B.1.: Graph of the angle scaling function Sc as the periodic continuous continuation of the antiderivative from $(-\pi, \pi)$ to $\mathbb{R}$ for three different values of $k$.

# C. Tables

Parts of this chapter have been previously published in [84] and have been reproduced with permission of the coauthors and in accordance with the publisher's policy. Content that was not generated by the author of this thesis is explicitly denoted, copyright is held by Elsevier.

In Tabs. C.1-C.26 all necessary functions with corresponding coefficients to perform the field calculation according to Sec. 4.4 are given. How the tables are to be read is shown in Tab. 4.2. All terms with $\pm$-sign must be considered twice, with plus and minus.

| | $1$ | $\log r_i$ |
|---|---|---|
| $H^{\varphi_j,r_i}_{\varphi,z_k}$ | $0$ | $\cos\theta_M$ |
| $H^{z_k,\varphi_j}_{z,r_i}$ | $-\sin\theta_M\sin\overline{\varphi}_M$ | $0$ |
| $H^{z_k,r_i}_{z,\varphi_j}$ | $0$ | $\sin\theta_M\sin\overline{\varphi}_M$ |

Table C.1.: Required functions and corresponding coefficients for $\mathscr{I}=112$.

| | $\log r$ |
|---|---|
| $H^{\varphi_j,r_i}_{\varphi,z_k}$ | $-\cos\theta_M$ |
| $H^{z_k,r_i}_{z,\varphi_j}$ | $-\sin\theta_M\sin\overline{\varphi}_M$ |

Table C.2.: Required functions and corresponding coefficients for $\mathscr{I}=113$.

| | $1$ | $\operatorname{sign}\overline{r}_i\log|\overline{r}_i|$ | $E\left(\frac{\overline{\varphi}_j}{2},-\frac{4rr_i}{\overline{r}_i^2}\right)$ | $F\left(\frac{\overline{\varphi}_j}{2},-\frac{4rr_i}{\overline{r}_i^2}\right)$ |
|---|---|---|---|---|
| $H^{r_i,\varphi_j}_{r,z_k}$ | $0$ | $0$ | $\dfrac{\cos\theta_M|\overline{r}_i|}{r}$ | $-\dfrac{\cos\theta_M\left(r^2+r_i^2\right)}{r|\overline{r}_i|}$ |
| $H^{\varphi_j,r_i}_{\varphi,z_k}$ | $-\dfrac{\cos\theta_M\operatorname{sign}\overline{r}_i r_i}{r}$ | $-\cos\theta_M$ | $0$ | $0$ |
| $H^{z_k,\varphi_j}_{z,r_i}$ | $\dfrac{\sin\theta_M\sin\overline{\varphi}_M|\overline{r}_i|}{r}$ | $0$ | $\dfrac{\sin\theta_M\cos\overline{\varphi}_M|\overline{r}_i|}{r}$ | $-\dfrac{\sin\theta_M\cos\overline{\varphi}_M\left(r^2+r_i^2\right)}{r|\overline{r}_i|}$ |
| $H^{z_k,r_i}_{z,\varphi_j}$ | $0$ | $-\sin\theta_M\sin\overline{\varphi}_M$ | $0$ | $0$ |

Table C.3.: Required functions and corresponding coefficients for $\mathscr{I}=115$.

| | $1$ | $\log r_i$ |
|---|---|---|
| $H^{\varphi_j,r_i}_{\varphi,z_k}$ | $0$ | $-\cos\theta_M$ |
| $H^{z_k,\varphi_j}_{z,r_i}$ | $\sin\theta_M\sin\overline{\varphi}_M$ | $0$ |
| $H^{z_k,r_i}_{z,\varphi_j}$ | $0$ | $-\sin\theta_M\sin\overline{\varphi}_M$ |

Table C.4.: Required functions and corresponding coefficients for $\mathscr{I}=122$.

| | $\log r$ |
|---|---|
| $H_{\varphi,z_k}^{\varphi_j,r_i}$ | $-\cos\theta_M$ |
| $H_{z,\varphi_j}^{z_k,r_i}$ | $-\sin\theta_M\sin\overline{\varphi}_M$ |

Table C.5.: Required functions and corresponding coefficients for $\mathscr{I} = 123$.

| | $1$ | $\log 2r$ |
|---|---|---|
| $H_{\varphi,z_k}^{\varphi_j,r_i}$ | $\cos\theta_M$ | $-\cos\theta_M$ |
| $H_{z,r_i}^{z_k,\varphi_j}$ | $2\sin\theta_M\sin\overline{\varphi}_M$ | $0$ |
| $H_{z,\varphi_j}^{z_k,r_i}$ | $0$ | $-\sin\theta_M\sin\overline{\varphi}_M$ |

Table C.6.: Required functions and corresponding coefficients for $\mathscr{I} = 124$.

| | $1$ | $\log(r+r_i)$ | $E\left(\frac{\overline{\varphi}_j}{2},-\frac{4rr_i}{\overline{r}_i^2}\right)$ | $F\left(\frac{\overline{\varphi}_j}{2},-\frac{4rr_i}{\overline{r}_i^2}\right)$ |
|---|---|---|---|---|
| $H_{r,z_k}^{r_i,\varphi_j}$ | $0$ | $0$ | $\frac{\cos\theta_M|\overline{r}_i|}{r}$ | $-\frac{\cos\theta_M\left(r^2+r_i^2\right)}{r|\overline{r}_i|}$ |
| $H_{\varphi,z_k}^{\varphi_j,r_i}$ | $\frac{\cos\theta_M r_i}{r}$ | $-\cos\theta_M$ | $0$ | $0$ |
| $H_{z,r_i}^{z_k,\varphi_j}$ | $\frac{\sin\theta_M\sin\overline{\varphi}_M(r+r_i)}{r}$ | $0$ | $\frac{\sin\theta_M\cos\overline{\varphi}_M|\overline{r}_i|}{r}$ | $-\frac{\sin\theta_M\cos\overline{\varphi}_M\left(r^2+r_i^2\right)}{r|\overline{r}_i|}$ |
| $H_{z,\varphi_j}^{z_k,r_i}$ | $0$ | $-\sin\theta_M\sin\overline{\varphi}_M$ | $0$ | $0$ |

Table C.7.: Required functions and corresponding coefficients for $\mathscr{I} = 125$.

| | $1$ | $\log r_i$ |
|---|---|---|
| $H_{r,z_k}^{r_i,\varphi_j}$ | $0$ | $\cos\theta_M\sin\overline{\varphi}_j$ |
| $H_{\varphi,z_k}^{\varphi_j,r_i}$ | $0$ | $\cos\theta_M\cos\overline{\varphi}_j$ |
| $H_{z,r_i}^{z_k,\varphi_j}$ | $-\sin\theta_M\sin\overline{\varphi}_{Mj}$ | $0$ |
| $H_{z,\varphi_j}^{z_k,r_i}$ | $0$ | $\sin\theta_M\sin\overline{\varphi}_{Mj}$ |

Table C.8.: Required functions and corresponding coefficients for $\mathscr{I} = 132$.

| | 1 | $\log\left(r\left(1-\cos\overline{\varphi}_j\right)\right)$ | $\operatorname{artanh}\left(\cos\overline{\varphi}_j\right)$ |
|---|---|---|---|
| $H_{r,z_k}^{r_i,\varphi_j}$ | $-\cos\theta_M\sin\overline{\varphi}_j$ | $\cos\theta_M\sin\overline{\varphi}_j$ | 0 |
| $H_{\varphi,z_k}^{\varphi_j,r_i}$ | $\cos\theta_M$ | 0 | $-\cos\theta_M\cos\overline{\varphi}_j$ |
| $H_{z,\varphi_j}^{z_k,r_i}$ | 0 | 0 | $-\sin\theta_M\sin\overline{\varphi}_{Mj}$ |

Table C.9.: Required functions and corresponding coefficients for $\mathscr{I}=133$.

| | 1 | $\sqrt{2}\sqrt{1-\cos\overline{\varphi}_j}$ | $\operatorname{artanh}\left(\sqrt{\frac{1-\cos\overline{\varphi}_j}{2}}\right)$ | $\operatorname{artanh}\left(\frac{\sin\overline{\varphi}_j}{\sqrt{2}\sqrt{1-\cos\overline{\varphi}_j}}\right)-\frac{\sqrt{2}\sin\overline{\varphi}_j}{\sqrt{1-\cos\overline{\varphi}_j}}$ | $\log\left(r\left(1-\cos\overline{\varphi}_j+\sqrt{2}\sqrt{1-\cos\overline{\varphi}_j}\right)\right)$ |
|---|---|---|---|---|---|
| $H_{r,z_k}^{r_i,\varphi_j}$ | $-\cos\theta_M\sin\overline{\varphi}_j$ | 0 | 0 | $\cos\theta_M$ | $\cos\theta_M\sin\overline{\varphi}_j$ |
| $H_{\varphi,z_k}^{\varphi_j,r_i}$ | 0 | $\cos\theta_M$ | $\cos\theta_M\cos\overline{\varphi}_j$ | 0 | 0 |
| $H_{z,r_i}^{z_k,\varphi_j}$ | 0 | $\sin\theta_M\sin\overline{\varphi}_M$ | 0 | $\sin\theta_M\cos\overline{\varphi}_M$ | 0 |
| $H_{z,\varphi_j}^{z_k,r_i}$ | 0 | 0 | $\sin\theta_M\sin\overline{\varphi}_{Mj}$ | 0 | 0 |

Table C.10.: Required functions and corresponding coefficients for $\mathscr{I}=134$.

| | 1 | $\frac{\sqrt{r^2+r_i^2-2rr_i\cos\overline{\varphi}_j}}{r}$ | $\log\left(r_i-r\cos\overline{\varphi}_j+\sqrt{r^2+r_i^2-2rr_i\cos\overline{\varphi}_j}\right)$ | $\operatorname{artanh}\left(\frac{r\cos\overline{\varphi}_j-r_i}{\sqrt{r^2+r_i^2-2rr_i\cos\overline{\varphi}_j}}\right)$ | $E\left(\frac{\overline{\varphi}_j}{2},-\frac{4rr_i}{\overline{r}_i^2}\right)$ | $F\left(\frac{\overline{\varphi}_j}{2},-\frac{4rr_i}{\overline{r}_i^2}\right)$ |
|---|---|---|---|---|---|---|
| $H_{r,z_k}^{r_i,\varphi_j}$ | $-\cos\theta_M\sin\overline{\varphi}_j$ | 0 | $\cos\theta_M\sin\overline{\varphi}_j$ | 0 | $\frac{\cos\theta_M|\overline{r}_i|}{r}$ | $-\frac{\cos\theta_M\left(r^2+r_i^2\right)}{r|\overline{r}_i|}$ |
| $H_{\varphi,z_k}^{\varphi_j,r_i}$ | 0 | $\cos\theta_M$ | 0 | $-\cos\theta_M\cos\overline{\varphi}_j$ | 0 | 0 |
| $H_{z,r_i}^{z_k,\varphi_j}$ | 0 | $\sin\theta_M\sin\overline{\varphi}_M$ | 0 | 0 | $\frac{\sin\theta_M\cos\overline{\varphi}_M|\overline{r}_i|}{r}$ | $-\frac{\sin\theta_M\cos\overline{\varphi}_M\left(r^2+r_i^2\right)}{r|\overline{r}_i|}$ |
| $H_{z,\varphi_j}^{z_k,r_i}$ | 0 | 0 | 0 | $-\sin\theta_M\sin\overline{\varphi}_{Mj}$ | 0 | 0 |

Table C.11.: Required functions and corresponding coefficients for $\mathscr{I}=135$.

| | $\mathrm{sign}\,\overline{z}_k$ | $\mathrm{sign}\,\overline{z}_k \log|\overline{z}_k|$ |
|---|:---:|:---:|
| $H^{r_i,z_k}_{r,\varphi_j}$ | $0$ | $-\sin\theta_M \sin\overline{\varphi}_M$ |
| $H^{r_i,\varphi_j}_{z,z_k}$ | $-\cos\theta_M \varphi_j$ | $0$ |

Table C.12.: Required functions and corresponding coefficients for $\mathscr{I} = 211$.

| | $\dfrac{r_i}{\sqrt{r_i^2+\overline{z}_k^2}}$ | $\mathrm{artanh}\left(\dfrac{r_i}{\sqrt{r_i^2+\overline{z}_k^2}}\right)$ | $\dfrac{\overline{z}_k}{\sqrt{r_i^2+\overline{z}_k^2}}$ | $\mathrm{artanh}\left(\dfrac{\overline{z}_k}{\sqrt{r_i^2+\overline{z}_k^2}}\right)$ |
|---|:---:|:---:|:---:|:---:|
| $H^{z_k,\varphi_j}_{r,r_i}$ | $0$ | $0$ | $\sin\theta_M\left(\dfrac{\cos\overline{\varphi}_M \varphi_j}{2} - \dfrac{\sin\overline{\varphi}_M}{4}\right)$ | $0$ |
| $H^{r_i,z_k}_{r,\varphi_j}$ | $0$ | $0$ | $0$ | $-\sin\theta_M \sin\overline{\varphi}_M$ |
| $H^{z_k,\varphi_j}_{\varphi,r_i}$ | $0$ | $0$ | $\sin\theta_M\left(\dfrac{\sin\overline{\varphi}_M \varphi_j}{2} - \dfrac{\cos\overline{\varphi}_M}{4}\right)$ | $0$ |
| $H^{\varphi_j,r_i}_{\varphi,z_k}$ | $-\cos\theta_M$ | $\cos\theta_M$ | $0$ | $0$ |
| $H^{z_k,\varphi_j}_{z,r_i}$ | $-\sin\theta_M \sin\overline{\varphi}_M$ | $0$ | $0$ | $0$ |
| $H^{z_k,r_i}_{z,\varphi_j}$ | $0$ | $\sin\theta_M \sin\overline{\varphi}_M$ | $0$ | $0$ |
| $H^{r_i,\varphi_j}_{z,z_k}$ | $0$ | $0$ | $-\cos\theta_M \varphi_j$ | $0$ |

Table C.13.: Required functions and corresponding coefficients for $\mathscr{I} = 212$.

| | $\mathrm{sign}\,\overline{z}_k$ | $\dfrac{\sqrt{r^2+\overline{z}_k^2}}{r}$ | $\mathrm{artanh}\left(\dfrac{r}{\sqrt{r^2+\overline{z}_k^2}}\right)$ | $\mathrm{artanh}\left(\dfrac{\overline{z}_k}{\sqrt{r^2+\overline{z}_k^2}}\right)$ |
|---|:---:|:---:|:---:|:---:|
| $H^{r_i,z_k}_{r,\varphi_j}$ | $0$ | $0$ | $0$ | $-\sin\theta_M \sin\overline{\varphi}_M$ |
| $H^{\varphi_j,r_i}_{\varphi,z_k}$ | $0$ | $\cos\theta_M$ | $-\cos\theta_M$ | $0$ |
| $H^{z_k,r_i}_{z,\varphi_j}$ | $0$ | $0$ | $-\sin\theta_M \sin\overline{\varphi}_M$ | $0$ |
| $H^{r_i,\varphi_j}_{z,z_k}$ | $\cos\theta_M \overline{\varphi}_j$ | $0$ | $0$ | $0$ |

Table C.14.: Required functions and corresponding coefficients for $\mathscr{I} = 213$.

| | $\operatorname{sign}\overline{z}_k$ | $\frac{|\overline{z}_k|}{r}$ | $\frac{\operatorname{sign}\overline{z}_k\overline{z}_k^2}{2r^2}$ | $\operatorname{sign}\overline{z}_k\log|\overline{z}_k|$ | $\operatorname{sign}\overline{z}_k\log\left(\frac{|\overline{z}_k|}{\sqrt{2}r}\right)$ | $E\left(\frac{\overline{\varphi}_j}{2},-\frac{4r^2}{\overline{z}_k^2}\right)$ | $F\left(\frac{\overline{\varphi}_j}{2},-\frac{4r^2}{\overline{z}_k^2}\right)$ | $\cdots$ |
|---|---|---|---|---|---|---|---|---|
| $H_{r,r_i}^{z_k,\varphi_j}$ | 0 | 0 | $-\sin\theta_M\sin\overline{\varphi}_M$ | 0 | 0 | $-\frac{\sin\theta_M\cos\overline{\varphi}_M\operatorname{sign}\overline{z}_k\overline{z}_k^2}{2r^2}$ | $\frac{\sin\theta_M\cos\overline{\varphi}_M\operatorname{sign}\overline{z}_k\left(2r^2+\overline{z}_k^2\right)}{2r^2}$ | |
| $H_{r,\varphi_j}^{r_i,z_k}$ | 0 | 0 | 0 | $-\sin\theta_M\sin\overline{\varphi}_M$ | 0 | 0 | 0 | |
| $H_{r,z_k}^{r_i,\varphi_j}$ | 0 | 0 | 0 | 0 | 0 | $\frac{\cos\theta_M|\overline{z}_k|}{r}$ | $-\frac{\cos\theta_M\left(2r^2+\overline{z}_k^2\right)}{r|\overline{z}_k|}$ | $\cdots$ |
| $H_{\varphi,r_i}^{z_k,\varphi_j}$ | $\frac{\sin\theta_M\left(\sin\overline{\varphi}_M\varphi_j-\cos\overline{\varphi}_M\right)}{2}$ | 0 | $-\sin\theta_M\cos\overline{\varphi}_M$ | 0 | $-\sin\theta_M\cos\overline{\varphi}_M$ | $\frac{\sin\theta_M\sin\overline{\varphi}_M\operatorname{sign}\overline{z}_k\overline{z}_k^2}{2r^2}$ | $-\frac{\sin\theta_M\sin\overline{\varphi}_M\operatorname{sign}\overline{z}_k\left(4r^2+\overline{z}_k^2\right)}{2r^2}$ | |
| $H_{\varphi,z_k}^{\varphi_j,r_i}$ | 0 | $\cos\theta_M$ | 0 | 0 | 0 | 0 | 0 | |
| $H_{z,r_i}^{z_k,\varphi_j}$ | 0 | $\sin\theta_M\sin\overline{\varphi}_M$ | 0 | 0 | 0 | $\frac{\sin\theta_M\cos\overline{\varphi}_M|\overline{z}_k|}{r}$ | $-\frac{\sin\theta_M\cos\overline{\varphi}_M\left(2r^2+\overline{z}_k^2\right)}{r|\overline{z}_k|}$ | |
| $H_{z,z_k}^{r_i,\varphi_j}$ | 0 | 0 | 0 | 0 | 0 | 0 | 0 | $\cdots$ |

| | $\cdots$ | $\Pi\left(\frac{\overline{\varphi}_j}{2},\frac{2r}{r\pm\sqrt{r^2+\overline{z}_k^2}},-\frac{4r^2}{\overline{z}_k^2}\right)$ | $\Pi\left(\frac{\overline{\varphi}_j}{2},1-\frac{\overline{z}_k^4}{\left(4r^2+\overline{z}_k^2\right)\left(r\pm\sqrt{r^2+\overline{z}_k^2}\right)^2},\frac{4r^2}{4r^2+\overline{z}_k^2}\right)$ |
|---|---|---|---|
| $H_{r,z_k}^{r_i,\varphi_j}$ | $\cdots$ | $-\frac{\cos\theta_M\left(\sqrt{r^2+\overline{z}_k^2}\mp r\right)\left(r\pm\sqrt{r^2+\overline{z}_k^2}\right)^2}{r|\overline{z}_k|\sqrt{r^2+\overline{z}_k^2}}$ | $\pm\frac{\cos\theta_M\overline{z}_k^4}{r\sqrt{\left(r^2+\overline{z}_k^2\right)\left(4r^2+\overline{z}_k^2\right)}\left(r\pm\sqrt{r^2+\overline{z}_k^2}\right)}$ |
| $H_{z,z_k}^{r_i,\varphi_j}$ | $\cdots$ | $\cos\theta_M\operatorname{sign}\overline{z}_k$ | 0 |

Table C.15.: Required functions and corresponding coefficients for $\mathscr{I}=214$.

| | $\sqrt{\overline{r}_i^2 + \overline{z}_k^2}$ | $\text{artanh}\left(\dfrac{\overline{r}_i}{\sqrt{\overline{r}_i^2+\overline{z}_k^2}}\right)$ | $\text{artanh}\left(\dfrac{\overline{z}_k}{\sqrt{\overline{r}_i^2+\overline{z}_k^2}}\right)$ | $E\left(\dfrac{\overline{\varphi}_j}{2}, -\dfrac{4rr_i}{\overline{r}_i^2+\overline{z}_k^2}\right)$ | $F\left(\dfrac{\overline{\varphi}_j}{2}, -\dfrac{4rr_i}{\overline{r}_i^2+\overline{z}_k^2}\right)$ | $\Pi\left(\dfrac{\overline{\varphi}_j}{2}, -\dfrac{4rr_i}{\overline{r}_i^2}, -\dfrac{4rr_i}{\overline{r}_i^2+\overline{z}_k^2}\right)$ | $\cdots$ |
|---|---|---|---|---|---|---|---|
| $H_{r,r_i}^{z_k,\varphi_j}$ | $-\dfrac{\sin\theta_M \sin\overline{\varphi}_M \overline{z}_k}{2r^2}$ | $0$ | $\dfrac{\sin\theta_M \sin\overline{\varphi}_M (r^2-r_i^2)}{2r^2}$ | $-\dfrac{\sin\theta_M \cos\overline{\varphi}_M \overline{z}_k \sqrt{\overline{r}_i^2+\overline{z}_k^2}}{2r^2}$ | $\dfrac{\sin\theta_M \cos\overline{\varphi}_M \overline{z}_k (2r_i^2+\overline{z}_k^2)}{2r^2\sqrt{\overline{r}_i^2+\overline{z}_k^2}}$ | $\dfrac{\sin\theta_M \cos\overline{\varphi}_M \overline{z}_k (r^2+r_i^2)(r+r_i)}{2r^2\overline{r}_i\sqrt{\overline{r}_i^2+\overline{z}_k^2}}$ | |
| $H_{r,\varphi_j}^{r_i,z_k}$ | $0$ | $0$ | $-\sin\theta_M \sin\overline{\varphi}_M$ | $0$ | $0$ | $0$ | |
| $H_{r,z_k}^{r_i,\varphi_j}$ | $0$ | $0$ | $0$ | $\dfrac{\cos\theta_M \sqrt{\overline{r}_i^2+\overline{z}_k^2}}{r}$ | $-\dfrac{\cos\theta_M (r^2+r_i^2+\overline{z}_k^2)}{r\sqrt{\overline{r}_i^2+\overline{z}_k^2}}$ | $0$ | $\cdots$ |
| $H_{\varphi,r_i}^{z_k,\varphi_j}$ | $-\dfrac{\sin\theta_M \cos\overline{\varphi}_M \overline{z}_k}{2r^2}$ | $0$ | $-\dfrac{\sin\theta_M \cos\overline{\varphi}_M (r^2+r_i^2)}{2r^2}$ | $\dfrac{\sin\theta_M \sin\overline{\varphi}_M \overline{z}_k \sqrt{\overline{r}_i^2+\overline{z}_k^2}}{2r^2}$ | $-\dfrac{\sin\theta_M \sin\overline{\varphi}_M \overline{z}_k (2r^2+2r_i^2+\overline{z}_k^2)}{2r^2\sqrt{\overline{r}_i^2+\overline{z}_k^2}}$ | $\dfrac{\sin\theta_M \sin\overline{\varphi}_M \overline{z}_k (r+r_i)^2}{2r^2\sqrt{\overline{r}_i^2+\overline{z}_k^2}}$ | |
| $H_{\varphi,z_k}^{\varphi_j,r_i}$ | $\dfrac{\cos\theta_M}{r}$ | $-\cos\theta_M$ | $0$ | $0$ | $0$ | $0$ | |
| $H_{z,r_i}^{z_k,\varphi_j}$ | $\dfrac{\sin\theta_M \sin\overline{\varphi}_M}{r}$ | $0$ | $0$ | $\dfrac{\sin\theta_M \cos\overline{\varphi}_M \sqrt{\overline{r}_i^2+\overline{z}_k^2}}{r}$ | $-\dfrac{\sin\theta_M \cos\overline{\varphi}_M (r^2+r_i^2+\overline{z}_k^2)}{r\sqrt{\overline{r}_i^2+\overline{z}_k^2}}$ | $0$ | |
| $H_{z,\varphi_j}^{z_k,r_i}$ | $0$ | $-\sin\theta_M \sin\overline{\varphi}_M$ | $0$ | $0$ | $0$ | $0$ | |
| $H_{z,z_k}^{r_i,\varphi_j}$ | $0$ | $0$ | $0$ | $0$ | $0$ | $0$ | $\cdots$ |

| | $\cdots$ | $\Pi\left(\dfrac{\overline{\varphi}_j}{2}, \dfrac{2r}{r\pm\sqrt{r^2+\overline{z}_k^2}}, -\dfrac{4rr_i}{\overline{r}_i^2+\overline{z}_k^2}\right)$ | $\Pi\left(\dfrac{\overline{\varphi}_j}{2}, 1-\dfrac{\overline{z}_k^2(\overline{r}_i^2+\overline{z}_k^2)}{\left((r+r_i)^2+\overline{z}_k^2\right)\left(r\pm\sqrt{r^2+\overline{z}_k^2}\right)^2}, \dfrac{4rr_i}{(r+r_i)^2+\overline{z}_k^2}\right)$ |
|---|---|---|---|
| $H_{r,z_k}^{r_i,\varphi_j}$ | $\cdots$ | $-\dfrac{\cos\theta_M \left(\sqrt{r^2+\overline{z}_k^2}\mp r\right)\left(r_i\pm\sqrt{r^2+\overline{z}_k^2}\right)^2}{r\sqrt{\left(r^2+\overline{z}_k^2\right)\left(\overline{r}_i^2+\overline{z}_k^2\right)}}$ | $\pm\dfrac{\cos\theta_M \overline{z}_k^2\left(\overline{r}_i^2+\overline{z}_k^2\right)}{r\sqrt{\left(r^2+\overline{z}_k^2\right)\left((r+r_i)^2+\overline{z}_k^2\right)\left(r\pm\sqrt{r^2+\overline{z}_k^2}\right)}}$ |
| $H_{z,z_k}^{r_i,\varphi_j}$ | $\cdots$ | $\dfrac{\cos\theta_M \overline{z}_k\left(r_i\pm\sqrt{r^2+\overline{z}_k^2}\right)}{\sqrt{\overline{r}_i^2+\overline{z}_k^2}\left(r\pm\sqrt{r^2+\overline{z}_k^2}\right)}$ | $0$ |

Table C.16.: Required functions and corresponding coefficients for $\mathscr{I} = 215$.

| | $\text{sign}\,\overline{z}_k$ | $\text{sign}\,\overline{z}_k \log|\overline{z}_k|$ |
|---|---|---|
| $H_{r,\varphi_j}^{r_i,z_k}$ | $0$ | $-\sin\theta_M \sin\overline{\varphi}_M$ |
| $H_{z,z_k}^{r_i,\varphi_j}$ | $-\cos\theta_M \varphi_j$ | $0$ |

Table C.17.: Required functions and corresponding coefficients for $\mathscr{I} = 221$.

| | $\dfrac{r_i}{\sqrt{r_i^2+\bar{z}_k^2}}$ | $\text{artanh}\left(\dfrac{r_i}{\sqrt{r_i^2+\bar{z}_k^2}}\right)$ | $\dfrac{\bar{z}_k}{\sqrt{r_i^2+\bar{z}_k^2}}$ | $\text{artanh}\left(\dfrac{\bar{z}_k}{\sqrt{r_i^2+\bar{z}_k^2}}\right)$ |
|---|---|---|---|---|
| $H_{r,r_i}^{z_k,\varphi_j}$ | 0 | 0 | $\sin\theta_M\left(\dfrac{\cos\overline{\varphi}_M\varphi_j}{2}-\dfrac{\sin\overline{\varphi}_M}{4}\right)$ | 0 |
| $H_{r,\varphi_j}^{r_i,z_k}$ | 0 | 0 | 0 | $-\sin\theta_M\sin\overline{\varphi}_M$ |
| $H_{\varphi,r_i}^{z_k,\varphi_j}$ | 0 | 0 | $\sin\theta_M\left(\dfrac{\sin\overline{\varphi}_M\varphi_j}{2}-\dfrac{\cos\overline{\varphi}_M}{4}\right)$ | 0 |
| $H_{\varphi,z_k}^{\varphi_j,r_i}$ | $\cos\theta_M$ | $-\cos\theta_M$ | 0 | 0 |
| $H_{z,r_i}^{z_k,\varphi_j}$ | $\sin\theta_M\sin\overline{\varphi}_M$ | 0 | 0 | 0 |
| $H_{z,\varphi_j}^{z_k,r_i}$ | 0 | $-\sin\theta_M\sin\overline{\varphi}_M$ | 0 | 0 |
| $H_{z,z_k}^{r_i,\varphi_j}$ | 0 | 0 | $-\cos\theta_M\varphi_j$ | 0 |

Table C.18.: Required functions and corresponding coefficients for $\mathscr{I}=222$.

| | $\text{sign}\,\bar{z}_k$ | $\dfrac{\sqrt{r^2+\bar{z}_k^2}}{r}$ | $\text{artanh}\left(\dfrac{r}{\sqrt{r^2+\bar{z}_k^2}}\right)$ | $\text{artanh}\left(\dfrac{\bar{z}_k}{\sqrt{r^2+\bar{z}_k^2}}\right)$ |
|---|---|---|---|---|
| $H_{r,\varphi_j}^{r_i,z_k}$ | 0 | 0 | 0 | $-\sin\theta_M\sin\overline{\varphi}_M$ |
| $H_{\varphi,z_k}^{\varphi_j,r_i}$ | 0 | $\cos\theta_M$ | $-\cos\theta_M$ | 0 |
| $H_{z,\varphi_j}^{z_k,r_i}$ | 0 | 0 | $-\sin\theta_M\sin\overline{\varphi}_M$ | 0 |
| $H_{z,z_k}^{r_i,\varphi_j}$ | $\cos\theta_M\overline{\varphi}_j$ | 0 | 0 | 0 |

Table C.19.: Required functions and corresponding coefficients for $\mathscr{I}=223$.

| | $\sqrt{4r^2+\bar{z}_k^2}$ | $\text{artanh}\left(\frac{2r}{\sqrt{4r^2+\bar{z}_k^2}}\right)$ | $\text{artanh}\left(\frac{\bar{z}_k}{\sqrt{4r^2+\bar{z}_k^2}}\right)$ | $E\left(\frac{\overline{\varphi}_j}{2},-\frac{4r^2}{\bar{z}_k^2}\right)$ | $F\left(\frac{\overline{\varphi}_j}{2},-\frac{4r^2}{\bar{z}_k^2}\right)$ | $\Pi\left(\frac{\overline{\varphi}_j}{2},\frac{2r}{r\pm\sqrt{r^2+\bar{z}_k^2}},-\frac{4r^2}{\bar{z}_k^2}\right)$ | $\cdots$ |
|---|---|---|---|---|---|---|---|
| $H_{r,r_i}^{z_k,\varphi_j}$ | $-\frac{\sin\theta_M\sin\overline{\varphi}_M\bar{z}_k}{2r^2}$ | $0$ | $0$ | $-\frac{\sin\theta_M\cos\overline{\varphi}_M\,\text{sign}\,\bar{z}_k\bar{z}_k^2}{2r^2}$ | $\frac{\sin\theta_M\cos\overline{\varphi}_M\,\text{sign}\,\bar{z}_k\left(2r^2+\bar{z}_k^2\right)}{2r^2}$ | $0$ | |
| $H_{r,\varphi_j}^{r_i,z_k}$ | $0$ | $0$ | $-\sin\theta_M\sin\overline{\varphi}_M$ | $0$ | $0$ | $0$ | |
| $H_{r,z_k}^{r_i,\varphi_j}$ | $0$ | $0$ | $0$ | $\frac{\cos\theta_M|\bar{z}_k|}{r}$ | $-\frac{\cos\theta_M\left(2r^2+\bar{z}_k^2\right)}{r|\bar{z}_k|}$ | $-\frac{\cos\theta_M\left(\sqrt{r^2+\bar{z}_k^2}\mp r\right)\left(r\pm\sqrt{r^2+\bar{z}_k^2}\right)^2}{r|\bar{z}_k|\sqrt{r^2+\bar{z}_k^2}}$ | $\cdots$ |
| $H_{\varphi,r_i}^{z_k,\varphi_j}$ | $-\frac{\sin\theta_M\cos\overline{\varphi}_M\bar{z}_k}{2r^2}$ | $0$ | $-\sin\theta_M\cos\overline{\varphi}_M$ | $\frac{\sin\theta_M\sin\overline{\varphi}_M\,\text{sign}\,\bar{z}_k\bar{z}_k^2}{2r^2}$ | $-\frac{\sin\theta_M\sin\overline{\varphi}_M\,\text{sign}\,\bar{z}_k\left(4r^2+\bar{z}_k^2\right)}{2r^2}$ | $0$ | |
| $H_{\varphi,z_k}^{\varphi_j,r_i}$ | $\frac{\cos\theta_M}{r}$ | $-\cos\theta_M$ | $0$ | $0$ | $0$ | $0$ | |
| $H_{z,r_i}^{z_k,\varphi_j}$ | $\frac{\sin\theta_M\sin\overline{\varphi}_M}{r}$ | $0$ | $0$ | $\frac{\sin\theta_M\cos\overline{\varphi}_M|\bar{z}_k|}{r}$ | $-\frac{\sin\theta_M\cos\overline{\varphi}_M\left(2r^2+\bar{z}_k^2\right)}{r|\bar{z}_k|}$ | $0$ | |
| $H_{z,\varphi_j}^{z_k,r_i}$ | $0$ | $-\sin\theta_M\sin\overline{\varphi}_M$ | $0$ | $0$ | $0$ | $0$ | |
| $H_{z,z_k}^{r_i,\varphi_j}$ | $0$ | $0$ | $0$ | $0$ | $0$ | $\cos\theta_M\,\text{sign}\,\bar{z}_k$ | |

| | $\cdots$ | $\Pi\left(\frac{\overline{\varphi}_j}{2},1-\frac{\bar{z}_k^4}{\left(4r^2+\bar{z}_k^2\right)\left(r\pm\sqrt{r^2+\bar{z}_k^2}\right)^2},\frac{4r^2}{4r^2+\bar{z}_k^2}\right)$ |
|---|---|---|
| $H_{r,z_k}^{r_i,\varphi_j}$ | $\cdots$ | $\pm\frac{\cos\theta_M\bar{z}_k^4}{r\sqrt{\left(r^2+\bar{z}_k^2\right)\left(4r^2+\bar{z}_k^2\right)}\left(r\pm\sqrt{r^2+\bar{z}_k^2}\right)}$ |

Table C.20.: Required functions and corresponding coefficients for $\mathscr{I}=224$.

| | $\sqrt{(r+r_i)^2+\bar{z}_k^2}$ | $\operatorname{artanh}\left(\frac{r+r_i}{\sqrt{(r+r_i)^2+\bar{z}_k^2}}\right)$ | $\operatorname{artanh}\left(\frac{\bar{z}_k}{\sqrt{(r+r_i)^2+\bar{z}_k^2}}\right)$ | $E\left(\frac{\overline{\varphi}_j}{2}, -\frac{4rr_i}{\bar{r}_i^2+\bar{z}_k^2}\right)$ | $F\left(\frac{\overline{\varphi}_j}{2}, -\frac{4rr_i}{\bar{r}_i^2+\bar{z}_k^2}\right)$ | $\Pi\left(\frac{\overline{\varphi}_j}{2}, -\frac{4rr_i}{\bar{r}_i^2+\bar{z}_k^2}, -\frac{4rr_i}{\bar{r}_i^2+\bar{z}_k^2}\right)$ | $\cdots$ |
|---|---|---|---|---|---|---|---|
| $H_{r,r_i}^{z_k,\varphi_j}$ | $-\frac{\sin\theta_M\sin\overline{\varphi}_M\bar{z}_k}{2r^2}$ | $0$ | $\frac{\sin\theta_M\sin\overline{\varphi}_M(r^2-r_i^2)}{2r^2}$ | $-\frac{\sin\theta_M\cos\overline{\varphi}_M\bar{z}_k\sqrt{\bar{r}_i^2+\bar{z}_k^2}}{2r^2}$ | $\frac{\sin\theta_M\cos\overline{\varphi}_M\bar{z}_k(2r_i^2+\bar{z}_k^2)}{2r^2\sqrt{\bar{r}_i^2+\bar{z}_k^2}}$ | $\frac{\sin\theta_M\cos\overline{\varphi}_M\bar{z}_k(r^2+r_i^2)(r+r_i)}{2r^2\bar{r}_i\sqrt{\bar{r}_i^2+\bar{z}_k^2}}$ | |
| $H_{r,\varphi_j}^{r_i,z_k}$ | $0$ | $0$ | $-\sin\theta_M\sin\overline{\varphi}_M$ | $0$ | $0$ | $0$ | |
| $H_{r,z_k}^{r_i,\varphi_j}$ | $0$ | $0$ | $0$ | $\frac{\cos\theta_M\sqrt{\bar{r}_i^2+\bar{z}_k^2}}{r}$ | $-\frac{\cos\theta_M(r^2+r_i^2+\bar{z}_k^2)}{r\sqrt{\bar{r}_i^2+\bar{z}_k^2}}$ | $0$ | $\cdots$ |
| $H_{\varphi,r_i}^{z_k,\varphi_j}$ | $-\frac{\sin\theta_M\cos\overline{\varphi}_M\bar{z}_k}{2r^2}$ | $0$ | $-\frac{\sin\theta_M\cos\overline{\varphi}_M(r^2+r_i^2)}{2r^2}$ | $\frac{\sin\theta_M\sin\overline{\varphi}_M\bar{z}_k\sqrt{\bar{r}_i^2+\bar{z}_k^2}}{2r^2}$ | $-\frac{\sin\theta_M\sin\overline{\varphi}_M\bar{z}_k(2r^2+2r_i^2+\bar{z}_k^2)}{2r^2\sqrt{\bar{r}_i^2+\bar{z}_k^2}}$ | $\frac{\sin\theta_M\sin\overline{\varphi}_M\bar{z}_k(r+r_i)^2}{2r^2\sqrt{\bar{r}_i^2+\bar{z}_k^2}}$ | |
| $H_{\varphi,z_k}^{\varphi_j,r_i}$ | $\frac{\cos\theta_M}{r}$ | $-\cos\theta_M$ | $0$ | $0$ | $0$ | $0$ | |
| $H_{z,r_i}^{z_k,\varphi_j}$ | $\frac{\sin\theta_M\sin\overline{\varphi}_M}{r}$ | $0$ | $0$ | $\frac{\sin\theta_M\cos\overline{\varphi}_M\sqrt{\bar{r}_i^2+\bar{z}_k^2}}{r}$ | $-\frac{\sin\theta_M\cos\overline{\varphi}_M(r^2+r_i^2+\bar{z}_k^2)}{r\sqrt{\bar{r}_i^2+\bar{z}_k^2}}$ | $0$ | |
| $H_{z,\varphi_j}^{z_k,r_i}$ | $0$ | $-\sin\theta_M\sin\overline{\varphi}_M$ | $0$ | $0$ | $0$ | $0$ | |
| $H_{z,z_k}^{r_i,\varphi_j}$ | $0$ | $0$ | $0$ | $0$ | $0$ | $0$ | $\cdots$ |

| | $\cdots$ | $\Pi\left(\frac{\overline{\varphi}_j}{2}, \frac{2r}{r\pm\sqrt{r^2+\bar{z}_k^2}}, -\frac{4rr_i}{\bar{r}_i^2+\bar{z}_k^2}\right)$ | $\Pi\left(\frac{\overline{\varphi}_j}{2}, 1-\frac{\bar{z}_k^2(\bar{r}_i^2+\bar{z}_k^2)}{\left((r+r_i)^2+\bar{z}_k^2\right)\left(r\pm\sqrt{r^2+\bar{z}_k^2}\right)^2}, \frac{4rr_i}{(r+r_i)^2+\bar{z}_k^2}\right)$ |
|---|---|---|---|
| $H_{r,z_k}^{r_i,\varphi_j}$ | $\cdots$ | $-\frac{\cos\theta_M\left(\sqrt{r^2+\bar{z}_k^2}\mp r\right)\left(r_i\pm\sqrt{r^2+\bar{z}_k^2}\right)^2}{r\sqrt{\left(r^2+\bar{z}_k^2\right)\left(\bar{r}_i^2+\bar{z}_k^2\right)}}$ | $\pm\frac{\cos\theta_M\bar{z}_k^2\left(\bar{r}_i^2+\bar{z}_k^2\right)}{r\sqrt{\left(r^2+\bar{z}_k^2\right)\left((r+r_i)^2+\bar{z}_k^2\right)\left(r\pm\sqrt{r^2+\bar{z}_k^2}\right)}}$ |
| $H_{z,z_k}^{r_i,\varphi_j}$ | $\cdots$ | $\frac{\cos\theta_M\bar{z}_k\left(r_i\pm\sqrt{r^2+\bar{z}_k^2}\right)}{\sqrt{\bar{r}_i^2+\bar{z}_k^2}\left(r\pm\sqrt{r^2+\bar{z}_k^2}\right)}$ | $0$ |

Table C.21.: Required functions and corresponding coefficients for $\mathscr{I}=225$.

| | $\operatorname{sign}\bar{z}_k$ | $\operatorname{sign}\bar{z}_k\log|\bar{z}_k|$ |
|---|---|---|
| $H_{r,\varphi_j}^{r_i,z_k}$ | $0$ | $-\sin\theta_M\sin\overline{\varphi}_{Mj}\cos\overline{\varphi}_j$ |
| $H_{\varphi,\varphi_j}^{z_k,r_i}$ | $0$ | $\sin\theta_M\sin\overline{\varphi}_{Mj}\sin\overline{\varphi}_j$ |
| $H_{z,z_k}^{r_i,\varphi_j}$ | $-\cos\theta_M\varphi_j$ | $0$ |

Table C.22.: Required functions and corresponding coefficients for $\mathscr{I}=231$.

| | $\dfrac{r_i}{\sqrt{r_i^2+\bar{z}_k^2}}$ | $\text{artanh}\left(\dfrac{r_i}{\sqrt{r_i^2+\bar{z}_k^2}}\right)$ | $\dfrac{\bar{z}_k}{\sqrt{r_i^2+\bar{z}_k^2}}$ | $\text{artanh}\left(\dfrac{\bar{z}_k}{\sqrt{r_i^2+\bar{z}_k^2}}\right)$ |
|---|---|---|---|---|
| $H_{r,r_i}^{z_k,\varphi_j}$ | $0$ | $0$ | $\sin\theta_M\left(\dfrac{\cos\overline{\varphi}_M\varphi_j}{2}-\dfrac{\sin\left(\overline{\varphi}_{Mj}+\overline{\varphi}_j\right)}{4}\right)$ | $0$ |
| $H_{r,\varphi_j}^{r_i,z_k}$ | $0$ | $0$ | $0$ | $-\sin\theta_M\sin\overline{\varphi}_{Mj}\cos\overline{\varphi}_j$ |
| $H_{r,z_k}^{r_i,\varphi_j}$ | $-\cos\theta_M\sin\overline{\varphi}_j$ | $\cos\theta_M\sin\overline{\varphi}_j$ | $0$ | $0$ |
| $H_{\varphi,r_i}^{z_k,\varphi_j}$ | $0$ | $0$ | $\sin\theta_M\left(\dfrac{\sin\overline{\varphi}_M\varphi_j}{2}-\dfrac{\cos\left(\overline{\varphi}_{Mj}+\overline{\varphi}_j\right)}{4}\right)$ | $0$ |
| $H_{\varphi,\varphi_j}^{z_k,r_i}$ | $0$ | $0$ | $0$ | $\sin\theta_M\sin\overline{\varphi}_{Mj}\sin\overline{\varphi}_j$ |
| $H_{\varphi,z_k}^{\varphi_j,r_i}$ | $-\cos\theta_M\cos\overline{\varphi}_j$ | $\cos\theta_M\cos\overline{\varphi}_j$ | $0$ | $0$ |
| $H_{z,r_i}^{z_k,\varphi_j}$ | $-\sin\theta_M\sin\overline{\varphi}_{Mj}$ | $0$ | $0$ | $0$ |
| $H_{z,\varphi_j}^{z_k,r_i}$ | $0$ | $\sin\theta_M\sin\overline{\varphi}_{Mj}$ | $0$ | $0$ |
| $H_{z,z_k}^{r_i,\varphi_j}$ | $0$ | $0$ | $-\cos\theta_M\varphi_j$ | $0$ |

Table C.23.: Required functions and corresponding coefficients for $\mathscr{I}=232$.

| | $1$ | $\log\left(-r\cos\overline{\varphi}_j+\sqrt{r^2+\bar{z}_k^2}\right)$ | $\dfrac{\sqrt{r^2+\bar{z}_k^2}}{r}$ | $\text{artanh}\left(\dfrac{r\cos\overline{\varphi}_j}{\sqrt{r^2+\bar{z}_k^2}}\right)$ | $\text{artanh}\left(\dfrac{\bar{z}_k}{\sqrt{r^2+\bar{z}_k^2}}\right)$ | $\arctan\left(\dfrac{r\sin\overline{\varphi}_j}{\bar{z}_k}\right)$ | $\arctan\left(\dfrac{\bar{z}_k\cos\overline{\varphi}_j}{\sin\overline{\varphi}_j\sqrt{r^2+\bar{z}_k^2}}\right)$ | $\cdots$ |
|---|---|---|---|---|---|---|---|---|
| $H_{r,\varphi_j}^{r_i,z_k}$ | $0$ | $0$ | $0$ | $0$ | $-\sin\theta_M\sin\overline{\varphi}_{Mj}\cos\overline{\varphi}_j$ | $0$ | $\sin\theta_M\sin\overline{\varphi}_{Mj}\sin\overline{\varphi}_j$ | |
| $H_{r,z_k}^{r_i,\varphi_j}$ | $-\cos\theta_M\sin\overline{\varphi}_j$ | $\cos\theta_M\sin\overline{\varphi}_j$ | $0$ | $0$ | $0$ | $\dfrac{\cos\theta_M\bar{z}_k}{r}$ | $0$ | $\cdots$ |
| $H_{\varphi,\varphi_j}^{z_k,r_i}$ | $0$ | $0$ | $0$ | $0$ | $\sin\theta_M\sin\overline{\varphi}_{Mj}\sin\overline{\varphi}_j$ | $0$ | $\sin\theta_M\sin\overline{\varphi}_{Mj}\cos\overline{\varphi}_j$ | |
| $H_{\varphi,z_k}^{\varphi_j,r_i}$ | $0$ | $0$ | $\cos\theta_M$ | $-\cos\theta_M\cos\overline{\varphi}_j$ | $0$ | $0$ | $0$ | |
| $H_{z,\varphi_j}^{z_k,r_i}$ | $0$ | $0$ | $0$ | $-\sin\theta_M\sin\overline{\varphi}_{Mj}$ | $0$ | $0$ | $0$ | |
| $H_{z,z_k}^{r_i,\varphi_j}$ | $0$ | $0$ | $0$ | $0$ | $0$ | $0$ | $0$ | $\cdots$ |

| | $\cdots$ | $\text{Sc}\left(2\overline{\varphi}_j,\dfrac{\sqrt{r^2+\bar{z}_k^2}}{|\bar{z}_k|}\right)$ | $\text{Sc}\left(\overline{\varphi}_j,\left|\dfrac{\bar{z}_k}{r\pm\sqrt{r^2+\bar{z}_k^2}}\right|\right)$ |
|---|---|---|---|
| $H_{r,z_k}^{r_i,\varphi_j}$ | $\cdots$ | $-\dfrac{\cos\theta_M\bar{z}_k}{r}$ | $\dfrac{\cos\theta_M\bar{z}_k}{r}$ |
| $H_{z,z_k}^{r_i,\varphi_j}$ | $\cdots$ | $\cos\theta_M\,\text{sign}\,\bar{z}_k$ | $0$ |

Table C.24.: Required functions and corresponding coefficients for $\mathscr{I}=233$.

| | $1$ | $\sqrt{2r^2\left(1-\cos\overline{\varphi}_j\right)+\overline{z}_k^2}$ | $\log\left(r\left(1-\cos\overline{\varphi}_j\right)+\sqrt{2r^2\left(1-\cos\overline{\varphi}_j\right)+\overline{z}_k^2}\right)$ | $\operatorname{artanh}\left(\frac{r\left(1-\cos\overline{\varphi}_j\right)}{\sqrt{2r^2\left(1-\cos\overline{\varphi}_j\right)+\overline{z}_k^2}}\right)$ | $\operatorname{artanh}\left(\frac{\overline{z}_k}{\sqrt{2r^2\left(1-\cos\overline{\varphi}_j\right)+\overline{z}_k^2}}\right)$ | $\cdots$ |
|---|---|---|---|---|---|---|
| $H_{r,r_i}^{z_k,\varphi_j}$ | $0$ | $-\frac{\sin\theta_M\sin\overline{\varphi}_M\overline{z}_k}{2r^2}$ | $0$ | $0$ | $0$ | $\cdots$ |
| $H_{r,\varphi_j}^{r_i,z_k}$ | $0$ | $0$ | $0$ | $0$ | $-\sin\theta_M\sin\overline{\varphi}_{Mj}\cos\overline{\varphi}_j$ | $\cdots$ |
| $H_{r,z_k}^{r_i,\varphi_j}$ | $-\cos\theta_M\sin\overline{\varphi}_j$ | $0$ | $\cos\theta_M\sin\overline{\varphi}_j$ | $0$ | $0$ | $\cdots$ |
| $H_{\varphi,r_i}^{z_k,\varphi_j}$ | $0$ | $-\frac{\sin\theta_M\cos\overline{\varphi}_M\overline{z}_k}{2r^2}$ | $0$ | $0$ | $-\sin\theta_M\cos\overline{\varphi}_M$ | $\cdots$ |
| $H_{\varphi,\varphi_j}^{z_k,r_i}$ | $0$ | $0$ | $0$ | $0$ | $\sin\theta_M\sin\overline{\varphi}_{Mj}\sin\overline{\varphi}_j$ | $\cdots$ |
| $H_{\varphi,z_k}^{\varphi_j,r_i}$ | $0$ | $\frac{\cos\theta_M}{r}$ | $0$ | $\cos\theta_M\cos\overline{\varphi}_j$ | $0$ | $\cdots$ |
| $H_{z,r_i}^{z_k,\varphi_j}$ | $0$ | $\frac{\sin\theta_M\sin\overline{\varphi}_M}{r}$ | $0$ | $0$ | $0$ | $\cdots$ |
| $H_{z,\varphi_j}^{z_k,r_i}$ | $0$ | $0$ | $0$ | $\sin\theta_M\sin\overline{\varphi}_{Mj}$ | $0$ | $\cdots$ |
| $H_{z,z_k}^{r_i,\varphi_j}$ | $0$ | $0$ | $0$ | $0$ | $0$ | $\cdots$ |

| | | $\arctan\left(\frac{r\sin\overline{\varphi}_j}{\overline{z}_k}\right)$ | $\arctan\left(\frac{\overline{z}_k\left(1-\cos\overline{\varphi}_j\right)}{\sin\overline{\varphi}_j\sqrt{2r^2\left(1-\cos\overline{\varphi}_j\right)+\overline{z}_k^2}}\right)$ | $E\left(\frac{\overline{\varphi}_j}{2},-\frac{4r^2}{\overline{z}_k^2}\right)$ | $F\left(\frac{\overline{\varphi}_j}{2},-\frac{4r^2}{\overline{z}_k^2}\right)$ | $\Pi\left(\frac{\overline{\varphi}_j}{2},\frac{2r}{r\pm\sqrt{r^2+\overline{z}_k^2}},-\frac{4r^2}{\overline{z}_k^2}\right)$ | $\cdots$ |
|---|---|---|---|---|---|---|---|
| $H_{r,r_i}^{z_k,\varphi_j}$ | $\cdots$ | $0$ | $0$ | $-\frac{\sin\theta_M\cos\overline{\varphi}_M\operatorname{sign}\overline{z}_k\overline{z}_k^2}{2r^2}$ | $\frac{\sin\theta_M\cos\overline{\varphi}_M\operatorname{sign}\overline{z}_k\left(2r^2+\overline{z}_k^2\right)}{2r^2}$ | $0$ | |
| $H_{r,\varphi_j}^{r_i,z_k}$ | $\cdots$ | $0$ | $-\sin\theta_M\sin\overline{\varphi}_{Mj}\sin\overline{\varphi}_j$ | $0$ | $0$ | $0$ | |
| $H_{r,z_k}^{r_i,\varphi_j}$ | $\cdots$ | $\frac{\cos\theta_M\overline{z}_k}{r}$ | $0$ | $\frac{\cos\theta_M|\overline{z}_k|}{r}$ | $-\frac{\cos\theta_M\left(2r^2+\overline{z}_k^2\right)}{r|\overline{z}_k|}$ | $-\frac{\cos\theta_M\left(\sqrt{r^2+\overline{z}_k^2}\mp r\right)\left(r\pm\sqrt{r^2+\overline{z}_k^2}\right)^2}{r|\overline{z}_k|\sqrt{r^2+\overline{z}_k^2}}$ | $\cdots$ |
| $H_{\varphi,r_i}^{z_k,\varphi_j}$ | $\cdots$ | $0$ | $0$ | $\frac{\sin\theta_M\sin\overline{\varphi}_M\operatorname{sign}\overline{z}_k\overline{z}_k^2}{2r^2}$ | $-\frac{\sin\theta_M\sin\overline{\varphi}_M\operatorname{sign}\overline{z}_k\left(4r^2+\overline{z}_k^2\right)}{2r^2}$ | $0$ | |
| $H_{\varphi,\varphi_j}^{z_k,r_i}$ | $\cdots$ | $0$ | $-\sin\theta_M\sin\overline{\varphi}_{Mj}\cos\overline{\varphi}_j$ | $0$ | $0$ | $0$ | |
| $H_{z,r_i}^{z_k,\varphi_j}$ | $\cdots$ | $0$ | $0$ | $\frac{\sin\theta_M\cos\overline{\varphi}_M|\overline{z}_k|}{r}$ | $-\frac{\sin\theta_M\cos\overline{\varphi}_M\left(2r^2+\overline{z}_k^2\right)}{r|\overline{z}_k|}$ | $0$ | |
| $H_{z,z_k}^{r_i,\varphi_j}$ | $\cdots$ | $0$ | $0$ | $0$ | $0$ | $\cos\theta_M\operatorname{sign}\overline{z}_k$ | |

| | | $\Pi\left(\operatorname{Sc}\left(\overline{\varphi}_j,\frac{\sqrt{4r^2+\overline{z}_k^2}}{|\overline{z}_k|}\right),1-\frac{\overline{z}_k^4}{\left(4r^2+\overline{z}_k^2\right)\left(r\pm\sqrt{r^2+\overline{z}_k^2}\right)^2},\frac{4r^2}{4r^2+\overline{z}_k^2}\right)$ |
|---|---|---|
| $H_{r,z_k}^{r_i,\varphi_j}$ | $\cdots$ | $\pm\frac{\cos\theta_M\overline{z}_k^4}{r\sqrt{\left(r^2+\overline{z}_k^2\right)\left(4r^2+\overline{z}_k^2\right)}\left(r\pm\sqrt{r^2+\overline{z}_k^2}\right)}$ |

Table C.25.: Required functions and corresponding coefficients for $\mathscr{I}=234$.

| | $1$ | $\sqrt{r^2+r_i^2-2rr_i\cos\overline{\varphi}_j+\overline{z}_k^2}$ | $\log\left(r_i-r\cos\overline{\varphi}_j+\sqrt{r^2+r_i^2-2rr_i\cos\overline{\varphi}_j+\overline{z}_k^2}\right)$ | $\text{artanh}\left(\frac{r\cos\overline{\varphi}_j-r_i}{\sqrt{r^2+r_i^2-2rr_i\cos\overline{\varphi}_j+\overline{z}_k^2}}\right)$ | $\cdots$ |
|---|---|---|---|---|---|
| $H_{r,r_i}^{z_k,\varphi_j}$ | $0$ | $-\frac{\sin\theta_M\sin\overline{\varphi}_M\overline{z}_k}{2r^2}$ | $0$ | $0$ | $\cdots$ |
| $H_{r,\varphi_j}^{r_i,z_k}$ | $0$ | $0$ | $0$ | $0$ | $\cdots$ |
| $H_{r,z_k}^{r_i,\varphi_j}$ | $-\cos\theta_M\sin\overline{\varphi}_j$ | $0$ | $\cos\theta_M\sin\overline{\varphi}_j$ | $0$ | $\cdots$ |
| $H_{\varphi,r_i}^{z_k,\varphi_j}$ | $0$ | $-\frac{\sin\theta_M\cos\overline{\varphi}_M\overline{z}_k}{2r^2}$ | $0$ | $0$ | $\cdots$ |
| $H_{\varphi,\varphi_j}^{z_k,r_i}$ | $0$ | $0$ | $0$ | $0$ | $\cdots$ |
| $H_{\varphi,z_k}^{\varphi_j,r_i}$ | $0$ | $\frac{\cos\theta_M}{r}$ | $0$ | $-\cos\theta_M\cos\overline{\varphi}_j$ | |
| $H_{z,r_i}^{z_k,\varphi_j}$ | $0$ | $\frac{\sin\theta_M\sin\overline{\varphi}_M}{r}$ | $0$ | $0$ | $\cdots$ |
| $H_{z,\varphi_j}^{z_k,r_i}$ | $0$ | $0$ | $0$ | $-\sin\theta_M\sin\overline{\varphi}_{Mj}$ | |
| $H_{z,z_k}^{r_i,\varphi_j}$ | $0$ | $0$ | $0$ | $0$ | $\cdots$ |

| | $\cdots$ | $\text{artanh}\left(\frac{\overline{z}_k}{\sqrt{r^2+r_i^2-2rr_i\cos\overline{\varphi}_j+\overline{z}_k^2}}\right)$ | $\arctan\left(\frac{r\sin\overline{\varphi}_j}{\overline{z}_k}\right)$ | $\arctan\left(\frac{\overline{z}_k(r\cos\overline{\varphi}_j-r_i)}{r\sin\overline{\varphi}_j\sqrt{r^2+r_i^2-2rr_i\cos\overline{\varphi}_j+\overline{z}_k^2}}\right)$ | $E\left(\frac{\overline{\varphi}_j}{2},-\frac{4rr_i}{\overline{r}_i^2+\overline{z}_k^2}\right)$ | $F\left(\frac{\overline{\varphi}_j}{2},-\frac{4rr_i}{\overline{r}_i^2+\overline{z}_k^2}\right)$ | $\cdots$ |
|---|---|---|---|---|---|---|---|
| $H_{r,r_i}^{z_k,\varphi_j}$ | $\cdots$ | $\frac{\sin\theta_M\sin\overline{\varphi}_M(r^2-r_i^2)}{2r^2}$ | $0$ | $0$ | $-\frac{\sin\theta_M\cos\overline{\varphi}_M\overline{z}_k\sqrt{\overline{r}_i^2+\overline{z}_k^2}}{2r^2}$ | $\frac{\sin\theta_M\cos\overline{\varphi}_M\overline{z}_k(2r^2+\overline{z}_k^2)}{2r^2\sqrt{\overline{r}_i^2+\overline{z}_k^2}}$ | $\cdots$ |
| $H_{r,\varphi_j}^{r_i,z_k}$ | $\cdots$ | $-\sin\theta_M\sin\overline{\varphi}_{Mj}\cos\overline{\varphi}_j$ | $0$ | $\sin\theta_M\sin\overline{\varphi}_{Mj}\sin\overline{\varphi}_j$ | $0$ | $0$ | |
| $H_{r,z_k}^{r_i,\varphi_j}$ | $\cdots$ | $0$ | $\frac{\cos\theta_M\overline{z}_k}{r}$ | $0$ | $\frac{\cos\theta_M\sqrt{\overline{r}_i^2+\overline{z}_k^2}}{r}$ | $-\frac{\cos\theta_M(r^2+r_i^2+\overline{z}_k^2)}{r\sqrt{\overline{r}_i^2+\overline{z}_k^2}}$ | $\cdots$ |
| $H_{\varphi,r_i}^{z_k,\varphi_j}$ | $\cdots$ | $-\frac{\sin\theta_M\cos\overline{\varphi}_M(r^2+r_i^2)}{2r^2}$ | $0$ | $0$ | $\frac{\sin\theta_M\sin\overline{\varphi}_M\overline{z}_k\sqrt{\overline{r}_i^2+\overline{z}_k^2}}{2r^2}$ | $-\frac{\sin\theta_M\sin\overline{\varphi}_M\overline{z}_k(2r^2+2r_i^2+\overline{z}_k^2)}{2r^2\sqrt{\overline{r}_i^2+\overline{z}_k^2}}$ | $\cdots$ |
| $H_{\varphi,\varphi_j}^{z_k,r_i}$ | $\cdots$ | $\sin\theta_M\sin\overline{\varphi}_{Mj}\sin\overline{\varphi}_j$ | $0$ | $\sin\theta_M\sin\overline{\varphi}_{Mj}\cos\overline{\varphi}_j$ | $0$ | $0$ | |
| $H_{z,r_i}^{z_k,\varphi_j}$ | $\cdots$ | $0$ | $0$ | $0$ | $\frac{\sin\theta_M\cos\overline{\varphi}_M\sqrt{\overline{r}_i^2+\overline{z}_k^2}}{r}$ | $-\frac{\sin\theta_M\cos\overline{\varphi}_M(r^2+r_i^2+\overline{z}_k^2)}{r\sqrt{\overline{r}_i^2+\overline{z}_k^2}}$ | |
| $H_{z,z_k}^{r_i,\varphi_j}$ | $\cdots$ | $0$ | $0$ | $0$ | $0$ | $0$ | $\cdots$ |

| | $\cdots$ | $\Pi\left(\frac{\overline{\varphi}_j}{2},-\frac{4rr_i}{\overline{r}_i^2},-\frac{4rr_i}{\overline{r}_i^2+\overline{z}_k^2}\right)$ | $\Pi\left(\frac{\overline{\varphi}_j}{2},\frac{2r}{r\pm\sqrt{r^2+\overline{z}_k^2}},-\frac{4rr_i}{\overline{r}_i^2+\overline{z}_k^2}\right)$ | $\Pi\left(\text{Sc}\left(\overline{\varphi}_j,\sqrt{\frac{(r+r_i)^2+\overline{z}_k^2}{\overline{r}_i^2+\overline{z}_k^2}}\right),1-\frac{\overline{z}_k^2(\overline{r}_i^2+\overline{z}_k^2)}{((r+r_i)^2+\overline{z}_k^2)(r\pm\sqrt{r^2+\overline{z}_k^2})^2},\frac{4rr_i}{(r+r_i)^2+\overline{z}_k^2}\right)$ |
|---|---|---|---|---|
| $H_{r,r_i}^{z_k,\varphi_j}$ | $\cdots$ | $\frac{\sin\theta_M\cos\overline{\varphi}_M\overline{z}_k(r^2+r_i^2)(r+r_i)}{2r^2\overline{r}_i\sqrt{\overline{r}_i^2+\overline{z}_k^2}}$ | $0$ | $0$ |
| $H_{r,z_k}^{r_i,\varphi_j}$ | $\cdots$ | $0$ | $-\frac{\cos\theta_M\left(\sqrt{r^2+\overline{z}_k^2}\mp r\right)\left(r_i\pm\sqrt{r^2+\overline{z}_k^2}\right)^2}{r\sqrt{\left(r^2+\overline{z}_k^2\right)\left(\overline{r}_i^2+\overline{z}_k^2\right)}}$ | $\pm\frac{\cos\theta_M\overline{z}_k^2(\overline{r}_i^2+\overline{z}_k^2)}{r\sqrt{\left(r^2+\overline{z}_k^2\right)\left((r+r_i)^2+\overline{z}_k^2\right)\left(r\pm\sqrt{r^2+\overline{z}_k^2}\right)}}$ |
| $H_{\varphi,r_i}^{z_k,\varphi_j}$ | $\cdots$ | $\frac{\sin\theta_M\sin\overline{\varphi}_M\overline{z}_k(r+r_i)^2}{2r^2\sqrt{\overline{r}_i^2+\overline{z}_k^2}}$ | $0$ | $0$ |
| $H_{z,z_k}^{r_i,\varphi_j}$ | $\cdots$ | $0$ | $\frac{\cos\theta_M\overline{z}_k\left(r_i\pm\sqrt{r^2+\overline{z}_k^2}\right)}{\sqrt{\overline{r}_i^2+\overline{z}_k^2}\left(r\pm\sqrt{r^2+\overline{z}_k^2}\right)}$ | $0$ |

Table C.26.: Required functions and corresponding coefficients for $\mathscr{I}=235$.

# D. Variational derivatives

Parts of this chapter have been previously published in [167] and have been reproduced with permission of the coauthors and in accordance with the publisher's policy. Content that was not generated by the author of this thesis is explicitly denoted, copyright is held by SSRN.

In general the variational derivative of a function $J(\rho)$ in some direction $\tilde{\rho}$ can be defined via

$$\frac{\delta J}{\delta \rho}(\rho)\tilde{\rho} := \lim_{\varepsilon \to 0} \frac{1}{\varepsilon}\big(J(\rho + \varepsilon\tilde{\rho}) - J(\rho)\big). \tag{D.1}$$

Applying the chain rule for the derivative $\delta J/\delta \rho$ in some direction $\tilde{\rho}$, we get

$$\frac{\delta J}{\delta \rho}(\rho)\tilde{\rho} = \frac{\delta J}{\delta u}\big(u(\rho)\big)\frac{\delta u}{\delta \rho}(\rho)\tilde{\rho} \tag{D.2}$$

and for the second derivative in directions $\tilde{\rho}$ and $\hat{\rho}$ further

$$\frac{\delta^2 J}{\delta \rho^2}(\rho)(\tilde{\rho},\hat{\rho}) = \frac{\delta^2 J}{\delta u^2}\big(u(\rho)\big)\left(\frac{\delta u}{\delta \rho}(\rho)\tilde{\rho}, \frac{\delta u}{\delta \rho}(\rho)\hat{\rho}\right) + \frac{\delta J}{\delta u}\big(u(\rho)\big)\frac{\delta^2 u}{\delta \rho^2}(\rho)(\tilde{\rho},\hat{\rho}) \tag{D.3}$$

How the two remaining derivatives can be calculated, is shown in the following.

## D.1. Derivatives of $u$

Without boundary conditions, the solution of Eq. (6.4) can be written with the Greens function of the Poisson equation [136]

$$G(\mathbf{x}) = -\frac{1}{4\pi\,|\mathbf{x}|} \tag{D.4}$$

as the convolution together the right-hand-side of Eq. (6.4)

$$u = \nabla \cdot \mathbf{M} * G = \nabla \cdot \rho\mathbf{M}_0 * G. \tag{D.5}$$

This representation can be used to calculate the variational derivatives of $u$ explicitly, which are used to determine the behavior of the objective function $J$ in Eq. (6.7). This calculation can be done in a much more general context (soft magnetic case and non-constant magnetization) using the adjoint method [193, 195], anyway we present the simple to understand explicit calculation here for our case.

The first variational derivative $\delta u/\delta \rho(\rho)$ in some direction $\tilde{\rho}$ is then

$$\begin{aligned}
\frac{\delta u}{\delta \rho}(\rho)\tilde{\rho} &= \lim_{\varepsilon \to 0} \frac{1}{\varepsilon}\big(u(\rho + \varepsilon\tilde{\rho}) - u(\rho)\big) \\
&= \lim_{\varepsilon \to 0} \frac{1}{\varepsilon}\big(\nabla \cdot (\rho\mathbf{M}_0 + \varepsilon\tilde{\rho}\mathbf{M}_0) * G - \nabla \cdot \rho\mathbf{M}_0 * G\big) \\
&= \lim_{\varepsilon \to 0} \frac{1}{\varepsilon}\big(\varepsilon\nabla \cdot \tilde{\rho}\mathbf{M}_0 * G\big) \\
&= \big(\nabla \cdot \tilde{\rho}\mathbf{M}_0 * G\big),
\end{aligned} \tag{D.6}$$

and we see that $u(\rho)$ and $\delta u/\delta\rho(\rho)\tilde{\rho}$ have the same representation via Greens function and therefore $u$ and $\delta u/\delta\rho(\rho)$ have to fulfill the same Poisson equation in Eq. (6.4).

The second variational derivative $\delta^2 u/\delta\rho^2(\rho)$ in directions $\tilde{\rho}$ and $\hat{\rho}$ is given by

$$
\begin{aligned}
\frac{\delta^2 u}{\delta\rho^2}(\rho)(\tilde{\rho},\hat{\rho}) &= \lim_{\varepsilon\to 0}\frac{1}{\varepsilon}\left(\frac{\delta u}{\delta\rho}(\rho+\varepsilon\hat{\rho})\tilde{\rho}-\frac{\delta u}{\delta\rho}(\rho)\tilde{\rho}\right) \\
&= \lim_{\varepsilon\to 0}\frac{1}{\varepsilon}\left(\nabla\cdot\tilde{\rho}\mathbf{M}_0 * G - \nabla\cdot\tilde{\rho}\mathbf{M}_0 * G\right) = 0,
\end{aligned}
\tag{D.7}
$$

which is clear, since the $\delta u/\delta\rho(\rho)$ does not depend on $\rho$.

## D.2. Derivatives of $J$

The derivative of $J$ in Eq. (6.7) after $u$ in direction $\tilde{u}$ and can be written as

$$
\frac{\delta J}{\delta u}(u)\tilde{u} = \int\left(\frac{\partial\mathscr{F}}{\partial u}\tilde{u}+\frac{\partial\mathscr{F}}{\partial\nabla u}\nabla\tilde{u}+\frac{\partial\mathscr{F}}{\partial\mathscr{H}u}\mathscr{H}\tilde{u}\right)\,d\mathbf{x}.
\tag{D.8}
$$

In the second derivative, all mixed derivatives also have to be considered and we obtain

$$
\begin{aligned}
\frac{\delta^2 J}{\delta u^2}(u)(\tilde{u},\hat{u}) = \int\Bigg( &\frac{\partial^2\mathscr{F}}{\partial u^2}(\tilde{u},\hat{u})+\frac{\partial^2\mathscr{F}}{\partial\nabla u^2}(\nabla\tilde{u},\nabla\hat{u})+\frac{\partial^2\mathscr{F}}{\partial\mathscr{H}u^2}(\mathscr{H}\tilde{u},\mathscr{H}\hat{u})+ \\
&\frac{\partial^2\mathscr{F}}{\partial u\partial\nabla u}(\nabla\tilde{u},\hat{u})+\frac{\partial^2\mathscr{F}}{\partial\nabla u\partial\mathscr{H}u}(\mathscr{H}\tilde{u},\nabla\hat{u})+\frac{\partial^2\mathscr{F}}{\partial\mathscr{H}u\partial u}(\tilde{u},\mathscr{H}\hat{u})+ \\
&\frac{\partial^2\mathscr{F}}{\partial\nabla u\partial u}(\tilde{u},\nabla\hat{u})+\frac{\partial^2\mathscr{F}}{\partial\mathscr{H}u\partial\nabla u}(\nabla\tilde{u},\mathscr{H}\hat{u})+\frac{\partial^2\mathscr{F}}{\partial u\partial\mathscr{H}u}(\mathscr{H}\tilde{u},\hat{u})\Bigg)\,d\mathbf{x}.
\end{aligned}
\tag{D.9}
$$

For the usual case that the second derivative is calculated in a single direction, i.e. $\tilde{u}=\hat{u}$, we obtain

$$
\begin{aligned}
\frac{\delta^2 J}{\delta u^2}(u)(\tilde{u},\tilde{u}) = \int\Bigg( &\frac{\partial^2\mathscr{F}}{\partial u^2}(\tilde{u},\tilde{u})+\frac{\partial^2\mathscr{F}}{\partial\nabla u^2}(\nabla\tilde{u},\nabla\tilde{u})+\frac{\partial^2\mathscr{F}}{\partial\mathscr{H}u^2}(\mathscr{H}\tilde{u},\mathscr{H}\tilde{u})+ \\
&2\frac{\partial^2\mathscr{F}}{\partial\nabla u\partial u}(\tilde{u},\nabla\tilde{u})+2\frac{\partial^2\mathscr{F}}{\partial\mathscr{H}u\partial\nabla u}(\nabla\tilde{u},\mathscr{H}\tilde{u})+2\frac{\partial^2\mathscr{F}}{\partial\mathscr{H}u\partial u}(\tilde{u},\mathscr{H}\tilde{u})\Bigg)\,d\mathbf{x}.
\end{aligned}
\tag{D.10}
$$

## D.3. Convexity

For the investigation of local and global minima, the objective function $J$ can be examined about convexity. It is previously discussed e.g. in [237]. For that, we use the following three mathematical theorems [238]:

**Theorem 1.** *Let $J$ be convex, i.e. its domain is a convex set and for every $\rho_1,\rho_2$ and $\lambda\in(0,1)$, it holds*

$$
J\big((1-\lambda)\rho_1+\lambda\rho_2\big)\leq(1-\lambda)J(\rho_1)+\lambda J(\rho_2).
\tag{D.11}
$$

*Then any local minimum of $J$ is a global minimum.*

**Theorem 2.** *Let $J$ be strict convex, i.e. the assumptions of Theorem 1 hold with $<$ instead of $\leq$ in Eq. (D.11). Then there exists a unique local minimum of $J$, which is also a global minimum.*

**Theorem 3.** *Let the domain of J be a convex set and for every $\rho$ and $\tilde{\rho}(\neq 0)$ we assume*

$$\frac{\delta^2 J}{\delta \rho^2}(\rho)(\tilde{\rho},\tilde{\rho}) \geq (>) \, 0. \tag{D.12}$$

*Then J is (strict) convex.*

Since Eq. (D.11) is usually not so easy to directly verify, the circumstances under which Eq. (D.12) holds can be seen expressing Eq. (D.3) with the results of the previous subsections in the form

$$\frac{\delta^2 J}{\delta \rho^2}(\rho)(\tilde{\rho},\tilde{\rho}) = \frac{\delta^2 J}{\delta u^2}\big(u(\rho)\big)\left(\nabla \cdot \tilde{\rho} \mathbf{M}_0 * G, \nabla \cdot \tilde{\rho} \mathbf{M}_0 * G\right). \tag{D.13}$$

A sufficient condition for Eq. (D.12) is therefore

$$\frac{\delta^2 J}{\delta u^2}(u)(\tilde{u},\tilde{u}) \geq 0 \tag{D.14}$$

for all $u,\tilde{u}$, what is a reasonable criterion for the investigation of convexity for simple choices of $\mathscr{F}$.

## D.4. Concavity

Concavity is in a way exactly the opposite of convexity of the previous subsection, since a function $J$ is called concave, if and only if $-J$ is convex. The following Theorem also makes this property very interesting in terms of optimization:

**Theorem 4.** *Let J be concave on a cuboid domain. Then every local minimum of the function lies at a corner of the domain.*

The basis of this theorem is that corners are the only points in the domain, which do not lie on a line between two other points of the domain (see Fig. D.1). For points on a line, concavity then implies that the value of the objective function is always smaller in at least one of the endpoints of the line. Therefore the only local minima could lie in the corners. This result is especially useful after the discretization of $\rho$, where the continuous function transforms to finitely many $\rho_i \in [0,1]$ and the domain of $J$ is a finite-dimensional unit cube.

In the case of a concave objective function, the binary states therefore cover already all local (and therefore also global) minima of the non-binary case. Therefore a binary algorithm as described in Subsec. 6.4.2 makes sense, but it is unfortunately still not guaranteed that the global minimum can be found with the algorithm as discussed in F.1 on the example of the concave objective function Eq. (F.1) illustrated in Fig. F.1.

## D.5. Examples for objective functions

For some common objective functions, the second derivative is calculated and the convexity/concavity is denoted in Tab. D.1.
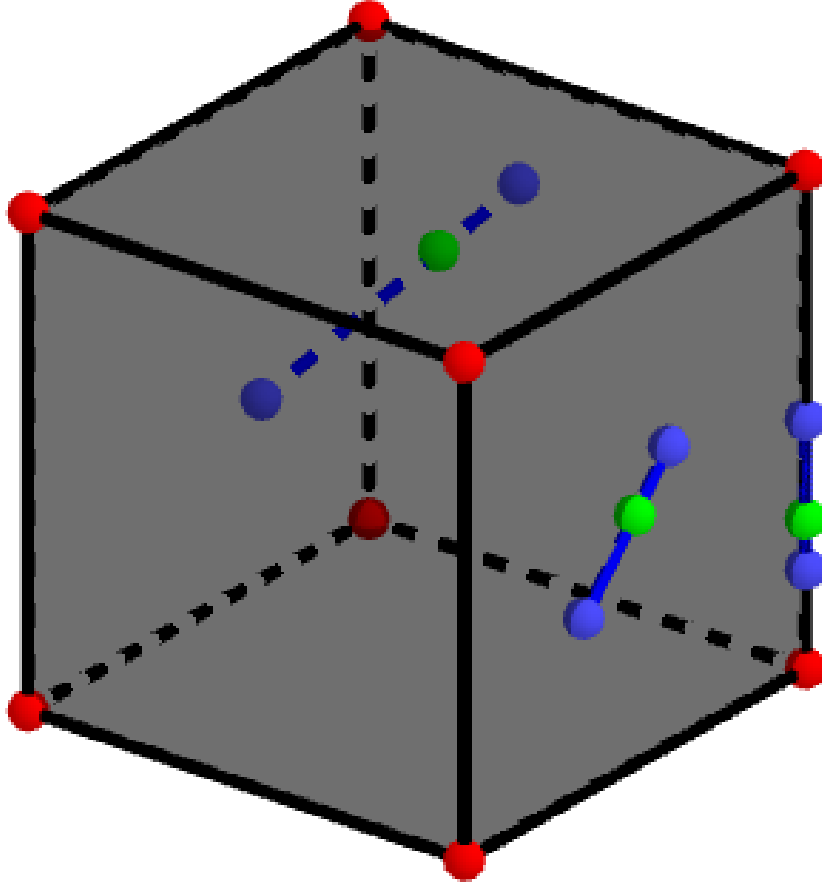
Figure D.1.: Illustration of a cuboid domain. The green points indicate that each point, except of the red corner points, lie always on the line between two other points of the domain.

| use case | $J(u)$ | $\frac{\delta^2 J}{\delta u^2}(u)(\tilde{u},\tilde{u})$ | property |
|---|---|---|---|
| max field component | $-\int_{\Omega_t} \partial_i u \, \mathrm{d}\mathbf{x}$ | $0$ | convex & concave |
| max derivative of field component | $-\int_{\Omega_t} \partial_i \partial_j u \, \mathrm{d}\mathbf{x}$ | $0$ | convex & concave |
| max field strength | $-\int_{\Omega_t} |\nabla u|^2 \, \mathrm{d}\mathbf{x}$ | $-2\int_{\Omega_t} |\nabla\tilde{u}|^2 \, \mathrm{d}\mathbf{x} \leq 0$ | concave |
| target field $\mathbf{H}_0$ | $\int_{\Omega_t} |-\nabla u - \mathbf{H}_0|^2 \, \mathrm{d}\mathbf{x}$ | $2\int_{\Omega_t} |\nabla\tilde{u}|^2 \, \mathrm{d}\mathbf{x} \geq 0$ | convex |
| max field gradient | $-\int_{\Omega_t} |\mathscr{H}u|^2 \, \mathrm{d}\mathbf{x}$ | $-2\int_{\Omega_t} |\mathscr{H}\tilde{u}|^2 \, \mathrm{d}\mathbf{x} \leq 0$ | concave |
| max field strength and gradient | $-\int_{\Omega_t} |\nabla u|^2|\mathscr{H}u|^2 \, \mathrm{d}\mathbf{x}$ | $-2\int_{\Omega_t} \big( |\nabla u|^2|\mathscr{H}\tilde{u}|^2 + |\nabla\tilde{u}|^2|\mathscr{H}u|^2 + 4\nabla u\nabla\tilde{u}\mathscr{H}u\mathscr{H}\tilde{u}\big) \, \mathrm{d}\mathbf{x} \leq 0$ | — |

Table D.1.: Common objective functions in applications with their properties.

# E. Local minima

In this section, we demonstrate that multiple minima in a magnetic topology optimization problem are easily present in already simple toy examples. Moreover, we discuss assumptions on the problem, that would in principle avoid the presence of multiple local minima and guarantee a unique local (i.e. global) minimum.

Therefore we first consider the objective function

$$J(\rho) = -\int_{\Omega_t} H_x(\rho)^2 \, \mathrm{d}\mathbf{x} \longrightarrow \min. \tag{E.1}$$

for an alignment of in Fig. E.1.

We assume that the magnets left and right to the target region with magnetic material densities $\rho_1, \rho_2$ result in (mean) field contributions $\mathbf{H}_1(\rho_1) = H_1 \rho_1 \mathbf{e}_x$ and $\mathbf{H}_2(\rho_2) = -H_2 \rho_2 \mathbf{e}_x$ with maximum field strengths $H_1 > H_2 > 0$ in $\Omega_t$. Inserting in the objective function Eq. (E.1) yields

$$J(\rho_1, \rho_2) = -(H_1 \rho_1 - H_2 \rho_2)^2 \Delta_{xyz}, \tag{E.2}$$

with the volume $\Delta_{xyz}$, which is assumed to be sufficiently small so that it is legit to insert just the mean field contributions. A typical graph of this function is shown in Fig. E.2.

We see that this function has two local minima, in which always one of the cells is fully magnetized and the other one is empty. This is intuitively clear considering Fig. E.1 since due to the magnetization in opposite directions, the resulting magnetic field is partly compensating for each other. Since the squared $H_x$-component in the objective function in Eq. (E.1) only measures the field direction and not the sign, both magnets can curse a local minimum, whereas only $\rho_1 = 1$ and $\rho_2 = 0$ yields in a global minimum, due to the stronger magnetization of the left magnet.
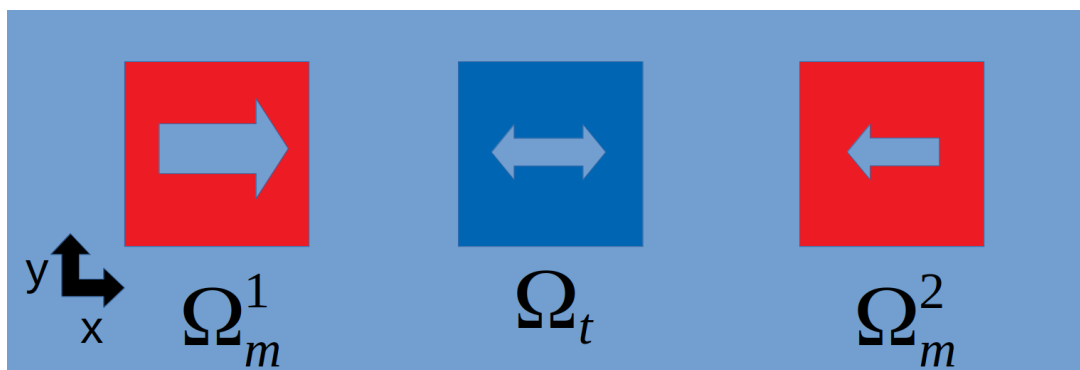


Figure E.1.: Alignment of the magnetic region $\Omega_m$ and the target region $\Omega_t$ with a simple discretization. The arrows show the magnetization direction $\mathbf{m}$ in $\Omega_m$ and the relevant field directions for the objective function in $\Omega_t$. The larger arrow in the left part of $\Omega_m$ indicated a stronger magnetization.
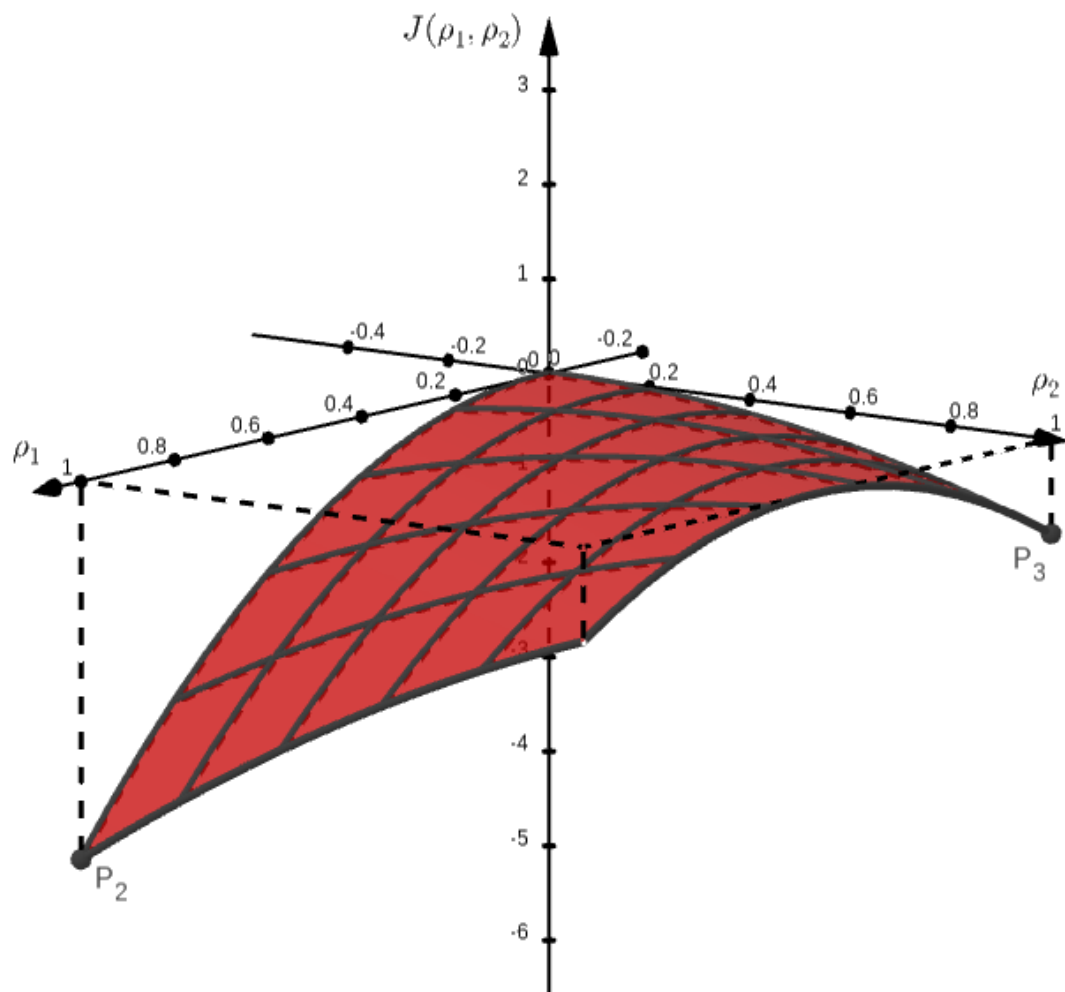
Figure E.2.: Graph of the objective function Eq. (E.2) for $H_1 = 2\,\text{A/m}, H_2 = 1\,\text{A/m}$ and $\Delta_{xyz} = 1\,\text{m}^3$. We observe two local minima in $P_2$ and $P_3$ for the configurations $(\rho_1 = 1, \rho_2 = 0)$ and $(\rho_1 = 0, \rho_2 = 1)$.

We see that even in this easy geometry, a local optimizing algorithm might probably converge to the wrong local and therefore miss the global minimum.

# F. Example for wrong convergence of the algorithm

In this section, we analyze the behavior of the BSA from Subsec. 6.4.2 in more detail. In particular, we consider the behavior of the gradient-assisted discrete optimization steps illustrated in the sub-image of Fig. 6.2 and the impact on the resulting "local" minima described in Subsec. 6.4.2.

We therefore assume an example analytic objective function $J$ in only two variables $\rho_1, \rho_2$ for all the following subsections and discuss the convergence behavior of the BSA using these examples. In the binary framework, only the four different states $(\rho_1, \rho_2) \in \{(0,0), (1,0), (0,1), (1,1)\}$ are possible. Depending on the analytical form of the function, the algorithm shows different behavior.

## F.1. No iteration

First, we consider the function

$$J_1(\rho_1, \rho_2) := -\left(\rho_1 - \frac{2}{3}\right)^2 - \left(\rho_2 - \frac{2}{3}\right)^2 \tag{F.1}$$

illustrated in Fig. F.1. Although there is a single global minimum $(0,0)$, every other point is also a local minimum, and the algorithm would terminate immediately in any of the initial configurations. This example clearly shows a very serious problem of gradient-based discrete optimization, namely that the derivative can also indicate the wrong direction due to the unconsidered gap between the boundary values 0 and 1. It is difficult to estimate how likely such configurations are for more complicated objective functions with more than two variables, however, the global optimization part of the algorithm is also based on trying new random configurations, so compared to a pure BSA, it is at least ensured that other initial configurations are also used and their function values are compared. To still overcome this problem, a tunneling approach within the algorithm could also be considered [219]. Then the agent could also be configured to continue the search path even if the derivatives indicate degradation.

## F.2. Unique local minimum

Consider the function

$$J_2(\rho_1, \rho_2) := \left(\rho_1 - \frac{2}{3}\right)^4 + \left(\rho_2 - \frac{2}{3}\right)^2 \tag{F.2}$$

illustrated in Fig. F.2.

It is clear that a global minimum is always also a local minimum in the sense of the algorithm in Subsec. 6.4.2 since in each iteration step the function values are compared and the steps are updated only
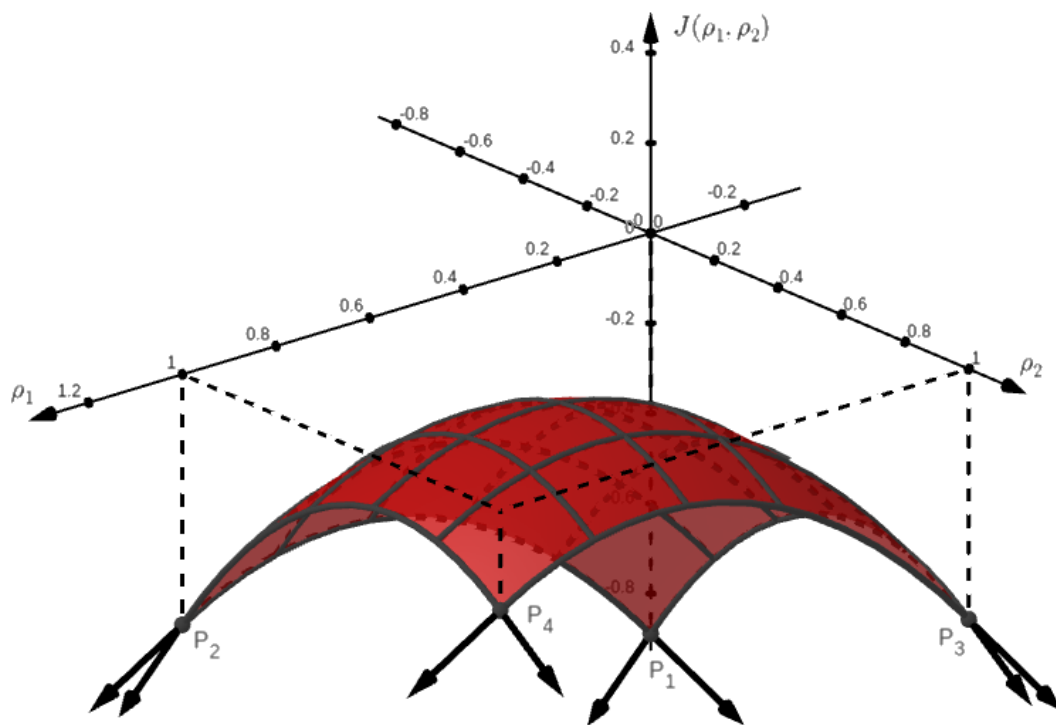
Figure F.1.: Graph of the function $J_1$. All four binary states in the corners are local minima in the sense of the algorithm in Subsec. 6.4.2, since the partial derivatives always indicate a local increase of the objective function (represented by arrows).
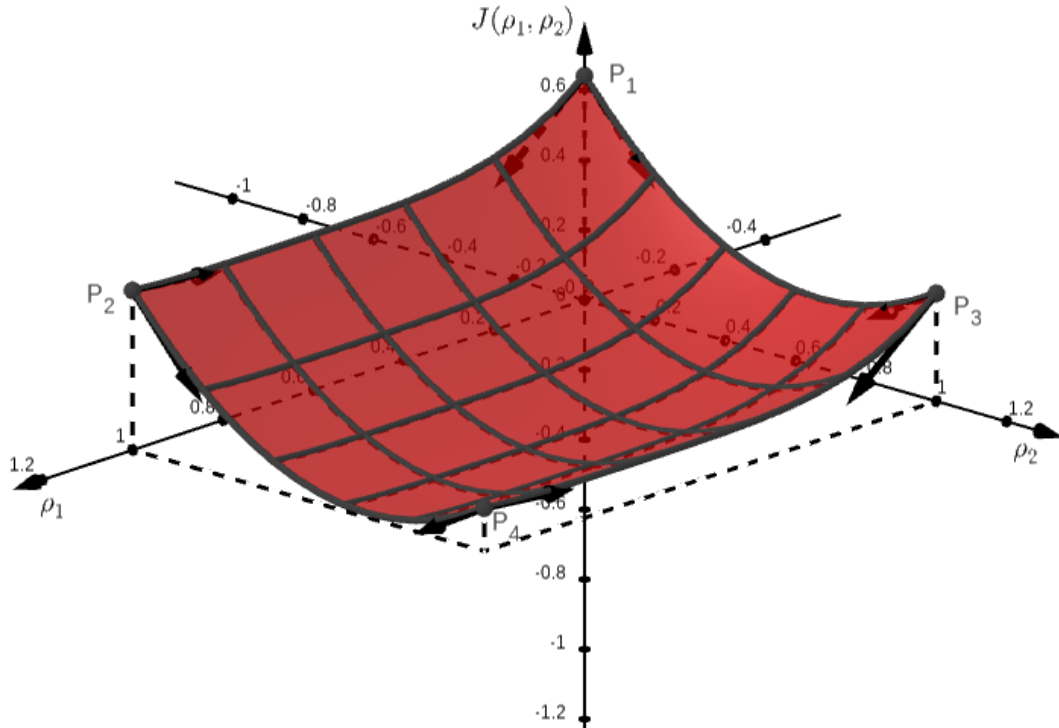
Figure F.2.: Graph of the function $J_2$. The global minimum $(1, 1)$ in $P_4$ of this function is also the only local minimum for a good choice of parameters $p$ and $f$.

when the objection function value decreases. Therefore, the iteration will always end at $(1, 1)$ when this point is reached. Whether this is the case depends on the local optimization parameters chosen. Since $p$ denotes the ratio of cells $\rho_i$ that may be changed within the iteration step, only the values $p = 1$ (both cells $\rho_1$ and $\rho_2$ may be changed), $p = 0.5$ (only one cell, with the steeper derivative, may be changed), and $p = 0$ (no cell is changed, i.e., the algorithm terminates) come into question in this simple model example. Looking at the arrows in Fig. F.2, we see that the local behavior in each of the four vertices indicates a necessary change in the values of the two variables $\rho_1$ and $\rho_2$. When $p = 1$, a change between $P_1 \leftrightarrow P_4$ and $P_2 \leftrightarrow P_3$ is always sought. However, when comparing the function values, only the change $P_1 \rightarrow P_4$ and $P_2 \rightarrow P_3$ happens. From $P_3$ on, after the unsuccessful attempt to change to $P_2$, there is still the possibility that the correction factor $0 < f < 1$ has reduced $p$ to a value $1 > p \geq 0.5$, so that only one variable is changed. In this case, the direction with the steeper derivative is always taken, which is $\rho_1$ in our test function (see arrows in Fig. F.2). This means that even in this case the algorithm would eventually reach $P_4$. However, if either $f$ is too small, so that $p$ is reduced too much, or the $\rho_2$ direction might have had a steeper descent relative to the $\rho_1$ direction ($P_1$ would not be reached anyway because of the comparison of function values), then $P_3$ would denote another local minimum to the global minimum $P_4$. If $0.5 \leq p < 1$ is already chosen at the beginning of each iteration step, then the algorithm has two unique paths: $P_1 \rightarrow P_3 \rightarrow P_4$ and $P_2 \rightarrow P_4$ So in this case there is no local minimum in addition to $P_4$. However, as above, there would be one in $P_3$ if the direction of $\rho_1$ had a steeper slope. This example is intended to show how the situation of local minima can change with slightly different optimization parameters. In a real optimization with many more variables, such unpredictable edge cases can occur much more frequently, which underlines the importance of using a hybrid optimization approach to start from different positions and also to choose the local optimization parameters with care. In particular, a high value of $f \approx 1$ can reduce $p$ more slowly and thus provides more chances to achieve a successful
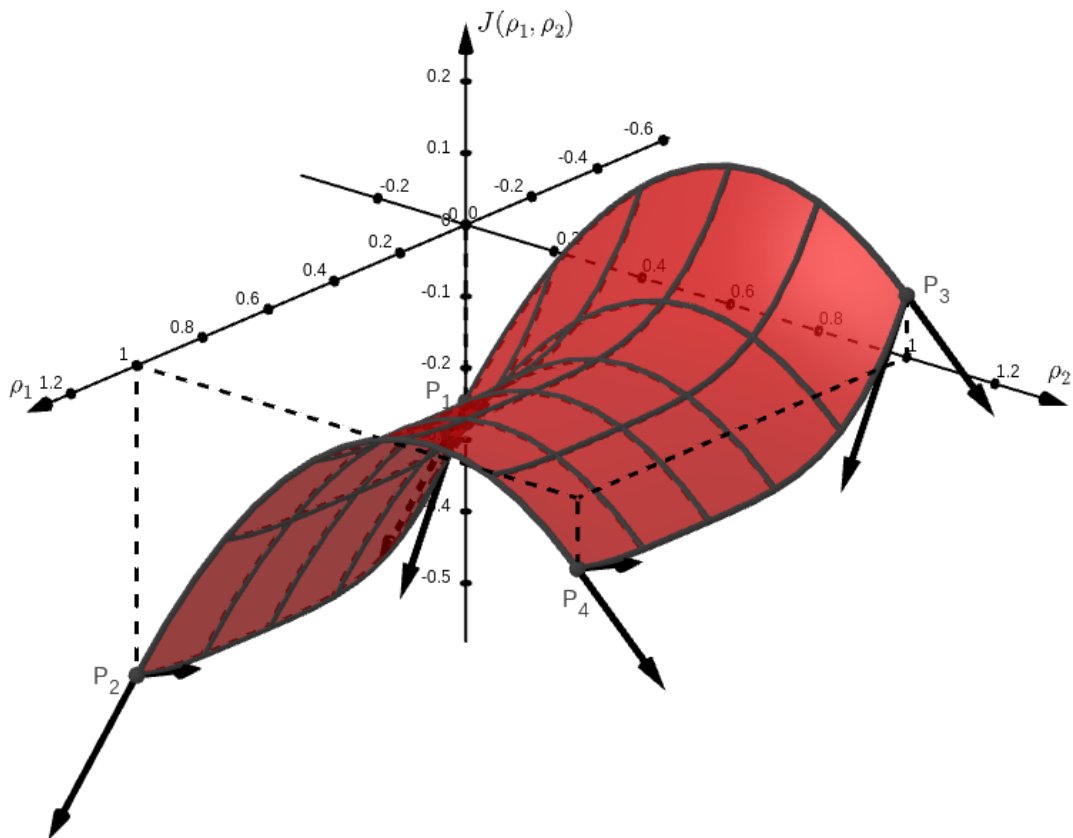
Figure F.3.: Graph of the function $J_3$. Depending on the start value, there are two local minima $P_2$ and $P_4$, where the algorithm tends to finish for $p \geq 0.5$.

reduction of the objective function. Furthermore, we see that comparing the derivative in different directions can also be misleading.

## F.3. Reduction in one variable

Consider the function

$$J_3(\rho_1, \rho_2) := \left( \rho_1 - \frac{2}{3} \right)^4 - \left( \rho_2 - \frac{2}{3} \right)^2 \tag{F.3}$$

illustrated in Fig. F.3.

In contrast to the two previous example functions, the saddle form of $J_3$ has only one descending direction for all vertices. This means that even for $p = 1$ at most one variable is changed. As seen in Fig. F.3, the iteration paths are $P_1 \leftrightarrow P_2$ and $P_3 \leftrightarrow P_4$. Comparing the function values leads to the local minima $P_2$ and $P_4$. Similar to App. F.1, in this case, the non-global minimum $P_4$ cannot be avoided by adjusting the parameters, since a step in a direction where the derivative has the wrong sign is forbidden in the algorithm. Again, an approach as in [219] would be required.

# G. Mesh-fineness-dependency of the objective function

Parts of this chapter have been previously published in [167] and have been reproduced with permission of the coauthors and in accordance with the publisher's policy. Content that was not generated by the author of this thesis is explicitly denoted, copyright is held by SSRN.

In this section, we briefly discuss why a finer discretization does not automatically imply a better global minimum of the objective function $J$. The reason is the different discretization in the target region $\Omega_t$. This behavior depends on the shape of the objective function, which we will also demonstrate.

For simplicity, we assume a cubic target region as shown in Fig. G.1 with a single-cell discretization (see Fig. G.1a) and an eight-cell subdivision (see Fig. G.1b).

Assume now to aim a minimum field $x$-component within this region for any reason. The optimization functional could be written as

$$J(\rho) = \int_{\Omega_t} H_x(\rho)^2 \, \mathrm{d}\mathbf{x} \longrightarrow \min. \tag{G.1}$$

In finite difference codes, the volume integration over a region is usually discretized as a sum over the individual cells multiplied by the volume of the elements. Therefore, for the different fineness, we observe

$$J^{\mathrm{coarse}}(\rho) = \Delta_{xyz} \cdot H_x^{\mathrm{coarse}}(\rho)^2, \tag{G.2}$$

$$J^{\mathrm{fine}}(\rho) = \frac{\Delta_{xyz}}{8} \cdot \sum_{i=1}^{8} H_x^{\mathrm{fine},i}(\rho)^2. \tag{G.3}$$

Let us now assume for simplicity that the optimal solution of the fine resolution leads to a configuration where four of the cells have a positive field component $H_0 > 0$ and the other four cells have a negative field component $-H_0 < 0$, i. e., $H_x^{\mathrm{fine},i}(\rho_{\mathrm{opt}}) = H_0$ for $i = 1, \ldots, 4$ and $H_x^{\mathrm{fine},i}(\rho_{\mathrm{opt}}) = -H_0$ for $i = 5, \ldots, 8$. The corresponding minimized objective function then gives $J^{\mathrm{fine}}(\rho_{\mathrm{opt}}) = \Delta_{xyz} H_0^2 > 0$. The same field, according to the formulas of [239], would lead to $H_x^{\mathrm{coarse}}(\rho_{\mathrm{opt}}) = 0$ and $J^{\mathrm{coarse}}(\rho_{\mathrm{opt}}) = 0$, since the field is simply averaged over the entire volume.

This shows why a coarse discretization in the target region can also lead to better values of the objective function, even though the resolution of the geometry in the magnetic region $\Omega_m$ is worse (see also Tab. 6.2). This apparent paradox results only from the larger discretization error of the integral in the objective function and, of course, does not represent a real improvement of the optimized geometry.

Although we have used a somewhat simpler analytic example for illustration, it is also obvious that especially in the case of gradients in the objective function (see, e.g., Eq. (6.8)), field averaging over larger volumes also significantly reduces the field oscillations and thus reduces the obtained gradient.
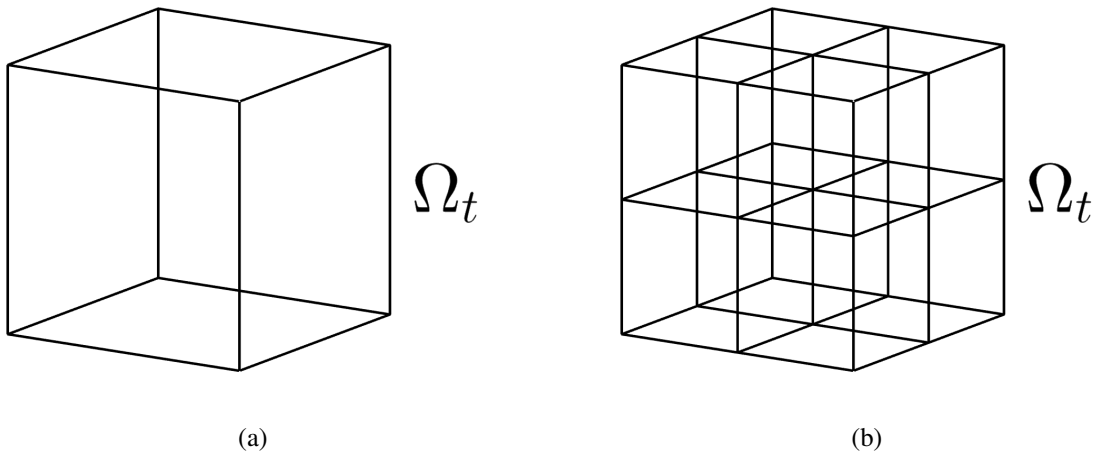
Figure G.1.: Cubic target cell with simple discretization by a single cell (a) and eight subcells (b).

# H. Symmetry of the solution

In the discrete binary setting, a certain symmetry of the regions and the objective function does not guarantee the same symmetry in the solution. We show this with a simple example and discuss the consequences.

To clarify what we mean by some symmetry in the optimization problem: For any choice of $\rho$, the symmetry operation (rotation, mirroring, etc.) must not change the value of the objective function $J(\rho)$.

Let us examine the two-dimensional arrangement shown in Fig. H.1. The corresponding objective function for the optimization on the target field $\mathbf{H}_0 = H_0 \mathbf{e}_x$ can be chosen as.

$$J(\rho) = \int_{\Omega_t} \left( H_x(\rho) - H_0 \right)^2 \, \mathrm{d}\mathbf{x} \longrightarrow \min. \tag{H.1}$$

It is obvious that this problem is symmetric in the $y$-direction since any reflection in the $y$ direction also implies a reflection of $H_x$ in the target region, but the total value of the integral in $J$ is not affected.

However, let us consider the simple two-cell discretization in $\Omega_m$ and the one-cell discretization of $\Omega_t$ in Fig. H.1 and further assume that the magnetization of each cell would produce the (mean) magnetic field $x$-component $H_0$ in the target region. Then we observe the following target function values for all four possible $\rho$ configurations:

$$J(0,0) = \Delta_{xy}(0 - H_0)^2 = \Delta_{xy}H_0^2 \tag{H.2}$$

$$J(1,0) = \Delta_{xy}(H_0 - H_0)^2 = 0 \tag{H.3}$$

$$J(0,1) = \Delta_{xy}(H_0 - H_0)^2 = 0 \tag{H.4}$$

$$J(1,1) = \Delta_{xy}(2H_0 - H_0)^2 = \Delta_{xy}H_0^2 \tag{H.5}$$

This means that both states where one magnetic cell is filled and one is empty are both global minima, but both solutions have no reflection symmetry in the $y$-component.
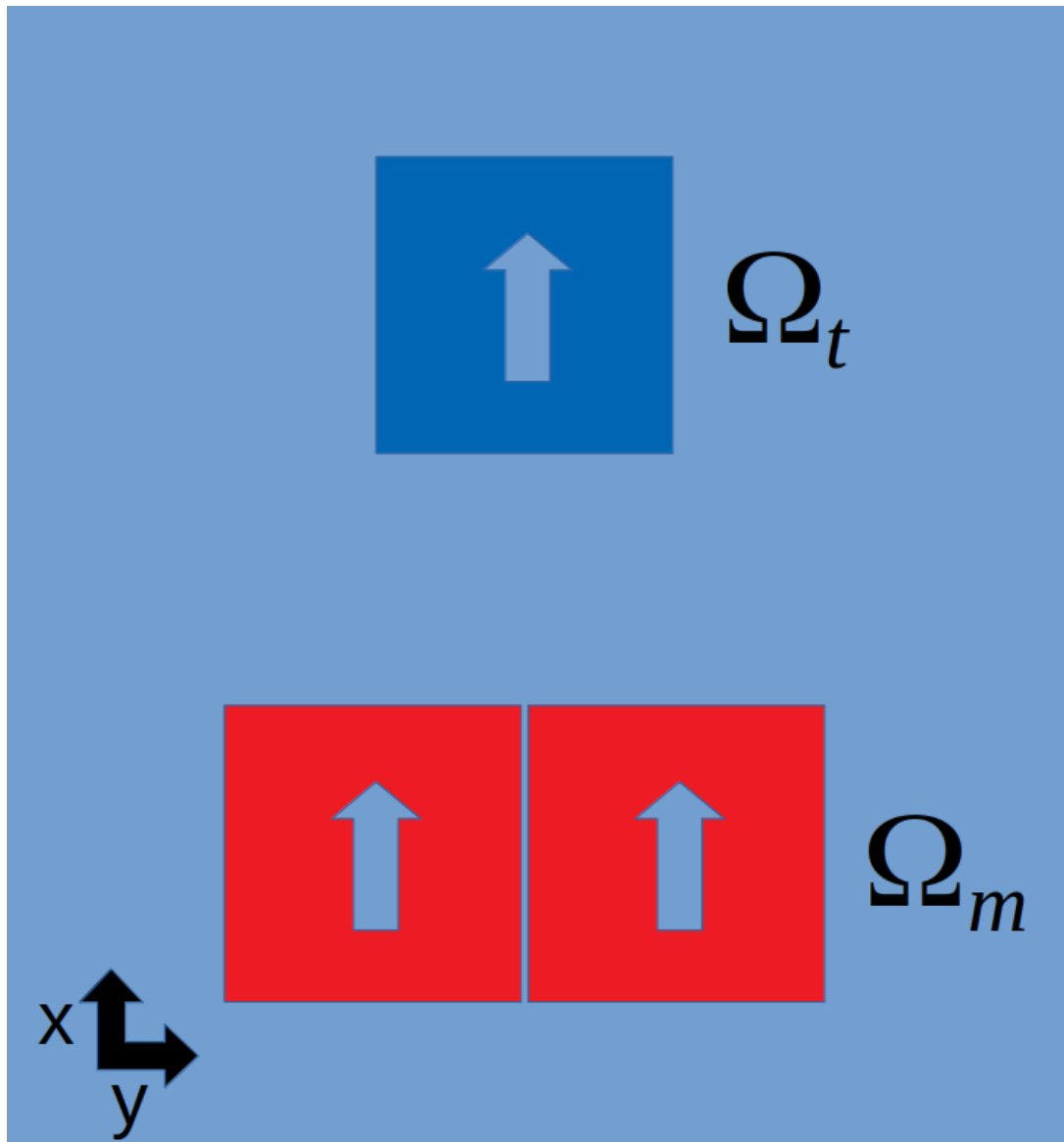
Figure H.1.: Alignment of the magnetic region $\Omega_m$ and the target region $\Omega_t$ with a simple dicecretization. The arrows show the magnetization direction **m** in $\Omega_m$ and the target field $\mathbf{H}_0 = H_0\mathbf{e}_x$ in $\Omega_t$.

# I. Supplementary data

We provide a Python3 implementation of the formulas derived in Chap. 4 for calculating the magnetic field of a cylinder tile as supplementary material of the open-access publication [84].

# J. List of publications

1. Dieter Suess et al. "Spin Torque Efficiency and Analytic Error Rate Estimates of Skyrmion Racetrack Memory". In: *Scientific Reports* 9.1 (Mar. 2019). DOI: 10.1038/s41598-019-41062-y

2. O. Muthsam et al. "Improving the signal-to-noise ratio for heat-assisted magnetic recording by optimizing a high/low Tc bilayer structure". In: *Journal of Applied Physics* 126.12 (Sept. 2019), p. 123907. DOI: 10.1063/1.5119407

3. Florian Slanovc et al. "Systematic parameterization of heat-assisted magnetic recording switching probabilities and the consequences for the resulting SNR". in: *Journal of Applied Physics* 126.21 (Dec. 2019), p. 213901. DOI: 10.1063/1.5119415

4. Florian Slanovc et al. "Statistical analysis of read-back signals in magnetic recording on granular media". In: *AIP Advances* 10.1 (Jan. 2020), p. 015307. DOI: 10.1063/1.5130418

5. O. Muthsam et al. "The superior role of the Gilbert damping on the signal-to-noise ratio in heat-assisted magnetic recording". In: *Journal of Magnetism and Magnetic Materials* 514 (Nov. 2020), p. 167125. DOI: 10.1016/j.jmmm.2020.167125

6. Sabri Koraltan et al. "Dependence of energy barrier reduction on collective excitations in square artificial spin ice: A comprehensive comparison of simulation techniques". In: *Physical Review B* 102.6 (Aug. 2020), p. 064410. DOI: 10.1103/physrevb.102.064410

7. Perla Malagò et al. "Magnetic Position System Design Method Applied to Three-Axis Joystick Motion Tracking". In: *Sensors* 20.23 (Dec. 2020), p. 6873. DOI: 10.3390/s20236873

8. Naëmi Leo et al. "Chiral switching and dynamic barrier reductions in artificial square ice". In: *New Journal of Physics* 23.3 (Mar. 2021), p. 033024. DOI: 10.1088/1367-2630/abe3ad

9. Sabri Koraltan et al. "Tension-free Dirac strings and steered magnetic charges in 3D artificial spin ice". In: *npj Computational Materials* 7.1 (Aug. 2021). DOI: 10.1038/s41524-021-00593-7

10. Gregor Wautischer et al. "A topology optimization algorithm for magnetic structures based on a hybrid FEM–BEM method utilizing the adjoint approach". In: *Scientific Reports* 12.1 (Jan. 2022). DOI: 10.1038/s41598-021-04246-z

11. Dieter Suess, Florian Slanovc and Udo Ausserlechner. "Comment to the paper "A new Hall-effect enabled voltage amplifier device based on magnetic and thermal properties of materials"". In: *Journal of Magnetism and Magnetic Materials* 547 (Apr. 2022), p. 168942. DOI: 10.1016/j.jmmm.2021.168942

12. Dieter Suess et al. *Accurate finite-difference micromagnetics of magnets including RKKY interaction – analytical solution and comparison to standard micromagnetic codes.* 2022. DOI: 10.48550/ARXIV.2206.11063

13. Florian Slanovc, Dieter Suess and Michael Ortner. "Designing Airgap-Stable Magnetic Linear Position Systems". In: *IEEE Transactions on Magnetics* 58.9 (Sept. 2022), pp. 1–5. DOI: 10.1109/tmag.2022.3188474

14. Claas Abert et al. "Origin of noncollinear magnetization coupling across RuX layers". In: *Physical Review B* 106.5 (Aug. 2022), p. 054401. DOI: 10.1103/physrevb.106.054401

15. F. Slanovc et al. "Full analytical solution for the magnetic field of uniformly magnetized cylinder tiles". In: *Journal of Magnetism and Magnetic Materials* 559 (Oct. 2022), p. 169482. DOI: 10.1016/j.jmmm.2022.169482

16. Florian Slanovc et al. "Global magnetic topology optimization". English. In: *SSRN eLibrary* (2022)

# Bibliography

[1]  D.R. Fredkin and T.R. Koehler. "Hybrid method for computing demagnetizing fields". In: *IEEE Transactions on Magnetics* 26.2 (Mar. 1990), pp. 415–417. DOI: 10.1109/20.106342.

[2]  Yi Liu, David J. Sellmyer and Daisuke Shindo. *Handbook of Advanced Magnetic Materials*. Springer US, Nov. 2005. 1864 pp. ISBN: 1402079834. URL: https://www.ebook.de/de/product/4480483/handbook_of_advanced_magnetic_materials.html.

[3]  I.A. Abrikosov et al. "Recent progress in simulations of the paramagnetic state of magnetic materials". In: *Current Opinion in Solid State and Materials Science* 20.2 (Apr. 2016), pp. 85–106. DOI: 10.1016/j.cossms.2015.07.003.

[4]  A. V. Chumak et al. "Roadmap on Spin-Wave Computing". In: *IEEE Transactions on Magnetics* (2022), pp. 1–1. DOI: 10.1109/tmag.2022.3149664.

[5]  J. Hellsvik et al. "Dynamics of diluted magnetic semiconductors from atomistic spin-dynamics simulations: Mn-doped GaAs". In: *Physical Review B* 78.14 (Oct. 2008), p. 144419. DOI: 10.1103/physrevb.78.144419.

[6]  B Skubic et al. "A method for atomistic spin dynamics simulations: implementation and examples". In: *Journal of Physics: Condensed Matter* 20.31 (July 2008), p. 315203. DOI: 10.1088/0953-8984/20/31/315203.

[7]  Pui-Wai Ma and S. L. Dudarev. "Longitudinal magnetic fluctuations in Langevin spin dynamics". In: *Physical Review B* 86.5 (Aug. 2012), p. 054416. DOI: 10.1103/physrevb.86.054416.

[8]  R F L Evans et al. "Atomistic spin model simulations of magnetic nanomaterials". In: *Journal of Physics: Condensed Matter* 26.10 (Feb. 2014), p. 103202. DOI: 10.1088/0953-8984/26/10/103202.

[9]  Xiankai Jiao, Zongzhi Zhang and Yaowen Liu. "Modeling of Temperature Dependence of Magnetization in TbFe Films — An Atomistic Spin Simulation Study". In: *SPIN* 06.01 (Mar. 2016), p. 1650003. DOI: 10.1142/s201032471650003x.

[10] P. Hohenberg and W. Kohn. "Inhomogeneous Electron Gas". In: *Physical Review* 136.3B (Nov. 1964), B864–B871. DOI: 10.1103/physrev.136.b864.

[11] G. Kresse and J. Hafner. "Ab initiomolecular dynamics for liquid metals". In: *Physical Review B* 47.1 (Jan. 1993), pp. 558–561. DOI: 10.1103/physrevb.47.558.

[12] V. P. Antropov et al. "*Ab Initio* Spin Dynamics in Magnets". In: *Physical Review Letters* 75.4 (July 1995), pp. 729–732. DOI: 10.1103/physrevlett.75.729.

[13] G. Kresse and J. Furthmüller. "Efficient iterative schemes for *ab initio* total-energy calculations using a plane-wave basis set". In: *Physical Review B* 54.16 (Oct. 1996), pp. 11169–11186. DOI: 10.1103/physrevb.54.11169.

[14] V. P. Antropov et al. "Spin dynamics in magnets: Equation of motion and finite temperature effects". In: *Physical Review B* 54.2 (July 1996), pp. 1019–1035. DOI: 10.1103/physrevb.54.1019.

[15]    J. Hafner and G. Kresse. "The Vienna AB-Initio Simulation Program VASP: An Efficient and Versatile Tool for Studying the Structural, Dynamic, and Electronic Properties of Materials". In: *Properties of Complex Inorganic Solids*. Springer US, 1997, pp. 69–82. DOI: `10.1007/978-1-4615-5943-6_10`.

[16]    Jürgen Hafner. "*Ab-initio* simulations of materials using VASP: Density-functional theory and beyond". In: *Journal of Computational Chemistry* 29.13 (Oct. 2008), pp. 2044–2078. DOI: `10.1002/jcc.21057`.

[17]    Kieron Burke. "Perspective on density functional theory". In: *The Journal of Chemical Physics* 136.15 (Apr. 2012), p. 150901. DOI: `10.1063/1.4704546`.

[18]    D.A Garanin. "Generalized equation of motion for a ferromagnet". In: *Physica A: Statistical Mechanics and its Applications* 172.3 (Apr. 1991), pp. 470–491. DOI: `10.1016/0378-4371(91)90395-s`.

[19]    D. A. Garanin. "Fokker-Planck and Landau-Lifshitz-Bloch equations for classical ferromagnets". In: *Physical Review B* 55.5 (Feb. 1997), pp. 3050–3057. DOI: `10.1103/physrevb.55.3050`.

[20]    O. Chubykalo-Fesenko et al. "Dynamic approach for micromagnetics close to the Curie temperature". In: *Physical Review B* 74.9 (Sept. 2006), p. 094436. DOI: `10.1103/physrevb.74.094436`.

[21]    U. Atxitia et al. "Micromagnetic modeling of laser-induced magnetization dynamics using the Landau-Lifshitz-Bloch equation". In: *Applied Physics Letters* 91.23 (Dec. 2007), p. 232507. DOI: `10.1063/1.2822807`.

[22]    U. Atxitia, P. Nieves and O. Chubykalo-Fesenko. "Landau-Lifshitz-Bloch equation for ferrimagnetic materials". In: *Physical Review B* 86.10 (Sept. 2012), p. 104414. DOI: `10.1103/physrevb.86.104414`.

[23]    R. F. L. Evans et al. "Stochastic form of the Landau-Lifshitz-Bloch equation". In: *Physical Review B* 85.1 (Jan. 2012), p. 014433. DOI: `10.1103/physrevb.85.014433`.

[24]    Lei Xu and Shufeng Zhang. "Self-consistent Bloch equation and Landau-Lifshitz-Bloch equation of ferromagnets: A comparison". In: *Journal of Applied Physics* 113.16 (Apr. 2013), p. 163911. DOI: `10.1063/1.4803150`.

[25]    Christoph Vogler et al. "Landau-Lifshitz-Bloch equation for exchange-coupled grains". In: *Physical Review B* 90.21 (Dec. 2014), p. 214431. DOI: `10.1103/physrevb.90.214431`.

[26]    R. Hertel and H. Kronmuller. "Adaptive finite element mesh refinement techniques in three-dimensional micromagnetic modeling". In: *IEEE Transactions on Magnetics* 34.6 (1998), pp. 3922–3930. DOI: `10.1109/20.728305`.

[27]    M. J. Donahue and D. G. Porter. *in Interagency Report NISTIR 6376 (National Institute of Standards and Technology, Gaithersburg, MD)*. 1999.

[28]    Josef Fidler and Thomas Schrefl. "Micromagnetic modelling - the current state of the art". In: *Journal of Physics D: Applied Physics* 33.15 (July 2000), R135–R156. DOI: `10.1088/0022-3727/33/15/201`.

[29]    Werner Scholz, Thomas Schrefl and Josef Fidler. "Micromagnetic simulation of thermally activated switching in fine particles". In: *Journal of Magnetism and Magnetic Materials* 233.3 (Aug. 2001), pp. 296–304. DOI: `10.1016/s0304-8853(01)00032-4`.

[30]    Xiao-Ping Wang, Carlos J. Garcia-Cervera and Weinan E. "A Gauss–Seidel Projection Method for Micromagnetics Simulations". In: *Journal of Computational Physics* 171.1 (July 2001), pp. 357–372. DOI: `10.1006/jcph.2001.6793`.

[31] Kai-Zhong Gao and H.N. Bertram. "Write field analysis and write pole design in perpendicular recording". In: *IEEE Transactions on Magnetics* 38.5 (Sept. 2002), pp. 3521–3527. DOI: 10.1109/tmag.2002.802744.

[32] Werner Scholz et al. "Scalable parallel micromagnetic solvers for magnetic nanostructures". In: *Computational Materials Science* 28.2 (Oct. 2003), pp. 366–383. DOI: 10.1016/s0927-0256(03)00119-8.

[33] N. Popović and D. Praetorius. "Applications of -Matrix Techniques in Micromagnetics". In: *Computing* 74.3 (Dec. 2004), pp. 177–204. DOI: 10.1007/s00607-004-0098-7.

[34] Carsten Carstensen and Dirk Praetorius. "Effective simulation of a macroscopic model for stationary micromagnetics". In: *Computer Methods in Applied Mechanics and Engineering* 194.2-5 (Feb. 2005), pp. 531–548. DOI: 10.1016/j.cma.2004.05.019.

[35] Thomas Fischbacher et al. "A Systematic Approach to Multiphysics Extensions of Finite-Element-Based Micromagnetic Simulations: Nmag". In: *IEEE Transactions on Magnetics* 43.6 (June 2007), pp. 2896–2898. DOI: 10.1109/tmag.2007.893843.

[36] Y. Kanai et al. "Landau–Lifshitz–Gilbert Micromagnetic Analysis of Single-Pole-Type Write Head for Perpendicular Magnetic Recording Using Full-FFT Program on PC Cluster System". In: *IEEE Transactions on Magnetics* 44.6 (June 2008), pp. 1602–1605. DOI: 10.1109/tmag.2007.916254.

[37] K M Lebecki, M J Donahue and M W Gutowski. "Periodic boundary conditions for demagnetization interactions in micromagnetic simulations". In: *Journal of Physics D: Applied Physics* 41.17 (Aug. 2008), p. 175005. DOI: 10.1088/0022-3727/41/17/175005.

[38] B. Van de Wiele et al. "Finite-Difference and Edge Finite-Element Approaches for Dynamic Micromagnetic Modeling". In: *IEEE Transactions on Magnetics* 44.11 (Nov. 2008), pp. 3137–3140. DOI: 10.1109/tmag.2008.2001601.

[39] J. W. Lau, R. D. McMichael and M. J. Donahue. "Implementation of Two-Dimensional Polycrystalline Grains in Object Oriented Micromagnetic Framework". In: *NIST J. Res.* 114.1 (2009), pp. 57–67. DOI: 10.6028/jres.114.005.

[40] Attila Kakay, Elmar Westphal and Riccardo Hertel. "Speedup of FEM Micromagnetic Simulations With Graphical Processing Units". In: *IEEE Transactions on Magnetics* 46.6 (June 2010), pp. 2303–2306. DOI: 10.1109/tmag.2010.2048016.

[41] R. Chang et al. "FastMag: Fast micromagnetic simulator for complex magnetic structures (invited)". In: *Journal of Applied Physics* 109.7 (Apr. 2011), p. 07D358. DOI: 10.1063/1.3563081.

[42] A. Vansteenkiste and B. Van de Wiele. "MuMax: A new high-performance micromagnetic simulation tool". In: *Journal of Magnetism and Magnetic Materials* 323.21 (Nov. 2011), pp. 2585–2591. DOI: 10.1016/j.jmmm.2011.05.037.

[43] Petra Goldenits, Dirk Praetorius and Dieter Suess. "Convergent geometric integrator for the Landau-Lifshitz-Gilbert equation in micromagnetics". In: *PAMM* 11.1 (Dec. 2011), pp. 775–776. DOI: 10.1002/pamm.201110376.

[44] Claas Abert et al. "A Fast Finite-Difference Method for Micromagnetics Using the Magnetic Scalar Potential". In: *IEEE Transactions on Magnetics* 48.3 (Mar. 2012), pp. 1105–1109. DOI: 10.1109/tmag.2011.2172806.

[45] L Lopez-Diaz et al. "Micromagnetic simulations using Graphics Processing Units". In: *Journal of Physics D: Applied Physics* 45.32 (July 2012), p. 323001. DOI: 10.1088/0022-3727/45/32/323001.

[46]  M. Dvornik, Y. Au and V. V. Kruglyak. "Micromagnetic Simulations in Magnonics". In: *Topics in Applied Physics*. Springer Berlin Heidelberg, Aug. 2012, pp. 101–115. DOI: 10.1007/978-3-642-30247-3_8.

[47]  Florian Bruckner et al. "Combining micromagnetism and magnetostatic Maxwell equations for multiscale magnetic simulations". In: *Journal of Magnetism and Magnetic Materials* 343 (Oct. 2013), pp. 163–168. DOI: 10.1016/j.jmmm.2013.04.085.

[48]  Claas Abert et al. "magnum.fe: A micromagnetic finite-element simulation code based on FEniCS". In: *Journal of Magnetism and Magnetic Materials* 345 (Nov. 2013), pp. 29–35. DOI: 10.1016/j.jmmm.2013.05.051.

[49]  F. Bruckner et al. "Multiscale modeling in micromagnetics: Existence of solutions and numerical integration". In: *Mathematical Models and Methods in Applied Sciences* 24.13 (Sept. 2014), pp. 2627–2662. DOI: 10.1142/s0218202514500328.

[50]  Arne Vansteenkiste et al. "The design and verification of MuMax3". In: *AIP Advances* 4.10 (Oct. 2014), p. 107133. DOI: 10.1063/1.4899186.

[51]  Claas Abert et al. "A three-dimensional spin-diffusion model for micromagnetics". In: *Scientific Reports* 5.1 (Oct. 2015). DOI: 10.1038/srep14855.

[52]  M. Aurada, J.M. Melenk and D. Praetorius. "FEM–BEM coupling for the large-body limit in micromagnetics". In: *Journal of Computational and Applied Mathematics* 281 (June 2015), pp. 10–31. DOI: 10.1016/j.cam.2014.11.042.

[53]  Claas Abert et al. "A self-consistent spin-diffusion model for micromagnetics". In: *Scientific Reports* 6.1 (Dec. 2016). DOI: 10.1038/s41598-016-0019-y.

[54]  D Kumar and A O Adeyeye. "Techniques in micromagnetic simulation and analysis". In: *Journal of Physics D: Applied Physics* 50.34 (July 2017), p. 343001. DOI: 10.1088/1361-6463/aa7c04.

[55]  J Leliaert et al. "Fast micromagnetic simulations on GPU—recent advances made with mumax$^3$". In: *Journal of Physics D: Applied Physics* 51.12 (Feb. 2018), p. 123002. DOI: 10.1088/1361-6463/aaab1c.

[56]  J. Leliaert and J. Mulkers. "Tomorrow's micromagnetic simulations". In: *Journal of Applied Physics* 125.18 (May 2019), p. 180901. DOI: 10.1063/1.5093730.

[57]  Carl-Martin Pfeiler et al. "Computational micromagnetics with Commics". In: *Computer Physics Communications* 248 (Mar. 2020), p. 106965. DOI: 10.1016/j.cpc.2019.106965.

[58]  Giovanni Di Fratta, Michael Innerberger and Dirk Praetorius. "Weak–strong uniqueness for the Landau–Lifshitz–Gilbert equation in micromagnetics". In: *Nonlinear Analysis: Real World Applications* 55 (Oct. 2020), p. 103122. DOI: 10.1016/j.nonrwa.2020.103122.

[59]  R. Bjørk et al. "MagTense: A micromagnetic framework using the analytical demagnetization tensor". In: *Journal of Magnetism and Magnetic Materials* 535 (Oct. 2021), p. 168057. DOI: 10.1016/j.jmmm.2021.168057.

[60]  Michael Bartsch et al. "Solution of Maxwell's equations". In: *Computer Physics Communications* 73.1-3 (Dec. 1992), pp. 22–39. DOI: 10.1016/0010-4655(92)90026-u.

[61]  J. M. Hyman and M. Shashkov. "Mimetic Finite Difference Methods for Maxwell's Equations and the Equations of Magnetic Diffusion". In: *Progress In Electromagnetics Research* 32 (2001), pp. 89–121. DOI: 10.2528/pier00080104.

[62]  Florian Bruckner et al. "3D FEM–BEM-coupling method to solve magnetostatic Maxwell equations". In: *Journal of Magnetism and Magnetic Materials* 324.10 (May 2012), pp. 1862–1866. DOI: 10.1016/j.jmmm.2012.01.016.

[63] Florian Slanovc et al. "Statistical analysis of read-back signals in magnetic recording on granular media". In: *AIP Advances* 10.1 (Jan. 2020), p. 015307. DOI: 10.1063/1.5130418.

[64] CA Ross. "Patterned Magnetic Recording Media". In: *Annual Review of Materials Research* 31.1 (Aug. 2001), pp. 203–235. DOI: 10.1146/annurev.matsci.31.1.203.

[65] Yukiko Kubota et al. "Heat-Assisted Magnetic Recording's Extensibility to High Linear and Areal Density". In: *IEEE Transactions on Magnetics* 54.11 (Nov. 2018), pp. 1–6. DOI: 10.1109/tmag.2018.2851973.

[66] Gaspare Varvaro and Casoli Francesca. *Ultra-High-Density Magnetic Recording*. Taylor & Francis Ltd., Mar. 2016. 544 pp. ISBN: 9814669598. URL: https://www.ebook.de/de/product/25901932/ultra_high_density_magnetic_recording.html.

[67] M.H. Kryder et al. "Heat Assisted Magnetic Recording". In: *Proceedings of the IEEE* 96.11 (Nov. 2008), pp. 1810–1835. DOI: 10.1109/jproc.2008.2004315.

[68] H. J. Richter et al. "Recording potential of bit-patterned media". In: *Applied Physics Letters* 88.22 (May 2006), p. 222512. DOI: 10.1063/1.2209179.

[69] Christoph Vogler et al. "Heat-assisted magnetic recording of bit-patterned media beyond 10 Tb/in2". In: *Applied Physics Letters* 108.10 (Mar. 2016), p. 102406. DOI: 10.1063/1.4943629.

[70] Stephanie Hernandez et al. "Using Ensemble Waveform Analysis to Compare Heat Assisted Magnetic Recording Characteristics of Modeled and Measured Signals". In: *IEEE Transactions on Magnetics* 53.2 (Feb. 2017), pp. 1–6. DOI: 10.1109/tmag.2016.2612230.

[71] Yipeng Jiao, Yao Wang and R. H. Victora. "A Study of SNR and BER in Heat-Assisted Magnetic Recording". In: *IEEE Transactions on Magnetics* 51.11 (Nov. 2015), pp. 1–4. DOI: 10.1109/tmag.2015.2451135.

[72] Jian-Gang Zhu and Hai Li. "Understanding Signal and Noise in Heat Assisted Magnetic Recording". In: *IEEE Transactions on Magnetics* 49.2 (Feb. 2013), pp. 765–772. DOI: 10.1109/tmag.2012.2231855.

[73] Jian-Gang (Jimmy) Zhu and Hai Li. "Write head field design for correcting transition curvature in heat assisted magnetic recording". In: *AIP Advances* 7.5 (Feb. 2017), p. 056505. DOI: 10.1063/1.4976733.

[74] Jian-Gang Jimmy Zhu and Hai Li. "Correcting Transition Curvature in Heat-Assisted Magnetic Recording". In: *IEEE Transactions on Magnetics* 53.2 (Feb. 2017), pp. 1–7. DOI: 10.1109/tmag.2016.2614836.

[75] Kenichi Takano. "Readback Spatial Sensitivity Function by Reciprocity Principle and Media Readback Flux". In: *IEEE Transactions on Magnetics* 49.7 (July 2013), pp. 3818–3821. DOI: 10.1109/tmag.2012.2236542.

[76] Florian Slanovc et al. "Systematic parameterization of heat-assisted magnetic recording switching probabilities and the consequences for the resulting SNR". In: *Journal of Applied Physics* 126.21 (Dec. 2019), p. 213901. DOI: 10.1063/1.5119415.

[77] Christoph Vogler et al. "Areal density optimizations for heat-assisted magnetic recording of high-density media". In: *Journal of Applied Physics* 119.22 (June 2016), p. 223903. DOI: 10.1063/1.4953390.

[78] O. Muthsam, C. Vogler and D. Suess. "Noise reduction in heat-assisted magnetic recording of bit-patterned media by optimizing a high/low Tc bilayer structure". In: *Journal of Applied Physics* 122.21 (Dec. 2017), p. 213903. DOI: 10.1063/1.5004244.

[79]  Y. Peng et al. "Heat Assisted Magnetic Recording on High Anisotropy Nanocomposite Media". In: *2008 8th IEEE Conference on Nanotechnology*. IEEE, Aug. 2008. DOI: `10.1109/nano.2008.180`.

[80]  Bernard Dieny et al. "Impact of Intergrain Spin-Transfer Torques Due to Huge Thermal Gradients in Heat-Assisted Magnetic Recording". In: *IEEE Transactions on Magnetics* 54.12 (Dec. 2018), pp. 1–11. DOI: `10.1109/tmag.2018.2863225`.

[81]  O. Muthsam et al. "Improving the signal-to-noise ratio for heat-assisted magnetic recording by optimizing a high/low Tc bilayer structure". In: *Journal of Applied Physics* 126.12 (Sept. 2019), p. 123907. DOI: `10.1063/1.5119407`.

[82]  Xiaobin Wang, Bogdan Valcu and Nan-Hsiung Yeh. "Transition width limit in magnetic recording". In: *Applied Physics Letters* 94.20 (May 2009), p. 202508. DOI: `10.1063/1.3141455`.

[83]  D. Weller and A. Moser. "Thermal effect limits in ultrahigh-density magnetic recording". In: *IEEE Transactions on Magnetics* 35.6 (1999), pp. 4423–4439. DOI: `10.1109/20.809134`.

[84]  F. Slanovc et al. "Full analytical solution for the magnetic field of uniformly magnetized cylinder tiles". In: *Journal of Magnetism and Magnetic Materials* 559 (Oct. 2022), p. 169482. DOI: `10.1016/j.jmmm.2022.169482`.

[85]  K.J. Strnat. "Modern permanent magnets for applications in electro-technology". In: *Proceedings of the IEEE* 78.6 (June 1990), pp. 923–946. DOI: `10.1109/5.56908`.

[86]  Rob H.J. Fastenau and Evert J. van Loenen. "Applications of rare earth permanent magnets". In: *Journal of Magnetism and Magnetic Materials* 157-158 (May 1996), pp. 1–6. DOI: `10.1016/0304-8853(95)01279-6`.

[87]  Z.J.J. Stekly. "Large scale applications of permanent magnets". In: *IEEE Transactions on Appiled Superconductivity* 10.1 (Mar. 2000), pp. 873–878. DOI: `10.1109/77.828370`.

[88]  J.M.D. Coey. "Permanent magnet applications". In: *Journal of Magnetism and Magnetic Materials* 248.3 (Aug. 2002), pp. 441–456. DOI: `10.1016/s0304-8853(02)00335-9`.

[89]  R.W. McCallum et al. "Practical Aspects of Modern and Future Permanent Magnets". In: *Annual Review of Materials Research* 44.1 (July 2014), pp. 451–477. DOI: `10.1146/annurev-matsci-070813-113457`.

[90]  Satoshi Hirosawa, Masamichi Nishino and Seiji Miyashita. "Perspectives for high-performance permanent magnets: applications, coercivity, and new materials". In: *Advances in Natural Sciences: Nanoscience and Nanotechnology* 8.1 (Mar. 2017), p. 013002. DOI: `10.1088/2043-6254/aa597c`.

[91]  J.M.D. Coey. "Perspective and Prospects for Rare Earth Permanent Magnets". In: *Engineering* 6.2 (Feb. 2020), pp. 119–131. DOI: `10.1016/j.eng.2018.11.034`.

[92]  Perla Malagò et al. "Magnetic Position System Design Method Applied to Three-Axis Joystick Motion Tracking". In: *Sensors* 20.23 (Dec. 2020), p. 6873. DOI: `10.3390/s20236873`.

[93]  C.P.O Treutler. "Magnetic sensors for automotive applications". In: *Sensors and Actuators A: Physical* 91.1-2 (June 2001), pp. 2–6. DOI: `10.1016/s0924-4247(01)00621-5`.

[94]  Udo Ausserlechner, Armin Satz and Ferdinand Gastinger. "Magnetic position sensors, systems and methods". English. U.S. pat. 8717010. May 2014.

[95]  R. I. Joseph and E. Schlömann. "Demagnetizing Field in Nonellipsoidal Bodies". In: *Journal of Applied Physics* 36.5 (May 1965), pp. 1579–1593. DOI: `10.1063/1.1703091`.

[96]     A. Smith et al. "The demagnetizing field of a nonuniform rectangular prism". In: *Journal of Applied Physics* 107.10 (May 2010), p. 103910. DOI: 10.1063/1.3385387.

[97]     J. Prat-Camps et al. "Exact Analytical Demagnetizing Factors for Long Hollow Cylinders in Transverse Field". In: *IEEE Magnetics Letters* 3 (2012), pp. 0500104–0500104. DOI: 10.1109/lmag.2012.2198617.

[98]     J. M. Camacho and V Sosa. "Alternative method to calculate the magnetic field of permanent magnets with azimuthal symmetry". en. In: *Revista mexicana de fisica E* 59 (June 2013), pp. 8–17. ISSN: 1870-3542. URL: http://www.scielo.org.mx/scielo.php?script=sci_arttext&pid=S1870-35422013000100002&nrm=iso.

[99]     Alessio Caciagli et al. "Exact expression for the magnetic field of a finite cylinder with arbitrary uniform magnetization". In: *Journal of Magnetism and Magnetic Materials* 456 (June 2018), pp. 423–432. DOI: 10.1016/j.jmmm.2018.02.003.

[100]    Norman Derby and Stanislaw Olbert. "Cylindrical magnets and ideal solenoids". In: *American Journal of Physics* 78.3 (Mar. 2010), pp. 229–235. DOI: 10.1119/1.3256157.

[101]    E.P. Furlani, S. Reznik and A. Kroll. "A three-dimensional field solution for radially polarized cylinders". In: *IEEE Transactions on Magnetics* 31.1 (Jan. 1995), pp. 844–851. DOI: 10.1109/20.364587.

[102]    R. Ravaud et al. "Cylindrical Magnets and Coils: Fields, Forces, and Inductances". In: *IEEE Transactions on Magnetics* 46.9 (Sept. 2010), pp. 3585–3590. DOI: 10.1109/tmag.2010.2049026.

[103]    John T. Conway. "Inductance Calculations for Circular Coils of Rectangular Cross Section and Parallel Axes Using Bessel and Struve Functions". In: *IEEE Transactions on Magnetics* 46.1 (Jan. 2010), pp. 75–81. DOI: 10.1109/tmag.2009.2026574.

[104]    JP Selvaggi, SJ Salon and MVK Chari. "Computing the Magnetic Induction Field Due to a Radially Magnetized Finite Cylindrical Permanent Magnet by Employing Toroidal Harmonics". In: *Progress In Electromagnetics Research* 245 (2010).

[105]    Tomohiro Taniguchi. "An analytical computation of magnetic field generated from a cylinder ferromagnet". In: *Journal of Magnetism and Magnetic Materials* 452 (Apr. 2018), pp. 464–472. DOI: 10.1016/j.jmmm.2017.11.078.

[106]    Michael Ortner and Lucas Gabriel Coliado Bandeira. "Magpylib: A free Python package for magnetic field computation". In: *SoftwareX* 11 (Jan. 2020), p. 100466. DOI: 10.1016/j.softx.2020.100466.

[107]    J. W. Jansen et al. "Overview of Analytical Models for the Design of Linear and Planar Motors". In: *IEEE Transactions on Magnetics* 50.11 (Nov. 2014), pp. 1–7. DOI: 10.1109/tmag.2014.2328556.

[108]    Michael Ortner. "Improving magnetic linear position measurement by field shaping". In: *2015 9th International Conference on Sensing Technology (ICST)*. IEEE, Dec. 2015. DOI: 10.1109/icsenst.2015.7438423.

[109]    Michael Ortner, Marcelo Ribeiro and Dietmar Spitzer. "Absolute Long-Range Linear Position System With a Single 3-D Magnetic Field Sensor". In: *IEEE Transactions on Magnetics* 55.1 (Jan. 2019), pp. 1–4. DOI: 10.1109/tmag.2018.2870597.

[110]    Michael Galea et al. "Demagnetization Analysis for Halbach Array Configurations in Electrical Machines". In: *IEEE Transactions on Magnetics* 51.9 (Sept. 2015), pp. 1–9. DOI: 10.1109/tmag.2015.2429645.

[111]  Z J Yang et al. "Potential and force between a magnet and a bulk Y1Ba2Cu3O7-$\delta$ superconductor studied by a mechanical pendulum". In: *Superconductor Science and Technology* 3.12 (Dec. 1990), pp. 591–597. DOI: 10.1088/0953-2048/3/12/004.

[112]  R. Engel-Herbert and T. Hesjedal. "Calculation of the magnetic stray field of a uniaxial magnetic domain". In: *Journal of Applied Physics* 97.7 (Apr. 2005), p. 074504. DOI: 10.1063/1.1883308.

[113]  O. Chadebec, J.-L. Coulomb and F. Janet. "A review of magnetostatic moment method". In: *IEEE Transactions on Magnetics* 42.4 (Apr. 2006), pp. 515–520. DOI: 10.1109/tmag.2006.870929.

[114]  Andre Drews et al. *magnum.fd - A finite-difference/fft package for the solution of dynamical micromagnetic problems.* 2013.

[115]  Paul Heistracher et al. "Hybrid FFT algorithm for fast demagnetization field calculations on non-equidistant magnetic layers". In: *Journal of Magnetism and Magnetic Materials* 503 (June 2020), p. 166592. DOI: 10.1016/j.jmmm.2020.166592.

[116]  Claas Abert et al. "A full-fledged micromagnetic code in fewer than 70 lines of NumPy". In: *Journal of Magnetism and Magnetic Materials* 387 (Aug. 2015), pp. 13–18. DOI: 10.1016/j.jmmm.2015.03.081.

[117]  Christian Huber et al. "3D Printing of Polymer-Bonded Rare-Earth Magnets With a Variable Magnetic Compound Fraction for a Predefined Stray Field". In: *Scientific Reports* 7.1 (Aug. 2017). DOI: 10.1038/s41598-017-09864-0.

[118]  Nicolas Dupré et al. "Experimental Demonstration of Stray-Field Immunity beyond 5 mT for an Automotive-Grade Rotary Position Sensor". In: *EUROSENSORS 2018*. MDPI, Dec. 2018. DOI: 10.3390/proceedings2130763.

[119]  Udo Ausserlechner. "CLOSED ANALYTICAL FORMULAE FOR MULTI-POLE MAGNETIC RINGS". In: *Progress In Electromagnetics Research B* 38 (2012), pp. 71–105. DOI: 10.2528/pierb11112606.

[120]  *Requirements for the technical representation of magnetic measurement scales in design drawins, E DIN SPEC 91411:2021-09.* Sept. 2021.

[121]  R. Ravaud et al. "Analytical Calculation of the Magnetic Field Created by Permanent-Magnet Rings". In: *IEEE Transactions on Magnetics* 44.8 (Aug. 2008), pp. 1982–1989. DOI: 10.1109/tmag.2008.923096.

[122]  Romain Ravaud, Guy Lemarquand and Valerie Lemarquand. "MAGNETIC FIELD CREATED BY A UNIFORMLY MAGNETIZED TILE PERMANENT MAGNET". In: *Progress In Electromagnetics Research B* 24 (2010), pp. 17–32. DOI: 10.2528/pierb10062209.

[123]  Romain Ravaud and Guy Lemarquand. "MAGNETIC COUPLINGS WITH CYLINDRICAL AND PLANE AIR GAPS: INFLUENCE OF THE MAGNET POLARIZATION DIRECTION." In: *Progress In Electromagnetics Research B* 16 (2009), pp. 333–349. DOI: 10.2528/pierb09051903.

[124]  R. Ravaud, G. Lemarquand and V. Lemarquand. "Magnetic Field Created by Tile Permanent Magnets". In: *IEEE Transactions on Magnetics* 45.7 (July 2009), pp. 2920–2926. DOI: 10.1109/tmag.2009.2014752.

[125]  Shuang Song et al. "6-D Magnetic Localization and Orientation Method for an Annular Magnet Based on a Closed-Form Analytical Model". In: *IEEE Transactions on Magnetics* 50.9 (Sept. 2014), pp. 1–11. DOI: 10.1109/tmag.2014.2315592.

[126]  K.K. Nielsen and R. Bjørk. "The magnetic field from a homogeneously magnetized cylindrical tile". In: *Journal of Magnetism and Magnetic Materials* 507 (Aug. 2020), p. 166799. DOI: 10.1016/j.jmmm.2020.166799.

[127] Toshio Fukushima. "Precise and Fast Computation of Elliptic Integrals and Functions". In: *2015 IEEE 22nd Symposium on Computer Arithmetic*. IEEE, June 2015. DOI: `10.1109/arith.2015.15`.

[128] Toshio Fukushima. "Fast computation of incomplete elliptic integral of first kind by half argument transformation". In: *Numerische Mathematik* 116.4 (July 2010), pp. 687–719. DOI: `10.1007/s00211-010-0321-8`.

[129] Toshio Fukushima. "Precise and fast computation of a general incomplete elliptic integral of second kind by half and double argument transformations". In: *Journal of Computational and Applied Mathematics* 235.14 (May 2011), pp. 4140–4148. DOI: `10.1016/j.cam.2011.03.004`.

[130] Toshio Fukushima. "Precise and fast computation of a general incomplete elliptic integral of third kind by half and double argument transformations". In: *Journal of Computational and Applied Mathematics* 236.7 (Jan. 2012), pp. 1961–1975. DOI: `10.1016/j.cam.2011.11.007`.

[131] Toshio Fukushima. "Fast computation of complete elliptic integrals and Jacobian elliptic functions". In: *Celestial Mechanics and Dynamical Astronomy* 105.4 (Oct. 2009), pp. 305–328. DOI: `10.1007/s10569-009-9228-z`.

[132] Toshio Fukushima and Hideharu Ishizaki. "Numerical computation of incomplete elliptic integrals of a general form". In: *Celestial Mechanics & Dynamical Astronomy* 59.3 (July 1994), pp. 237–251. DOI: `10.1007/bf00692874`.

[133] Toshio Fukushima. "Precise and fast computation of the general complete elliptic integral of the second kind". In: *Mathematics of Computation* 80.275 (Feb. 2011), pp. 1725–1743. DOI: `10.1090/s0025-5718-2011-02455-5`.

[134] Toshio Fukushima. "Fast computation of Jacobian elliptic functions and incomplete elliptic integrals for constant values of elliptic parameter and elliptic characteristic". In: *Celestial Mechanics and Dynamical Astronomy* 105.1-3 (Dec. 2008), pp. 245–260. DOI: `10.1007/s10569-008-9177-y`.

[135] Toshio Fukushima. "Precise and fast computation of complete elliptic integrals by piecewise minimax rational function approximation". In: *Journal of Computational and Applied Mathematics* 282 (July 2015), pp. 71–76. DOI: `10.1016/j.cam.2014.12.038`.

[136] John David Jackson. *Classical Electrodynamics*. WILEY, Aug. 1998. 832 pp. ISBN: 047130932X. URL: `https://www.ebook.de/de/product/3240907/john_david_jackson_classical_electrodynamics.html`.

[137] J.M.D. Coey. "Rare-earth magnets". In: *Endeavour* 19.4 (Jan. 1995), pp. 146–151. DOI: `10.1016/0160-9327(96)82876-6`.

[138] T. J. Nummy et al. "Large coercivity in nanostructured rare-earth-free MnxGa films". In: *Applied Physics Letters* 99.25 (Dec. 2011), p. 252506. DOI: `10.1063/1.3671329`.

[139] Marian Stingaciu et al. "High magnetic coercive field in Ca-Al-Cr substituted strontium hexaferrite". In: *Journal of Alloys and Compounds* 883 (Nov. 2021), p. 160768. DOI: `10.1016/j.jallcom.2021.160768`.

[140] Travis E. Oliphant. "Python for Scientific Computing". In: *Computing in Science & Engineering* 9.3 (2007), pp. 10–20. DOI: `10.1109/mcse.2007.58`.

[141] Pauli Virtanen et al. "SciPy 1.0: fundamental algorithms for scientific computing in Python". In: *Nature Methods* 17.3 (Feb. 2020), pp. 261–272. DOI: `10.1038/s41592-019-0686-2`.

[142] *Ansys® Academic Research Mechanical, Release 18.1*. May 2017.

[143]  R. Bjørk et al. "Comparison of adjustable permanent magnetic field sources". In: *Journal of Magnetism and Magnetic Materials* 322.22 (Nov. 2010), pp. 3664–3671. DOI: `10.1016/j.jmmm.2010.07.022`.

[144]  H. Raich and P. Blümler. "Design and construction of a dipolar Halbach array with a homogeneous field from identical bar magnets: NMR Mandhalas". In: *Concepts in Magnetic Resonance Part B: Magnetic Resonance Engineering* 23B.1 (Oct. 2004), pp. 16–25. DOI: `10.1002/cmr.b.20018`.

[145]  Paulo V. Trevizoli et al. "Design of nested Halbach cylinder arrays for magnetic refrigeration applications". In: *Journal of Magnetism and Magnetic Materials* 395 (Dec. 2015), pp. 109–122. DOI: `10.1016/j.jmmm.2015.07.023`.

[146]  Dibin Zhu et al. "Vibration energy harvesting using the Halbach array". In: *Smart Materials and Structures* 21.7 (June 2012), p. 075020. DOI: `10.1088/0964-1726/21/7/075020`.

[147]  R. Bjørk et al. "Optimization and improvement of Halbach cylinder design". In: *Journal of Applied Physics* 104.1 (July 2008), p. 013910. DOI: `10.1063/1.2952537`.

[148]  R. Bjørk. "The ideal dimensions of a Halbach cylinder of finite length". In: *Journal of Applied Physics* 109.1 (Jan. 2011), p. 013915. DOI: `10.1063/1.3525646`.

[149]  Kaspar K. Nielsen et al. "Optimizing a Halbach cylinder for field homogeneity by remanence variation". In: *Journal of Magnetism and Magnetic Materials* 514 (Nov. 2020), p. 167175. DOI: `10.1016/j.jmmm.2020.167175`.

[150]  Samuel Huber et al. "A Gradiometric Magnetic Sensor System for Stray-Field-Immune Rotary Position Sensing in Harsh Environment". In: *Proceedings* 2.13 (Dec. 2018), p. 809. DOI: `10.3390/proceedings2130809`.

[151]  Florian Slanovc, Dieter Suess and Michael Ortner. "Designing Airgap-Stable Magnetic Linear Position Systems". In: *IEEE Transactions on Magnetics* 58.9 (Sept. 2022), pp. 1–5. DOI: `10.1109/tmag.2022.3188474`.

[152]  Pavel Ripka. *Magnetic sensors and magnetometers*. Norwood, MA: Artech House, 2021. ISBN: 9781630817428.

[153]  J.E. Lenz. "A review of magnetic sensors". In: *Proceedings of the IEEE* 78.6 (June 1990), pp. 973–989. DOI: `10.1109/5.56910`.

[154]  A.E Mahdi, L Panina and D Mapps. "Some new horizons in magnetic sensing: high-Tc SQUIDs, GMR and GMI materials". In: *Sensors and Actuators A: Physical* 105.3 (Aug. 2003), pp. 271–285. DOI: `10.1016/s0924-4247(03)00106-7`.

[155]  J. Lenz and S. Edelstein. "Magnetic sensors and their applications". In: *IEEE Sensors Journal* 6.3 (June 2006), pp. 631–649. DOI: `10.1109/jsen.2006.874493`.

[156]  Alireza Samavati et al. "Magnetic field detection using a highly sensitive FBG probe". In: *Physica Scripta* 95.3 (Feb. 2020), p. 035509. DOI: `10.1088/1402-4896/ab51ed`.

[157]  Nana Yang et al. "Ultrasensitive flexible magnetoelectric sensor". In: *APL Materials* 9.2 (Feb. 2021), p. 021123. DOI: `10.1063/5.0039089`.

[158]  Yuanyuan Zhao et al. "Magnetic field sensor based on helical long-period fiber grating with a three-core optical fiber". In: *Optics Express* 29.13 (June 2021), p. 20649. DOI: `10.1364/oe.429957`.

[159]  Marina Diaz-Michelena. "Small Magnetic Sensors for Space Applications". In: *Sensors* 9.4 (Mar. 2009), pp. 2271–2288. DOI: `10.3390/s90402271`.

[160]    Daniel Cichon et al. "A Hall-Sensor-Based Localization Method With Six Degrees of Freedom Using Unscented Kalman Filter". In: *IEEE Sensors Journal* 19.7 (Apr. 2019), pp. 2509–2516. DOI: 10.1109/jsen.2018.2887299.

[161]    Nathan Campbell and Estella Atekwana. "Evaluating the efficacy of magnetic sensors in smartphones for geophysical investigations". In: *SEG Technical Program Expanded Abstracts 2018*. Society of Exploration Geophysicists, Aug. 2018. DOI: 10.1190/segam2018-2998607.1.

[162]    Vahid Nabaei, Rona Chandrawati and Hadi Heidari. "Magnetic biosensors: Modelling and simulation". In: *Biosensors and Bioelectronics* 103 (Apr. 2018), pp. 69–86. DOI: 10.1016/j.bios.2017.12.023.

[163]    Yee-Pien Yang and Yi-Yuan Ting. "Improved Angular Displacement Estimation Based on Hall-Effect Sensors for Driving a Brushless Permanent-Magnet Motor". In: *IEEE Transactions on Industrial Electronics* 61.1 (Jan. 2014), pp. 504–511. DOI: 10.1109/tie.2013.2247013.

[164]    Infineon Technologies AG. *XENSIV - sensing the world*. 2019.

[165]    Joseph P. Heremans. "Magnetic Field Sensors for Magnetic Position Sensing in Automotive Applications". In: *MRS Proceedings* 475 (1997). DOI: 10.1557/proc-475-63.

[166]    Rahaman. "Contactless magnetic linear position sensor". 9,448,087 B2. Sept. 2016.

[167]    Florian Slanovc et al. "Global magnetic topology optimization". English. In: *SSRN eLibrary* (2022).

[168]    J. Kang and S. Wang. "Shape optimization of BLDC motor using 3-D finite element method". In: *IEEE Transactions on Magnetics* 36.4 (July 2000), pp. 1119–1123. DOI: 10.1109/20.877637.

[169]    Semyung Wang, Soonkyu Jeong and Heesoo Yoon. "Continuum shape design sensitivity analysis of magnetostatic field using finite element method". In: *IEEE Transactions on Magnetics* 35.3 (May 1999), pp. 1159–1162. DOI: 10.1109/20.767154.

[170]    R. Bjørk et al. "An optimized magnet for magnetic refrigeration". In: *Journal of Magnetism and Magnetic Materials* 322.21 (Nov. 2010), pp. 3324–3328. DOI: 10.1016/j.jmmm.2010.06.017.

[171]    Martin Philip Bendsøe and Noboru Kikuchi. "Generating optimal topologies in structural design using a homogenization method". In: *Computer Methods in Applied Mechanics and Engineering* 71.2 (Nov. 1988), pp. 197–224. DOI: 10.1016/0045-7825(88)90086-2.

[172]    Chang-Seop Koh et al. "A sensitivity analysis using boundary element method for shape optimization of electromagnetic devices". In: *IEEE Transactions on Magnetics* 28.2 (Mar. 1992), pp. 1577–1580. DOI: 10.1109/20.124000.

[173]    Chang-Seop Koh et al. "Design sensitivity analysis for shape optimization of 3-D electromagnetic devices". In: *IEEE Transactions on Magnetics* 29.2 (Mar. 1993), pp. 1753–1757. DOI: 10.1109/20.250744.

[174]    Chang-Seop Koh et al. "A continuum approach in shape design sensitivity analysis of magnetostatic problems using the boundary element method". In: *IEEE Transactions on Magnetics* 29.2 (Mar. 1993), pp. 1771–1774. DOI: 10.1109/20.250748.

[175]    K. Weeber and S.R.H. Hoole. "The subregion method in magnetic field analysis and design optimization". In: *IEEE Transactions on Magnetics* 28.2 (Mar. 1992), pp. 1561–1564. DOI: 10.1109/20.123996.

[176]    S. Gitosusastro, J.L. Coulomb and J.C. Sabonnadiere. "Performance derivative calculations and optimization process". In: *IEEE Transactions on Magnetics* 25.4 (July 1989), pp. 2834–2839. DOI: 10.1109/20.34299.

[177] D.N. Dyck and D.A. Lowther. "Automated design of magnetic devices by optimizing material distribution". In: *IEEE Transactions on Magnetics* 32.3 (May 1996), pp. 1188–1193. DOI: 10.1109/20.497456.

[178] Song-Yop Hahn et al. "Inverse problem application of topology optimization method with mutual energy concept and design sensitivity". In: *IEEE Transactions on Magnetics* 36.4 (July 2000), pp. 1144–1147. DOI: 10.1109/20.877643.

[179] R. Bjørk, C.R.H. Bahl and A.R. Insinga. "Topology optimized permanent magnet systems". In: *Journal of Magnetism and Magnetic Materials* 437 (Sept. 2017), pp. 78–85. DOI: 10.1016/j.jmmm.2017.04.028.

[180] R. Bjørk and A.R. Insinga. "A topology optimized switchable permanent magnet system". In: *Journal of Magnetism and Magnetic Materials* 465 (Nov. 2018), pp. 106–113. DOI: 10.1016/j.jmmm.2018.05.076.

[181] Yoshifumi Okamoto et al. "Topology Optimization of Rotor Core Combined With Identification of Current Phase Angle in IPM Motor Using Multistep Genetic Algorithm". In: *IEEE Transactions on Magnetics* 50.2 (Feb. 2014), pp. 725–728. DOI: 10.1109/tmag.2013.2285580.

[182] Piotr Putek, Piotr Paplicki and Ryszard Palka. "Low Cogging Torque Design of Permanent Magnet Machine Using Modified Multi-Level Set Method With Total Variation Regularization". In: *IEEE Transactions on Magnetics* 50.2 (Feb. 2014), pp. 657–660. DOI: 10.1109/tmag.2013.2286297.

[183] Takeo Ishikawa et al. "Optimization of Rotor Topology in PM Synchronous Motors by Genetic Algorithm Considering Cluster of Materials and Cleaning Procedure". In: *IEEE Transactions on Magnetics* 50.2 (Feb. 2014), pp. 637–640. DOI: 10.1109/tmag.2013.2282365.

[184] A. R. Insinga et al. "Globally Optimal Segmentation of Permanent-Magnet Systems". In: *Physical Review Applied* 5.6 (June 2016), p. 064014. DOI: 10.1103/physrevapplied.5.064014.

[185] A. R. Insinga et al. "Optimally Segmented Permanent Magnet Structures". In: *IEEE Transactions on Magnetics* 52.12 (Dec. 2016), pp. 1–6. DOI: 10.1109/tmag.2016.2593685.

[186] A.R. Insinga et al. "Optimal Segmentation of Three-Dimensional Permanent-Magnet Assemblies". In: *Physical Review Applied* 12.6 (Dec. 2019), p. 064034. DOI: 10.1103/physrevapplied.12.064034.

[187] Takahiro Sato, Kota Watanabe and Hajime Igarashi. "Multimaterial Topology Optimization of Electric Machines Based on Normalized Gaussian Network". In: *IEEE Transactions on Magnetics* 51.3 (Mar. 2015), pp. 1–4. DOI: 10.1109/tmag.2014.2359972.

[188] Hidenori Sasaki and Hajime Igarashi. "Topology Optimization Accelerated by Deep Learning". In: *IEEE Transactions on Magnetics* 55.6 (June 2019), pp. 1–5. DOI: 10.1109/tmag.2019.2901906.

[189] X. Huang et al. "Evolutionary topology optimization of periodic composites for extremal magnetic permeability and electrical permittivity". In: *Structural and Multidisciplinary Optimization* 46.3 (Jan. 2012), pp. 385–398. DOI: 10.1007/s00158-012-0766-8.

[190] Claas Abert et al. "A fast finite-difference algorithm for topology optimization of permanent magnets". In: *Journal of Applied Physics* 122.11 (Sept. 2017), p. 113904. DOI: 10.1063/1.4998532.

[191] Florian Bruckner et al. "Solving Large-Scale Inverse Magnetostatic Problems using the Adjoint Method". In: *Scientific Reports* 7.1 (Jan. 2017). DOI: 10.1038/srep40816.

[192] C. Huber et al. "Topology optimized and 3D printed polymer-bonded permanent magnets for a predefined external field". In: *Journal of Applied Physics* 122.5 (Aug. 2017), p. 053904. DOI: `10.1063/1.4997441`.

[193] Gregor Wautischer et al. "A topology optimization algorithm for magnetic structures based on a hybrid FEM–BEM method utilizing the adjoint approach". In: *Scientific Reports* 12.1 (Jan. 2022). DOI: `10.1038/s41598-021-04246-z`.

[194] Mehmet Akgun et al. "Sensitivity of lumped constraints using the adjoint method". In: *40th Structures, Structural Dynamics, and Materials Conference and Exhibit*. American Institute of Aeronautics and Astronautics, Apr. 1999. DOI: `10.2514/6.1999-1314`.

[195] Michael Hinze, Rene Pinnau and Stefan Ulbrich. *Optimization with PDE Constraints*. Springer Netherlands, Nov. 2008. 284 pp. ISBN: 1402088388. URL: `https://www.ebook.de/de/product/7592733/michael_hinze_rene_pinnau_stefan_ulbrich_optimization_with_pde_constraints.html`.

[196] Joaquim R. R. A. Martins and Graeme J. Kennedy. "Enabling large-scale multidisciplinary design optimization through adjoint sensitivity analysis". In: *Structural and Multidisciplinary Optimization* 64.5 (Oct. 2021), pp. 2959–2974. DOI: `10.1007/s00158-021-03067-y`.

[197] Howard M. Adelman and Raphael T. Haftka. "Sensitivity Analysis of Discrete Structural Systems". In: *AIAA Journal* 24.5 (May 1986), pp. 823–832. DOI: `10.2514/3.48671`.

[198] Mehmet A. Akgun et al. "Efficient Structural Optimization for Multiple Load Cases Using Adjoint Sensitivities". In: *AIAA Journal* 39.3 (Mar. 2001), pp. 511–516. DOI: `10.2514/2.1336`.

[199] Jasbir S. Arora and Edward J. Haug. "Methods of Design Sensitivity Analysis in Structural Optimization". In: *AIAA Journal* 17.9 (Sept. 1979), pp. 970–974. DOI: `10.2514/3.61260`.

[200] J. S. Arora and E. J. Haug. "Efficient optimal design of structures by generalized steepest descent programming". In: *International Journal for Numerical Methods in Engineering* 10.4 (1976), pp. 747–766. DOI: `10.1002/nme.1620100404`.

[201] George Biros and Omar Ghattas. "Parallel Lagrange–Newton–Krylov–Schur Methods for PDE-Constrained Optimization. Part I: The Krylov–Schur Solver". In: *SIAM Journal on Scientific Computing* 27.2 (Jan. 2005), pp. 687–713. DOI: `10.1137/s106482750241565x`.

[202] George Biros and Omar Ghattas. "Parallel Lagrange–Newton–Krylov–Schur Methods for PDE-Constrained Optimization. Part II: The Lagrange–Newton Solver and Its Application to Optimal Control of Steady Viscous Flows". In: *SIAM Journal on Scientific Computing* 27.2 (Jan. 2005), pp. 714–739. DOI: `10.1137/s1064827502415661`.

[203] Chang-Hwan Im, Hyun-Kyo Jung and Yong-Joo Kim. "Hybrid genetic algorithm for electromagnetic topology optimization". In: *IEEE Transactions on Magnetics* 39.5 (Sept. 2003), pp. 2163–2169. DOI: `10.1109/tmag.2003.817094`.

[204] John Holland. *Adaptation in natural and artificial systems : an introductory analysis with applications to biology, control, and artificial intelligence*. Cambridge, Mass: MIT Press, 1992. ISBN: 9780262581110.

[205] Zbigniew Michalewicz. *Genetic algorithms + data structures = evolution programs*. Berlin New York: Springer-Verlag, 1996. ISBN: 3540606769.

[206] David Goldberg. *Genetic algorithms in search, optimization, and machine learning*. Reading, Mass: Addison-Wesley Publishing Company, 1989. ISBN: 0201157675.

[207]  C. D. Chapman, K. Saitou and M. J. Jakiela. "Genetic Algorithms as an Approach to Configuration and Topology Design". In: *Journal of Mechanical Design* 116.4 (Dec. 1994), pp. 1005–1012. DOI: 10.1115/1.2919480.

[208]  Mark J. Jakiela et al. "Continuum structural topology design with genetic algorithms". In: *Computer Methods in Applied Mechanics and Engineering* 186.2-4 (June 2000), pp. 339–356. DOI: 10.1016/s0045-7825(99)00390-4.

[209]  Xin-She Yang and Suash Deb. "Cuckoo Search via Lévy flights". In: *2009 World Congress on Nature & Biologically Inspired Computing (NaBIC)*. IEEE, 2009. DOI: 10.1109/nabic.2009.5393690.

[210]  Xiangtao Li and Minghao Yin. "Modified cuckoo search algorithm with self adaptive parameter method". In: *Information Sciences* 298 (Mar. 2015), pp. 80–97. DOI: 10.1016/j.ins.2014.11.042.

[211]  Yoshifumi Okamoto and Norio Takahashi. "A Novel Topology Optimization of Nonlinear Magnetic Circuit Using ON/OFF Method". In: *IEEJ Transactions on Fundamentals and Materials* 125.6 (2005), pp. 549–553. DOI: 10.1541/ieejfms.125.549.

[212]  Ole Sigmund Martin Philip Bendsoe. *Topology Optimization*. Springer Berlin Heidelberg, Dec. 2003. 388 pp. ISBN: 3540429921. URL: https://www.ebook.de/de/product/5640654/martin_philip_bendsoe_ole_sigmund_topology_optimization.html.

[213]  Paul Heistracher et al. "GPU-Accelerated Atomistic Energy Barrier Calculations of Skyrmion Annihilations". In: *IEEE Transactions on Magnetics* 54.11 (Nov. 2018), pp. 1–5. DOI: 10.1109/tmag.2018.2847446.

[214]  Saad Hikmat Haji and Adnan Mohsin Abdulazeez. "COMPARISON OF OPTIMIZATION TECHNIQUES BASED ON GRADIENT DESCENT ALGORITHM: A REVIEW". In: *PalArch's Journal of Archaeology of Egypt / Egyptology* 18.4 (Feb. 2021), pp. 2715–2743. URL: https://www.archives.palarch.nl/index.php/jae/article/view/6705.

[215]  C. G. Broyden. "Quasi-Newton methods and their application to function minimisation". In: *Mathematics of Computation* 21.99 (1967), pp. 368–381. DOI: 10.1090/s0025-5718-1967-0224273-2.

[216]  Philipp Hennig and Martin Kiefel. "Quasi-Newton Methods: A New Direction". In: *J. Mach. Learn. Res.* 14.1 (Mar. 2013), pp. 843–865. ISSN: 1532-4435.

[217]  R. Fletcher. "An Overview of Unconstrained Optimization". In: *Algorithms for Continuous Optimization*. Springer Netherlands, 1994, pp. 109–143. DOI: 10.1007/978-94-009-0369-2_5.

[218]  Seif-Eddeen K. Fateen and Adrián Bonilla-Petriciolet. "Gradient-Based Cuckoo Search for Global Optimization". In: *Mathematical Problems in Engineering* 2014 (2014), pp. 1–12. DOI: 10.1155/2014/493740.

[219]  P.R. Chowdhury, Y.P. Singh and R.A. Chansarkar. "Hybridization of gradient descent algorithms with dynamic tunneling methods for global optimization". In: *IEEE Transactions on Systems, Man, and Cybernetics - Part A: Systems and Humans* 30.3 (May 2000), pp. 384–390. DOI: 10.1109/3468.844362.

[220]  Mahmud Iwan Solihin and Mohd Fauzi Zanil. "Performance Comparison of Cuckoo Search and Differential Evolution Algorithm for Constrained Optimization". In: *IOP Conference Series: Materials Science and Engineering* 160 (Nov. 2016), p. 012108. DOI: 10.1088/1757-899x/160/1/012108.

[221] Nobuo Hayashi, Koji Saito and Yoshinobu Nakatani. "Calculation of Demagnetizing Field Distribution Based on Fast Fourier Transform of Convolution". In: *Japanese Journal of Applied Physics* 35.Part 1, No. 12A (Dec. 1996), pp. 6065–6073. DOI: 10.1143/jjap.35.6065.

[222] Karl Fabian et al. "Three-dimensional micromagnetic calculations for magnetite using FFT". In: *Geophysical Journal International* 124.1 (Jan. 1996), pp. 89–104. DOI: 10.1111/j.1365-246x.1996.tb06354.x.

[223] C. Huber et al. "3D print of polymer bonded rare-earth magnets, and 3D magnetic field scanning with an end-user 3D printer". In: *Applied Physics Letters* 109.16 (Oct. 2016), p. 162401. DOI: 10.1063/1.4964856.

[224] Ling Li et al. "Big Area Additive Manufacturing of High Performance Bonded NdFeB Magnets". In: *Scientific Reports* 6.1 (Oct. 2016). DOI: 10.1038/srep36212.

[225] Christian Huber et al. "Additive Manufactured and Topology Optimized Passive Shimming Elements for Permanent Magnetic Systems". In: *Scientific Reports* 8.1 (Oct. 2018). DOI: 10.1038/s41598-018-33059-w.

[226] Zhongxu Wang et al. "An electrodynamic energy harvester with a 3D printed magnet and optimized topology". In: *Applied Physics Letters* 114.1 (Jan. 2019), p. 013902. DOI: 10.1063/1.5074123.

[227] Ester Maria Palmero et al. "Magnetic-Polymer Composites for Bonding and 3D Printing of Permanent Magnets". In: *IEEE Transactions on Magnetics* 55.2 (Feb. 2019), pp. 1–4. DOI: 10.1109/tmag.2018.2863560.

[228] Christian Huber et al. "Polymer-bonded anisotropic $SrFe_{12}O_{19}$ filaments for fused filament fabrication". In: *Journal of Applied Physics* 127.6 (Feb. 2020), p. 063904. DOI: 10.1063/1.5139493.

[229] Klaus Sonnleitner et al. "3D printing of polymer-bonded anisotropic magnets in an external magnetic field and by a modified production process". In: *Applied Physics Letters* 116.9 (Mar. 2020), p. 092403. DOI: 10.1063/1.5142692.

[230] Julia Simińska-Stanny et al. "4D printing of patterned multimaterial magnetic hydrogel actuators". In: *Additive Manufacturing* 49 (Jan. 2022), p. 102506. DOI: 10.1016/j.addma.2021.102506.

[231] Xiangxia Wei et al. "Advances in 3D printing of magnetic materials: Fabrication, properties, and their applications". In: *Journal of Advanced Ceramics* 11.5 (Apr. 2022), pp. 665–701. DOI: 10.1007/s40145-022-0567-5.

[232] Wolfram Research Inc. *Mathematica, Version 10.1*. Champaign, IL, 2015.

[233] Albert Rich, Patrick Scheibe and Nasser Abbasi. "Rule-based integration: An extensive system of symbolic integration rules". In: *Journal of Open Source Software* 3.32 (Dec. 2018), p. 1073. DOI: 10.21105/joss.01073.

[234] I. S. Gradshteyn. *Table of integrals, series and products*. Oxford: Academic, 2007. ISBN: 9780080471112.

[235] Roland Bulirsch. "Numerical calculation of elliptic integrals and elliptic functions". In: *Numerische Mathematik* 7.1 (Feb. 1965), pp. 78–90. DOI: 10.1007/bf01397975.

[236] R. Bulirsch. "Numerical calculation of elliptic integrals and elliptic functions. III". In: *Numerische Mathematik* 13.4 (Aug. 1969), pp. 305–315. DOI: 10.1007/bf02165405.

[237] Thibaut Labbe and Bruno Dehez. "Convexity-Oriented Mapping Method for the Topology Optimization of Electromagnetic Devices Composed of Iron and Coils". In: *IEEE Transactions on Magnetics* 46.5 (May 2010), pp. 1177–1185. DOI: 10.1109/tmag.2009.2037754.

[238]   Stefan Hildebrandt Mariano Giaquinta. *Calculus of Variations I*. Springer Berlin Heidelberg, June 2004. 508 pp. ISBN: 354050625X. URL: `https://www.ebook.de/de/product/3019789/mariano_giaquinta_stefan_hildebrandt_calculus_of_variations_i.html`.

[239]   Andrew J. Newell, Wyn Williams and David J. Dunlop. "A generalization of the demagnetizing tensor for nonuniform magnetization". In: *Journal of Geophysical Research* 98.B6 (1993), p. 9551. DOI: `10.1029/93jb00694`.

[240]   Dieter Suess et al. "Spin Torque Efficiency and Analytic Error Rate Estimates of Skyrmion Racetrack Memory". In: *Scientific Reports* 9.1 (Mar. 2019). DOI: `10.1038/s41598-019-41062-y`.

[241]   O. Muthsam et al. "The superior role of the Gilbert damping on the signal-to-noise ratio in heat-assisted magnetic recording". In: *Journal of Magnetism and Magnetic Materials* 514 (Nov. 2020), p. 167125. DOI: `10.1016/j.jmmm.2020.167125`.

[242]   Sabri Koraltan et al. "Dependence of energy barrier reduction on collective excitations in square artificial spin ice: A comprehensive comparison of simulation techniques". In: *Physical Review B* 102.6 (Aug. 2020), p. 064410. DOI: `10.1103/physrevb.102.064410`.

[243]   Naëmi Leo et al. "Chiral switching and dynamic barrier reductions in artificial square ice". In: *New Journal of Physics* 23.3 (Mar. 2021), p. 033024. DOI: `10.1088/1367-2630/abe3ad`.

[244]   Sabri Koraltan et al. "Tension-free Dirac strings and steered magnetic charges in 3D artificial spin ice". In: *npj Computational Materials* 7.1 (Aug. 2021). DOI: `10.1038/s41524-021-00593-7`.

[245]   Dieter Suess, Florian Slanovc and Udo Ausserlechner. "Comment to the paper "A new Hall-effect enabled voltage amplifier device based on magnetic and thermal properties of materials"". In: *Journal of Magnetism and Magnetic Materials* 547 (Apr. 2022), p. 168942. DOI: `10.1016/j.jmmm.2021.168942`.

[246]   Dieter Suess et al. *Accurate finite-difference micromagnetics of magnets including RKKY interaction – analytical solution and comparison to standard micromagnetic codes*. 2022. DOI: `10.48550/ARXIV.2206.11063`.

[247]   Claas Abert et al. "Origin of noncollinear magnetization coupling across RuX layers". In: *Physical Review B* 106.5 (Aug. 2022), p. 054401. DOI: `10.1103/physrevb.106.054401`.